

Development of Spectroscopic Identification and Analysis of Haemoglobin Components in Bruises

by

Josie Pearl Nunn

*Thesis
Submitted to Flinders University
for the degree of*

Doctor of Philosophy
College of Science and Engineering
19th March 2020

All we know is infinitely less than all that remains unknown.

~ William Harvey

Contents

Thesis Summary	1
Declaration	2
Acknowledgements	3
Abbreviations	4
1 Introduction.....	5
1.1 The Bruise	5
1.1.1 The Blood.....	6
<i>1.1.1.1 Haemoglobin.....</i>	<i>7</i>
1.1.1.1.1 Structure and Bonding.....	7
1.1.1.1.2 Oxyhaemoglobin, Deoxyhaemoglobin & Transport	11
1.1.1.1.3 Carboxyhaemoglobin.....	15
1.1.1.1.4 Sulphaemoglobin.....	16
1.1.1.1.5 Methaemoglobin.....	17
1.1.1.1.6 Breakdown of Haemoglobin in a Bruise	18
1.1.1.1.7 Biliverdin and Bilirubin.....	20
1.1.1.1.8 Ferritin and Haemosiderin	25
1.1.2 Establishing Bruise Age	26
1.2 Spectroscopy	29
1.2.1 Transmission vs. Reflectance Spectroscopy	30
<i>1.2.1.1 The Integrating Sphere.....</i>	<i>32</i>
<i>1.2.1.2 Attenuated Total Reflectance (ATR)</i>	<i>33</i>
1.2.2 The Australian Synchrotron	33
<i>1.2.2.1 Far Infrared (FIR) / Terahertz (THz) Beamline</i>	<i>34</i>

1.2.2.1.1	Diamond Window Liquid Cell (DWLC).....	35
2	Project Aims	36
3	Materials and Methods	37
3.1	Materials	37
3.1.1	Commercial Materials	37
3.1.2	Prepared Materials.....	39
3.2	Instrumentation.....	42
3.2.1	Novel Instrumentation Arrangements	44
3.2.1.1	<i>Perkin Elmer UV-Vis.-NIR Lambda 950 Spectrophotometer</i>	44
3.2.1.1.1	Calibration Validation for Disclaimer Error! Bookmark not defined.	
3.2.1.2	<i>ASD FieldSpec. with Integrating Sphere</i>	45
3.2.1.3	<i>CHEMUSB4-Vis.-NIR Spectrophotometer with Integrating Sphere</i> 46	
3.2.1.4	<i>Far Infrared (FIR) / THz Beamline</i>	47
3.3	Methods	47
3.3.1	Transport of Samples.....	47
3.3.2	Solution Preparations	48
3.3.2.1	<i>Phosphate Buffered Saline Solution</i>	48
3.3.2.2	<i>Blood Plasma</i>	48
3.3.2.3	<i>Methaemoglobin Formation</i>	48
3.3.2.4	<i>Biliverdin Solutions</i>	49
3.3.2.5	<i>Bilirubin Solutions</i>	49
3.3.2.6	<i>Ferritin Dilutions</i>	50
3.3.3	Sample Preparation for UV-Vis. Transmission Spectroscopy	50
3.3.4	Sample Preparation for UV-Vis.-NIR Reflectance Spectroscopy.....	50

3.3.4.1	<i>Re-suspension of Dried Blood</i>	50
3.3.5	Sample Preparation for FIR / THz Beamline	51
3.3.5.1	<i>Pellets</i>	51
3.3.5.1.1	Dried Blood and Ferritin.....	51
3.3.5.2	<i>Diamond Window Liquid Cells</i>	52
3.3.6	Analysis using UV-Vis. Transmission Spectroscopy.....	52
3.3.7	Analysis using UV-Vis.-NIR Reflectance Spectroscopy	53
3.3.7.1	<i>Perkin Elmer UV-Vis.-NIR Spectrophotometer</i>	53
3.3.7.1.1	Spectra Smoothing.....	53
3.3.7.2	<i>ASD FieldSpec. with Integrating Sphere</i>	53
3.3.7.3	<i>CHEMUSB4-Vis.-NIR Spectrophotometer with Integrating Sphere</i> 54	
3.3.7.4	<i>FTIR Microscope with ATR Accessory</i>	54
3.3.8	Analysis using the FIR / THz Beamline.....	54
3.3.8.1	<i>Acquisition and Processing</i>	54
3.3.8.2	<i>Detectors</i>	55
3.3.8.3	<i>Diamond Window Liquid Cells</i>	55
3.3.8.4	<i>Cryostat Cryogenic Analysis</i>	55
3.3.8.5	<i>Processing Fringed Spectra</i>	56
3.3.8.6	<i>ATR Accessory</i>	57
4	Results	57
4.1	Transmission Spectroscopy.....	57
4.1.1	Ultraviolet-Visible-Near Infrared (UV-Vis.-NIR)	57
4.1.1.1	<i>Stored Blood</i>	57
4.1.1.2	<i>Methaemoglobin</i>	58
4.1.1.3	<i>Biliverdin</i>	59

4.1.2	Far Infrared (FIR).....	60
4.1.2.1	<i>Pellets</i>	60
4.1.2.1.1	Pure.....	60
4.1.2.1.1.1	Biliverdin.....	60
4.1.2.1.1.2	Bilirubin.....	60
4.1.2.1.1.3	Bilirubin Conjugate	60
4.1.2.1.1.4	Ferritin	61
4.1.2.1.2	Polyethylene (PE).....	61
4.1.2.1.2.1	Blood.....	61
4.1.2.1.2.2	Biliverdin.....	63
4.1.2.1.2.3	Bilirubin.....	64
4.1.2.1.2.4	Bilirubin Conjugate	65
4.1.2.1.2.5	Biliverdin, Bilirubin and Bilirubin Conjugate Mixtures....	67
4.1.2.1.2.6	Ferritin	69
4.1.2.1.3	Polytetrafluorethylene (PTFE).....	70
4.1.2.1.3.1	Bilirubin.....	70
4.1.2.1.4	Potassium Bromide (KBr)	71
4.1.2.1.4.1	Blood.....	71
4.1.2.1.4.2	Biliverdin.....	72
4.1.2.1.4.3	Bilirubin.....	74
4.1.2.1.4.4	Biliverdin and Bilirubin Mixtures	76
4.1.2.1.4.5	Ferritin	Error! Bookmark not defined.
4.1.2.1.5	Paraffin Wax.....	78
4.1.2.1.5.1	Human Haemoglobin.....	78
4.1.2.1.5.2	Biliverdin.....	78
4.1.2.1.5.3	Bilirubin.....	79

4.1.2.1.5.4	Bilirubin Conjugate	80
4.1.2.1.6	Biliverdin and Bilirubin Pellet Comparisons.....	81
4.1.2.2	<i>Diamond Window Liquid Cells</i>	83
4.1.2.2.1	Solvents.....	83
4.1.2.2.1.1	Water.....	83
4.1.2.2.1.2	Dimethyl Sulfoxide (DMSO)	87
4.1.2.2.1.3	Chloroform	100
4.1.2.2.1.4	Ethanol.....	100
4.1.2.2.1.5	Methanol.....	101
4.1.2.2.2	Human Haemoglobin.....	101
4.1.2.2.3	Blood.....	106
4.1.2.2.4	Biliverdin	107
4.1.2.2.5	Bilirubin.....	119
4.1.2.2.6	Bilirubin Conjugate	127
4.2	Reflectance Spectroscopy	129
4.2.1	Ultraviolet-Visible-Near Infrared (UV-Vis.-NIR)	129
4.2.1.1	<i>Perkin Elmer UV-Vis.-NIR Spectrophotometer</i>	129
4.2.1.1.1	Validation Disclaimer.....	Error! Bookmark not defined.
4.2.1.1.2	Solvents.....	129
4.2.1.1.3	Blood.....	130
4.2.1.1.3.1	Oxyhaemoglobin.....	130
4.2.1.1.3.2	Methaemoglobin.....	135
4.2.1.1.4	Biliverdin	137
4.2.1.1.5	Bilirubin.....	138
4.2.1.1.6	Ferritin	140
4.2.1.2	<i>ASD FieldSpec.[®] 4 Hi-Res Spectroradiometer with ISP-REF</i>	

<i>Integrating Sphere</i>	142
4.2.1.2.1 Blood.....	142
4.2.1.2.2 Biliverdin.....	143
4.2.1.2.3 Ferritin.....	144
4.2.1.3 <i>Ocean Optics CHEMUSB4-Vis.-NIR Spectrophotometer with ISP-REF Integrating Sphere</i>	144
4.2.1.3.1 Blood.....	144
4.2.2 Mid Infrared (MIR).....	146
4.2.2.1 <i>Thermo Fisher Nicolet™ Continuum™ FTIR Microscope with ATR Accessory</i> 146	
4.2.2.1.1 Blood.....	146
4.2.2.1.2 Biliverdin.....	147
4.2.2.1.3 Bilirubin.....	149
4.2.2.1.4 Biliverdin & Bilirubin Mixtures.....	151
4.2.2.1.5 Ferritin.....	154
4.2.3 Far Infrared (FIR).....	155
4.2.3.1 <i>ATR</i>	155
4.2.3.1.1 Blood.....	155
4.2.3.1.2 Methaemoglobin.....	156
4.2.3.1.3 Human Haemoglobin.....	157
4.2.3.1.4 Biliverdin.....	158
4.2.3.1.5 Bilirubin.....	159
4.2.3.1.6 Bilirubin Conjugate.....	161
4.2.3.1.7 Biliverdin & Bilirubin Mixtures.....	163
4.2.3.1.8 Ferritins.....	164
5 Discussion and Conclusions.....	165

5.1	UV-Vis. Spectroscopy.....	166
5.2	NIR Spectroscopy.....	168
5.3	MIR Spectroscopy	169
5.4	FIR Spectroscopy	171
5.4.1	Pellets	172
5.4.2	Paraffin Wax Pellets.....	176
5.4.3	Diamond Window Liquid Cells	177
5.4.4	ATR-FIR Spectroscopy.....	184
5.5	Concluding Remarks	187
6	Future Studies.....	188
7	References.....	190

Thesis Summary

Bruises form with blunt trauma to the surface of the skin that ruptures vessels, releasing blood which breaks down into biliverdin and bilirubin exhibiting a variety of discolouration over time. Identification of bruise age is crucial in forensic investigations into suspicious deaths, however current methods of gathering information from the breakdown process of blood can be misleading. The original contribution to knowledge in this thesis is the development of spectroscopic (particularly far infrared) identification of differences in key indicators of a bruise's age; haemoglobin breakdown components.

Analysis with an ASD FieldSpec[®]4 Hi-Res: high resolution spectroradiometer coupled to a 150 mm integrating sphere has potential for mobile and rapid preliminary scanning in the UV-Vis.-NIR region of the electromagnetic spectrum but NIR sensitivity is low. A main concern is water, a physiological solvent, which was found to strongly absorb in the IR region.

MIR and FIR out-of-vacuum ATR analyses at Flinders University and the Australian Synchrotron (THz/FIR beamline) of samples in solid and liquid phase at various concentrations (low to high) presented distinguishable spectra of biliverdin and bilirubin. Different vibrations presented, some attributed to the presence or lack of intramolecular hydrogen bonding in bilirubin, may be fundamental information for identification of early to late stages of bruise breakdown, hence establishment of age.

Additionally, FIR transmission analysis of pure material, PE and KBr pellets provided extended wavenumber range (with Siolo, Si:B and MCT_N detectors on the THz beamline) for key biliverdin and bilirubin differences. However, Diamond Window Liquid Cells require further research and development as little to no characteristic vibrations are detected when samples are analysed in dilute liquid phase, possibly due to fundamentally different interactions in liquid phase as compared to solid state.

Declaration

I declare that this thesis does not incorporate without acknowledgment any material previously submitted for a degree in any university; and that to the best of my knowledge and belief it does not contain any material previously published or written by another person except where due reference is made in the text.

Josie Pearl Nunn

17 December 2018

Acknowledgements

This project has been an incredible feat and there are people I would like to acknowledge for their constructive support to completion.

Firstly, I would thank my principal supervisor, Associate Professor Stewart Walker of Flinders University for accepting me as his doctorate student, for his suggestions and advice towards the project which he can provide at the drop of a hat, and for his fascinating ability to inspire me to learn more.

I thank my adjunct supervisor, Associate Professor Neil Langlois of the Forensic Science Centre of South Australia for his suggestions and guidance from a medico perspective, for the supply of oxyhaemoglobin and its derivatives for the project, and for his black humour.

Thank you to the Australian Synchrotron for accepting 5 applications relating to this project and to their FIR/THz beamline scientists, Dominique Appadoo and Ruth Plathe for beamtime support. Your help and intelligence have been truly invaluable to this project.

Thank you also to the technical staff at Flinders University, David Vincent, Lydia Dieu, Peter Pfeiffer, Sandra Marshall and Melissa Schlein for instrumental training, glassware loans, chemical purchasing and general assistance.

I'd like to offer an extended word of thanks to Stewart Walker's research group for their progressive feedback and making the research laboratory a fun workspace.

I also thank the Australian Government Research Training Program Support and Flinders University Finance and Procurement for understanding when I needed time off from employment to pursue my academic development.

I thank my family and friends, particularly Russell Fuller and Pinkham Thanavanh for challenging my thoughts and opinions as well as giving me motivation and determination to work on this project.

Lastly, I would like to say a thank you to my fiancé, Kristijan Ramesa. Without you, I would have quit. You have given me so much strength and intent to reach my goal.

It's been a rollercoaster of a project and I sincerely appreciate all the encouragement and feedback received. I've always treasured science and knowledge in my heart, and now this project has given me a once in a lifetime experience to cherish.

Abbreviations

HbO ₂	Oxyhaemoglobin
Hb	Haemoglobin
Met-Hb	Methaemoglobin
HbCO	Carboxyhaemoglobin
Sulf-Hb	Sulphaemoglobin
PBS	Phosphate Buffered Saline solution
Def	Defibrinated
ACD	Acid Citrate Dextrose
LiHep	Lithium Heparin
PE	Polyethylene
PTFE	Polytetrafluoroethylene
KBr	Potassium Bromide
DWLC	Diamond Window Liquid Cell
UV-Vis	Ultraviolet-Visible
IR	Infrared
NIR	Near-infrared
FIR	Far-infrared
Approx	Approximately
min	Minute
nm	Nanometre
a.u.	Absorbance Unit
μL	Microliter
mL	Millilitre
L	Litres
M	Mole/Litre (mol/L)
Å	Ångström
THz	Tera-Hertz
mA	Milli-Amp
mBar	Millibar

1 Introduction

1.1 The Bruise

Human skin is part of the integumentary system and is composed of three layers as shown in Figure 1-1: (A); the outermost epidermis (approximately 0.2 mm thick), dermis (1-4 mm) and innermost hypodermis or subcutaneous tissue (4-9 mm) [1, 2]. The hypodermis is semi-fluid, containing blood vessels that branch into the dermis layer as well as adipose tissue (fat that acts as insulation and padding for underlying muscle tissue) [1, 2].

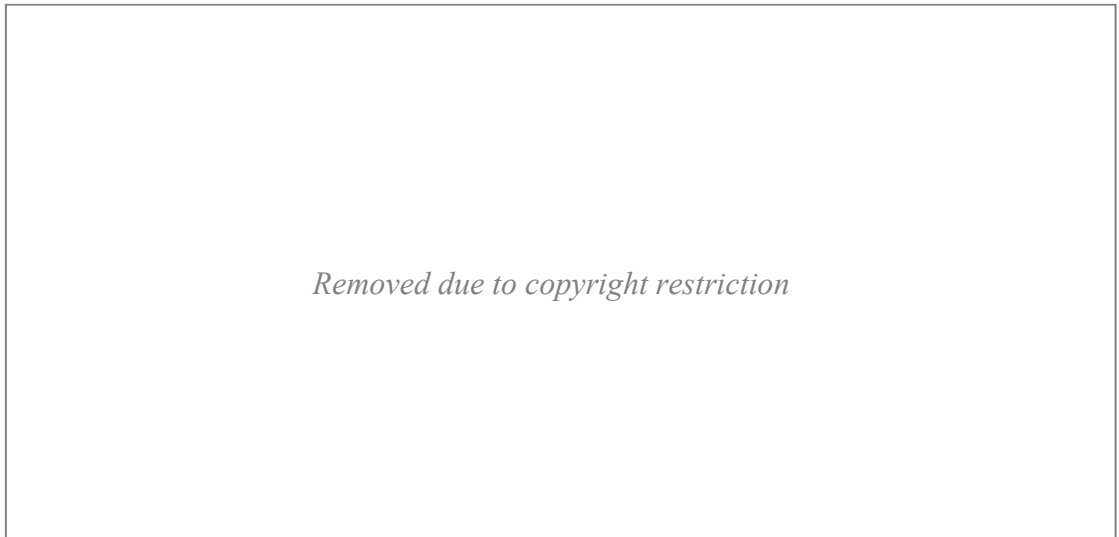


Figure 1-1: (A) Illustration of the mammalian integumentary system [1] and (B) a photograph of discolouration in a bruise [3].

The thickness of the skin may vary depending on sex, age and location on the body [4]. For example, the supporting elastic tissue in the elderly is fragile [5, 6].

With blunt trauma or compression to the surface of skin [7, 8], blood vessels may tear or rupture, causing the release of blood or bleeding into the skin layers [5, 6, 9], while the epiderms and demis layers of skin remain intact [10, 11]. This may result in visible discolouration of the skin surface as seen in Figure 1-1: (B) which is called a bruise [3, 6, 11, 12].

This apparent discolouration is dependent on the incident light, age of the injured person, a person's tendency to bruise, temperature, medication, force of impact, skin pigmentation, location of the bruise and depth of the blood in the skin tissue [6, 7,

10, 11, 13-22]. It can change with time due to the presence or lack of blood and its derivatives as the blood in the tissue breaks down [6, 7, 10, 11, 13, 15, 18, 20, 22].

1.1.1 The Blood

Blood is a fundamental component of the cardiovascular system and is primarily concerned with transport of nutrients and waste products [23-25].

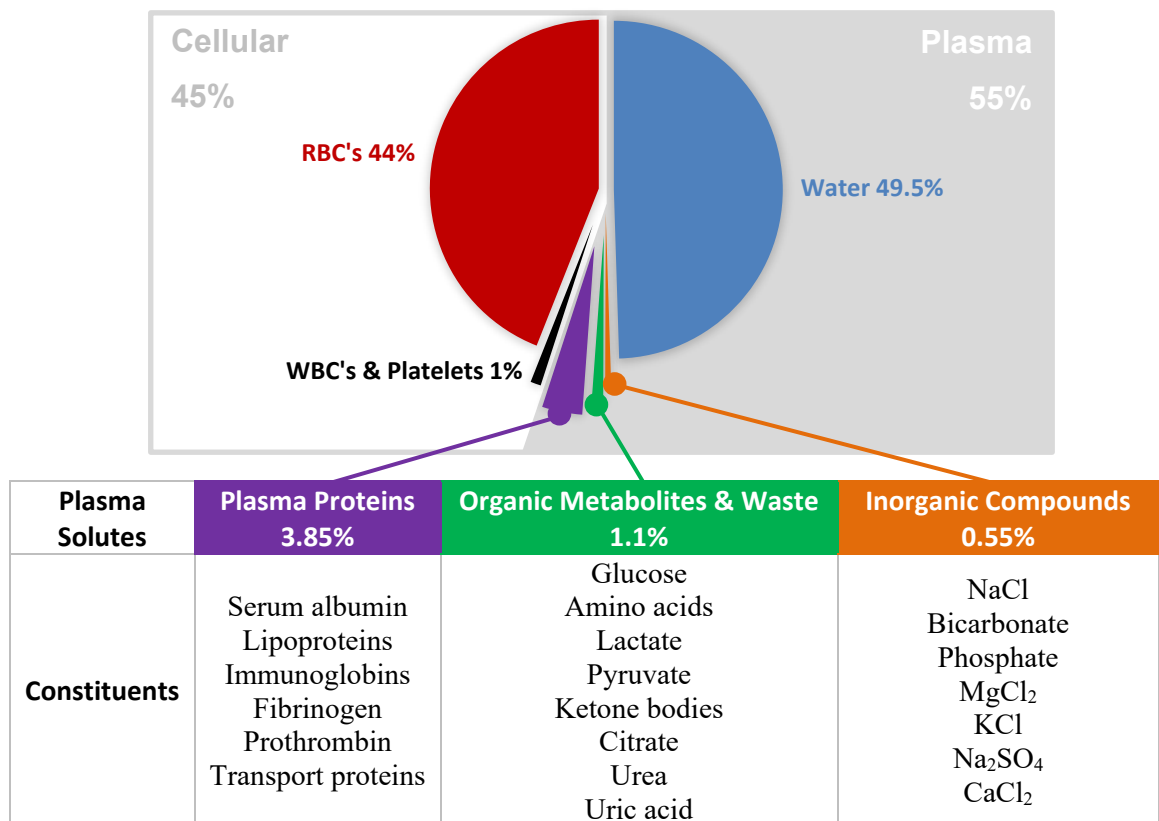


Figure 1-2: Cellular and Plasma constituents of whole blood adapted from [2, 23, 25].

An average adult human being contains 5-6 litres of whole blood consisting of approximately 55% plasma (see Figure 1-2) [2, 23, 25]. This is a clear-yellow liquid that predominately contains water in which gases, inorganic compounds, organic metabolites and waste constituents (See Table 1-1) are soluble [23]. Some of these constituents are responsible for maintaining blood pH and osmotic balance [2, 23].

The remaining 45% of whole blood comprises cells and cell fragments with specialised function; white blood cells (WBC's), platelets and red blood cells

(RBC's) [2, 23, 25]. WBC's are produced in the bone marrow and although they make up less than 1% of blood's cellular component, they have significant purpose; to recognise and neutralise pathogens as part of the immune response [2, 23]. There are five main types of WBC's having varying lifetimes from hours to years, but all of which contain a nucleus and mitochondria [2, 23]. Some recognise specific microorganisms to initiate an immune response, and others such as macrophages are responsible for engulfing and breaking down pathogenic invaders [2, 23, 26, 27].

Red blood cells (erythrocytes) are the major cell component in whole blood [2, 23, 25]. Each person has 25-30 trillion RBC's in their blood, which approximates to 5 billion erythrocytes in 1 mL of blood [2]. Similar to WBC's, RBC's are also produced in bone marrow, however they possess an average lifespan of 120 days (70 days in a newborn) and lack a nucleus and mitochondria [23, 28]. During their lifetime in blood, RBC's transport oxygen (O₂) and carbon dioxide (CO₂) to and from tissues in the body via passive diffusion of the gases in the lungs, as they contain the oxygen-binding protein, haemoglobin [1, 2, 25].

1.1.1.1 Haemoglobin

A single red blood cell contains 250 million haemoglobin molecules, delivering the potential to transport 1 billion molecules of oxygen [2]. This is only possible due to the highly evolved structure and bonding of haemoglobin [2].

1.1.1.1.1 Structure and Bonding

Haemoglobin is a protein, which varies slightly between mammalian species, but the basic structure is similar [1, 25, 29]. Proteins begin as amino acids (Figure 1-3), which are compounds that contain a carboxyl and amine functional group attached to the same carbon atom, differing only by the side chain, R-group [25]. Side chains categorise amino acids into polar, nonpolar, aromatic, positively charged and negatively charged groups, hence influence the solubility and electronegativity of the overall amino acid [25].

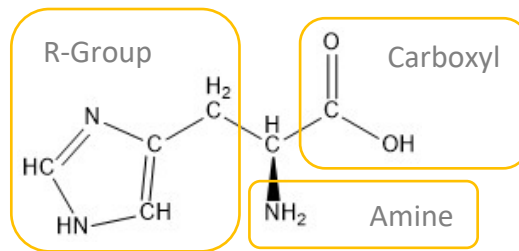


Figure 1-3: Chemical structure of an amino acid, histidine adapted from [25].

Two amino acids polymerise with the loss of a water molecule as in Figure 1-4, forming a covalent backbone of $-C_a-C_b-N-C_a-$, where the C_b-N bond is planar with the oxygen bound to C_b in trans confirmation to the hydrogen bound to the nitrogen (illustrated in red in Figure 1-4) [25]. There is free rotation about the C_a-C_b and $N-C_a$ bonds, allowing a variety of spatial arrangements concerning R-groups [25]. When several amino acids polymerise with one another in a sequence, this is known as the primary structure of the protein, a polypeptide chain [25].

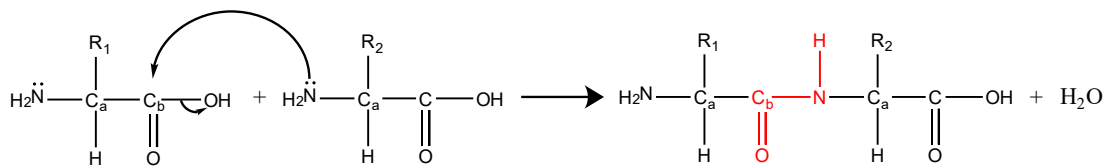


Figure 1-4: Amino acid polymerisation adapted from [25].

Protein structure is stabilised by thermodynamically favoured conformations having the lowest Gibbs free energy, referred to as the native conformation [25]. Disulphide bonding, hydrogen bonding, hydrophobic and ionic interactions may also contribute to structure stability [25]. Although 4-30 kJ/mol is required to break the latter weaker interactions compared to 200-460 kJ/mol for a single covalent bond, weaker bonds tend to enhance stability farther due to larger quantities present in proteins [25].

Such bonding of atoms in a segment of a polypeptide, regardless of R-group conformations and other segments in the chain, give rise to a protein's secondary structure [25]. Common types of secondary structures include α helix, β confirmation, β turn and undefined (random structure) [25].

An α helix arranges polypeptide backbone atoms ($-C_a-C_b-N-C_a-$) in a longitudinal left-handed or right-handed spiral, where a single helical turn consists of on average

3.6 amino acids (see Figure 1-5: A) [25]. R-groups extend outward and hydrogen bonding of almost every peptide bond in a turn to adjacent turns conserves the structure; the hydrogen on the N atom hydrogen bonds to the carbonyl oxygen on the C_β atom, 3 amino acids along the polypeptide chain [25]. Not all amino acids have an affinity for the helical structure due to R-group steric bulk, restriction of rotation or dipole characteristics [25].

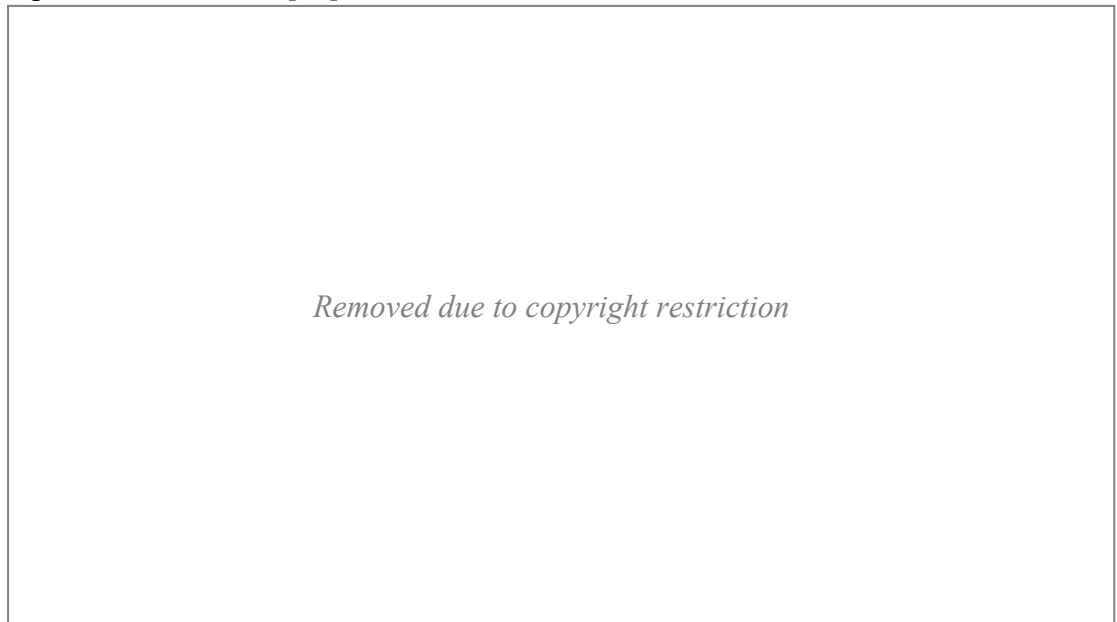


Figure 1-5: Secondary structures of a protein (A) an alpha helix and (B) a beta sheet [25].

In contrast to the α helix, a β confirmation arranges polypeptide backbone atoms in a zigzag series of sheets (β sheets, as shown in Figure 1-5: B), where adjacent polypeptide segments hydrogen bond, keeping R-groups extended perpendicular to the β sheets (Figure 1-5 (B) side view) [25]. β sheets can be formed with parallel (similar amine and carboxyl alignments) or antiparallel segments close to one another or further down the polypeptide chain [25]. Figure 1-5 illustrates an antiparallel segment bonding in the top view. Like α helix arrangements, some amino acids hinder the β confirmation as β sheets are layered close together, requiring smaller R-groups [25].

A polypeptide chain can often turn 180° to reverse direction forming a β turn (Figure 1-6), which involves four amino acids, having the oxygen on the first amino acid's C_β atom hydrogen bond to the hydrogen on the fourth amino acid's nitrogen [25]. Amino acids that are small and readily employ a cis- configuration are favourable for

particularly tight β turns [25]. In fact, a third of amino acids in globular proteins are β turns as they satisfy compactly folded structures [25].

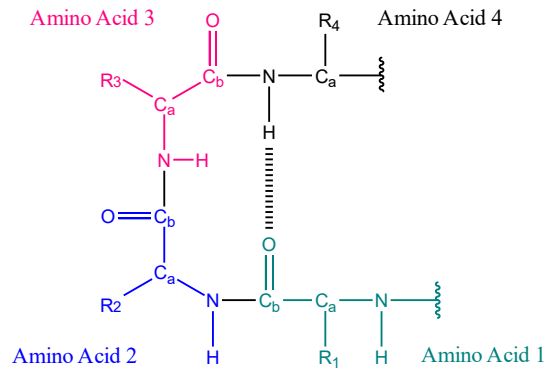


Figure 1-6: A beta turn involving four amino acids adapted from [25].

The completely folded three-dimensional arrangement of a protein is called the tertiary structure and is governed by the interactions between segments that are otherwise far apart [25]. When this structure combines with another or more, it is referred to as a subunit of a larger protein, the resulting confirmation being the quaternary structure [25].

Proteins with quaternary structures can be classified as fibrous, where subunits employ thread-like confirmation, or globular, where subunits utilise spherical confirmation [25]. Fibrous proteins, such as collagen (found in connective tissue, tendons, cartilage, bone and the eye's cornea), provide support, shape and protection [25]. However, the globular confirmation is exercised by enzymes and proteins related to motor, immune, regulatory and transport functions, such as haemoglobin [25].

Haemoglobin is almost 5.5 nm in diameter, with a total molecular weight of 64,500 g/mol and consists of two subunit pairs, each containing an ' α ' (141 amino acids long) and ' β ' (146 amino acids long) polypeptide chain in adults [2, 25, 30]. Rather than the ' β ' subunit, a fetus contains a ' γ ' subunit, which has a higher affinity for oxygen [25].

The ' α ' and ' β ' subunits in haemoglobin are related by twofold cyclic symmetry, where one $\alpha\beta$ pair is superimposable on the other with rotation about one axis [25].

The subunits in haemoglobin possess 70% α helices with intermittent β turns and accommodate almost all R-groups within their centres, creating internal hydrophobicity [25]. Each subunit incorporates a protoporphyrin that complexes a ferrous ion (Fe^{2+}) via four nitrogens (Figure 1-7) [1, 25, 29, 31, 32]. This is referred to as a protoporphyrin structure or prosthetic heme group (a compound required for biological activity that binds to a protein but is not made of amino acids) [2, 25, 31, 33-35].

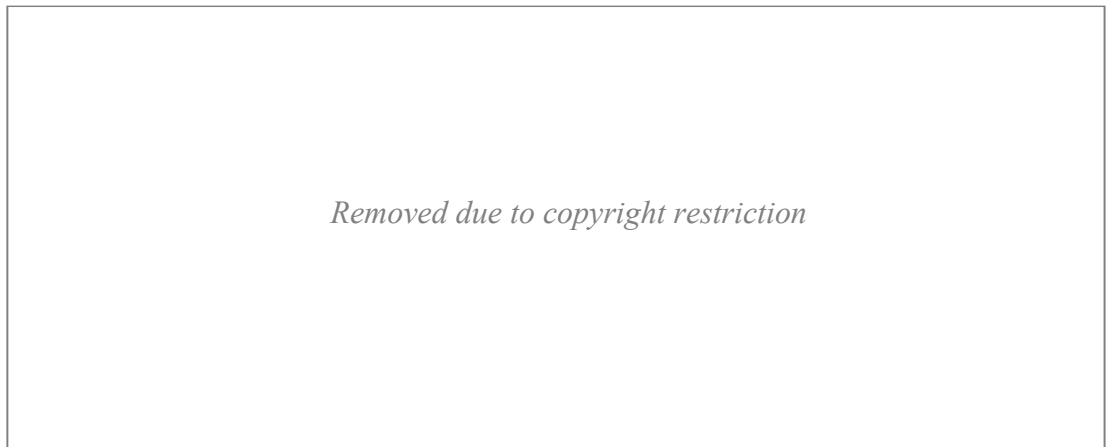


Figure 1-7: An illustration of the structure of haemoglobin (contains 4 subunits; 2 pairs of 1 blue & 1 grey subunit) [25] and inset, the heme group embedded in the protein.

On one plane of the heme group, the ferrous ion is also coordinated by a nitrogen (see Figure 1-8: A) on the imidazole side chain ring of histidine (histidine structure in Figure 1-3), an amino acid attached to the subunit [25, 29, 32]. This sits in a crevice where solvent access is restricted to prevent ferrous oxidation to Fe^{3+} [6, 25].

The rear plane of the ferrous ion is a binding site for a single diatomic oxygen molecule that X-ray studies have found associates in a bent end-on orientation; an Fe-O-O angle of approximately 130° (See Figure 1-8: B) [2, 25, 29, 32]. A single haemoglobin protein can bind and hence transport 4 oxygen molecules [2, 25, 32].

1.1.1.1.2 Oxyhaemoglobin, Deoxyhaemoglobin & Transport

Haemoglobin may be present in blood and a bruise in a deoxygenated (dark red) or oxygenated (red) form [2, 6, 7, 13, 18, 25]. Haemoglobin is approximately 96% saturated with oxygen when travelling from the lungs ($p\text{O}_2 \approx 13.3$ kPa) to tissues ($p\text{O}_2 \approx 4$ kPa) and 64% saturated when travelling from tissues to the lungs. This is

due to 2,3-Bisphosphoglycerate (BPG) regulation at sea level where oxygen transported in blood and released to the tissues is maintained at 40% [2, 25, 32].

Deoxyhaemoglobin has a confirmation known as the tense state (T-state) when no oxygen is present, stabilised by ion pairs primarily at the interfaces of the protein's subunit pairs [25, 32]. In deoxyhaemoglobin, the ferrous iron in a subunit heme has a high spin electron distribution [31]. Thus, due to a single electron occupying the $d_{x^2-y^2}$ orbital, pointing directly at the protoporphyrin nitrogens, nitrogen lone-pair of electrons are repelled [29]. This results in square pyramidal coordination geometry between the iron and four protoporphyrin nitrogens as shown in Figure 1-8 (A) [29].

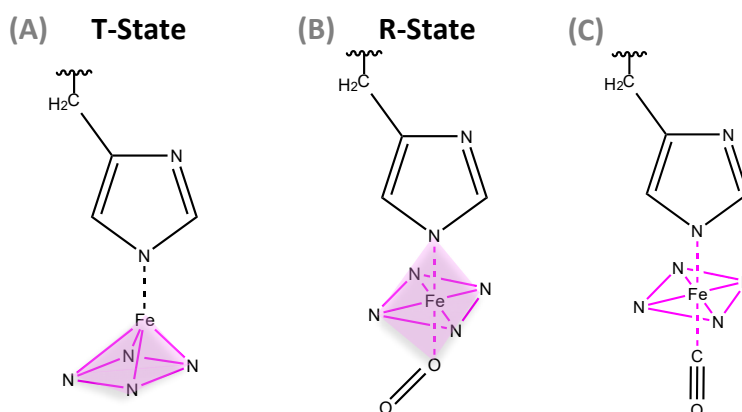


Figure 1-8: Illustrations of (A) the square pyramidal coordination geometry of heme and (B) the octahedral geometry of heme when bound to oxygen. (C) Coordination geometry of heme when bound to carbon monoxide, adapted from [25].

When oxygen (O_2) binds to the ferrous iron in haemoglobin's T-state, this sixth ligand alters the strength of the ligand field resulting in a low spin state of the iron, where six d electrons now occupy d_{xy} , d_{yz} and d_{zx} orbitals [25, 29]. With this, the $d_{x^2-y^2}$ orbital is empty and protoporphyrin nitrogen repulsions recede; the iron is planar with the four protoporphyrin nitrogens, exhibiting an octahedral geometry as illustrated in Figure 1-8 (B) [29].

With the ferrous ion movement to the centre of the porphyrin structure (a distance difference of approximately 0.75 \AA), the imidazole ring is pulled also, hence initiating conformational change to the histidine it is bound to as well as the rest of the protein, to what is called the relaxed state (R-state) [25, 29, 32]. This involves the

‘ α ’ and ‘ β ’ pairs of subunits rotating past each other, breaking ion pairs that stabilise the T-state [32]. The bound oxygen creates stability via hydrogen bonding to a Histidine amino acid on the subunit, otherwise too far to interact with the ferrous ion in heme [25]. It is also possible for this histidine and other amino acids in haemoglobin to rotate and flex for oxygen molecules to move throughout the protein to reversibly bind to hemes [25, 32].

The initial binding of oxygen to deoxyhaemoglobin is weak; however, it increases the affinity of subsequent oxygen binding to other subunits in the protein [25]. This is referred to as cooperative ligand binding, is sensitive to ligand concentration and can be quantitatively expressed by the equilibrium equation below [25]:

Removed due to copyright restriction

Equation 1

Where P is a protein with n binding sites and L is an oxygen ligand. The affinity of the ligands for the protein can be measured using an association constant (K_a):

Removed due to copyright restriction

Equation 2

Where k_a is the rate of association ($M^{-1}s^{-1}$) and k_d is the rate of dissociation (s^{-1}). Hence a larger K_a (association constant) corresponds to a larger affinity for ligand binding [25]. This is better approximated by considering the fraction of binding sites occupied by ligands on the protein (θ):

Removed due to copyright restriction

Equation 3

Where K_d (dissociation constant) is equivalent to the ligand molar concentration when the protein is half-saturated [25]. Rearranging and taking the log of both sides gives the Hill equation, Equation 4 (where $K_d = [L]_{0.5}^n$) [25]. This can be adapted in Equation 5 to show the degree of oxygen cooperativity with haemoglobin by substituting $[L]$ for the partial pressure of oxygen and K_d for P_{50}^n , which when plotted

in Figure 1-9, illustrates a positive slope for haemoglobin, corroborating the binding of one ligand supporting subsequent ligand binding [25].



Equation 4

Equation 5

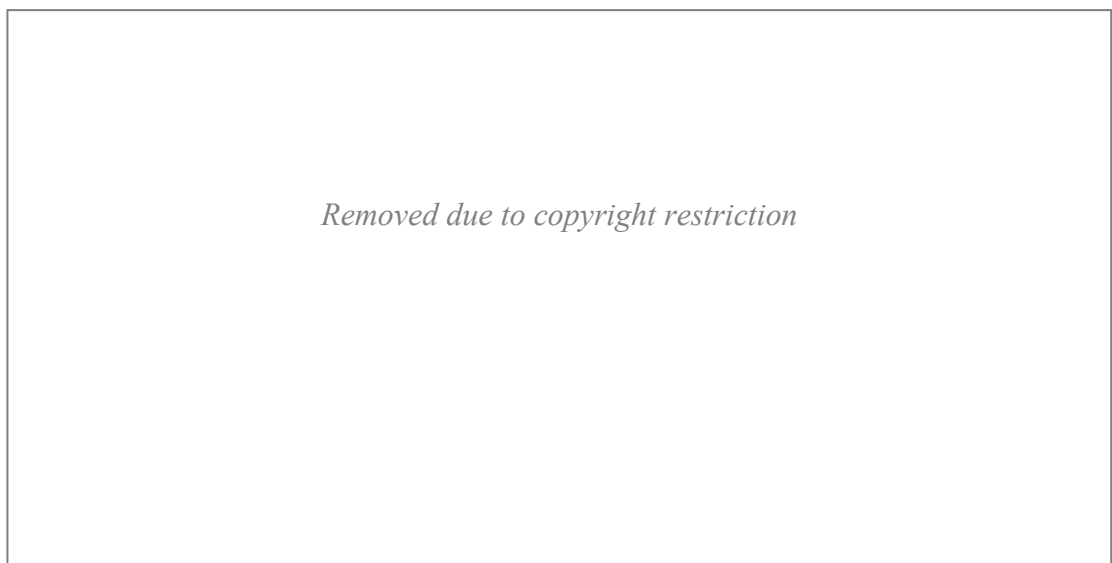


Figure 1-9: Hill Plot for Oxygen Interaction with Haemoglobin marked in red [25]. When n_H is greater than 1, ligand binding is cooperative [25].

It is thought that the blood released into a bruise becomes deoxygenated [6, 36], but previous work by Watchman et al (2009) has shown that deoxyhaemoglobin may interconvert to oxyhaemoglobin through passive diffusion of oxygen into the skin in post mortem conditions [19]. This may be relevant to bruises present after death [11, 19]. Although as diffusion of O_2 through tissue is ineffective over distances of a few millimetres [25], it may be that blood nearest the skin surface re-oxygenates, which may subsequently affect the overall colouration of the bruise [13, 18].

Carbon dioxide (CO_2) and hydrogen cations (H^+) are also transported by haemoglobin in blood, as these are waste products of muscle tissue respiration [2, 25, 32]. CO_2 binds to an amine at the end of a polypeptide chain in haemoglobin (Figure 1-10) for transport to the lungs, forming carbaminohemoglobin and H^+ ions [25, 32].

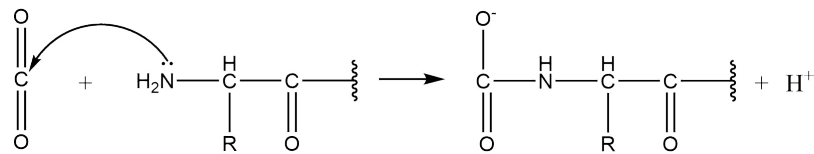


Figure 1-10: Binding of carbon dioxide to haemoglobin, adapted from [25].

H⁺ ions can protonate amino acids in haemoglobin (HHb⁺) for transport to the kidneys [25]. CO₂ and H⁺ ions stabilise the T-state of haemoglobin as they form salt bridges and ionic pairs, respectively, with amino acids within subunits [25, 32].

Following the Bohr effect, high concentrations of H⁺, thus environments with low pH decrease haemoglobin's affinity for binding oxygen following Equation 6 [2, 25, 32].

Removed due to copyright restriction

Equation 6

Hence, oxyhaemoglobin readily releases oxygen in environments of acidic nature or of high CO₂ concentration to bind the waste products [25]. Another waste product, carbon monoxide, may also bind to haemoglobin as described below.

1.1.1.1.3 Carboxyhaemoglobin

Oxygen bound to haemoglobin may be replaced with a carbon monoxide (CO) molecule, binding with octahedral geometry as shown in Figure 1-8 (C) [3, 6, 25, 32, 37]. When this occurs, it is referred to as carboxyhaemoglobin (COHb) which possesses a brighter red hue in comparison to oxyhaemoglobin (red) and deoxyhaemoglobin (darker red) [3, 25, 36]. This is supported by an investigation in 2011 by Moretta, who converted oxyhaemoglobin to carboxyhaemoglobin and injected various amounts of each into pig skin, generating 'artificial bruises' and analysing the degree of redness created by carboxyhaemoglobin [36].

The binding of CO to haemoglobin is not favourable for heme as the linear geometry of the CO molecule, although strong, is not stabilised as compared to the bent geometry of O₂ when bound, which as mentioned earlier is stabilised by hydrogen bonding to a histidine on a subunit [25]. Nonetheless, CO has a 250-fold higher

affinity to adult haemoglobin in comparison to oxygen; this affinity is amplified in fetal haemoglobin [2, 25, 32].

For this reason, the binding of CO to haemoglobin eliminates available binding sites for oxygen [25]. Even so, CO bound to one or two sites on haemoglobin influences the remaining subunits; their affinity for oxygen is increased considerably, where after binding oxygen, it is not released into tissues, depriving them of the molecule [3, 25, 37].

Carboxyhaemoglobin is naturally present in a healthy body at approximately 1% saturation of total haemoglobin for regulating blood vessel contraction and relaxation [3, 37], however this proportion is larger if the individual is a smoker or exposed to CO for long periods of time [3, 25]. At levels between 10-50%, symptoms such as headaches to respiratory failure may develop, where above 60% results in death [25, 37, 38]. The half-life of CO in the body is approximately 1 hour before it is breathed out [3].

The relevance of carboxyhaemoglobin formation in bruises will be explored later in Breakdown of Haemoglobin in a Bruise.

1.1.1.1.4 Sulfhaemoglobin

It is postulated that oxyhaemoglobin and carboxyhaemoglobin may decompose irreversibly into sulfhaemoglobin, which has a green colour and exhibits a characteristic wavelength at approximately 620 nm, depending on whether conditions are anaerobic or aerobic; in anaerobic conditions the characteristic wavelength is shorter [39-46]. To this day, the exact structure of sulfhaemoglobin and mechanism of its formation is unknown [44].

Sulfur is present in pathological settings due to certain drugs, environmental exposure or breakdown of some amino acids, which may occur in a bruise [42]. One suggestion of sulfhaemoglobin formation is that sulfur (from H₂S) may bind within the protoporphyrin structure clear of the central iron, perhaps adding across the double bonded carbon attached to the pyrrole rings in heme via catalysis from

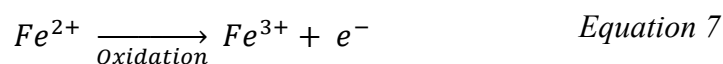
reducing agents [40, 42-44].

Sulphaemoglobin can be formed experimentally by exposure of haemoglobin to sulfur-based chemicals and in some preparations, haemoglobin purification methods are required for the binding of sulfur to occur [39-45]. Sulphaemoglobin can be formed in situ as successfully carried out in 2006 by Fergusson [41], although experimental preparations may be 75-90% saturated with sulfur [39].

It is reported that the affinity of sulphaemoglobin for oxygen is poor due to sulphated subunit influence on the overall protein, although sulphated subunits are indeed able to reversibly bind oxygen [40, 44]. In addition, it can be observed that preparations containing sulphaemoglobin with excess sulfide readily oxidise when exposed to oxygen [43, 45].

1.1.1.1.5 Methaemoglobin

In haemoglobin, the ferrous ion (Fe^{2+}) present in heme's centre spontaneously oxidises to a ferric ion (Fe^{3+}) in the presence of oxygen forming methaemoglobin (orange-brown), following equation 7 [6, 7].



Haemoglobin naturally oxidises to methaemoglobin in the body at a rate of 3% per day however is regulated to be less than 1% in red blood cells at any one time via reduction by the enzyme, NADH-cytochrome b5-methaemoglobin reductase [6, 47, 48]. When haemoglobin is partially saturated with oxygen, the rate of methaemoglobin production may increase [6, 47].

Oxidation to methaemoglobin may also occur as RBC's escape blood vessels in the case of a bruise as the heme groups are susceptible to oxidative stress [7], particularly by neutrophils (first white blood cells to arrive at the site of an infection), which can oxidise heme via cell-cell contact, without phagocytosing a red blood cell [6, 49].

Once ferrous oxyhaemoglobin is oxidised to methaemoglobin, bound oxygen is

either not released easily because the oxidation distorted the protein structure, or oxygen is released as superoxide radicals, which may further react with methaemoglobin yielding heme degradation [47, 48]. Hence at this stage, the protein is no longer useful for oxygen transport [32, 48].

1.1.1.1.6 Breakdown of Haemoglobin in a Bruise

The breakdown of haemoglobin in a bruise begins when oxygenated blood (red) is released into the skin [3, 6, 46]. This initiates an inflammatory response where initially neutrophils (50-75% of WBC's) arrive to attack via oxidation and then macrophages (another type of WBC) in the blood and skin are attracted to the site of the bruise activating phagocytosis (ingestion) of the red blood cells [2, 6, 18, 34, 35, 46, 50, 51]. Neutrophils will arrive within an hour at the site of a bruise, however the largest accumulation of macrophages is reached at approximately 18-48 hours at which stage neutrophils decrease in number [6, 11, 46].

Macrophages have a life span of a month to years depending on the amount of material ingested as a limited amount of phagocytosis of material may occur before its expiry [46]. Once activated for phagocytosis, macrophages are unstable hence carry out breakdown only in the injured area such that any other cells are safeguarded from attack [2].

The engulfing of a red blood cell stimulates lysosomal hydrolases contained in the macrophage that liberate heme from the subunits of the protein, digesting the amino acid structure [46]. An enzyme with a molecular weight of 32,000 g/mol, heme oxygenase 1 (HO-1) is also present in macrophages (as well as in the skin) and is induced by heme-responsive gene expression due to the previous digestion, to break down the prosthetic heme group by oxidation as shown in Figure 1-11 [3, 6, 18, 34, 35, 37, 46, 52-55]. This is the rate-limiting step in the breakdown of haemoglobin [35, 37]. HO-1 may also break down ferric methaemoglobin, but at a lower rate compared to ferrous haemoglobin [7].

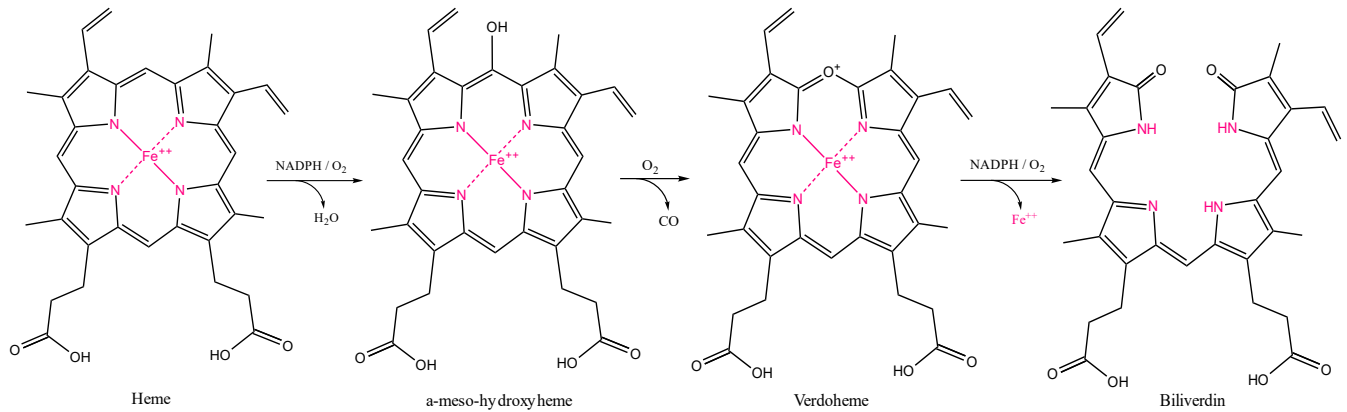


Figure 1-11: Prosthetic Heme group breakdown to Biliverdin by heme oxygenase (HO-1), adapted from [3].

This results in an open porphyrin structure called biliverdin (green pigment), releasing a single carbon monoxide molecule and an Fe^{2+} ion [3, 6, 18, 22, 28, 37, 46, 56-58]. The oxidation reaction requires nicotinamide adenine dinucleotide phosphate (NADPH or energy) and consumes 3 moles of O_2 creating an anaerobic environment in the bruise and generating hydrogen peroxide (H_2O_2) [3, 6, 46]. Anaerobic conditions inhibit nitric oxide (NO) production from the breakdown of amino acids at the site of a bruise, reducing inflammation and reaction with H_2O_2 which may form detrimental reactive oxidising species [3, 31, 37].

As breakdown of haemoglobin releases CO and this diatom inhibits heme oxygenase, CO acts as a regulator for HO-1 enzyme activity, although it may also be diffusely taken up as waste by haemoglobin forming carboxyhaemoglobin (bright red) as discussed in the Carboxyhaemoglobin section [3, 34, 37].

Free ferrous ions can inhibit HO-1 activity and promote the formation of hydroxyl radicals that can damage DNA and other macromolecules [32, 34, 35, 37, 59] hence these are taken up by ferritin, an iron-storage protein in macrophages, and converted to Fe^{3+} [6, 25, 34, 37, 60]. Ferritin will be discussed in more detail later.

Biliverdin is rapidly converted to bilirubin (yellow) by biliverdin reductase; for 10 mg of protein, 0.25 μmoles of bilirubin is formed per minute [3, 6, 18, 35, 46, 51, 52, 61]. This very interaction with biliverdin reductase enhances anti-inflammatory responses [53]. Biliverdin and bilirubin will be discussed in more detail later.

The relationships between haemoglobin and its derivatives as described above are presented in Figure 1-13.

It is reported that HO-1 activity in the skin equilibrates to normal levels 2 weeks after an injury has occurred [35]. The macrophage will eventually leave the bruise site and transfer iron and bilirubin bound to albumin in the liver, where the bilirubin is conjugated and becomes bile [34, 62].

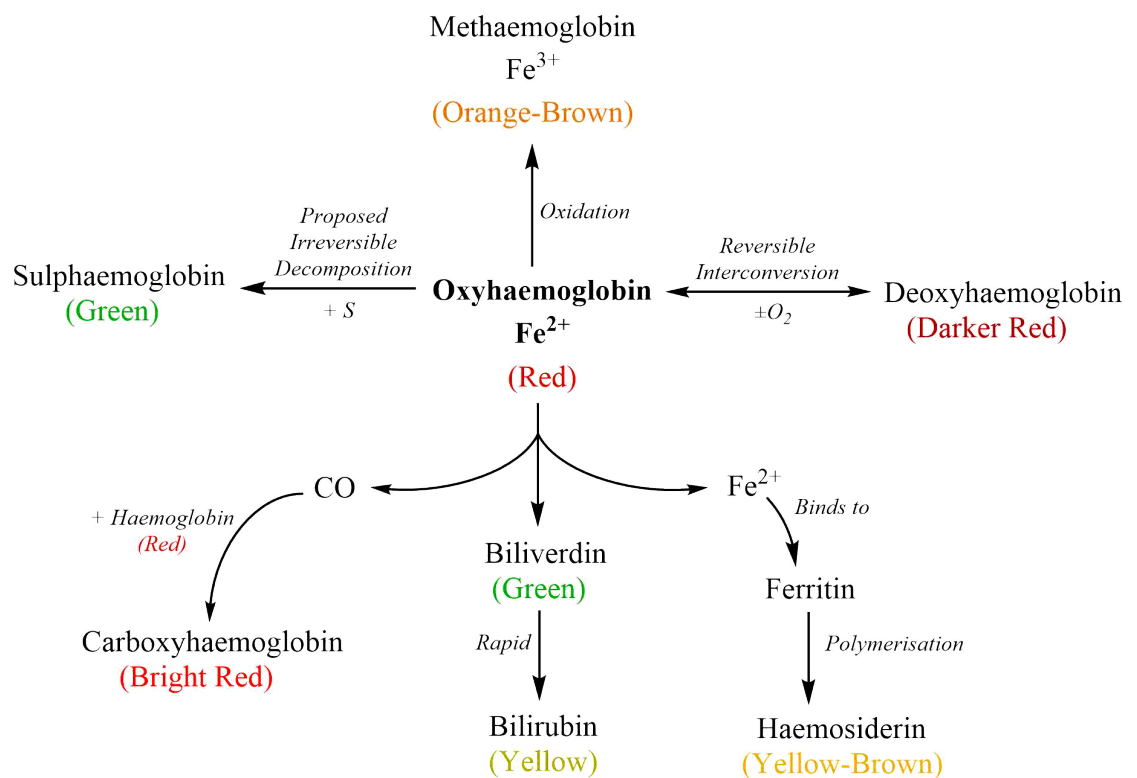


Figure 1-12: The various known forms of haemoglobin and its breakdown products [63].

1.1.1.1.7 Biliverdin and Bilirubin

Biliverdin (green pigment) is an open porphyrin structure (Figure 1-11) containing pyrole, amine and carboxylic acid functionality [35, 61]. It may exist as diketo, keto-enol and dienol isomers as illustrated in Figure 1-13, where the diketo isomer is calculated to be the most stable in gas and solid states, crystal packing having no effect on the relative stability [28, 52]. Biliverdin is known to have an affinity for collagen, a structural protein [64].

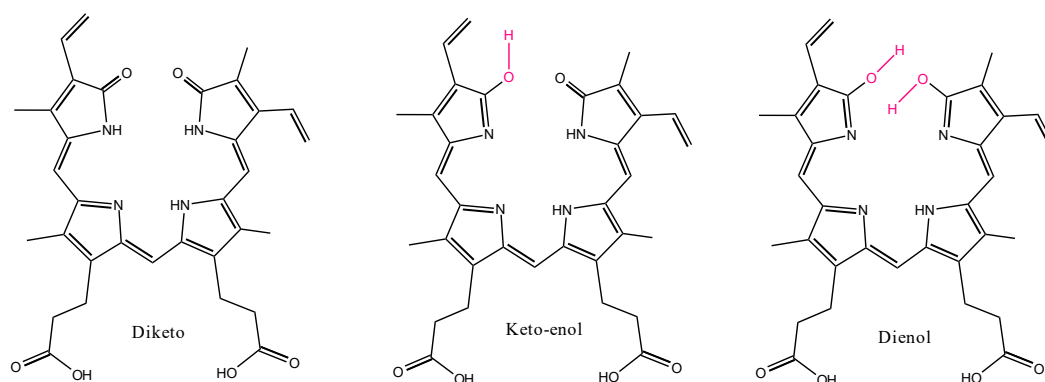


Figure 1-13: Three tautomeric isomers of biliverdin, adapted from [52].

The central C=C double bond in biliverdin may be reduced with biliverdin reductase to give bilirubin (yellow compound) as shown in Figure 1-14 [6, 7, 35, 37, 53, 55, 61, 65].

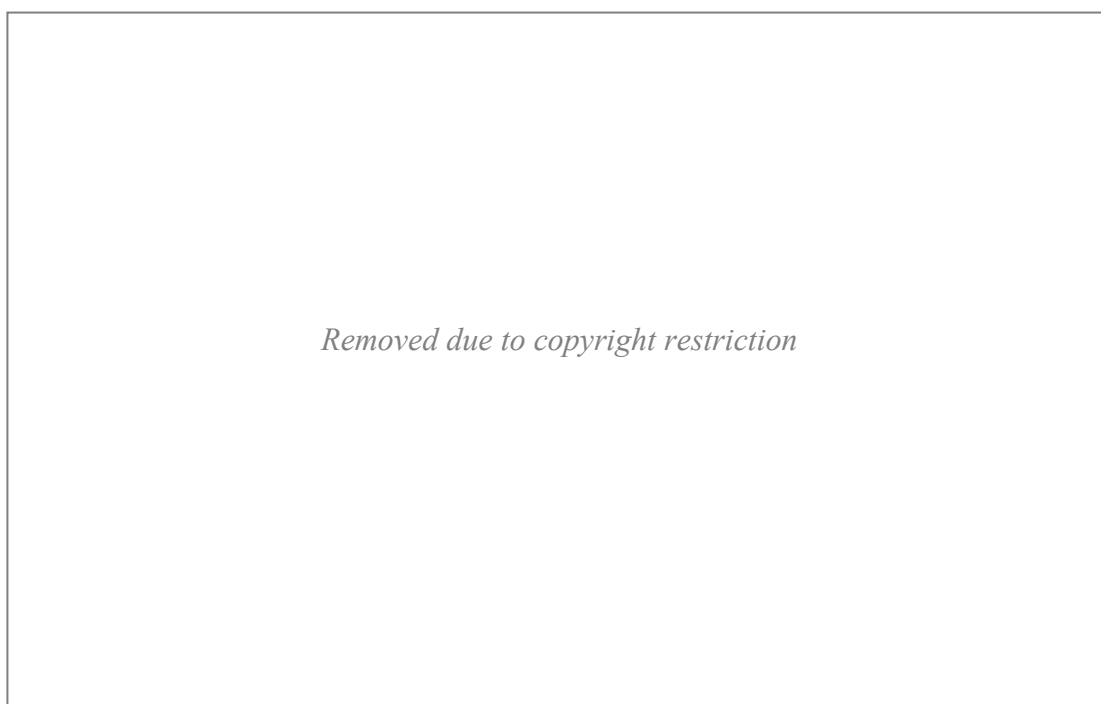


Figure 1-14: The conversion of biliverdin to bilirubin via biliverdin reductase [61].

In the body, 300 mg of bilirubin is produced daily, 80% of which is a result of the above conversion [62]. Bilirubin may exist as three isomers illustrated in Figure 1-15; bilirubin III- α , bilirubin IX- α and bilirubin XIII- α [65]. This occurs when heme is non-enzymatically cleaved [66]. Biliverdin is also reported to isomerise similarly [56].

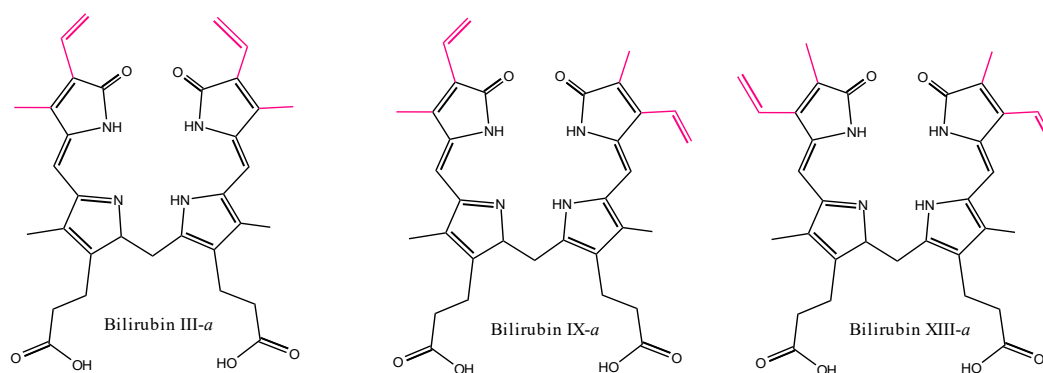


Figure 1-15: Three constitutional isomers of Bilirubin, adapted from [65].

Bilirubin is naturally found in the IX- α isomeric form, although commercially it may be a racemic mixture with small amounts of III- α and XIII- α isomers [65]. It is possible to isolate biliverdin's IX- α isomer under controlled conditions by dehydrogenation of commercially available bilirubin with 2,3-dichloro-5,6-dicyanobenzoquinone in dimethyl sulfoxide (DMSO) [56].

Bilirubin is present in the body at any one time to modulate the inflammatory response, although at different concentrations dependent on age; 1.2×10^{-2} M in adults and 0.1 M in newborns [37, 62, 67, 68]. As such, its solubility is important for human physiology [69]. Bilirubin formed by the breakdown of haemoglobin will be bound to water soluble albumin (during which it is called unconjugated bilirubin) to be transported to the liver to become bile and join its glucuronide derivatives (conjugated bilirubin); bilirubin is conjugated in the liver by the enzyme, uridyl diphosphate glucuronyl transferase [28, 35, 62, 66, 68, 69]. Total bilirubin refers to the sum of unconjugated and conjugated bilirubin [62, 68].

Unconjugated bilirubin in its fully protonated form, particularly in its crystalline state, may establish intra-molecular hydrogen bonds via carboxyl and pyrrole ring amines on opposite sides of the molecule as shown in Figure 1-16 [66]. This occurs due to the allowable rotation about the single-bonded carbon (denoted with arrows in Figure 1-16), where in biliverdin possessed a double bond [66]. This carbon also acts as the ridge in a 'folded book' three dimensional structure of the molecule, where the two pyrrole rings on the left hand side of this carbon are on one plane and the two pyrrole rings on the right hand side of this carbon are on another plane, at an angle of

approximately 98 degrees apart [66].

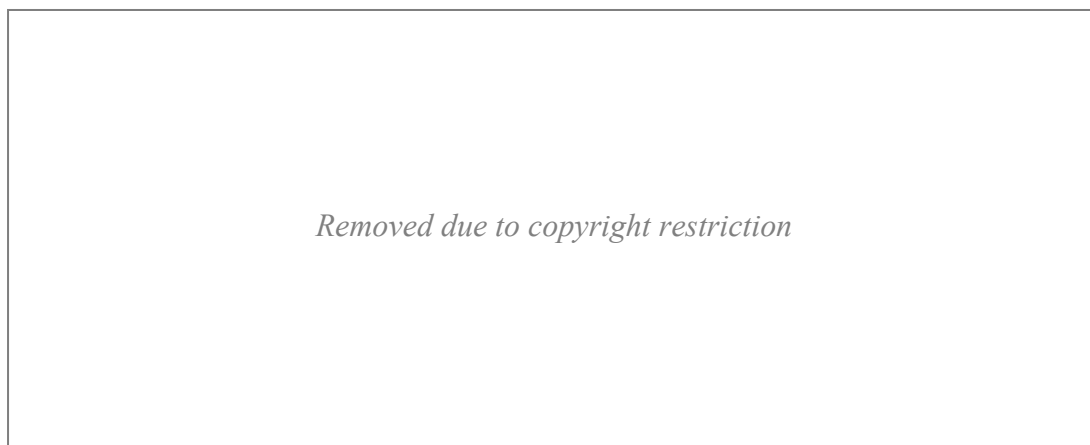


Figure 1-16: Intra-molecular hydrogen bonding present in bilirubin [66]. Hydrogen bonds are presented by dashed lines and arrows denote the carbon on the ridge of a folded-book 3D structure [66].

The 6 hydrogen bonds in this structure protect bilirubin's carboxyl groups from ionisation and provide enhanced rigidity in conformation hence stability [66]. However, as the majority of available polar groups in the molecule are utilised, interaction with water is limited, rendering the molecule insoluble in solutions at physiological pH; solubility of crystalline bilirubin is less than 1 nM at pH less than 7.0 [28, 66].

There are five structural variations of bilirubin that may inhibit this intra-molecular hydrogen bonding. This includes constitutional isomerism (Figure 1-16), geometric isomerism (polar groups are sterically hindered), tautomerism (Figure 1-14), conformers (rotation of pyrrole rings about single bonds) and state of ionisation of the molecule which is pH dependent [66].

The two carboxyl groups in bilirubin may ionise to monoanion and dianion forms; the loss of one proton from one carboxylic acid at pH above 3.8 or the loss of two protons, one from each carboxylic acid in bilirubin at pH above 6.8, respectively [66, 68]. These anions may further develop into dimers or aggregates where bilirubin molecules stack parallel creating micelles of enhanced solubility [66]. This is stabilised primarily by hydrophobic interactions [66]. The diacid, monoanion and dianion forms are all soluble in this micelle, however the monoanionic form of bilirubin is predominant in the micelle when the pH is 6-8 [66]. It is also likely that the albumin bound form of bilirubin mentioned earlier is dianionic [66].

It is possible for micelles of bilirubin to reach metastable supersaturation by dissolving in alkaline solution and raising the pH dropwise to achieve physiological pH of 7 [66]. In this instance, bilirubin is partially protonated yet maintained in the open structure confirmation, increasing micelle solubility [66].

Elevated total bilirubin can occur when an individual has an obstruction in the bile duct, hepatitis, cirrhosis, a haemolytic disorder, an inherited enzyme deficiency (hyperbilirubinemia) or liver disease [28, 37, 62, 68]. Jaundice is a common occurrence in newborns (50%) and is due to RBC haemolysis resulting in accumulated unconjugated bilirubin in the blood serum (above double the concentration compared to normal), where if not bound to albumin and untreated, the pigment can cross the blood brain barrier and cause cerebral harm [37, 62, 68]. Additionally, the greater skin to body mass ratio in newborns (up to 1 week old), thus higher rate of skin heme oxidation (HO-1 activity) may contribute to the development of jaundice [35]. However, it is documented that exposure of bilirubin to the blue region of visible light (phototherapy) converts it via photooxidation to isomers, such as lumirubin (Figure 1-17), that possesses greater water solubility [6, 28].

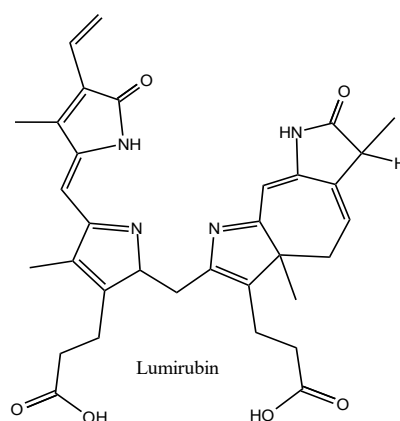


Figure 1-17: Structure of lumirubin, a photo-isomer of bilirubin, adapted from [70].

Bilirubin in its unconjugated form can also be found in black and brown gallstones within the gallbladder, an organ responsible for concentrating bile solutes by absorption of water and sodium, reducing bile volume by 80-90% [69, 70]. It is reported that gallstones of this kind, where the only treatment is surgery, is an increasing trend in children [70].

1.1.1.1.8 Ferritin and Haemosiderin

Ferritin is produced by macrophages and is released into the blood. Normal ferritin levels in the blood are 12-300 ng/mL for males and 12-150 ng/mL for females, however these may increase when in the presence of oxidative stress such as in a bruise [37, 71, 72]. The structure of ferritin consists of five α helix conformations as illustrated in Figure 1-18 (b), where 7 amino acids from four of the helices participate in reversibly binding iron cores, 6-8 nm in size (Figure 1-18: c) [60, 73-75].

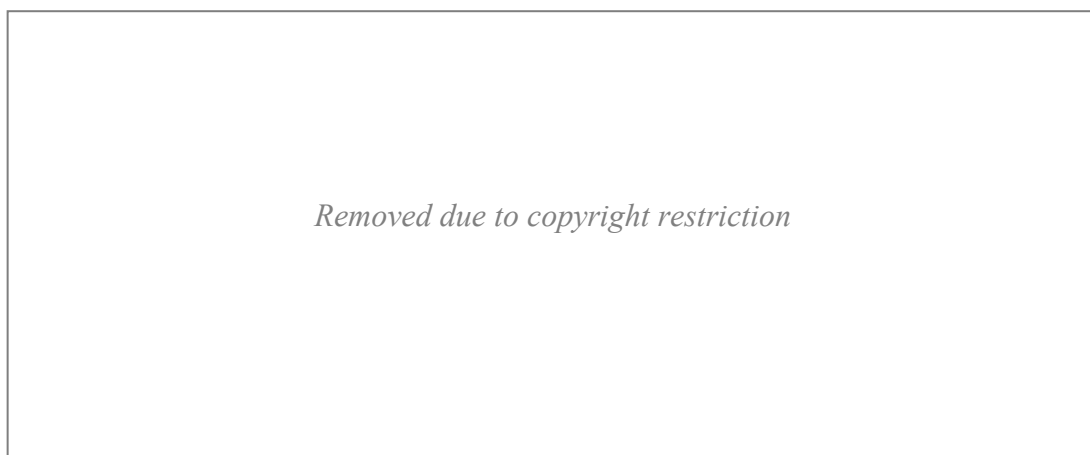


Figure 1-18: (a) Polymerised form of ferritin, (b) ferritin structure and (c) the binding sites in a ferritin molecule [73].

For this reason, free ferrous ions released from the breakdown of haemoglobin may be taken up by ferritin, which can be found in the cytoplasm of macrophages as mentioned in Breakdown of Haemoglobin in a Bruise [6, 25, 37, 60, 76]. Although in ferritin, iron is primarily in the ferric state (Fe^{3+}) as hydrated ferric oxide (FeOOH) cores [34, 74, 75, 77].

When the iron uptake rate exceeds that of ferritin production by a macrophage, up to 24 ferritins can act as subunits, polymerising to form the yellow-brown globular protein, hemosiderin (see Figure 1-13: a) which can contain almost 4500 iron atoms and be stored in macrophages [6, 34, 46, 55, 60, 73, 75, 77]. As an aggregate, haemosiderin is amorphous, varying in shape as well as size, and it is suggested that the slow conversion of the protein into crystalline mineral occurs in cells [60, 75].

1.1.2 Establishing Bruise Age

As blood breaks down in the skin tissue, the colour of a bruise changes with time [6, 7, 12, 20]. As such, in a clinical forensic assessment, it may be used to infer information about the age of the bruise and hence a timeframe of when the incident that caused the mark took place [6, 7, 10, 12, 78]. With this, a bruise may be significant evidence for forensic investigation such as that performed post mortem (autopsy) to link an assault to an injury, provided they both occurred at the same time [12, 13, 18, 78].

Currently, the main methodology employed to determine the age of a bruise at the Forensic Science Centre of South Australia (FSSA) is visual observation of the degree of yellow discolouration (bilirubin formation) indicating a bruise is not recent (it is more than 18 hours old), although as a standalone technique, visualisation can be inconsistent due to perception [6, 8, 11, 17, 18, 20, 51, 55, 78]. For example, the colour orange-brown could be a result of methaemoglobin formation which may occur in the early stages of a bruise and reflected light scattering effects of melanin and carotenes in adult skin can mask the perception of yellow [6, 14-16]. Additionally, post mortem hypostasis and bodily decomposition are factors that can affect the colouration and hence perception of yellow in bruise marks [6, 11].

In fact, the perception of colour varies between observers and the sensitivity in perceiving the yellow region of colour decreases with population age [6, 8, 10, 17, 18, 51, 79]. This is largely dependent on the condition of the eye's colour receptors (cones), which normally have the potential to identify the three primary colours red, green and blue (RGB), and overlay of these in different ratios [6, 18, 55, 80]. Therefore, visual examination is limited by the physiology of the human eye-brain system [6, 17, 51].

To compensate for the issue of human eye perception, digital images of bruises accompanied by standardised colour scales or references (Figure 1-19), and controlled lighting conditions are used and offer some objectivity in visual analysis [6, 18, 78-80]. Colour data such as from images or colorimetry in conjunction with the Commission Internationale d'Eclairage (CIE) $L^*a^*b^*$ (L^* = luminosity, a^* =

green to red data points & b^* = blue to yellow data points) colour model program can assign values to respective colour data delivering further quantitative interpretation of bruise mark colouration, however this technique is dependent on background colour of the skin and is limited to a three dimensional colour space [6, 7, 16, 17, 51, 78, 80].



Figure 1-19: (A) A Munsell Color X-rite ColorChecker® standardised colour scale reference example (B) corresponding RGB values for the standardised colour scale reference and (C) use of a standardised colour scale reference for a bruise mark [18]

Visual observation is coupled with histology if further investigation is required at the FSSA, where the structure of the bruised tissue cells is examined [6, 11]. Histological analysis of healthy tissue presents intact epidermis, dermis, hypodermis and blood vessels [81]. Red blood cells are confined to the blood vessels [81]. Areas of the connective tissue of the dermis predominately contain collagen fibres as well as several fibrocytes and the hypodermis comprises consistent adipose tissue masses [81].

Bruised tissue within 24 hours old can be stained with haematoxylin-eosin to show a change in the hypodermis layer of skin only; extravasated red blood cells are present in areas surrounding damaged vessels and infiltrate disfigured connective fibres and adipose tissues [81]. Neutrophils and some macrophages are present in the boundary of the bleeding area initiating the inflammatory response [11, 81].

Bruised tissue 3 to 7 days old stained with Pearls Prussian Blue, detects an

accumulation of macrophages in all areas of bleeding and consequently haemosiderin (dark blue coloured with the staining) and bilirubin particles (light brown coloured with the staining) as the mononuclear cells carry out phagocytosis [11, 55, 81]. It is possible to detect bilirubin as localised crystals (hematoidin), however rare as these are frequently dissolved in the tissue processing methodology [6]. Macrophages are observed at their greatest concentration in 5-day old bruises and red blood cells permeate throughout fine connective fibres, enlarging them [81]. By day 7 of a bruise, muscle tissue regeneration has commenced [11].

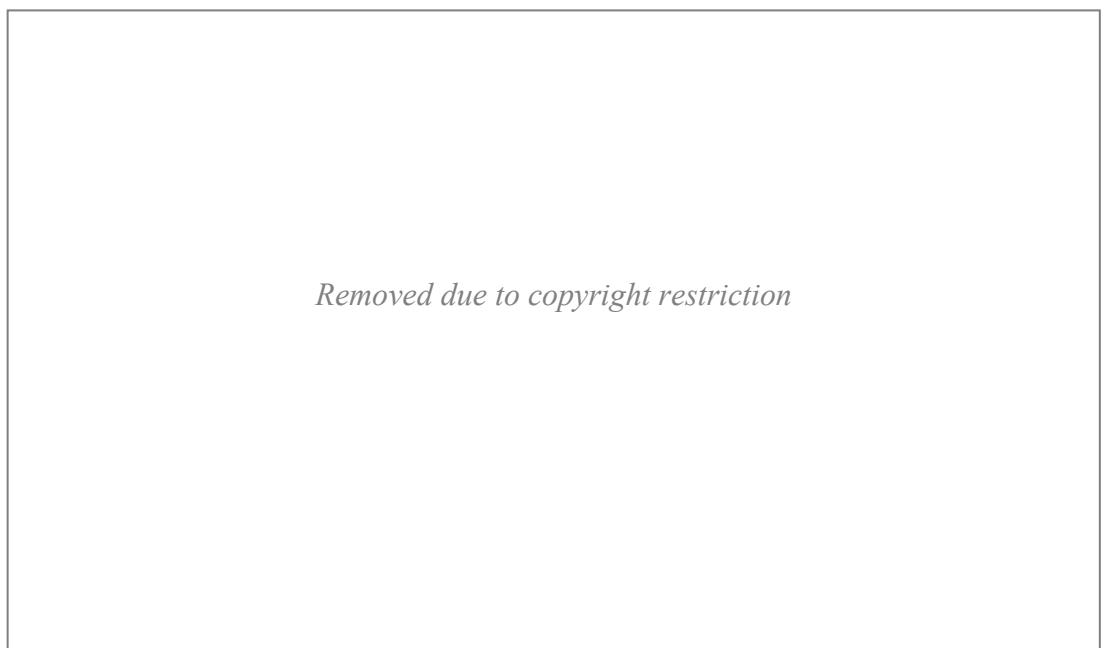


Figure 1-20: Histological thin section (x100 magnification) of human skin 5-day old bruise taken at autopsy and stained with Pearls Prussian Blue. This thin section exhibits macrophage infiltration not seen in a fresh bruise younger than 3 days, where they are now filled with haemosiderin. Hematoidin granules can also be observed between some RBC's. [81]

Enzyme histochemistry may be employed to detect changes in cellular enzyme levels in bruises as early as 1 hour after the wound has occurred, however results are greatly affected by age and the type of injury [11].

Another method for age determination of a bruise currently is the expression of HO-1 (heme oxygenase-1), an enzyme expressed in macrophages that breaks down heme by oxidation releasing CO and biliverdin as discussed in section 1.1.1.1.6 [35, 37, 82, 83]. The enzyme has been investigated to be present in a bruise model at high levels from 6 hours to 1-3 days of injury attributing the delay in bilirubin formation in a bruise to macrophage migration to the bruise site [35, 37, 82, 83].

Most of the above methods of bruise age determination are classified as invasive as an incision of the skin as thin sections are analysed [84]. In contrast, spectroscopy is a non-invasive avenue of establishing bruise age, allowing potential qualitative and quantitative measurement at multiple regions on the electromagnetic spectrum [6]. This invites spectroscopy as a prospective technique to establish the age of a bruise.

A variety of spectroscopic methods have been used in literature for establishing bruise age, notably the quantitative UV-Visible reflective spectra of bilirubin which provides trend information; bilirubin concentration increases up to the 7th day after a bruise injury, then decreases over a week period after day 7 [7, 55]. However reflectance spectroscopy results exhibit large variation due to discolouration variables as listed in section 1.1, particularly in relation to the age of a mark and depth of the bruise in the skin [7, 55].

Mathematical models that predict photon propagation through layers of the skin considering light scattering effects of melanin, index of refraction and error associated with nonlinear absorbance attributed to the presence of H-bonds are suggested to have the potential to monitor the breakdown of haemoglobin as a bruise ages, however these models may require validation and reliability development [16, 85].

Furthermore, hyperspectral imaging in the infrared (IR) 920-2500 nm and 400-850 nm regions of the electromagnetic spectrum may prove useful in visual characterisation of the early onset of bruises where accumulating fluids and surrounding blood vessels are detected independent of skin pigmentation, however is not useful for age determination [22].

1.2 Spectroscopy

Light or electromagnetic radiation may be described to behave like a wave, where the type is defined by the frequency of the waves (wavelength) [86]. The various types of light exist on an electromagnetic spectrum and include, from longest to shortest wavelength, radio waves (1×10^{12} - 1×10^6 nm), infrared radiation (approximately 1×10^6 - 800 nm or $10 - 12,500$ cm^{-1}), visible light (approximately

700 – 400 nm or $14,286 - 25,000 \text{ cm}^{-1}$), ultraviolet light (400 – 10 nm or $25,000 - 100,000 \text{ cm}^{-1}$), X-rays (10 – 0.005 nm) and gamma rays (less than 0.005 nm) [86].

Human eyes can identify visible wavelength ranges on the electromagnetic spectrum between 400-700 nm [17]. A prism can disperse visible light into violet (400-450 nm), blue (450-490 nm), green (490-560 nm), yellow (560-590 nm), orange (590-630 nm) and red (630-700 nm) [17]. These wavelengths, similar to most other regions of the electromagnetic spectrum, can be utilised and measured by a spectrophotometer in spectroscopy [6, 86].

Spectroscopy is the study of emission (such as reflectance) or absorption when light or radiation interacts with matter, developing the understanding of molecular bonding and chemical composition [17, 87].

Chemical compounds resulting from Haemoglobin breakdown are responsible for the discolouration in bruise marks [46]. Haemoglobin breakdown factors that may contribute to this discolouration include ferritin and haemosiderin [46]. These breakdown compounds are conjugated (coloured) and infrared (IR) active, hence ultraviolet-visible (UV-Vis.) and IR light may be used to achieve transmission and reflectance spectroscopic analyses.

1.2.1 Transmission vs. Reflectance Spectroscopy

Commonly referred to as the method of colorimetry [84, 88], transmission spectroscopy utilises a light source and monochromator to produce incident light at a particular wavelength that is then passed through a sample of low concentration (dilute) as illustrated in Figure 1-21 [89].

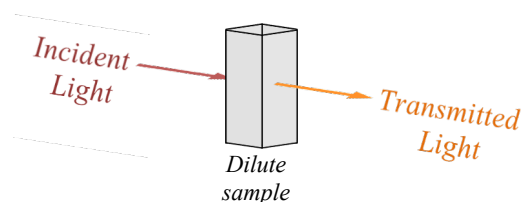


Figure 1-20: Schematic of sample absorbance in transmission spectroscopy.

The electromagnetic radiation can be absorbed by the analyte, and resultant diffuse

transmittance signals are sensed by a detector, dependent on concentration and pathlength, following the Beer-Lambert Law [89]:

$$A = \varepsilon \times b \times c$$

Where A is absorbance, ε is the molar absorptivity ($\text{L}\cdot\text{mol}^{-1}\cdot\text{cm}^{-1}$), b is the pathlength (cm) and c is the analyte concentration (mol/L) [89]. This assumes that absorbance is directly proportional to the concentration of absorbing analyte [89]. A disadvantage of transmission spectroscopy is that the technique can be invasive and as such not appropriately applied to the clinical forensic setting [84].

In contrast to detection of diffuse transmittance through a sample, reflectance spectrophotometry operates based on the reflectance off of the surface of a sample to which the radiation source is incident upon (see Figure 1-22); the radiation beam passes from a denser to a less dense medium [89]. The angle of incidence and the fraction of radiation reflected have a directly proportional relationship hence the instrumental platform may be adjusted to produce a suitable signal and therefore spectrum [89].

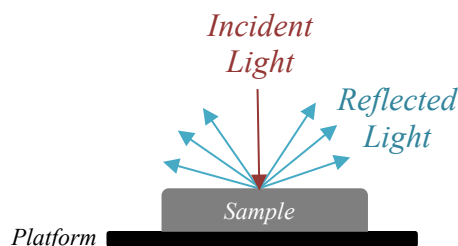


Figure 1-21: Schematic of sample absorbance using reflectance spectroscopy.

Reflectance spectrophotometry has been forensically applied to the identification of inks in pens [90-93] and car paint analyses [94-97]. It is also utilised in monitoring jaundice and the assessment of bruises (see 1.1.2. Establishing Bruise Age) considering that blue and red light may penetrate the skin $100\ \mu\text{m}$ and $500\text{-}750\ \mu\text{m}$ deep, respectively, keeping in mind that skin is a light scattering medium [6, 14, 98]. Hence, reflectance makes use of sample surfaces to produce spectra.

1.2.1.1 The Integrating Sphere

To optimise spectra from sample surfaces, an integrating sphere can be used. This is a spherical spectrophotometer accessory, internally coated with a highly diffuse reflecting material [99]. As illustrated in Figure 1-23, incident spectrometer beam light is directed into the sphere and onto the sample port, which is mounted externally allowing for experimentation on small to large samples [99].

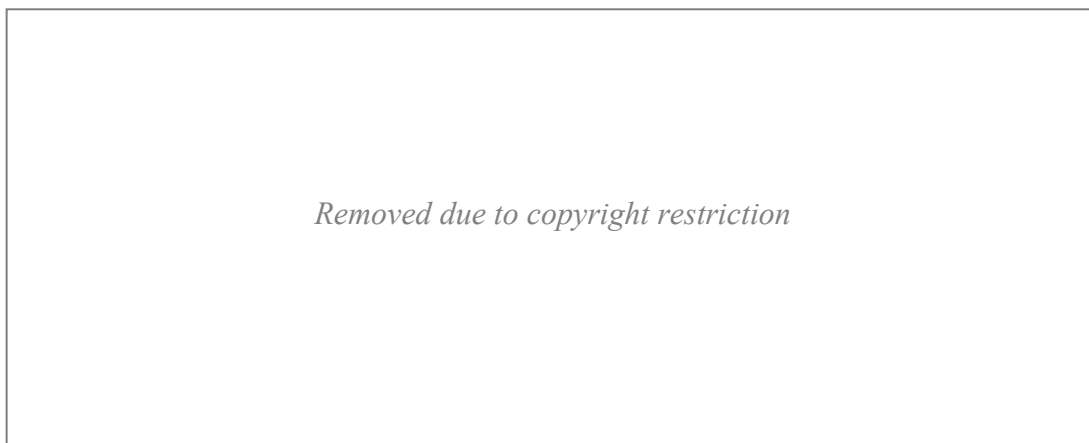


Figure 1-22: Birdseye view schematic of an integrating sphere accessory showing beam pathways [99].

Reflected light from the sample surface is scattered into the enclosed integrating sphere (Figure 1-24), where it is continuously reflected, eventually being detected by a photomultiplier tube (PMT) and thermoelectrically cooled lead sulfide (PbS) photocell (or indium gallium arsenide) detector [99]. Hence the integrating sphere increases signal detected by collecting scattered light that would otherwise be lost, particularly from a surface that is uneven such as skin [99].



Figure 1-23: Scattering of reflected light from an opaque sample with incident spectrometric light [99].

The PMT detector can collect electromagnetic radiation in the wavelength range of 160-900 nm, and the PbS detector in the range of 800-3500 nm [99]. However, the integrating sphere's internal reflective coating limits measurement accuracy beyond 2500 nm [99].

1.2.1.2 Attenuated Total Reflectance (ATR)

Attenuated total reflectance (ATR) extends sample measurements with electromagnetic radiation beyond 2500 nm [85]. It does this by passing incident infrared light through a prism with a high refractive index at an angle which produces reflections within the prism at the surface the sample is in contact with as illustrated in Figure 1-25 [100].

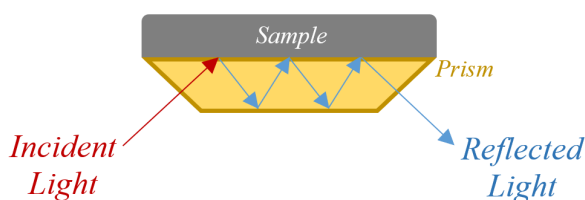


Figure 1-24: Schematic of attenuated total reflectance (ATR), adapted from [101].

It is at this point of contact that penetration $0.5 - 5 \mu$ in the sample from infrared light may occur [101]. Consequently, the energy from each reflection is weakened (attenuated) and the resulting IR light exiting the prism is detected and generates a characteristic infrared spectrum [100, 101].

1.2.2 The Australian Synchrotron

Sample measurements may be extended into the far-infrared (FIR) region of the electromagnetic spectrum at the Australian Synchrotron (Figure 1-26; A). A synchrotron creates intense beam of light by firstly producing a cluster of electrons from a tungsten matrix cathode electron gun at point 1 in Figure 1-26 (B) [102].

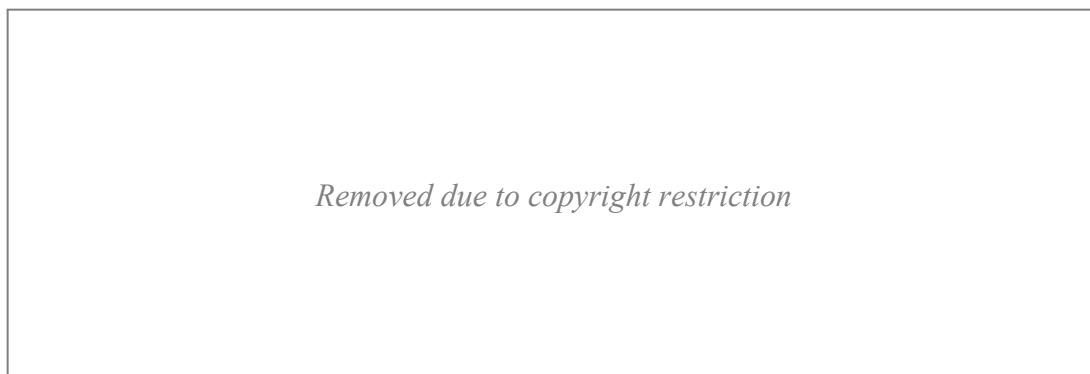


Figure 1-25: (A) The Australian Synchrotron and (B) a schematic layout of a synchrotron numbering its fundamental functional parts [102].

These are then accelerated over a 10 m distance in a linear accelerator at point 2 increasing in energy in the booster ring (point 3) due to magnetic fields [102]. The storage ring at point 4 stores accelerated electrons, keeping them at a beam current of 200 mA with lifetime of 20 hours using bent and straight magnets [102]. Electromagnetic radiation (ionising and non-ionising) is emitted when electrons are deflected through the bent magnets in the storage ring, travelling along a beamline under vacuum (point 5) towards a radiation-shielded enclosure or end station (point 6) for analysis using this customised light [102].

This light possesses a higher brightness intensity compared to conventional sources, allowing analysis of weak absorbers, samples of low concentration [103] and proteins that typically have a high absorbance [104]. Additionally, the light is collimated to provide high spectral resolution, and polarised to reduce background scattering and improve sensitivity [102, 103]. There are currently ten beamlines in operation at the Australian Synchrotron that capture light emission from the storage ring ranging from microwave to hard x-rays and including far-infrared [103].

1.2.2.1 Far Infrared (FIR) / Terahertz (THz) Beamline

The Far-infrared (FIR) or Terahertz (THz) beamline is one of the Australian Synchrotron's operational beamlines and produces light that is detected in the wavenumber range of 10 - 5,000 cm^{-1} (1,000,000 - 2000 nm) over a variety of detectors [105]. The three detectors used in this project were Si Bolometer (10-370 cm^{-1}), Si:B Photodetector (300-1850 cm^{-1}) and MCT_N (700-5000 cm^{-1}).

The beamline is suitable to analyse molecules with rotational and oriented IR absorbing bonds via transmission as condensed pellets (solid phase) utilising a cryogen-cooled cryostat (Janis Research) accessory under vacuum (4×10^{-3} Torr) [105]. To decrease sample absorbance, pellets may also be created using sample homogeneously mixed with compounds that exhibit low absorbance in the FIR region of the electromagnetic spectrum, such as polyethylene [106]. More recently, the beamline has employed transmission in the liquid phase by the means of diamond window liquid cells, and reflectance via a fitted ATR accessory external to the system under vacuum with a depth of penetration of 2-10 μ dependent on

wavenumber [107].

1.2.2.1.1 Diamond Window Liquid Cell (DWLC)

Transmission FIR analysis in the liquid phase has previously been performed at the Australian Synchrotron using a metallic cell consisting of large polyethylene (PE) windows, where incident light passes through one window, the liquid and the second window to the detector as transmitted light, resulting in a spectrum for data analysis [107]. However, the PE windows bend to a concave shape under vacuum due to their surface area, effecting the cell pathlength hence transmission results [107]. Sample leakage under vacuum is also an issue with this cell [107].

The diamond window liquid cell (DWLC) was developed by Dominique Appadoo, the FIR / THz beamline scientist at the Australian synchrotron [107]. It utilises strong and small diamond crystal windows that retain their structure in vacuum conditions [107, 108]. Sample leakage is also decreased with the use of a spacer and rubber seal, where the liquid sample is clamped in the cell between the two diamond windows, spacer and rubber seal as illustrated in Figure 1-27 [107].

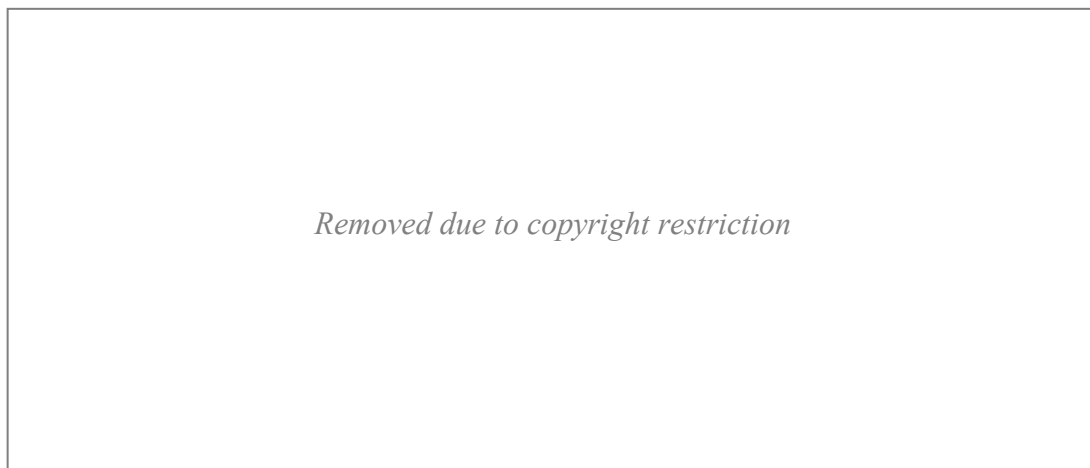


Figure 1-26: Photographs of (A) DWLC ready for sample prior to assembly, deconstructed DWLC (B) top window (C) spacer of various sizes and (D) bottom flange window, & (E) DWLC ready for assembly [107].

Water in liquid and frozen states have been analysed by the DWLC system in conjunction with cryogenic freezing of the sample compartment, finding that transmission results may be affected by sample temperatures [107, 108]. This has

potential for analysis of proteins as they can change structure when frozen, particularly when hydrated as it is likely that the protein's hydration layer stabilises the structure from the interaction of water with amino acids [104].

2 Project Aims

Current methods of establishing the age of a bruise may be invasive and the information presented in the breakdown process may be misleading. This project aims to expand and build on previous studies and knowledge by optimising analytical techniques for spectral identification of human haemoglobin (or Sheep if human haemoglobin is unavailable) and its various breakdown derivatives, individually and as mixtures, that contribute to the colour and spectrum of a bruise.

As bruise investigation in the laboratory is based on transmission and reflectance measurements to eliminate bruise discolouration variables, this project will specifically focus on spectroscopy of haemoglobin and its protoporphyrin's individual breakdown chemical products, particularly in the UV-Vis. region of the electromagnetic spectrum. However, as there is spectral overlap, data will also be collected in the more penetrative IR region (aiming to extend this beyond 2500 nm) to search for unique inter- and intra-molecular interactions and characteristics that may be used to identify and quantify the individual components. As there is a lack of literature regarding this and FIR analysis of haemoglobin and its breakdown products for this application, this thesis will be an original contribution to knowledge. Investigation into appropriate solvents for sample preparation and analysis will be carried out, particularly as bilirubin forms intra-molecular hydrogen bonds hence has low solubility in physiological solutions. This may involve cryogenic analysis to isolate differentiating chemical behaviours of analytes at different temperatures which is novel.

Other techniques that may be used for identification and quantification of the breakdown products in bruises such as Raman spectroscopy [59], hyperspectral imaging [11], dual-photon imaging of skin [109], histology, math models, and HO-1 gene expression (immunohistochemistry) [6, 21, 81, 110, 111] have not been

explored in this project due to impracticality and unavailability at the time the project was initiated.

The identification of bruises may be crucial in an investigation into a suspicious death. Hence, further scientifically rigorous analyses of bruise breakdown components will aid in the successful detection of crimes, exoneration of falsely accused related cases and improve our understanding of the process of development and aging of bruise marks.

3 Materials and Methods

3.1 Materials

3.1.1 Commercial Materials

College of Science of Engineering Store of Flinders University = SCSEFU

Lab. stock, College of Science of Engineering, Flinders University = LCSEFU

Lab. stock, ANSTO, Australian Synchrotron = LAS

Applied Biological Products Management-Australia = ABPM

Compound	#	Purity	Properties	Supplier
Acid-citrate-dextrose (ACD) blood	01	Anti-clotting factor added	Sheep, Liquid, Red, Pathogen-free	ABPM
Barnstead e-pure water	02	-	-	LCSEFU
Bilirubin	03	≥ 98%	Powder, Orange, 584.66 g/mole 91.49% Bilirubin IX α , 4.02% Bilirubin III α , 3.33% Bilirubin XIII α	Sigma-Aldrich [®]
Bilirubin conjugate ditaurate, disodium salt	04	May contain bilirubin 60-80% by weight	Powder, Orange-brown, 842.91 g/mol	Calbiochem [®]
Biliverdin	05	> 95 %	Powder, Green,	Santa Cruz

hydrochloride			619.12 g/mol	Biotechnology Inc.
Chloroform	06	≥ 99.5 %	Liquid, with stabiliser	Sigma-Aldrich®
Defibrinated (Def) blood	07	Clotting factors and fibrinogen removed	Sheep, Liquid, Red, Pathogen-free	ABPM
Dimethyl sulfoxide (DMSO-D₆)	08	> 98 %	Deuterated, Liquid, 84.17 g/mol	Sigma-Aldrich®
Dimethyl sulfoxide (DMSO-H₆)	09	≥ 99.9 %	Liquid, 78.13 g/mol	LAS
Ethanol	10	≥ 99.5 %	Liquid	LAS
Ferritin	11	in 0.15M NaCl	Type I from Horse Spleen 44 mg/mL, Liquid, Brown	Sigma-Aldrich®
Human haemoglobin (Hb)	12	> 96 %, Predominantly methaemoglobin	Red-brown Human lyophilized powder	Sigma-Aldrich®
Hydrochloric acid	13	2M	-	SCSEFU
Lithium heparin (LiHep) blood	14	Anti-clotting factor added	Sheep, Liquid, Red, Pathogen-free	ABPM
Methanol	15	≥ 99.5 %	Liquid	LAS
Neat blood	16	-	Sheep, Liquid, Red, Pathogen-free	ABPM
Paraffin oil	17	-	Liquid	LAS
Paraffin wax	18	-	Flakes	LAS
PE bag	19	-	Transparent, thin sheet	LAS
Polyethylene (PE)	20	-	Powder	SCSEFU
Polytetrafluoro-ethylene (PTFE)	21	-	Powder	SCSEFU
Potassium bromide (KBr)	22	≥ 99 %	Powder, 119 g/mol	SCSEFU
Potassium chloride (KCl)	23	≥ 99 %	Crystals, 74.5 g/mol	SCSEFU
Potassium phosphate monobasic (KH₂PO₄)	24	-	Powder, anhydrous, 136.09 g/mol	LCSEFU
Sodium	25	≥ 99.5 %	Crystals, 58.44	SCSEFU

chloride (NaCl)			g/mol	
Sodium hydroxide (NaOH)	26	> 98 %	Solid, 39.9 g/mol	LCSEFU
Sodium nitrite (NaNO₂)	27	> 98 %	Powder, pH 9, 69 g/mole	SCSEFU
Sodium phosphate dibasic (Na₂HPO₄)	28	98-100 %	Powder, anhydrous, 156.01 g/mol	LCSEFU
Ultrapure milliQ water (Water)	29	-	Liquid	LCSEFU, LAS

The Animal Ethics Committee has acknowledged the use of scavenged blood for the purposes of this research.

3.1.2 Prepared Materials

Preparation	#	Properties	Ingredients
ACD blood dried	30	Powder	ACD blood (#01)
ACD blood in PE	31	0.67 µL/mg of PE	ACD blood (#01), PE (#20)
ACD blood plasma	32	Centrifuged, Filtered	-
ACD blood plasma dried	33	Powder	ACD blood plasma (#01)
Bilirubin & bilirubin conjugate in PE	34	% by weight	37.5% BBC (#04) + 37.5% BB (#03) + 25% PE (#20) 37.5% BBC + 18.75% BB + 43.75% PE
Bilirubin (concentration in blood)	35	0.012 M 5 mL stock pH 7	3.26×10^{-2} g bilirubin (#03), few drops NaOH (#97), HCl (#89), PBS (#95)
Bilirubin conjugate in blood	36	82.5 & 800 mg/mL, 1:1 ratio of 0.8 mg each	Bilirubin conjugate (#04), defibrinated sheep's blood (#07)
Bilirubin conjugate in paraffin wax	37	1:2.5 & 2:1 ratios by weight	Bilirubin conjugate (#04), paraffin wax (#18)
Bilirubin conjugate in PE	38	25, 37.5, 50 % by weight	Bilirubin conjugate (#04), PE (#20)
Bilirubin conjugate in water	39	10 mg/mL	Bilirubin conjugate (#04), water (#02)

Bilirubin in neat blood	40	0.019 M	Bilirubin concentration in blood (#35), neat sheep's blood (#16)
Bilirubin in def blood	41	1.33 & 71 mg/mL	Bilirubin (#03), defibrinated sheep's blood (#07)
Bilirubin in chloroform	42	5 & 10 mg/mL	Bilirubin (#03), chloroform (#06)
Bilirubin in DMSO-d₆	43	65 & 160 mg/mL	Bilirubin (#03), DMSO-d ₆ (#08)
Bilirubin in DMSO-H₆	44	45 mg/mL	Bilirubin (#03), DMSO-H ₆ (#09)
Bilirubin in ethanol	45	1.45 mg/mL	Bilirubin (#03), ethanol (#10)
Bilirubin in KBr	46	5% by weight & 100-fold dilution	Bilirubin (#03), KBr (#21)
Bilirubin in methanol	47	6.4 mg/mL	Bilirubin (#03), methanol (#15)
Bilirubin in paraffin oil	48	5% by volume	Bilirubin (#03), paraffin oil (#17)
Bilirubin in paraffin wax	49	1:90 ratio by weight	Bilirubin (#03), paraffin wax (#18)
Bilirubin in PE	50	12.5, 25 & 50 % by weight	Bilirubin (#03), PE (#20)
Bilirubin in plasma	51	0.012 M, 20% & 50% 0.012 M by volume, 1:1000 by volume, Aqueous	Bilirubin (#03), filtered plasma (#77), 0.1 M NaOH (#97)
Bilirubin in PTFE	52	12.5, 25, 50 % by weight	Bilirubin (#03), PTFE (#22)
Bilirubin slurry	53	200 mg/mL	Bilirubin (#03), 0.1 M NaOH (#97)
Biliverdin & bilirubin in KBr	54	1:1, 1:3 ratios by weight	Biliverdin hydrochloride (#05), bilirubin (#03), KBr (#22)
Biliverdin & bilirubin in PE	55	% by weight	6.25% BV (#05) + 12.5% BB (#03) + 81.25 PE (#20) 1.5% BV + 6.25% BB + 92.25 PE
Biliverdin (estimated concentration in blood)	56	2.28 mg/mL (5 mL stock) pH 7	1.14×10^{-2} g biliverdin (#05), few drops NaOH (#97), HCl (#89), PBS (#95)
Biliverdin in DMSO-d₆	57	520, 400, 250 & 140 mg/mL	Biliverdin hydrochloride (#05), DMSO-d ₆ (#08)
Biliverdin in KBr	58	5% by weight	Biliverdin hydrochloride (#05), KBr (#22)
Biliverdin in	59	250 mg/mL	Biliverdin hydrochloride (#05),

methanol			methanol (#15)
Biliverdin in paraffin oil	60	10% by volume	Biliverdin hydrochloride (#05), paraffin oil (#17)
Biliverdin in paraffin wax	61	1:9 ratio by weight	Biliverdin hydrochloride (#05), paraffin wax (#18)
Biliverdin in PBS	62	1.14, 2.28 mg/mL, 1:1000 dilution (1 μ L/mL)	Biliverdin concentration in blood (#56), PBS (#95)
Biliverdin in PE	63	12.5, 25 & 30 % by weight	Biliverdin hydrochloride (#05), PE (#20)
Biliverdin in plasma	64	Aqueous	Biliverdin estimated concentration in blood (#56), filtered plasma (#77)
Biliverdin in sheep's blood	65	1:1 of 0.8 mg by weight, 17 mg/mL	Biliverdin hydrochloride (#05), defibrinated sheep's blood (#07)
Biliverdin slurry	66	625 mg/mL	Biliverdin hydrochloride (#05), 0.1 M NaOH (#97)
Biliverdin with bilirubin	67	1:1 approx	Biliverdin hydrochloride (#05), bilirubin (#03)
Biliverdin with bilirubin in blood	68	33 mg/mL	Biliverdin (#05) with bilirubin (#03) 1:1 mixture, defibrinated sheep's blood (#07)
Biliverdin, bilirubin & bilirubin conjugate in PE	69	% by weight	1% BV (#05) + 3.75% BBC (#04) + 3.75% BB (#03) + 91.5% PE (#20)
Def blood airdried	70	Powder	Def sheep blood (#07)
Def blood airdried in KBr	71	5% by weight	Def sheep blood (#07), KBr (#22)
Def blood dried - desiccator	72	0.67 μ L/mg of PE	Def blood (#07), PE (#20)
Def blood dried – vacuum desiccator	73	Powder	Def sheep blood (#07)
Def blood dried (vacuum) in KBr	74	5% by weight	Def sheep blood dried (#73), KBr (#22)
Def blood in PBS	75	6.7 μ L/mL	Def sheep blood (#07), PBS (#95)
Def blood in PE	76	0.67 μ L/mg of PE	LiHep blood (#14), PE (#20)
Def blood plasma	77	Centrifuged, Filtered	-
Def blood plasma airdried	78	Powder	Def sheep blood plasma (#77)
Def blood plasma dried - desiccator	79	Powder	Def sheep blood (#07)
Def blood plasma dried – vacuum desiccator	80	Powder	Def sheep blood (#07)
Ferritin dried	81	Powder	Ferritin protein (#11)

Ferritin in KBr	82	5% by weight & 50-fold dilution	Ferritins dried (#11), KBr (#22)
Ferritin in NaCl solution	83	1.0×10^{-4} , 0.88 & 44 mg/mL	Ferritins (#11), 0.15 M NaCl (#96)
Ferritin in PBS	84	Liquid	Ferritin (#11), PBS (#95)
Ferritin in PE	85	3, 6, 12.5, 25 & 50 % by weight	Ferritin dried (#81), PE (#20)
Human Hb in DMSO-d₆	86	180 mg/mL	Human haemoglobin (#12), DMSO-d ₆ (#08)
Human Hb in paraffin wax	87	1:70 ratio by weight	Human haemoglobin (#12), paraffin wax (#18)
Human Hb in water	88	20 mg/mL	Human haemoglobin (#12), water (#02)
Hydrochloric acid (HCl)	89	0.10 M 1.0 M	HCl (#13), water (#02)
LiHep blood dried	90	Powder	LiHep sheep blood (#14)
LiHep blood in PE	91	0.67 μ L/mg of PE	LiHep blood (#14), PE (#20)
LiHep blood plasma	92	Centrifuged, Filtered	-
LiHep blood plasma dried	93	Powder	LiHep blood plasma (#92)
Methaemoglobin	94	Aqueous	Def sheep's blood (#07), PBS (#95) or neat sheep's blood (#16), NaNO ₂ (#27)
Phosphate buffered saline solution (PBS)	95	pH 7.4 1L	8 g NaCl (#25), 0.2 g KCl (#23), 1.44 g Na ₂ HPO ₄ (sodium phosphate dibasic, #28), 0.24 g KH ₂ PO ₄ (potassium phosphate monobasic, #24), water (#02)
Sodium chloride (NaCl)	96	0.15 M	NaCl (#25), water (#02)
Sodium hydroxide (NaOH)	97	0.10 M	NaOH (#26), water (#02)
Stored neat sheep's blood in PBS	98	Refrigerated, 4 μ L/mL	Blood (#16), PBS (#95)

3.2 Instrumentation

Instrument	#	Range	Detector	Parameters
Analytical Balance	99	± 0.0001 g	-	-
Australian Synchrotron FIR/THz beamline, Bruker IFS125HR	100	10-5000 cm^{-1} (2000- 1,000,00	SiBolometer (10-370 cm^{-1}) Si:B Photodetector	200 mA, Cryogen-cooled Cryostat, Diamond Window Liquid Cells,

FTIR Spectrometer		0 nm)	(300-1850 cm ⁻¹) MCT _N narrow band (700-5000 cm ⁻¹)	GladiATR™Single Reflection ATR Accessory, OPUS™7.2.139.1294, Lake Shore Temperature Control, OriginPro 7.5, Aperture and Scan settings as described in Methods section
Bruker TOPSPIN 3 600 MHz NMR	101	C ¹² NMR H ¹ NMR	-	5 mm 600 MHz 541-PP NMR tubes, automatic sample injection
Electronic pH Meter	102	-	-	For solutions, calibrated at 20 degrees Celsius
Hand Pellet Press	103	-	-	3 & 5 mm pellet moulds
ISP-REF Integrating sphere coupled to ASD FieldSpec® 4 Hi- Res: High Resolution Spectroradiometer	104	350- 2300 nm	512 element silicon array, Graded Index InGaAs Photodiode Two Stage TE Cooled	12 Volts, 19 optic fibers, 3 nm VNIR & 8 nm SWIR resolution, pistol grip accessory connected to integrating sphere (Spectralon® coated doped with Barium Sulfate & 10.32 mm sample port aperture)
ISP-REF Integrating sphere coupled to Ocean Optics CHEMUSB4-Vis.- NIR Spectrophotometer	105	370-985 nm	Toshiba TCD1304AP Linear CCD array	1 nm resolution, 10.32 mm sample port aperture, Spectralon® coated doped with Barium Sulfate, parallel desktop utilising SpectraSuite software
Leica MZ55 Stereomicroscope	106	-	-	Available at the Australian Synchrotron
Mortar and pestle	107	-	-	Available at the Australian Synchrotron
Nikon D50 Digital SLR camera	108	-	-	Munsell Color X-rite ColorChecker® image reproduction target
Perkin Elmer UV- Vis.-NIR Lambda 950 Spectrophotometer	109	175- 3300 nm	Photomultiplier Tube (PMT), InGaAs	6Q Quartz Cuvette for Transmission, ≤ 0.2 nm resolution for NIR & ≤ 0.05 nm for UV/Vis, 150 mm Integrating Sphere Accessory for

				Reflectance, Scan Intervals: 1-5 nm, Scan Time: As Fast As Possible, 0 A /100% T ran with no samples/references, auto zeroed each analysis
Thermo Fisher Nicolet™ Continuum™ FT-IR Microscope	110	550-6500 cm ⁻¹ (18,182-1538 nm)	DTGS TEC	Beamsplitter KBr, ATR accessory, Ge window, Reflectance mode, KBr Beamsplitter, Gain 8 autogain, Optical velocity 0.5747-1.8, Aperture 37, screen wheel open, Diagnostic min and max -0.45-7, scans 16, resolution 1-4, experiment Smart Orbit
Vacuum Desiccator	111	-	-	Connected to vacuum pump, Available at the Australian Synchrotron
Varian Cary 50 UV-Vis. Spectrophotometer	112	190-1100 nm	2 silicon diode detectors	6Q Quartz Cuvette, Data Collection Time: Medium ≤1.5 resolution
Vortex Mixer	113	-	-	-
Water Bath at the Australian Synchrotron	114	-	-	40 Degrees

Instrumentation was utilised according to safe operating procedures. Changes to normal operating methodology is documented in Novel Instrumentation Arrangements, below.

3.2.1 Novel Instrumentation Arrangements

3.2.1.1 Perkin Elmer UV-Vis.-NIR Lambda 950 Spectrophotometer

Samples and references pipetted on to filter paper were mounted to the 150 mm integrating sphere accessory as shown in the below inset figure at 90° (perpendicular to the workbench). Samples were mounted with a second filter paper layer as to prevent seepage to the reflective reference covering the sample and reference ports.



Figure 3-1: Perkin Elmer UV-Vis.-NIR Lambda 950 Spectrophotometer setup with the 150 mm integrating sphere accessory. Inset: open sample compartment for 150 mm integrating sphere accessory showing the vertical reference sample port.

3.2.1.2 ASD FieldSpec. with Integrating Sphere

Once switched on, the instrument warmed for 1 hour prior to beginning analysis. A pistol grip accessory was connected to the fibre optic cable of the spectroradiometer and held by foam and a bulldog clip approximately 2-10 mm apart from the fibre optic cable of the ISP-REF Integrating sphere. Tape was used to secure fibre optic cables in place. Fibre optic cables were connected to the integrating sphere's (S) SMC Connector and the integrating sphere was set to internal reflectance (I). This novel arrangement in the figure below was utilised with laboratory lights off to minimise light interference from the environment.

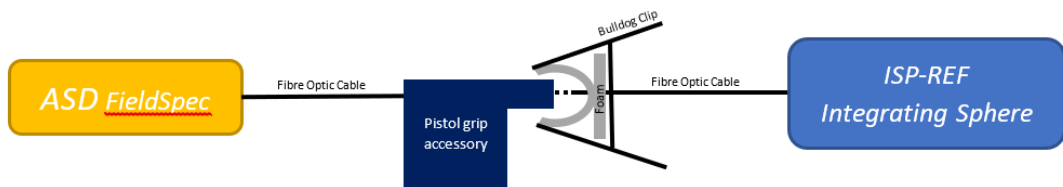


Figure 3-2: Schematic of ISP-REF Integrating Sphere coupled to ASD FieldSpec[®] 4 Hi-Res Spectroradiometer.



Figure 3-3: ISP-REF Integrating Sphere shown here with the aperture upwards. Also shown is the sphere's fiber optic cable and bulldog clip utilised for the novel setup when coupled to the ASD FieldSpec.

3.2.1.3 CHEMUSB4-Vis.-NIR Spectrophotometer with Integrating Sphere

An Apple MacBook installed with parallel desktop was used to run Ocean Optics XR software, SpectraSuite. This produced spectral output received by USB from the Ocean Optics CHEMUSB4-Vis.-NIR Spectrophotometer, which was connected to the ISP-REF Integrating Sphere via fibre optic cable as shown in the figure below. A large transparent Ziplock bag was utilised to contain the integrating sphere and nitrogen inlet when required. This was sealed, leaving approximately 3 cm open for nitrogen outlet.

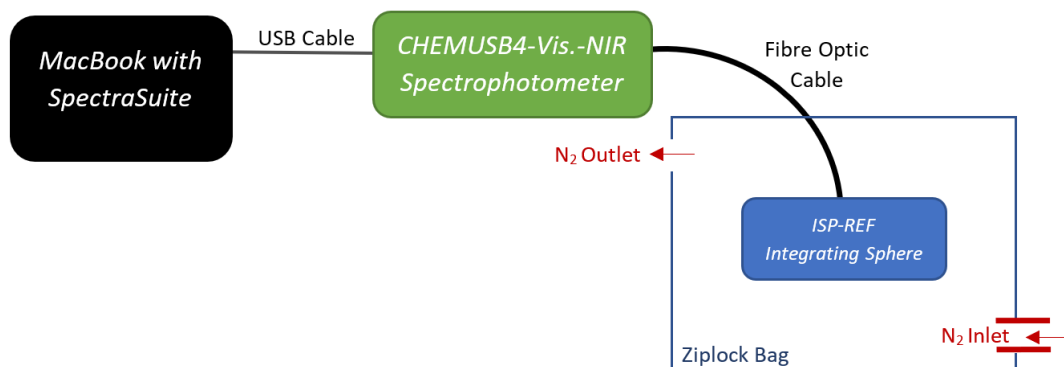


Figure 3-4: Schematic of ISP-REF Integrating Sphere coupled to CHEMUSB4-Vis.-NIR Spectrophotometer.

3.2.1.4 Far Infrared (FIR) / THz Beamline

Three machined diamond liquid window cells were available to use at the Australian Synchrotron. These were labelled 'A', 'B' and 'C', having 'A' created as the prototype and 'B' and 'C' together later.

A retainer was utilised on the ATR accessory for liquid samples.

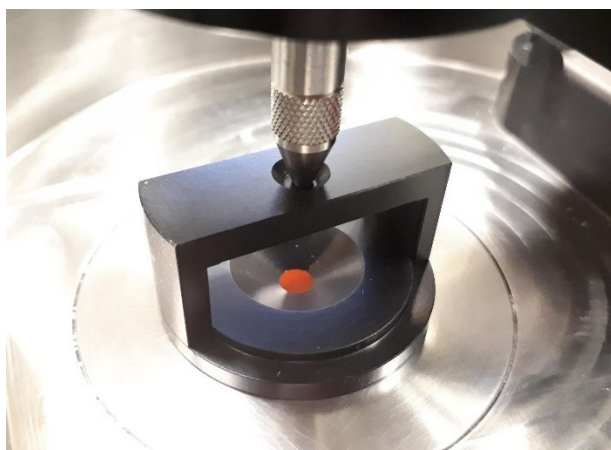


Figure 5: Image of ATR Retainer taken at the Australian Synchrotron with bilirubin liquid sample.

3.3 Methods

3.3.1 Transport of Samples

Blood samples provided from the Forensic Science Centre of South Australia were transported in a Styrofoam cooler box containing ice packs in an air-conditioned

motor vehicle. Temperature and relative humidity during transport were reported by the Weatherzone.com website as approximately 25 degrees Celsius and 54%, respectively.

Samples transported to and from the Australian Synchrotron were also contained in a Styrofoam cooler box with ice packs. The cooler box remained in checked bag luggage until arrival at the facility where samples were stored at 4 and -15 degrees Celsius.

3.3.2 Solution Preparations

Solutions were quantitatively prepared with ingredients listed under the Prepared Materials section, however particular methodology to note are reported below. A vortex mixer was utilised to aid in mixing some solutions that appeared to have low solubility.

3.3.2.1 Phosphate Buffered Saline Solution

PBS solution (#95) was quantitatively prepared using a known method [112] at a volume of 1L by weighing each dry ingredient using an analytical balance (#99). This provided a solution of pH 7.4 as tested using a pH meter (#102). The resulting PBS solution was stored at 5 degrees Celsius.

3.3.2.2 Blood Plasma

Blood supplied (#01, 07, 14) involved several test tubes of red blood cells and small urine containers of supernatant plasma; whole blood was centrifuged at the Forensic Science Centre. Plasma was filtered using filter paper in a Styrofoam box containing ice packs (prevent decomposition) at Flinders University to remove opaque proteins that would hinder spectroscopy pathlength. Prepared plasma was stored both at 5 and -15 degrees Celsius.

3.3.2.3 Methaemoglobin Formation

Sodium nitrite (#27) was added to blood (#01, 07, 14, 16), PBS (#95), and Plasma (#32, 77, 92) or mixtures of these with agitation until all solid dissolved [113]. These

preparations were stored at 5 degrees Celsius and some analysed 3 days later. In some cases, filter paper samples were kept in a Styrofoam cooler box at standard laboratory temperature and conditions over 3 days to analyse again. Filtered plasma (#32, 77, 92) or PBS (#95) containing equivalent sodium nitrite amounts were used as the baseline and stored in the same conditions. Refrigerated methaemoglobin samples were not kept for longer than 12 days.

3.3.2.4 Biliverdin Solutions

A 2.28×10^{-3} g/mL solution of biliverdin (1/3 that of bilirubin expected concentration in adult blood) was quantitatively prepared [63] by adding 0.1 M sodium hydroxide (#97) dropwise to 1.14×10^{-2} g biliverdin (#05) with agitation until all solute dissolved. PBS (#95) was added bringing the total volume to 2/3. 0.1 and 0.01 M hydrochloric acid (#89) was used dropwise to adjust the pH to approximately 7. The remaining quantitative volume was made up with PBS.

A 1:1000 dilution by volume of this biliverdin solution (#56) was prepared in PBS solution.

Biliverdin solution (#56) was quantitatively pipetted into plasma (#77) for analysis in this matrix. All solutions were stored at 5 degrees Celsius.

3.3.2.5 Bilirubin Solutions

A 0.012 M solution of bilirubin (expected concentration of bilirubin in adult blood) was quantitatively prepared [63, 66, 68] by adding approximately 2.5mL of 0.1 M sodium hydroxide (#97) dropwise to approximately 0.0350 g bilirubin (#03) with vigorous agitation until all solute dissolved. PBS (#95) was added bringing the total volume to two thirds. 0.1 M hydrochloric acid (#89) was used dropwise to adjust the pH to approximately 7. The remaining quantitative volume was made up with PBS.

A 1:1000 dilution by volume of this bilirubin solution was prepared in filtered sheep blood plasma (#77).

A 0.012 M solution of bilirubin in plasma was quantitatively prepared by adding approximately 2mL of filtered plasma (#77) to approximately 0.0350 g bilirubin

(#03) with vigorous agitation. 0.1 M added sodium hydroxide (#97) was then added dropwise until all solute dissolved. 0.1 M hydrochloric acid (#89) was used dropwise to adjust the pH to approximately 7. The remaining quantitative volume was made up with filtered plasma. All solutions were stored at 5 degrees Celsius.

3.3.2.6 Ferritin Dilutions

Baseline solution for ferritin stock solution (#11) was sodium chloride solution (#96). The ferritin stock solution was stored at -15 degrees Celsius.

A 1.76 and 0.88 mg/mL solution was quantitatively prepared from the thawed stock solution and 0.15 M sodium chloride (#96). For analysis, sodium chloride solution (#96) was used as the baseline.

The 0.88 mg/mL solution was then used to prepare a dilution at concentration 0.0001 mg/mL with PBS solution (#95). PBS solution was utilised as the baseline for this preparation. All diluted solutions were stored at 5 degrees Celsius.

3.3.3 Sample Preparation for UV-Vis. Transmission Spectroscopy

Prepared samples were pipetted into a 6Q Quartz cuvette for transmission analysis. Respective solvents were used as references.

3.3.4 Sample Preparation for UV-Vis.-NIR Reflectance Spectroscopy

Generally, approximately 1-3 drops of sample were pipetted on double layered filter paper (90-110 mm, folded) for analysis. Appropriate solvents relating to the samples were used as the baseline (1-3 drops on folded 90-110 mm filter paper). Photographs were taken of some samples using a Nikon D50 Digital SLR camera with aid of a Munsell Color X-rite ColorChecker[®] image reproduction target (#108).

3.3.4.1 Re-suspension of Dried Blood

Filter paper samples were dried by placing in a Styrofoam cooler box and leaving

undisrupted at standard laboratory temperature and conditions. Humidity data was collected from the website, Weatherzone.com.

Dried filter paper sample spotted with blood (#07) was dampened by pipetting 8 drops of water (#02) onto the blood spot. The process was repeated with the dried reference sample. These were left for approximately 30-40 seconds to soak prior to analysis. This analysis was duplicated.

The dried result of the previous re-suspension in water was dampened by pipetting 8 drops of plasma (#77) onto the blood spot. The process was repeated with the dried reference sample. These were left for approximately 1 minute to soak prior to analysis.

3.3.5 Sample Preparation for FIR / THz Beamline

3.3.5.1 Pellets

Pellets were created by grinding sample in a small mortar and pestle (#107), then compressing approximately 1.5 mg (for 3 mm pellet size) in a hand pellet press (#103). In the cases where compounds with low absorbance were used to dilute analyte, a mixture at determined ratio of analyte and diluting compound was homogenously crushed with mortar and pestle where approximately 1-1.5 mg of this was compressed into a 3 mm pellet. In some instances, 7 mm pellets were pressed with approximately 5-6 mg of ground sample.

3.3.5.1.1 Dried Blood and Ferritin

Blood and plasma samples (#01, 07, 14, 32, 77, 92) were airdried, dried in a desiccator and dried with a vacuum desiccator (#111) overnight by pipetting 20 μ L each on to approximately 30 mg of diluting compound (#20). This was mixed as a slurry with a spatula before allowing to dry.

Ferritins were dried overnight for pellet pressing as described above with a vacuum desiccator (#111) available at the Australian Synchrotron. Salt (#25) dried in the same way was used as baseline.

3.3.5.2 Diamond Window Liquid Cells

Before use, the cell components were flushed with compressed nitrogen. During assembly, vertical lines inscribed on the cell (windows components) were matched such that window alignment was optimum.

Volumes of samples pipetted into cells were dependent on the cell spacer used as per table below.

Spacer (μm)	Volume (μL)
5	0.5
10	0.8
15	1.2
20	1.6
25	2.0
50	4.0
60	4.5

Table 3-1: Volumes of liquid samples pipetted into DWLC's for analysis.

Cells were assembled with the aid of calipers such that compression was even for both screws. Once assembled, cells were checked for air gaps under a microscope at the Australian Synchrotron on the IR beamline when this was available to use.

Cells were mounted to the cryostat such that the flange side (Figure 1-26 (D)) was directed towards the synchrotron beam. Hence flange side was in contact with the cryostat finger.

For haemoglobin and protein-based samples, soapy water was used to clean diamond windows after use.

3.3.6 Analysis using UV-Vis. Transmission Spectroscopy

For the Perkin Elmer UV-Vis.-NIR Lambda 950 Spectrophotometer, both the sample in one cuvette and its respective reference in another cuvette were inserted into the sample compartment.

3.3.7 Analysis using UV-Vis.-NIR Reflectance Spectroscopy

3.3.7.1 Perkin Elmer UV-Vis.-NIR Spectrophotometer

Samples and references were mounted in the integrating sphere accessory compartment such that spotted samples were in the centre of the integrating sphere's aperture. Data collected was saved in *.CSV format to be reproduced with Microsoft Office 365 Excel® software. Sample analysis was repeated at least 3 times unless being used for time studies greater than 5 days.

3.3.7.1.1 Spectra Smoothing

In the UV-WinLab – Run window of the spectrophotometer's computer program interface, the 'Processing' tab was selected. The 'Smooth' function was added to the process settings with the following settings: Type: Triangular, Width: 13, 37, 49, Range Selection: 2500-800. These were sent to the Data Processing Viewer (DPV) where they could be then saved in .sp file format.

Smoothing algorithm types: **Block Average** – all points are weighted equally, giving the maximum noise reduction for a chosen range; **Triangular** – the weighting coefficients decrease linearly from the center of the smoothing range, causing less broadening than Block Averaging but achieving less noise reduction; **Savitsky-Golay** – uses least squares fitting a cubic polynomial to achieve minimum distortion [114].

Various algorithm types (Block Average, Triangular and Savitsky-Golay) and Widths (5, 9, 13, 19, 25, 37, 49 and 149) were explored for optimisation of the smoothing function (smoothed the data enough but also didn't lose too much spectral information) [115].

3.3.7.2 ASD FieldSpec. with Integrating Sphere

White references were acquired every 10-15 minutes where applicable to prevent drift in measurements. Spectral data was saved as .txt collated files and imported to Microsoft Office 365 Excel® for processing including normalisation.

3.3.7.3 CHEMUSB4-Vis.-NIR Spectrophotometer with Integrating Sphere

Analysis was carried out inside a fume hood in proximity of a nitrogen inlet. The Ziplock bag containing the integrating sphere was flushed with nitrogen for 15 minutes before samples were placed in the bag and scans were initiated on the MacBook. Integration time was adjusted in SpectraSuite to produce a reference and dark spectrum with the least noise. Data was saved as .txt files which were later imported to Microsoft Office 365 Excel® Software for processing.

3.3.7.4 FTIR Microscope with ATR Accessory

Approximately 5-10 mg of ground, homogenous sample was placed on the platform and pressed with the diamond (anvil) on to the window. After analysis, the sample was cleaned from the contact surfaces using mild soapy demineralised water with a lint-free soft cloth. Spectral data was printed from OMNOC programming and saved as SPA and CSV files. CSV files were imported to Microsoft Office 365 Excel® for processing including normalisation. Biliverdin and bilirubin sample experiments were carried out in duplicate.

3.3.8 Analysis using the FIR / THz Beamline

3.3.8.1 Acquisition and Processing

For general spectra acquisition ‘Repeated Measurements’ was selected where the following general parameters were adjusted from default settings:

Repeat the Measurement (Run)	10 times
Delay Between Measurements (Runs)	0 sec
Sample Scan Time	100
Background Scan Time	20 Scans
Save Data From	0-1000 cm^{-1}
Aperture Setting	2.5-3.5 mm
Resolution	1 cm^{-1}

Table 3-2: Default parameters set for spectral acquisition with the SiBolo detector from the FIR/THz beamline at the Australian Synchrotron.

Amplitude and Position in OPUS software’s ‘Check Signal’ tab was optimised such that the amplitude was at the highest and noted. Amplitude or ‘sensitivity’ varied

depending on concentration of absorbing (IR active) analyte and thickness of sample, particularly if in pellet form.

Each set of 10 repeated measurements were averaged. For overnight measurements, the parameters, Repeat the Measurement, Delay Between Measurements and Sample Scan Time were adjusted to suit and are documented in figure captions. Raw synchrotron files from OPUS processing software were saved as .dpt format to be viewed on Microsoft Office 365 Excel® and OriginPro software for further processing. Manual background subtractions, transmission to absorbance conversions and vector normalisations (in frequency ranges of interest) were carried out using OPUS software. In some instances, normalisation was carried out using Microsoft Excel.

Sample blanks (synchrotron light only) were checked to amplitude of approximately 20000-24000.

3.3.8.2 Detectors

When the detector was changed to Si:B or MCT_N, the sample scan time was adjusted to 10 or 4, respectively, as required to account for speed and less spectral noise.

Detectors were replenished with liquid nitrogen every 4-6 hours and liquid helium every 24 hours. Detector gain was adjusted to high when utilising liquid cells.

3.3.8.3 Diamond Window Liquid Cells

DWLC samples were mounted to the cryostat for transmission analysis on the top and middle positions.

3.3.8.4 Cryostat Cryogenic Analysis

For cooling cycles of samples, the cryostat and hence samples were cooled with liquid nitrogen to 78 degrees Kelvin, heated with a heater coupled to the cryostat to 298 degrees Kelvin, cooled again to 78 degrees Kelvin then heated to room temperature. Some samples were not cooled twice.

A thermocouple connected to a Lake Shore Temperature Control program was used

to monitor, set and control the temperature of the cryostat and hence the samples. This was done by opening the Lake Shore software and creating a name for a Microsoft Excel spreadsheet that would be generated once the analysis was complete. Temperature was set at the maximum point of 298 Kelvin and a heater was applied manually by the user of the program during analysis as required by selecting 'Low', 'Medium' or 'High' heating settings. Heating was set to 'Off' when liquid nitrogen was being poured into the cryostat during periods of cooling.

For acquisition, the repeat the measurement parameter was adjusted to 30 times as each run was 30 seconds in duration. Once 'Begin' was clicked on the acquisition software, 2-5 scans were taken before liquid nitrogen was poured into the cryostat inlet whilst scans continued. After analysis, a heat gun was used to defrost and dry the frozen cryostat if required.

Most cryogenic sample data produced in OPUS required processing of fringed spectra as described below. OPUS runs were then allocated (via time parameters) to respective time and temperature data generated as Excel spreadsheets from the temperature control program.

3D colourmap surface contour plots do not contain temperature as an axis option as it is not in ascending/descending order.

3.3.8.5 Processing Fringed Spectra

OPUS format files of spectral averages were opened in the OPUS software. The inverse Fourier Transform of the spectra was taken by selecting 'Inverse FT.' In the pop-up window for this function, 'Use file limits' was selected and then 'Get Interferogram' was clicked. The 'Zoom In' function was used to select a single interference. 'Straight Line Generation' was then applied for this frequency range when selecting 'Get Display Limits,' followed by 'Generate.' Using the 'zoom Out' function, more interferences could be selected to generate straight lines. To return to Fourier Transformed version of spectra, 'Interferogram to Spectrum' function was applied with parameters varying from default; Frequency first: 1000 and last: 0, and Limit Data Resolution to: 1 and Phase 0.

3.3.8.6 ATR Accessory

A retainer was employed for containment of most liquid samples which were covered once they were transferred to the ATR window for the duration of analysis unless drying was intended. A small desk fan was utilised to promote drying of samples when required. The anvil was utilised for all solid (included powdered) samples. Mild soapy demineralised water with a lint-free soft cloth was used to clean the ATR diamond and anvil for haemoglobin and protein-based samples.

4 Results

4.1 Transmission Spectroscopy

4.1.1 Ultraviolet-Visible-Near Infrared (UV-Vis.-NIR)

4.1.1.1 Stored Blood

The spectrum of stored neat blood diluted in PBS contains oxyhaemoglobin (539 & 576 nm) and methaemoglobin (502 & 630 nm) peaks in the UV-Vis.-NIR region. There is an additional absorption peak at approximately 983 nm. Below 450 nm and above 1150 nm absorbance is saturated. The NIR spectral profile appears to be similar to water and PBS (spectra in section 4.2.1.1.1).

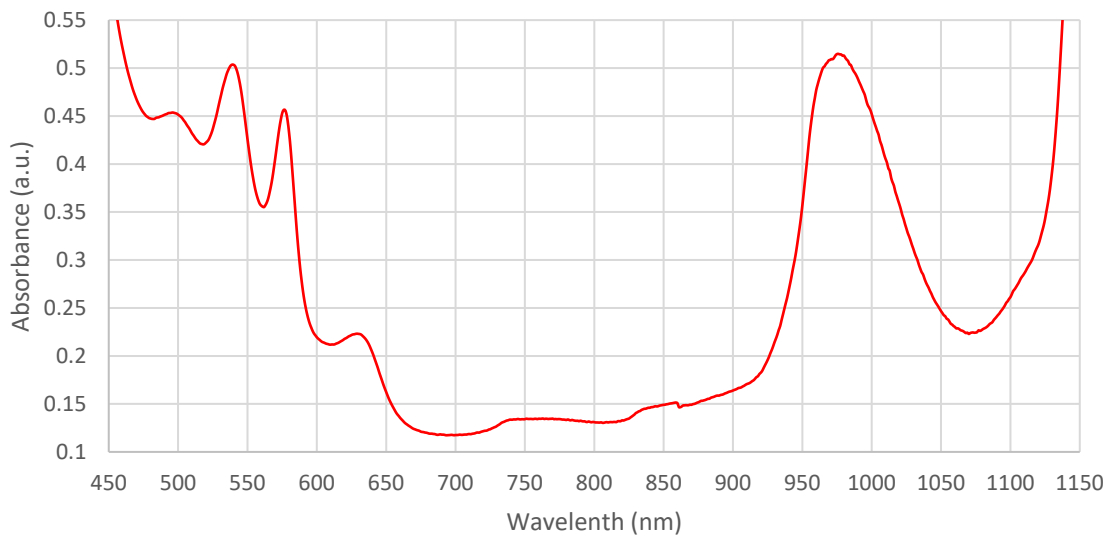


Figure 4-1: UV-Vis.-NIR spectrum of stored neat blood diluted in PBS (4 µL/mL) analysed on a Perkin Elmer UV-Vis.-NIR Lambda 950 Spectrophotometer at Flinders University in a quartz cuvette using PBS as a baseline.

4.1.1.2 Methaemoglobin

An in vitro formation of methaemoglobin exhibited peaks at 520, 541, 555, 577, 590 and 629 nm.

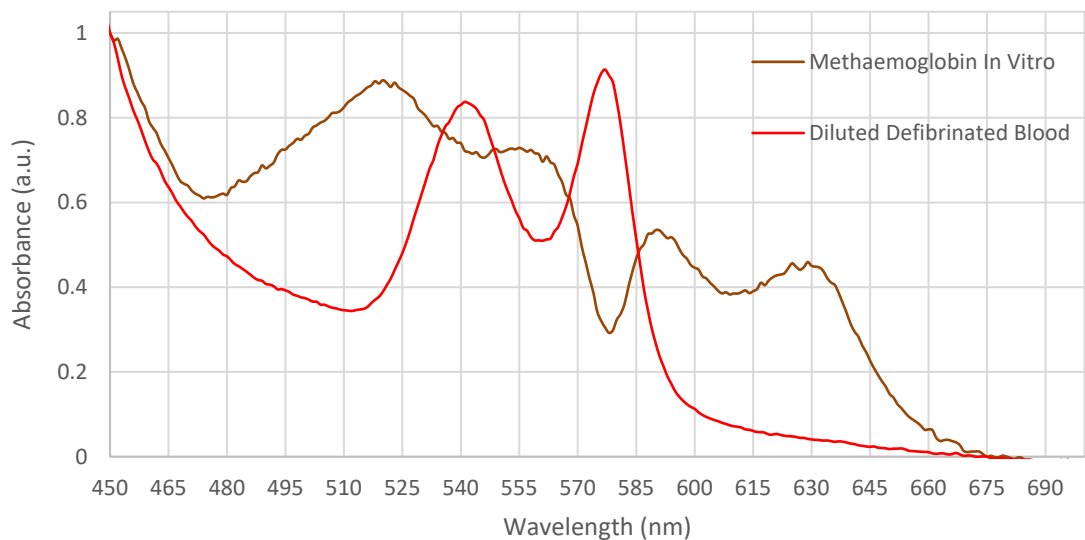


Figure 4-2: UV-Vis. Spectrum of methaemoglobin formation in a quartz cuvette (6.7 µL/mL with 294.1 mg sodium nitrite), analysed on a Perkin Elmer UV-Vis.-NIR Lambda 950 Spectrophotometer at Flinders University.

A colour change from red to brown was observed for formation of methaemoglobin in vitro. Peaks and colour change are as expected as discussed in section 5.

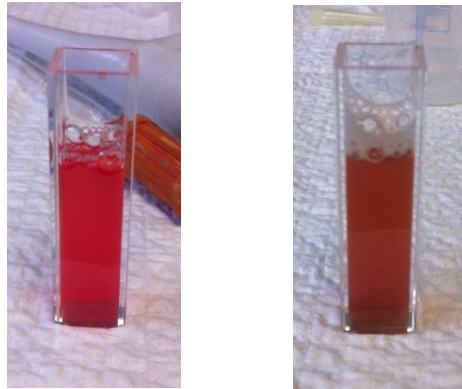


Figure 4-3: Images of defibrinated sheep's blood in plasma (6.7 $\mu\text{L}/\text{mL}$) in a quartz cuvette before (left) and after (right) addition of sodium nitrite (294.1 mg).

4.1.1.3 Biliverdin

Biliverdin diluted in PBS produces a green solution and broad absorption observed at approximately 650 nm. Additionally, strong absorption peaks are evident at 378 and 975 nm. Absorbance is saturated below 200 nm and above 1150 nm. UV-Vis spectra is similar to UV-Vis reflectance spectra. Additionally, NIR spectra is similar to that of water and PBS as seen in section 4.2.1.1.1.

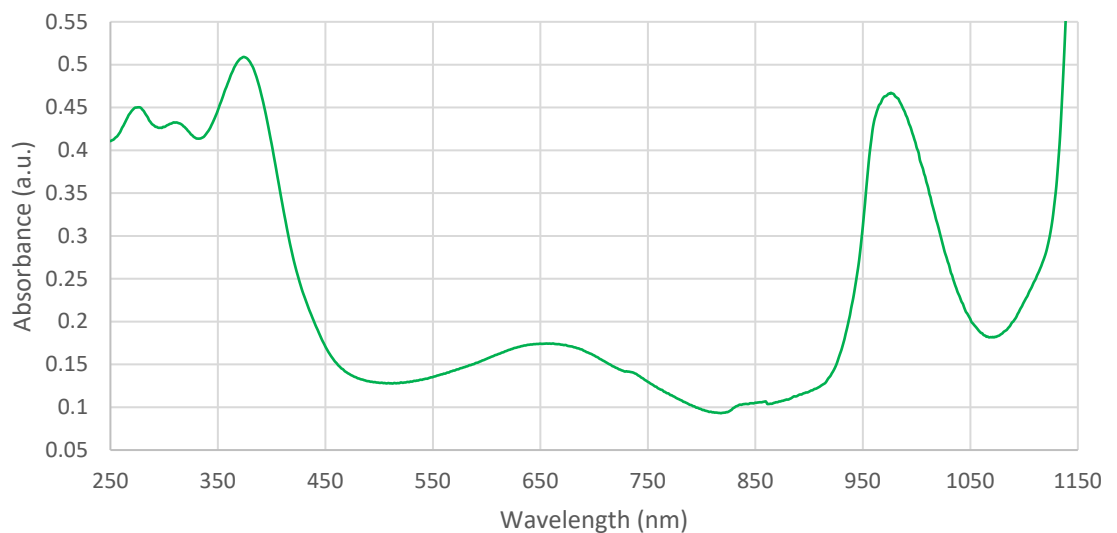


Figure 4-4: UV-Vis.-NIR spectrum of biliverdin diluted in PBS (1 $\mu\text{L}/\text{mL}$) analysed in a quartz cuvette on a Perkin Elmer UV-Vis.-NIR Lambda 950 Spectrophotometer at Flinders University.

4.1.2 Far Infrared (FIR)

Beam current for beamtimes varied between 165-200 mA, giving a maximum reduction of spectral intensity of 60%.

4.1.2.1 Pellets

4.1.2.1.1 Pure

4.1.2.1.1.1 BILIVERDIN

Peaks are observed at approximately 70, 92, 118, 140, 206, 262, 288, 300, 340 and 370 wavenumbers. Absorbance saturation occurs above 480 wavenumbers.

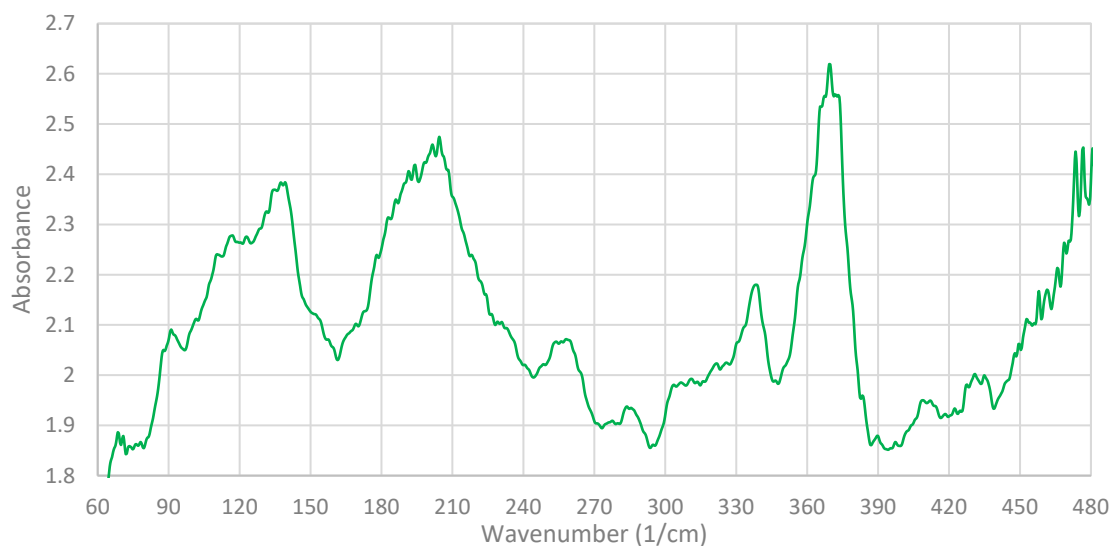


Figure 4-5: FIR spectra of pressed biliverdin pellet (approx. 1 mg) analysed on the THz/FIR beamline at the Australian Synchrotron using the SiBolo detector at an amplitude of 170.

4.1.2.1.1.2 BILIRUBIN

Attempts to pellet pure bilirubin were unsuccessful as the pellet crumbled after compression with the hand pellet press.

4.1.2.1.1.3 BILIRUBIN CONJUGATE

Peaks are observed at approximately 220, 300, 350 and 395 wavenumbers, with oversaturation occurring above 460 wavenumbers. Peaks are broader than those observed in the pure biliverdin pellets.

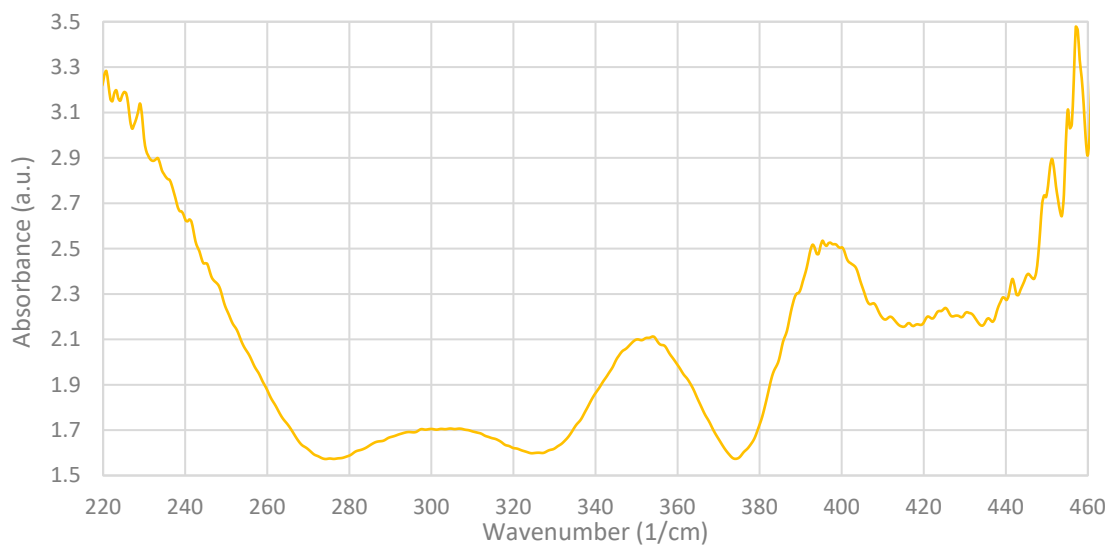


Figure 4-6: FIR spectra of pressed bilirubin conjugate pellet (approx. 5 mg) on the THz/FIR beamline at the Australian Synchrotron using the SiBolo detector at an amplitude of 470.

4.1.2.1.1.4 FERRITIN

Amplitude for the first ferritin pellet (approximately 2 mg) was 40 and resultant spectral acquisition saturated absorbance, hence no average was taken. A duplicate pellet of this sample was too thin and fell out of sample holder due to internal sample compartment vacuum.

4.1.2.1.2 Polyethylene (PE)

4.1.2.1.2.1 BLOOD

Small and weak peaks are observed across 60-360 cm^{-1} , with a general increase in absorbance towards larger wavenumbers. These are observed at 70, 91, 100, 110, 125, 135, 143, 160, 170, 185, 200, 222, 235, 245, 250, 262, 270, 285, 302, 310, 320, 340 and 360 wavenumbers, Airdried blood presents a broader band between 135 and 210 wavenumbers.

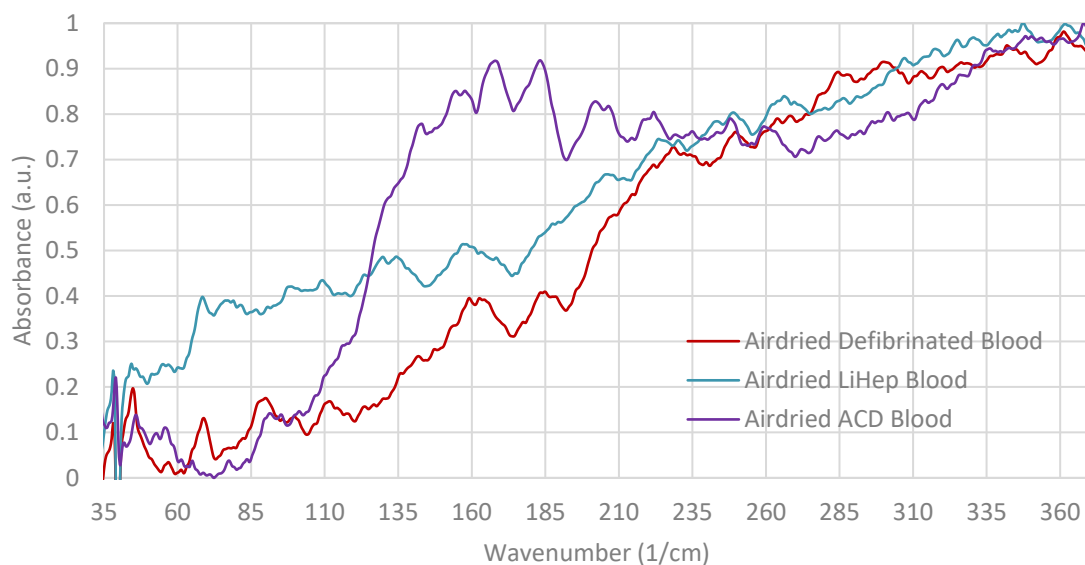


Figure 4-7: FIR overlaid pressed dried defibrinated, LiHep and ACD blood samples in PE pellets (0.67 $\mu\text{L}/\text{mg}$, weights approx. 1 mg), normalised between 40 and 400 wavenumbers, analysed on the THz/FIR beamline at the Australian Synchrotron using a SiBolo detector with amplitudes 2800 (Def), 3230 (LiHep) & 6000 (ACD).

Airdried samples increased the wait time for the beamline instrument pressure to drop to an appropriate range to perform analyses using synchrotron light, hence samples dried using a desiccator and instrument vacuum compartment were investigated below.

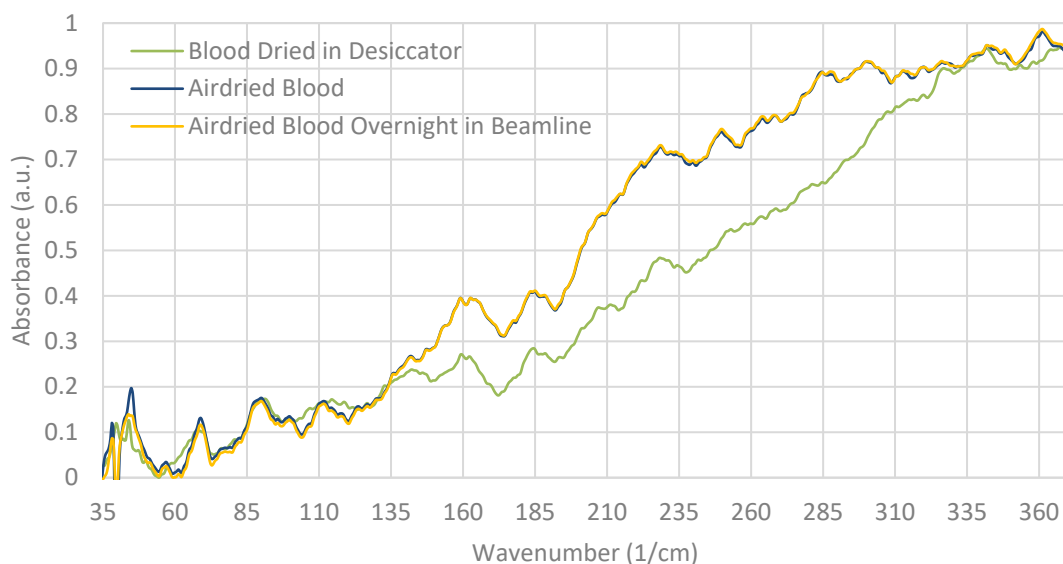


Figure 4-8: FIR overlaid spectra of pressed variously dried defibrinated blood samples in PE pellets (0.67 $\mu\text{L}/\text{mg}$, weights approx. 1 mg), normalised between 40 and 400 wavenumbers, analysed on the THz/FIR beamline at the Australian Synchrotron using a SiBolo detector with amplitudes of approximately 2800. Overnight (8.86 hours) parameters in acquisition: ‘Delay between Measurements’ was set to 1200 secs & ‘Repeat the Measurement’ was set to 100.

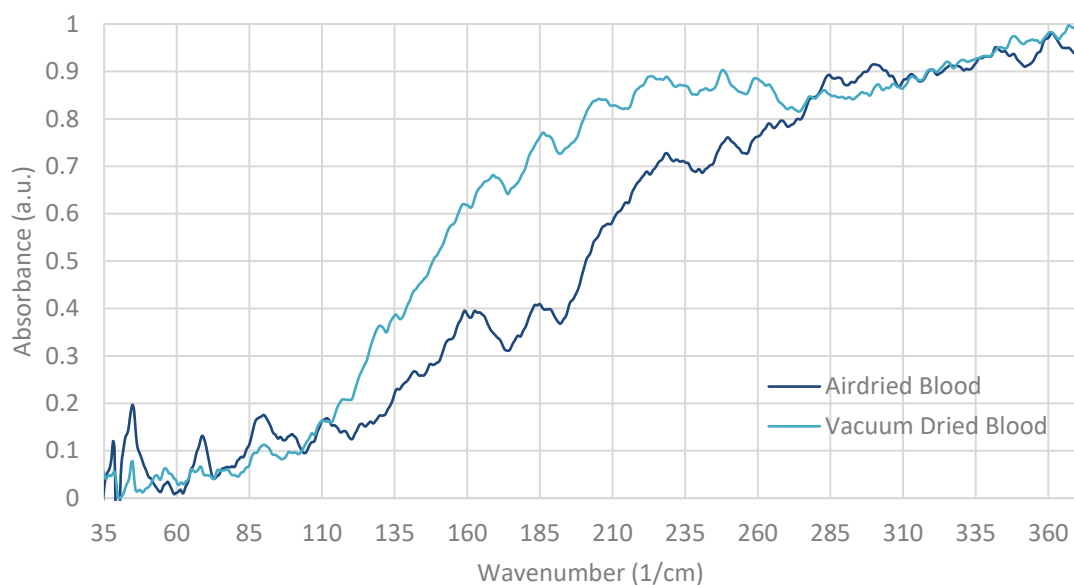


Figure 4-9: FIR overlaid spectra of pressed variously dried defibrinated blood samples in PE pellets (0.67 $\mu\text{L}/\text{mg}$, weights approx. 1 mg), normalised between 40 and 400 wavenumbers, analysed on the THz/Fir beamline at the Australian Synchrotron using a SiBolo detector with amplitudes of 2800 (airdried) & 1450 (vacuum-dried).

Vacuum dried blood was also analysed overnight with parameters: delay between measurements set to 1200 secs and Repeat the Measurement 100 times. As the result of this was a series of spectra the same to that presented above, it is not included here. Variance in drying methods was observed in general absorbance in the 100 – 300 wavenumber regions.

4.1.2.1.2.2 BILIVERDIN

Biliverdin mixed in a ratio of 1:1 with PE (50%) was attempted 4 times, however when grinding samples in mortar and pestle, it became ‘sticky’ in consistency and difficult to manage pressing into a pellet. Hence this ratio mix was abandoned, and lower ratios attempted. The 30% biliverdin in PE sample is a rough dilution.

Peaks in three dilutions were observed at approximately 210 and 370 wavenumbers. There is also a strong saturated absorbance at approximately 540 wavenumbers.

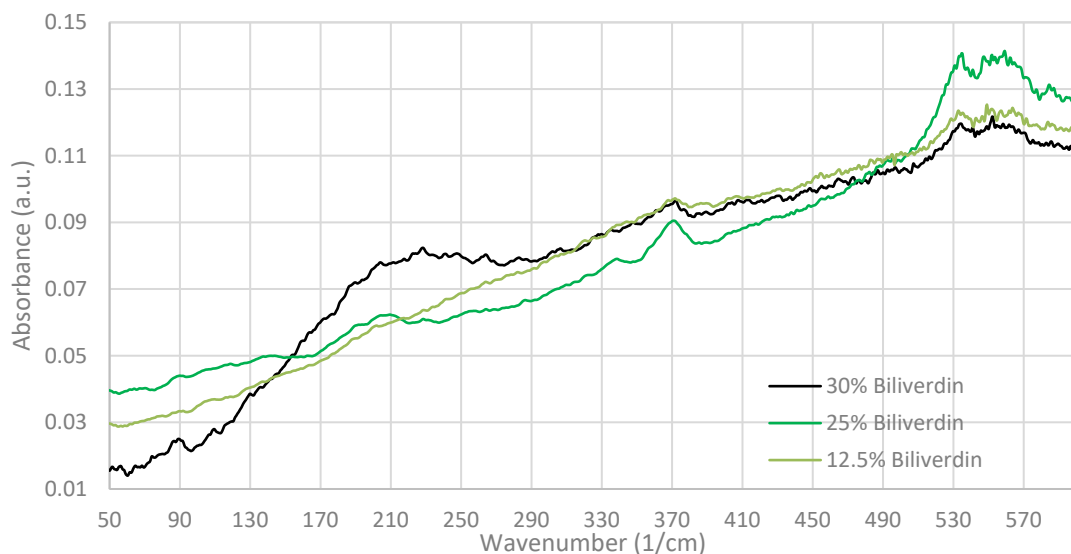


Figure 4-10: FIR overlaid spectra of pressed biliverdin in PE at different concentrations (pellet weights approx. 1 mg), normalised between 50 and 600 wavenumbers, analysed on the THz/FIR beamline at the Australian Synchrotron using a SiBolo detector with amplitudes of 3300 (30% biliverdin), 7000 (25% biliverdin) and 6500 (12.5% biliverdin).

4.1.2.1.2.3 BILIRUBIN

Peaks are observed at approximately 74, 188 (broad), 300, 321, 364, 384, 433 and 484, with saturated absorbance above 540 wavenumbers.

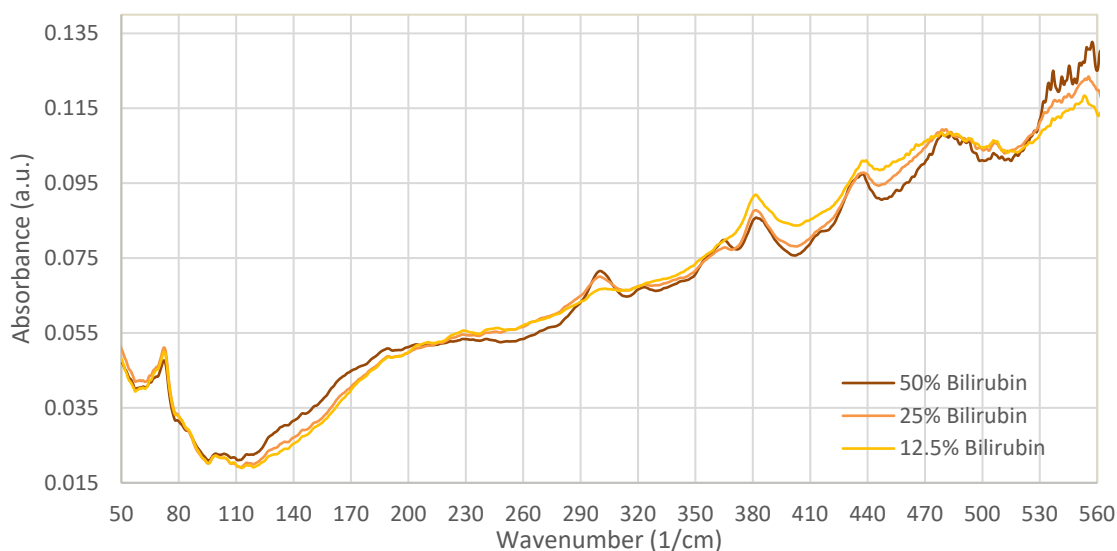


Figure 4-11: FIR overlaid spectra of pressed bilirubin in PE pellets (weights approx. 1 mg) at different concentrations, normalised between 40 and 590 wavenumbers, analysed on the THz/FIR beamline at the Australian Synchrotron using a SiBolo detector with amplitudes of 2760 (50 % bilirubin), 3000 (25% bilirubin) & 3760 (12.5% bilirubin).

4.1.2.1.2.4 BILIRUBIN CONJUGATE

In the 50% bilirubin conjugate sample, peaks are distinguishable at approximately 200, 300, 357, 398, 461 and 531 wavenumbers. These become less evident with decreasing concentration of bilirubin conjugate.

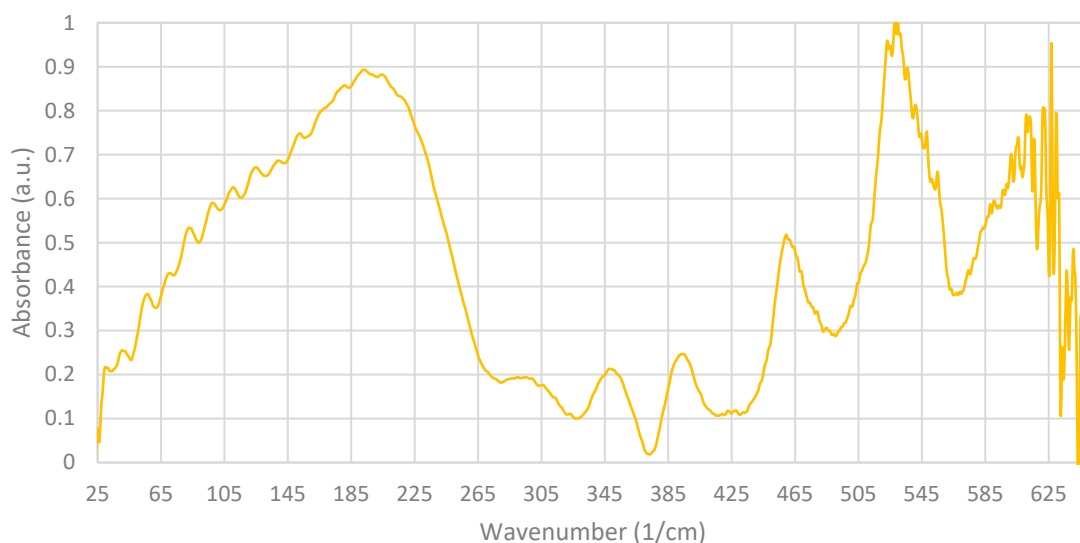


Figure 4-12: FIR spectrum of pressed 50% bilirubin conjugate in PE pellet (weight approx. 5 mg), analysed on the THz/FIR beamline at the Australian Synchrotron using a SiBolo detector with an amplitude of 4730.

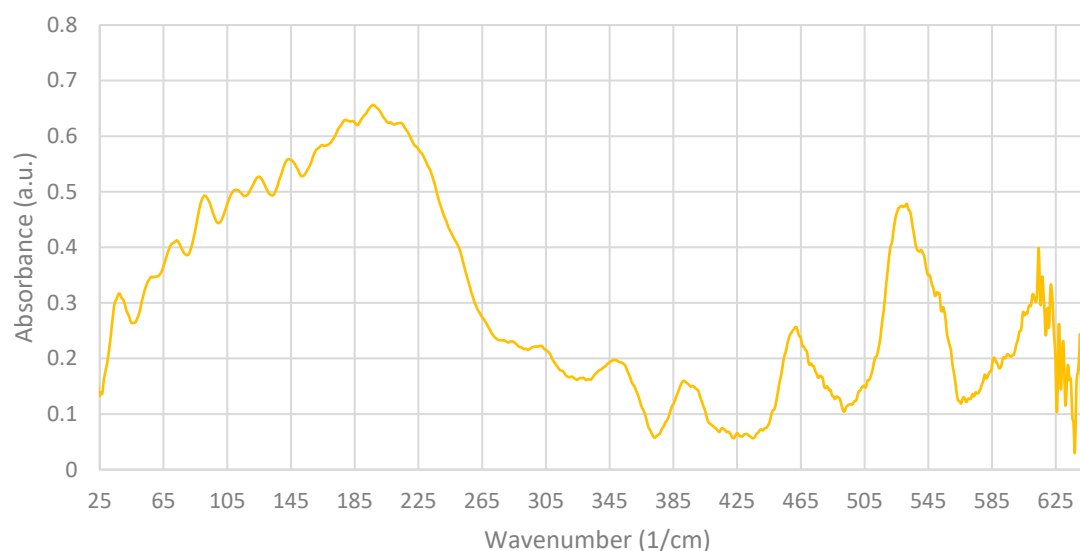


Figure 4-13: FIR spectrum of pressed 37.5% bilirubin conjugate in PE pellet (weight approx. 5 mg), analysed on the THz/FIR beamline at the Australian Synchrotron using a SiBolo detector with amplitude of 9470.

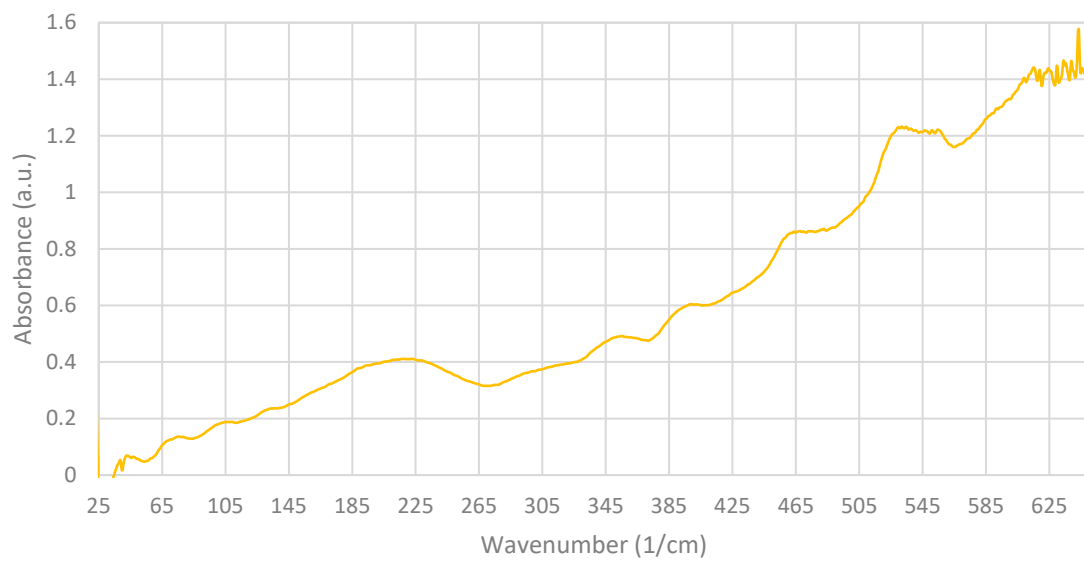


Figure 4-14: FIR spectrum of pressed 25% bilirubin conjugate in PE pellet (weight approx. 5 mg), analysed on the THz/FIR beamline at the Australian Synchrotron using a SiBolo detector with amplitude of 12480.

4.1.2.1.2.5 BILIVERDIN, BILIRUBIN AND BILIRUBIN CONJUGATE MIXTURES

Biliverdin and bilirubin mixture pellets appeared brown in colouration. Very weak peaks are observed at 300, 329, 367, 388, 412, 434, 483, 537 and 558 wavenumbers, which appear to correspond to peaks found in both biliverdin and bilirubin when analysed individually.

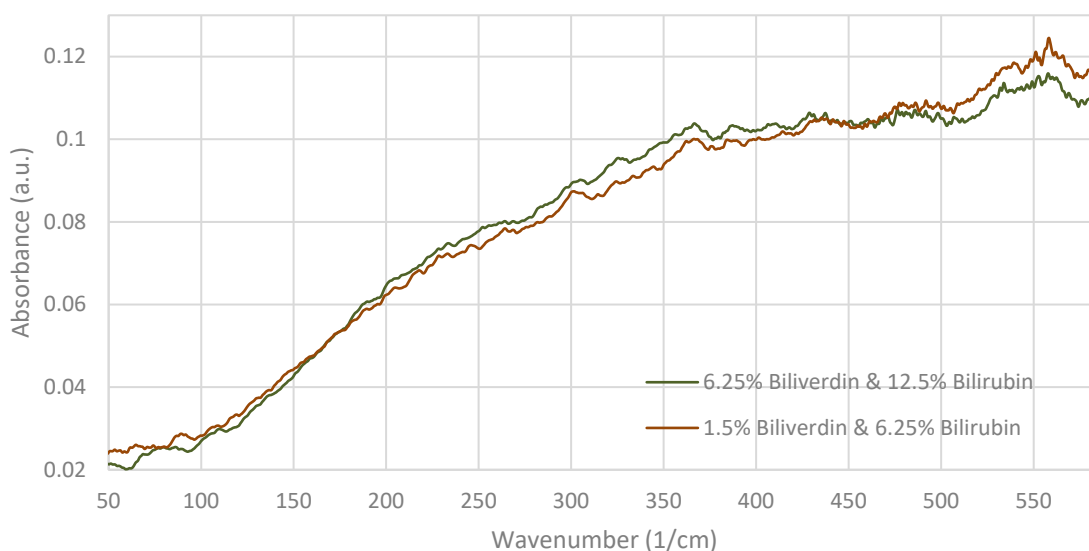


Figure 4-15: FIR overlaid spectra of pressed biliverdin and bilirubin in PE pellets (weights approx. 1 mg) at different concentrations, normalised between 50 and 586 wavenumbers, analysed on the THz/FIR beamline at the Australian Synchrotron using a SiBolo detector with amplitudes of 4420 (6.25% biliverdin with 12.5% bilirubin) and 4900 (1.5% biliverdin with 6.25% bilirubin).

Peaks for bilirubin and bilirubin conjugate mixture 37.5 : 37.5 are observed at approximately 190, 300, 324, 341, 358, 364, 390, 417, 430, 463, 476, 540 wavenumbers. These appear to correspond to peaks found in both bilirubin and bilirubin conjugate when analysed individually.

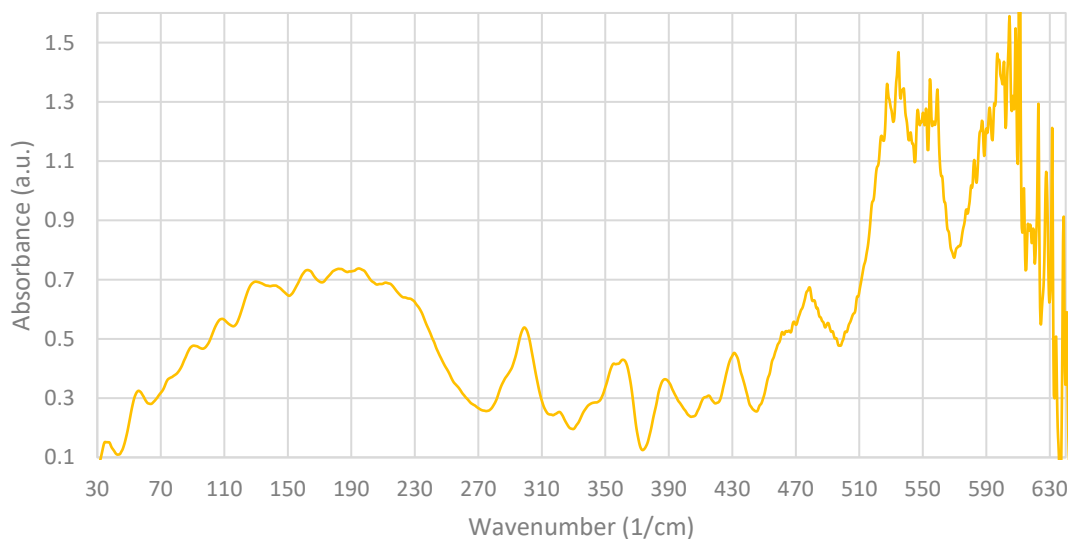


Figure 4-16: FIR spectrum of pressed 37.5% Bilirubin with 37.5% bilirubin conjugate in PE pellet (approx. 5 mg), analysed on the THz/FIR beamline at the Australian Synchrotron using a SiBolo detector with amplitude of 5030.

Peaks for bilirubin and bilirubin conjugate mixture 18.75 : 37.5 are observed at approximately 190, 287, 300, 322, 341, 358, 364, 390, 417, 430, 463, 476, 534 wavenumbers.

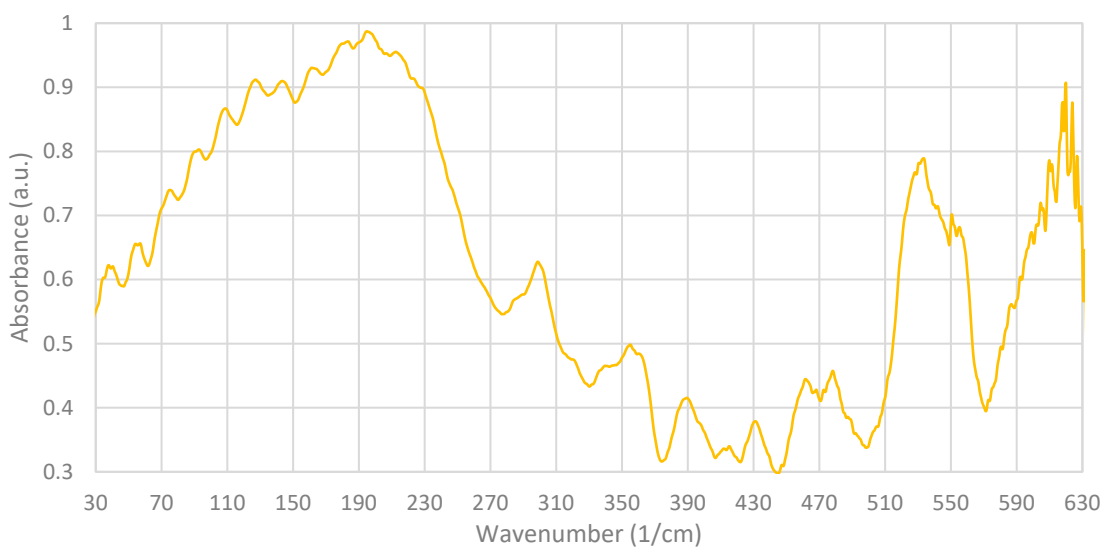


Figure 4-17: FIR spectrum of pressed 18.75% bilirubin with 37.5% bilirubin conjugate in PE pellet (approx. 5 mg), analysed on the THz/FIR beamline at the Australian Synchrotron using a SiBolo detector with amplitude of 8880.

Peaks for bilirubin, biliverdin and bilirubin conjugate mixture 1 : 3.75 : 3.75 are observed at approximately 190, 289, 300, 322, 340, 364, 390, 417, 430 and 470 (broad) wavenumbers. These appear to correspond to peaks found in biliverdin,

bilirubin and bilirubin conjugate when analysed individually.

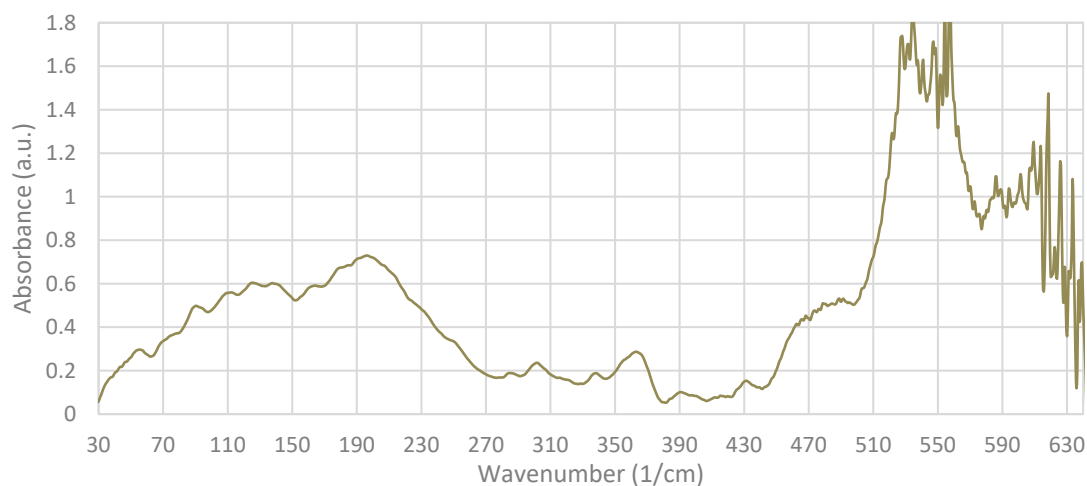


Figure 4-18: FIR spectrum of pressed 1% bilirubin, 3.75% biliverdin and 3.75% bilirubin conjugate in PE pellet (approx. 2 mg), analysed on the THz/FIR beamline at the Australian Synchrotron using a SiBolo detector with amplitude of 5700.

4.1.2.1.2.6 FERRITIN

Oscillation was observed in the low ferritin concentrations. Broad and weak bands are observed at approximately 100, 150, 175, 262 and 550 wavenumbers.

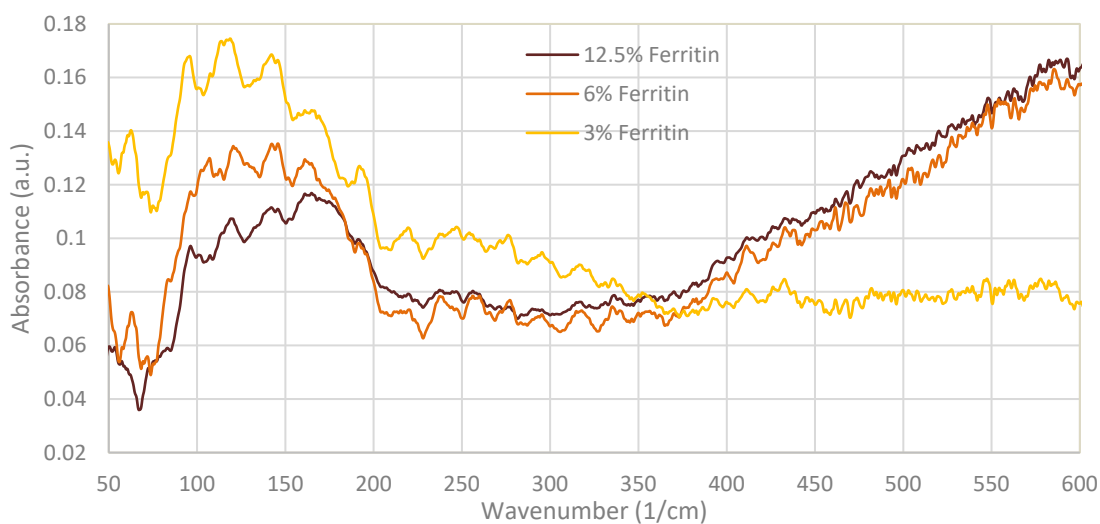


Figure 4-19: FIR overlaid spectra of pressed vacuum-dried ferritins in PE pellets (weights approx. 1 mg) at different concentrations, normalised between 50 and 600 wavenumbers, analysed on the THz/FIR beamline at the Australian Synchrotron using a SiBolo detector at amplitudes of 9177 (12.5% ferritin), 11608 (6% ferritin) & 14441 (3% ferritin).

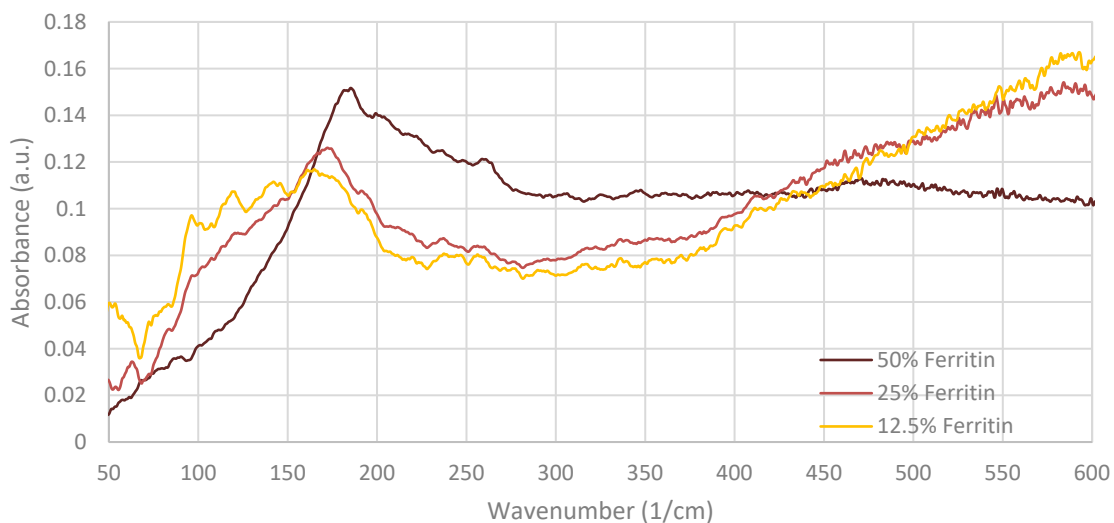


Figure 4-20: FIR overlaid spectra of pressed vacuum-dried ferritins in PE pellets (weights approx. 1 mg) at different concentrations, normalised between 50 and 600 wavenumbers, analysed on the THz/FIR beamline at the Australian Synchrotron using a SiBolo detector with amplitudes of 1258 (50% ferritin), 4700 (25% ferritin) & 9177 (12.5% ferritin).

4.1.2.1.3 Polytetrafluorethylene (PTFE)

4.1.2.1.3.1 BILIRUBIN

Peaks observed to correlate between samples are at 68, 101, 111, 124, 132, 162, 300, 320, 340, 363, 387, 415 and 432 wavenumbers. A disturbance in the absorption spectrum occurs at approximately 200 wavenumbers, hence the total FIR spectral range is reported in two figures.

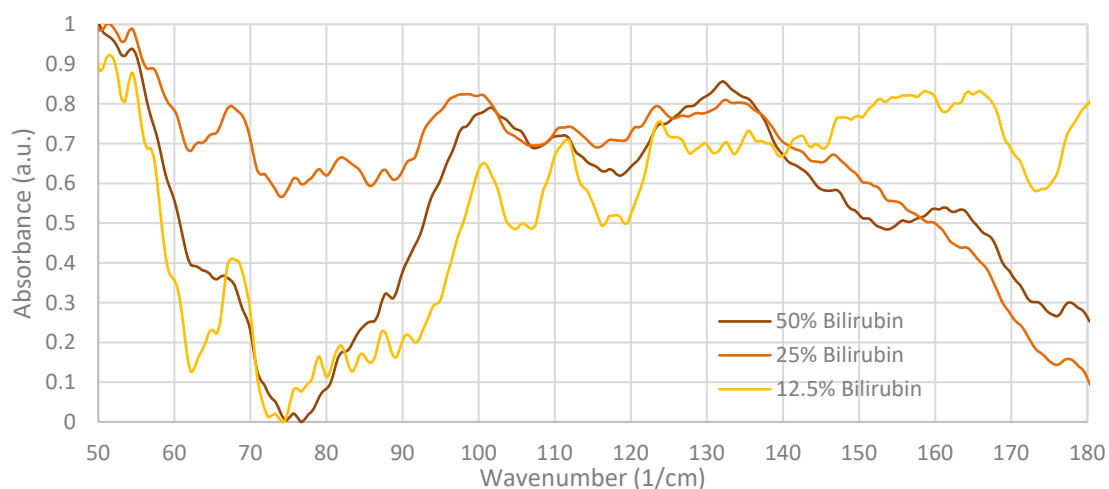


Figure 4-21: FIR overlaid spectra of pressed bilirubin in PTFE pellets (weights approx. 1 mg) at various concentrations, normalised between 50 and 190 wavenumbers, analysed on the THz/FIR beamline at the Australian Synchrotron using a SiBolo detector with amplitudes of 5410 (50% bilirubin), 9600 (25% bilirubin) & 3700 (12.5% bilirubin).

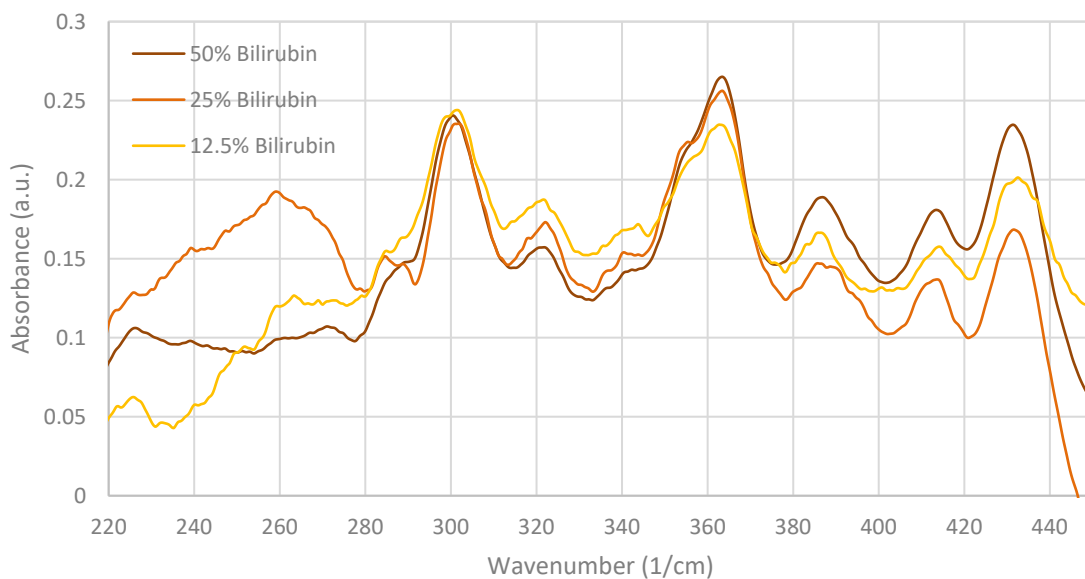


Figure 4-22: FIR overlaid spectra of pressed bilirubin in PTFE pellets (weights approx. 1 mg) at various concentrations, normalised between 225 and 450 wavenumbers, analysed on the THz/FIR beamline at the Australian Synchrotron using a SiBolo detector with amplitudes of 5410 (50% bilirubin), 9600 (25% bilirubin) & 3700 (12.5% bilirubin).

4.1.2.1.4 Potassium Bromide (KBr)

4.1.2.1.4.1 BLOOD

A single spectrum using the MCT_N detector could not be averaged as sample presented spectral change over time. There is a general broad and weak absorption from 900-1050 wavenumbers. A small peak appears at 1214 wavenumbers from 2 hours and sharpens over time. Literature suggests this is indicative of protein nature [116]. The peak was observed to be at its sharpest at 4 hours into analysis. Additionally, overall spectral absorbance increases over time by a magnitude of 0.017 absorbance units. This spectral behaviour may be an indication of deoxygenation or structural decay under the beamline's vacuum.

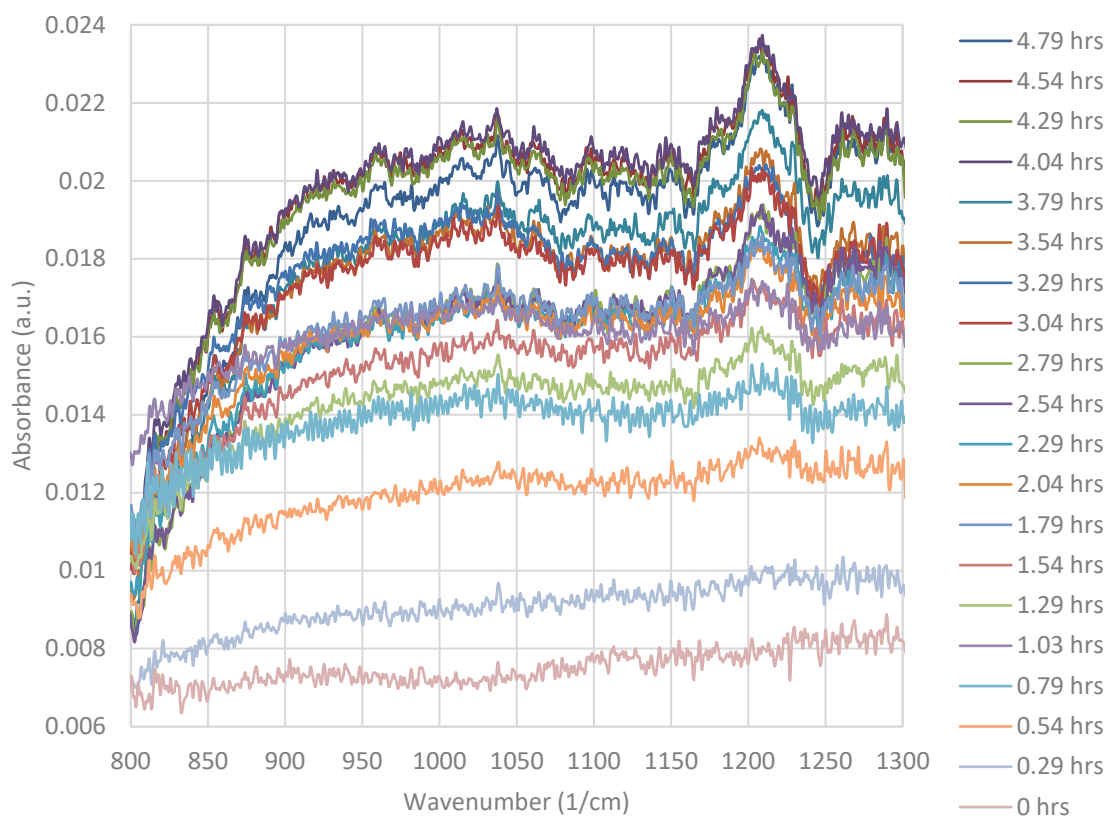


Figure 4-23: MIR overlaid spectra of overnight (4.79 hours) pressed 5% airdried defibrinated blood in KBr pellet (weight approx. 1 mg), analysed on the THz/FIR beamline at the Australian Synchrotron using an MCT_N detector with amplitude of approx. 20289. Delay between Measurements parameter in acquisition was set to 900 secs and Repeat the Measurement was set to 100.

4.1.2.1.4.2 BILIVERDIN

Peaks using the Si:B detector are observed at 496, 530, 556, 587, 690, 710, 729, 759 and 770 wavenumbers, although the spectrum contains fringing. Unfortunately, this fringing was a direct result from beamline issues unable to be troubleshooted by the Beamline Scientist during that beamtime. It is noted that the absorbance peak previously seen at approximately 550 wavenumbers (Figure 4-10) appears to have either shifted or is more resolved when analysed in KBr as compared to PE.

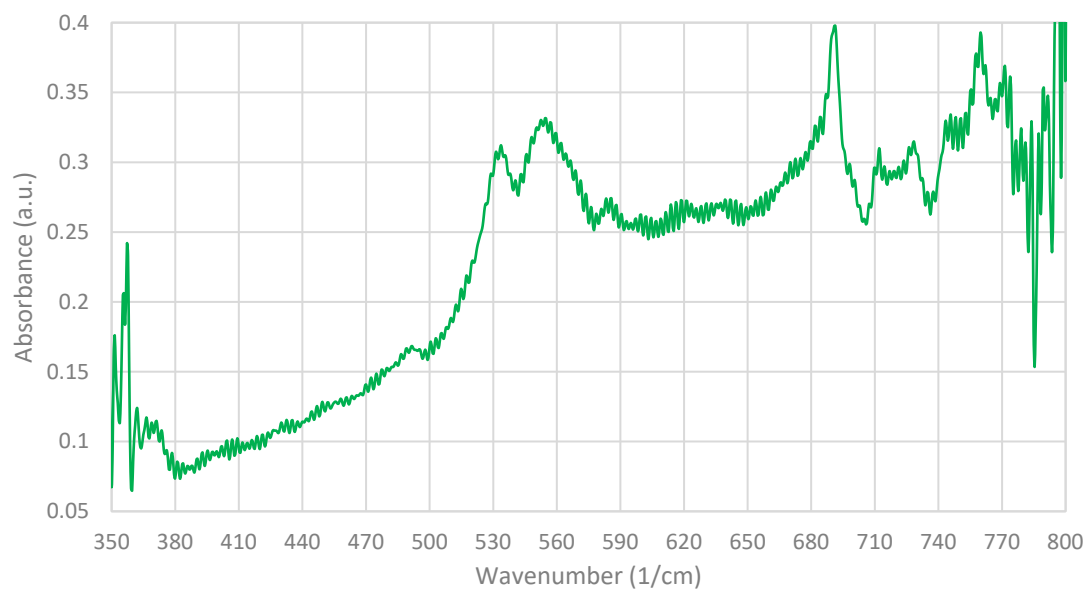


Figure 4-24: FIR spectrum of pressed 5% Biliverdin in KBr pellet (approx. 1 mg) analysed on the THz/FIR beamline at the Australian Synchrotron using a Si:B detector with amplitude of 16000.

Analyses in the MIR range provided a greater number of resolved peaks as shown below.

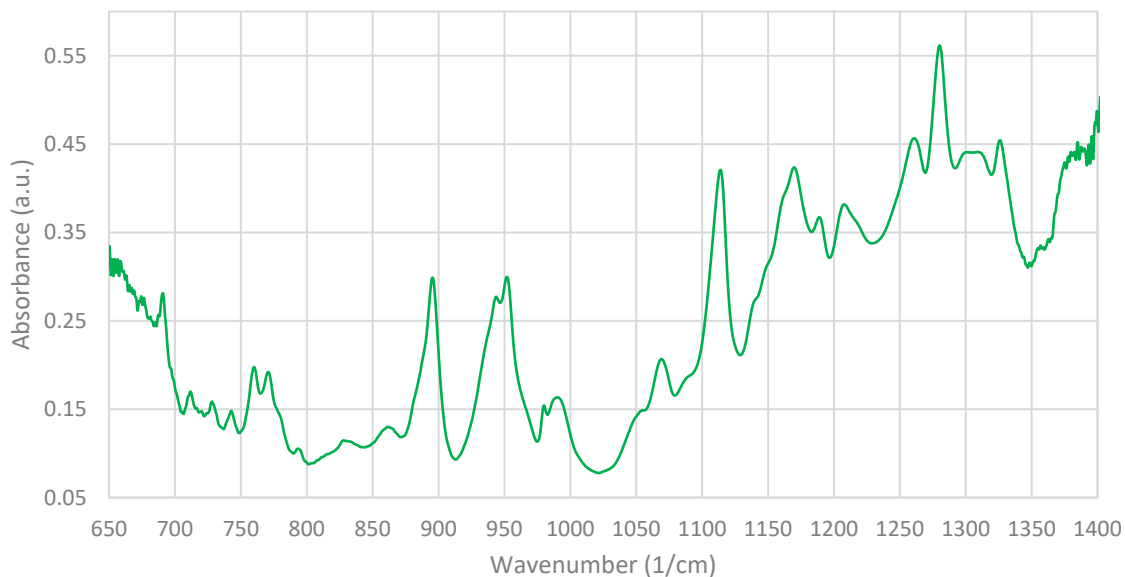


Figure 4-25: MIR spectrum of pressed 5% biliverdin in KBr pellet (approx. 1 mg) analysed on the THz/FIR beamline at the Australian Synchrotron using an MCT_N detector with amplitude of 19400.

Observed Peaks (cm ⁻¹)	Characterisation
714, 730	Alkene or aromatic C-H out-of-plane bend, C=C-H alkenes, chloride C-X [89, 117]
745, 867, 897	Alkene or aromatic C-H out-of-plane bend, C=C-H alkenes [89, 117]
770-773	Alkene or aromatic C-H out-of-plane bend, C=C-H alkenes, neighbouring C-H (5, 4, 3 neighbours) [89, 117]
835	Alkene or aromatic C-H out-of-plane bend, C=C-H Alkenes, neighbouring C-H (2 neighbours) [89, 117]
946-953, 994	C=C-H Alkenes, -CH=CH- Trans [89, 117]
1072, 1115, 1172, 1191	Amine C-N, alcohol or carboxylic acid C-O [89, 117]
1212	Amine C-N, alcohol or carboxylic acid C-O, N ⁺ -O ⁻ [89, 117]
1263, 1281	Amine C-N, alcohol or carboxylic acid C-O, -OH, N ⁺ -O ⁻ [89, 117]
1313, 1328	Amine C-N, -OH, C-NO ₂ [89, 117]
1383	-OH [89, 117]

Table 4-1: Characterisation designations to observed peaks for MIR analysis of pressed 5% biliverdin in KBr pellet (approx. 1 mg) analysed on the THz/FIR beamline at the Australian Synchrotron using an MCT_N detector with amplitude of 19400.

4.1.2.1.4.3 BILIRUBIN

A mixture of 10 % bilirubin in KBr was produced, however did not form a pellet as the sample exhibited a ‘sticky’ consistency, pasting on to mixing apparatus.

Peaks using the Si:B detector are observed at 386, 415, 433, 480, 495 533, 556, 600, 628, 655, 664, 673, 699, 742 and 758 wavenumbers, although the spectrum contains some fine fringing. Unfortunately, this fringing was a direct result from beamline issues unable to be troubleshooted by the Beamline Scientist during that beamtime.

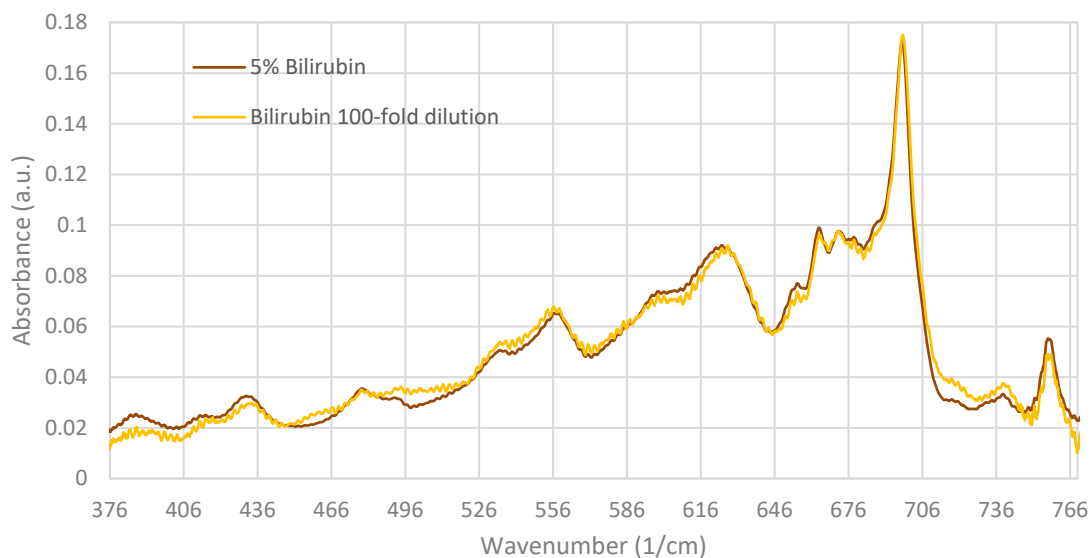


Figure 4-26: FIR overlaid spectra of pressed Bilirubin in KBr pellets (weights approx 1 mg) at various concentrations, normalised between 376-769 wavenumbers, analysed on the THz/FIR beamline at the Australian Synchrotron using an Si:B detector with amplitudes of 17039 (5% bilirubin) & 21500 (100-fold bilirubin dilution).

Analyses in the MIR range provided a greater number of resolved peaks as shown below.

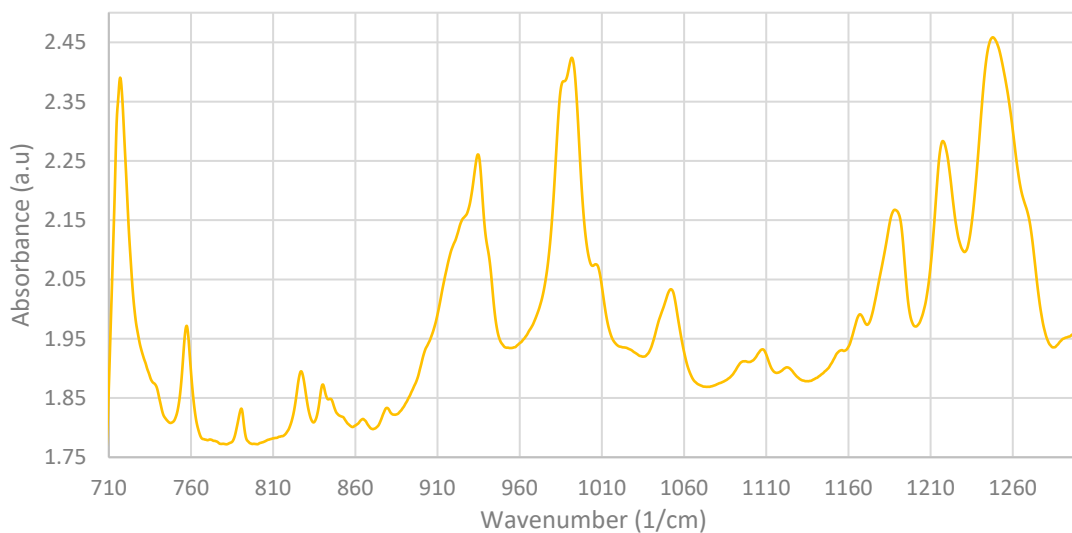


Figure 4-27: MIR spectrum of pressed 5% bilirubin in KBr pellet (approx. 1 mg) analysed on the THz/FIR beamline at the Australian Synchrotron using a MCT_N detector with amplitude 25600.

Observed Peaks (cm ⁻¹)	Characterisation
718	Alkene or aromatic C-H out-of-plane bend, C=C-H alkenes [89, 117]
758	Alkene or aromatic C-H out-of-plane bend, C=C-H alkenes, neighbouring C-H (5, 4, 3 neighbours) [89, 117]
792	Alkene or aromatic C-H out-of-plane bend, C=C-H alkenes, neighbouring C-H (3 neighbours) [89, 117]
828, 842	Alkene or aromatic C-H out-of-plane bend, C=C-H alkenes, neighbouring C-H (2 neighbours) [89, 117]
870, 883, 936	Alkene or aromatic C-H out-of-plane bend, C=C-H alkenes [89, 117]
993	Alkane C-H out-of-plane bend, C=C-H alkenes, -CH=CH-Trans [89, 117]
1009	Alkane C-H out-of-plane bend, -CH=CH-Trans, amine C-N, alcohol or carboxylic acid C-O [89, 117]
1054, 1099, 1111, 1127, 1158, 1170, 1191	alcohol or carboxylic acid C-O, amine C-N [89, 117]
1219	alcohol or carboxylic acid C-O, amine C-N, N ⁺ -O ⁻ [89, 117]
1251, 1300	alcohol or carboxylic acid C-O, amine C-N, N ⁺ -O ⁻ , O-H [89, 117]

Table 4-2: Characterisation designations to observed peaks for MIR analysis of pressed 5% bilirubin in KBr pellet (approx. 1 mg) analysed on the THz/FIR beamline at the Australian Synchrotron using an MCTN detector with amplitude of 25600.

4.1.2.1.4.4 BILIVERDIN AND BILIRUBIN MIXTURES

Spectra present similar peaks as biliverdin and bilirubin analysed individually. Main discernible differences are observed at 458, 474, 488, 725, 741, 847, 917, 950 and 1275 wavenumbers. Spectra was reproduced in a duplicate which is presented in the Appendix (Additional FIR Results).

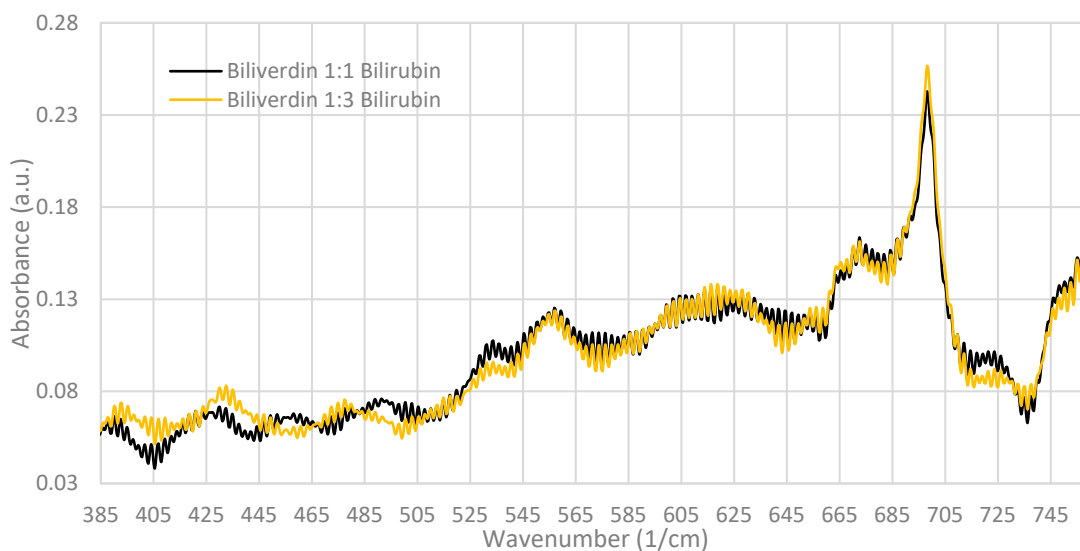


Figure 4-28: FIR overlaid spectra of pressed biliverdin and bilirubin mixtures in KBr pellets (weights approx. 1 mg) at various concentrations, normalised between 385-760 wavenumbers analysed on the THz/FIR beamline at the Australian Synchrotron using a Si:B detector with amplitudes 23680 (1:1 dilution) & 23300 (1:3 dilution).

The above spectrum contains some fine fringing which was a direct result from beamline issues unable to be troubleshooted by the Beamline Scientist during that beamtime.

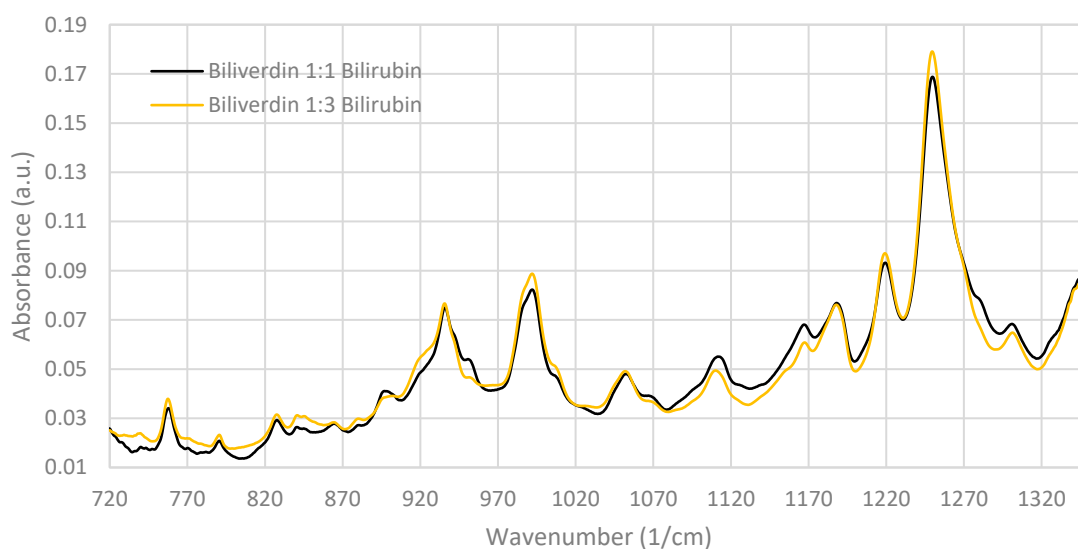


Figure 4-29: FIR overlaid spectra of pressed biliverdin and bilirubin mixtures in KBr pellets (weights approx. 1 mg) at various concentrations, normalised between 720-1350 wavenumbers analysed on the THz/FIR beamline at the Australian Synchrotron using a MCT_N detector with amplitudes of 19400 (1:1 dilution) & 26000 (1:3 dilution).

4.1.2.1.5 Paraffin Wax

When mixing sample powders with paraffin wax flakes, the sample immediately attached to the flakes and hence sample was non-homogenous, where local areas of sample was observed when pelleted. Most pellets were also concave in shape when dismounted from the cryostat post analysis. Some pellets experienced a hole in the middle, where the pellet appeared to have popped.

4.1.2.1.5.1 HUMAN HAEMOGLOBIN

Weak, broad peaks are observed at approximately 308, 397, 510, 591 and 650 wavenumbers for the 298 K sample. These appear more resolved when the sample is cooled to 78 K with more finer peaks arising, such as at 363, 466 and 480 wavenumbers.

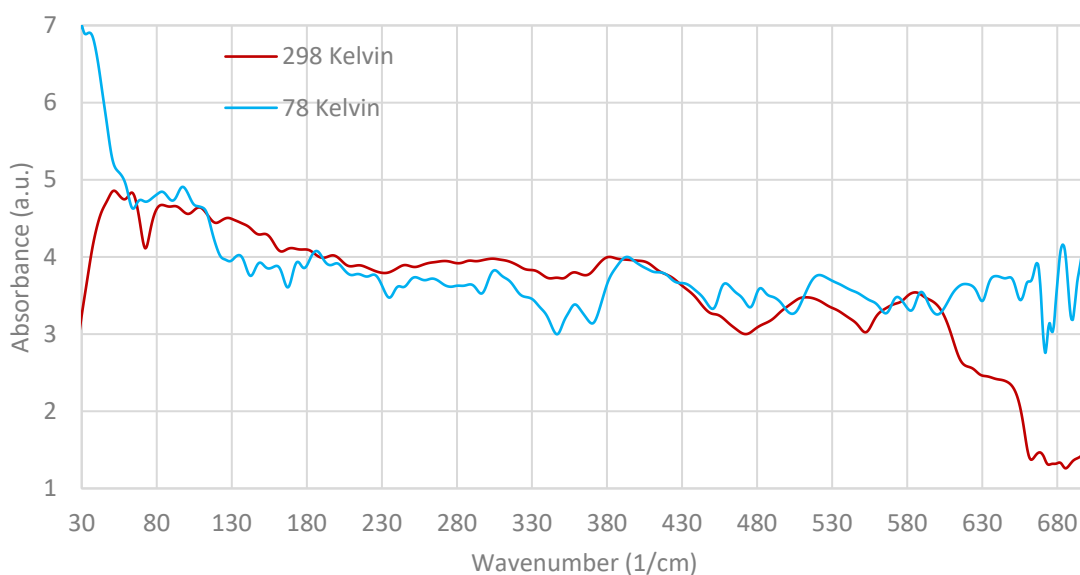


Figure 4-30: : FIR overlaid spectra of human haemoglobin in paraffin wax (1:70 mix ratio), pressed as a 7 mm pellet, normalised between 200 and 600 wavenumbers, analysed at the Australian Synchrotron (THz/FIR Beamline) using a SiBolo detector with amplitudes of 27000 for 298 K and 8600 for 78 K.

4.1.2.1.5.2 BILIVERDIN

Peaks are observed at 56, 65, 90, 114, 135, 155, 180, 201, 223, 247 (broad), 265, 318, 330, 363, 380, 405 (broad), 455, 530, 568, 587, 625 and 636 wavenumbers for the 298 K sample. These appear more resolved when the sample is cooled to 78 K with finer peaks arising, such as at 45, 290, 430, 478 and 556 wavenumbers. 298 K duplicate refers to when the sample is heated again after being cooled to 78 K. This

is included as it is different to its original spectral profile.

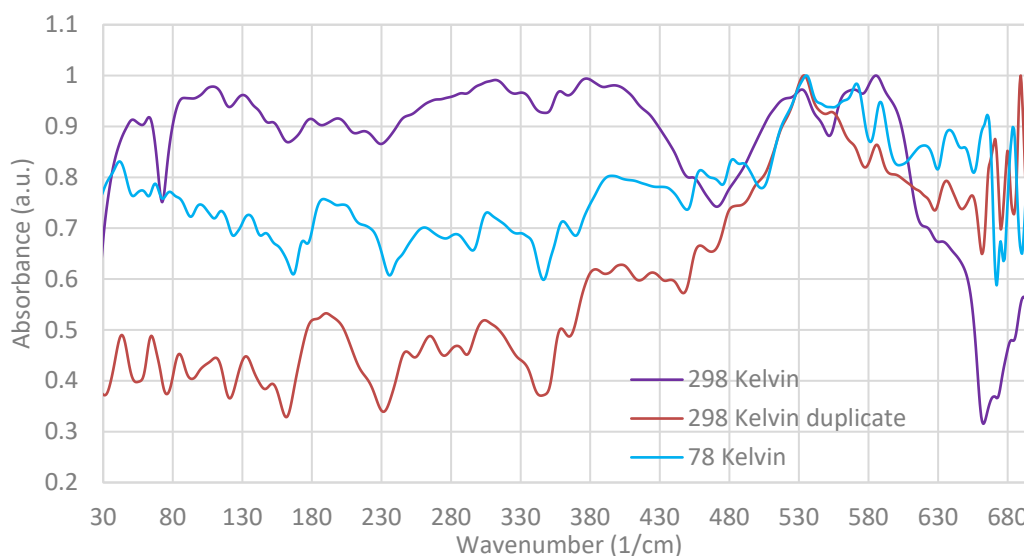


Figure 4-31: Normalised absorbance overlaid spectra of biliverdin in paraffin wax (1:9 mix ratio), pressed as a 7 mm pellet, analysed at the Australian Synchrotron (FIR Beamline) with SiBolo detector, normalised between 200 and 600 wavenumbers. Amplitude 12000 for 298 K, 9139 for duplicate and 9600 for 78 K.

4.1.2.1.5.3 BILIRUBIN

Peaks are observed over a broad absorption band at 46, 65, 89, 110, 130, 146, 159, 171, 180, 202, 220, 246, 271, 298, 363, 381, 406, 430, 462, 515, 539, 566, 580, 624 and 651 wavenumbers for the 298 K sample. These appear more resolved when the sample is cooled to 78 K with finer peaks arising, such as at 480 and 603 wavenumbers. Similar to the Biliverdin spectra in Figure 4-36, the reheated spectrum is dissimilar to the original spectral profile at the same temperature.

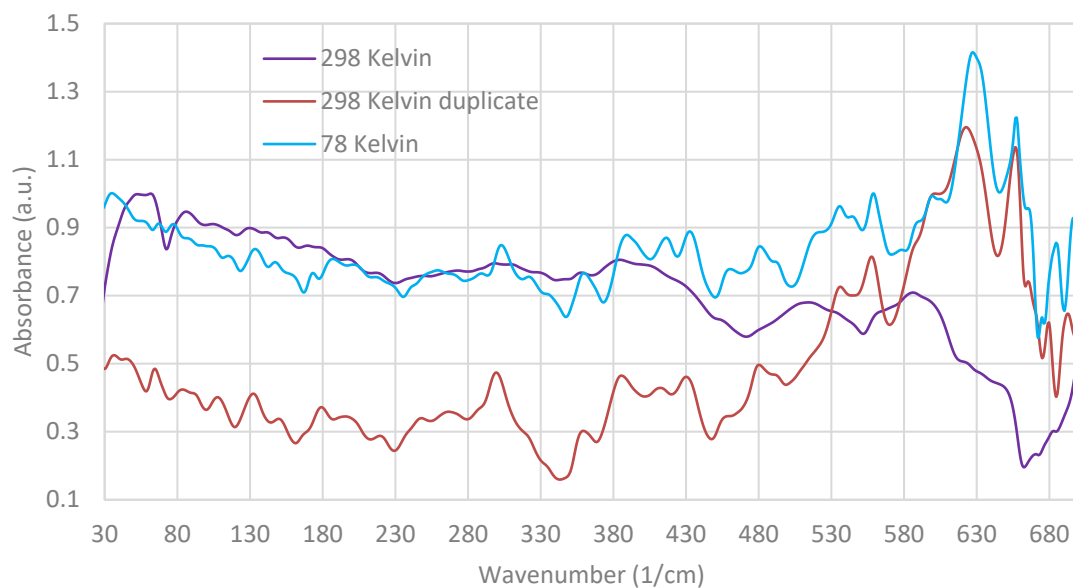


Figure 4-32: FIR overlaid spectra of bilirubin in paraffin wax (1:9 mix ratio), pressed as a 7 mm pellet, normalised between 50 and 600 wavenumbers, analysed at the Australian Synchrotron (THz/FIR Beamline) using a SiBolo detector amplitudes of 12000 for 298 K, 13800 for duplicate and 14000 for 78 K.

4.1.2.1.5.4 BILIRUBIN CONJUGATE

Peaks are observed at 209 (broad), 287, 310, 350, 394 and 467 wavenumbers. These appear more resolved when the bilirubin conjugate concentration is increased, with additional peaks observed at 417 and 430 wavenumbers. Saturation is experienced above 480 wavenumbers and oscillation below 180 wavenumbers.



Figure 4-33: FIR spectrum of pressed bilirubin conjugate in paraffin wax pellet (1:2.5 ratio mix), analysed at the Australian Synchrotron (THz/FIR Beamline) using a SiBolo detector with amplitude of 1370.

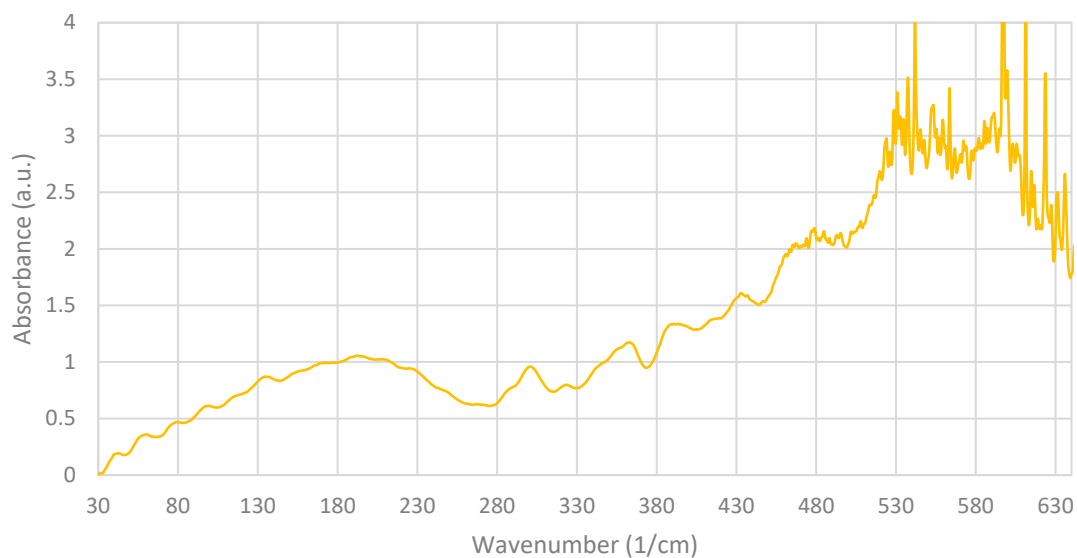


Figure 4-34: FIR spectrum of pressed bilirubin conjugate in paraffin wax pellet (2:1 ratio mix), analysed at the Australian Synchrotron (THz/FIR Beamline) using a SiBolo detector with amplitude of 3370.

4.1.2.1.6 Biliverdin and Bilirubin Pellet Comparisons

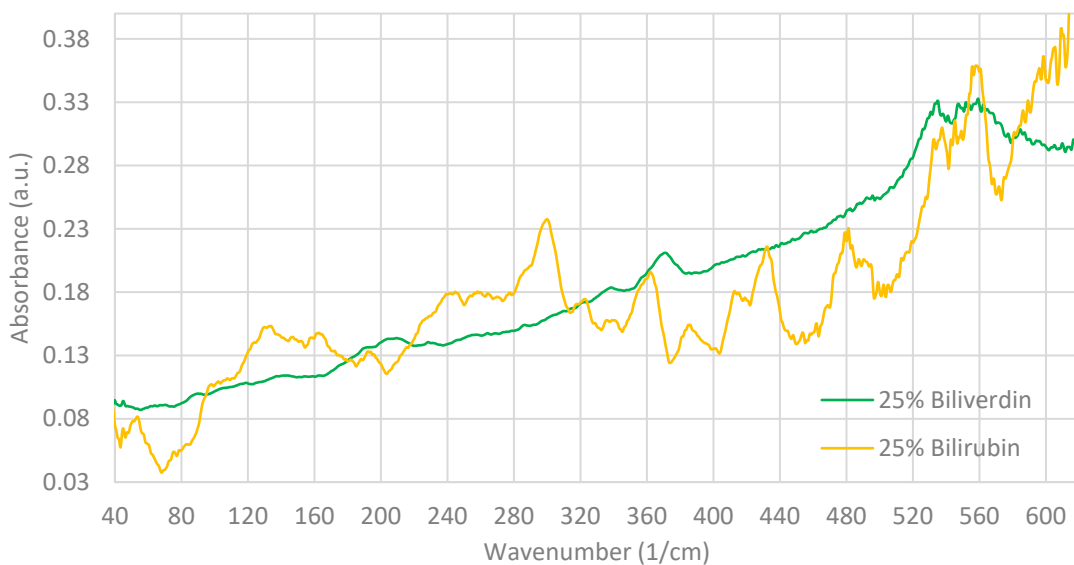


Figure 4-35: FIR overlaid spectra of previously presented pressed biliverdin and bilirubin pellets in PE, analysed at the Australian Synchrotron (THz/FIR Beamline) using the SiBolo detector, normalised between 50 and 450 wavenumbers.

Main differences in peaks occur at 165, 205, 229, 241, 251, 337 and 585 wavenumbers using SiBolo and Si:B detectors.

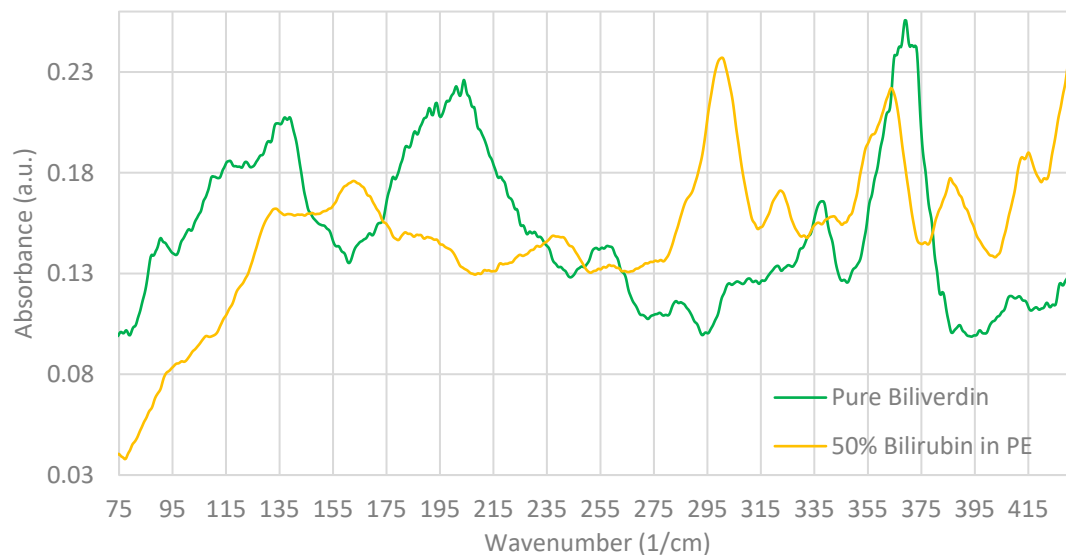


Figure 4-36: FIR overlaid spectra of previously presented pressed biliverdin and bilirubin pellets, analysed at the Australian Synchrotron (THz/FIR Beamline) using the SiBolo detector, normalised between 50 and 450 wavenumbers.

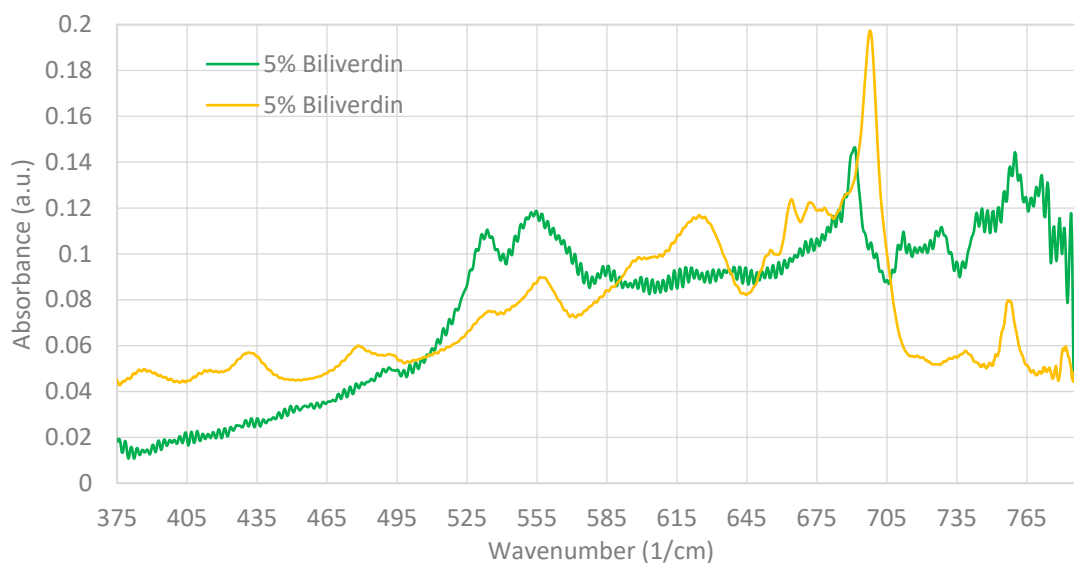


Figure 4-37: FIR overlaid spectra of previously presented pressed biliverdin and bilirubin pellets in KBr, analysed at the Australian Synchrotron (THz/FIR Beamline) using the Si:B detector, normalised between 376 and 769 wavenumbers.

Main peaks detected only in bilirubin using the MCT_N detector were at 792, 842, 883, 936 (strong), 1009, 1009, 1127, 1158, 1220 and 1249 (strong) wavenumbers. Biliverdin presented peaks not in bilirubin at 730 (weak), 771, 894 (strong), 950 (strong), 1070, 1213, 1260 (strong) and 1280 (strong) wavenumbers.

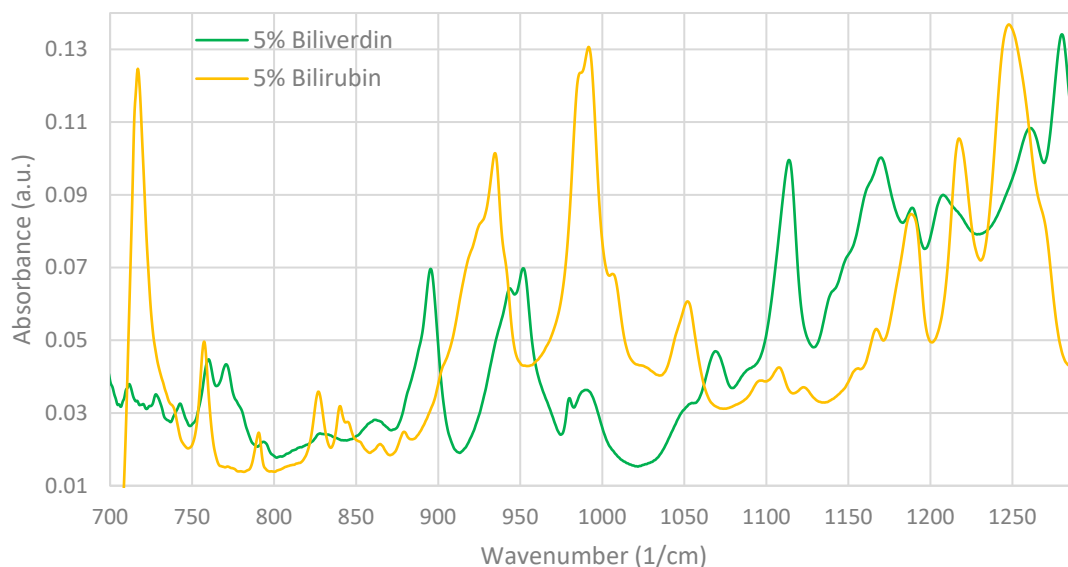


Figure 4-38: FIR overlaid spectra of previously presented pressed biliverdin and bilirubin pellets in KBr, analysed at the Australian Synchrotron (THz/FIR Beamline) using the MCT_N detector, normalised between 750 and 1300 wavenumbers.

4.1.2.2 Diamond Window Liquid Cells

An empty diamond window liquid cell (cell C) with a 50 μm spacer was analysed overnight with an amplitude of 22400 (Acquisition settings: Measurement Repeated 20 times, Delay Between Measurements of 1800 secs and Sample Scan Time of 100). No significant change between collective spectra was observed.

4.1.2.2.1 Solvents

4.1.2.2.1.1 WATER

In all cases, a broad absorbance is observed at 197 wavenumbers and absorbance increases linearly above 300 wavenumbers. Increasing the spacer size, increased the overall spectral absorbance as shown below. Additionally, the usable range is 60-1000 wavenumbers (excluding the 720 wavenumber absorbance and shoulder dip in absorbance) for the 5, 10 and 15 μm spacer, 60-480 wavenumbers for the 20 μm spacer and 60-360 wavenumbers for the 50 μm spacer.

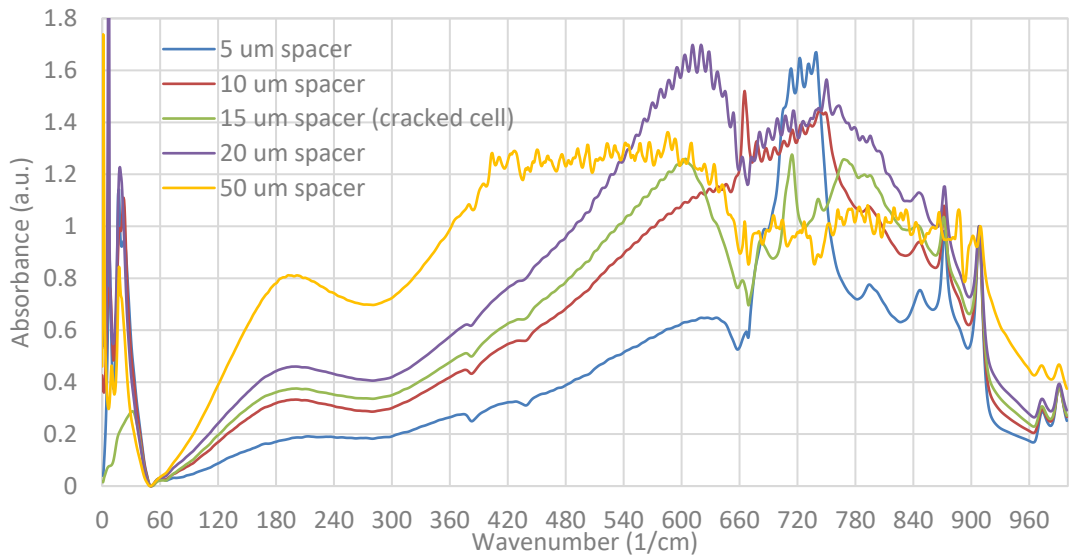


Figure 4-39: FIR overlaid spectra of water in DWLC B with various spacers, normalised between 0 and 1000 wavenumbers, analysed at the Australian Synchrotron (THz/FIR Beamline) using a SiBolo detector, with amplitudes 21900 (5 μm), 12200 (10 μm), 9600 (15 μm), 7100 (20 μm) & 990 (50 μm).

Variation between DWLC's with varying spacer sizes was tested below. Little variation is observed between cells when their 20 μm spacer is used.

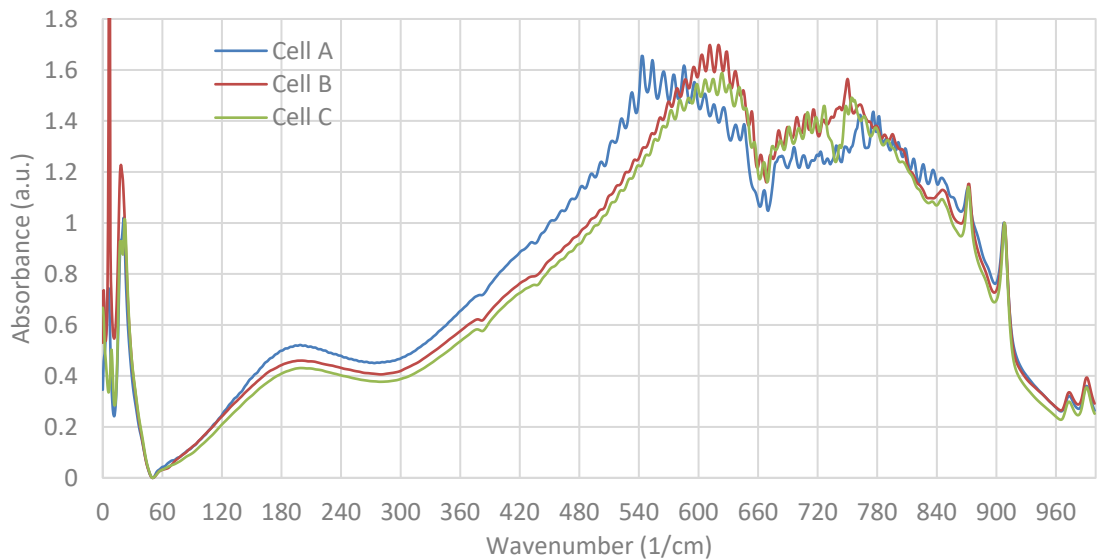


Figure 4-40: FIR overlaid spectra of water in DWLC's A, B and C with a 20 μm spacer, normalised between 0 and 1000 wavenumbers, analysed at the Australian Synchrotron (THz/FIR Beamline) using a SiBolo detector with amplitudes of 3200 (Cell A), 7100 (Cell B) & 6400 (Cell C).

Although normalised, some variation is observed regarding absorbance between DWLC's when using their 10 μm spacer.

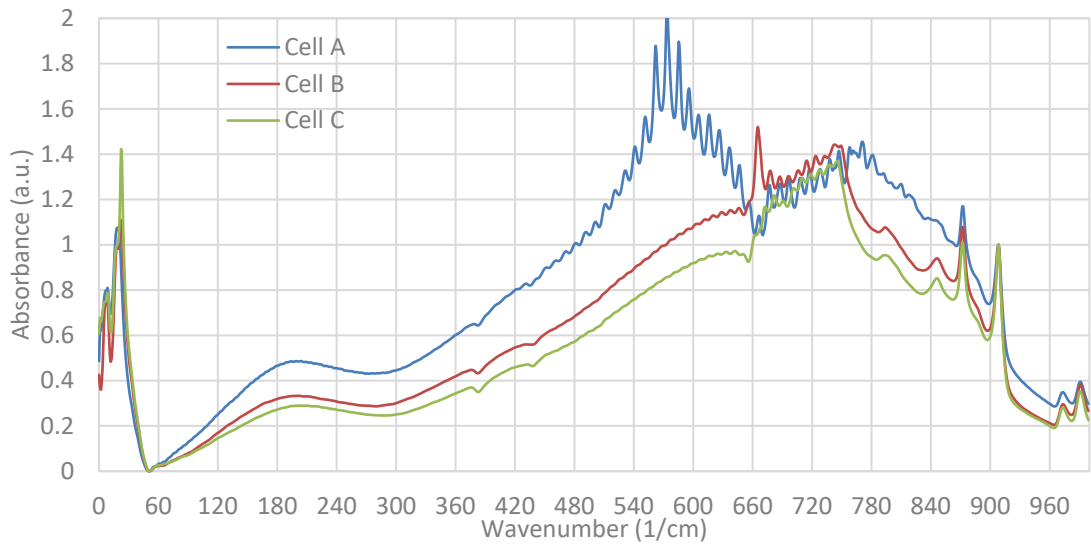


Figure 4-41: FIR overlaid spectra of water in DWLC's A, B and C with a 10 µm spacer, normalised between 0 and 1000 wavenumbers, analysed at the Australian Synchrotron (THz/FIR Beamline) using a SiBolo detector with amplitudes 5300 (Cell A), 12200 (Cell B) & 15000 (Cell C).

No significant variation is observed between DWLC's when using their 5 µm spacer as shown below.

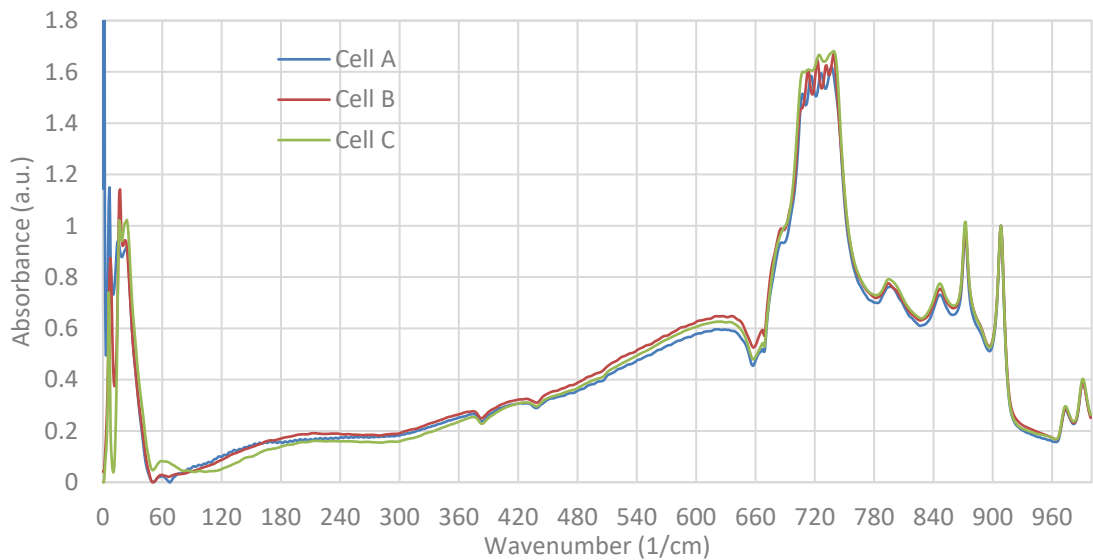


Figure 4-42: FIR overlaid spectra of water in DWLC's A, B and C with a 5 µm spacer, normalised between 0 and 1000 wavenumbers, analysed at the Australian Synchrotron (THz/FIR Beamline) using a SiBolo detector with amplitudes of 23300 (Cell A), 21900 (Cell B) & 20300 (Cell C).

DWLC's come with their corresponding machined spacers. Using the spacer of Cell B in Cell A and vice versa produced little variation as seen in the next figure.

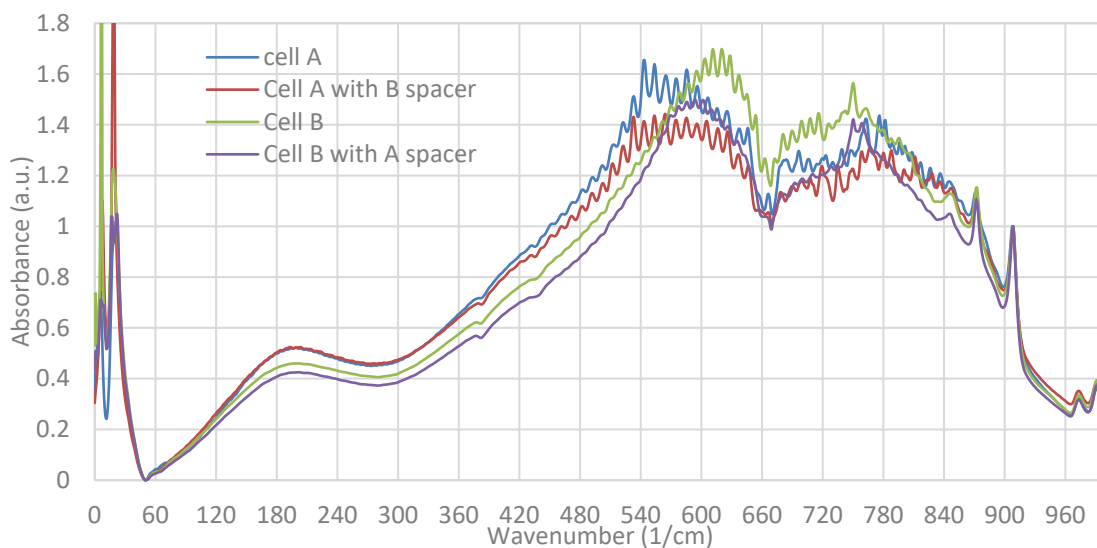


Figure 4-43: FIR overlaid spectra of water in DWLC's A and B with swapped 20 μm spacer, normalised between 0 and 1000 wavenumbers, analysed at the Australian Synchrotron (THz/FIR Beamline) using a SiBolo detector with amplitude 3200 (Cell A), 7100 (Cell B), 3700 (Cell A with B's spacer) & 7100 (Cell B with Cell A's spacer).

However variation in absorbance is observed when swapping the 5 μm spacer between Cells A and C.

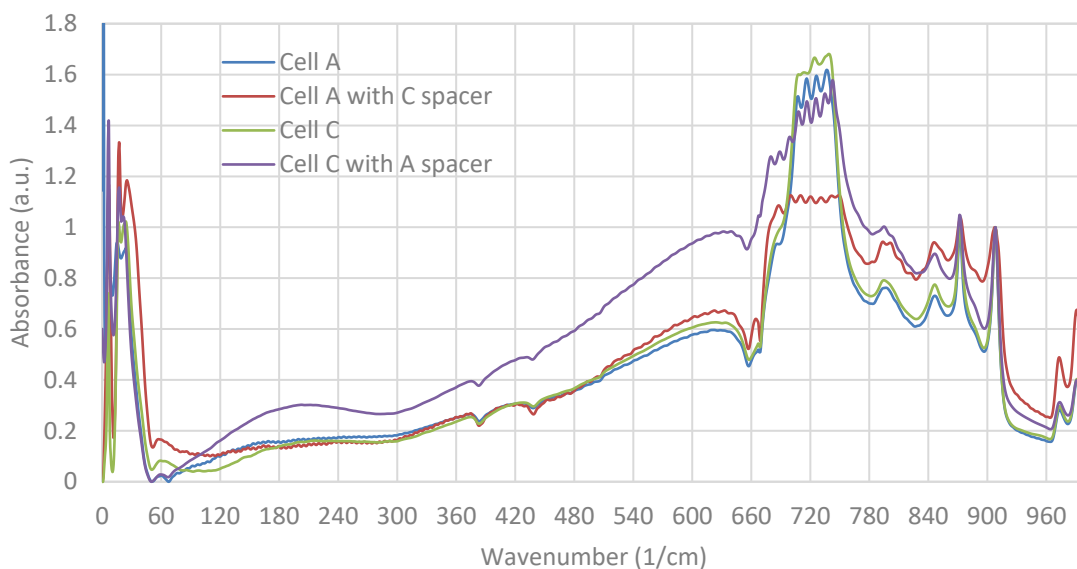


Figure 4-44: FIR overlaid spectra of water in DWLC's A and C with swapped 5 μm spacer, normalised between 0 and 1000 wavenumbers, analysed at the Australian Synchrotron (THz/FIR Beamline) using a SiBolo detector with amplitude of 23300 (Cell A), 20300 (Cell C), 23500 (Cell A with C's spacer) & 1600 (Cell C with Cell A's spacer).

4.1.2.2.1.2 DIMETHYL SULFOXIDE (DMSO)

Spectra produced utilising the 20 μm spacer was observed to be the most resolved, hence was utilised in most sample analyses.

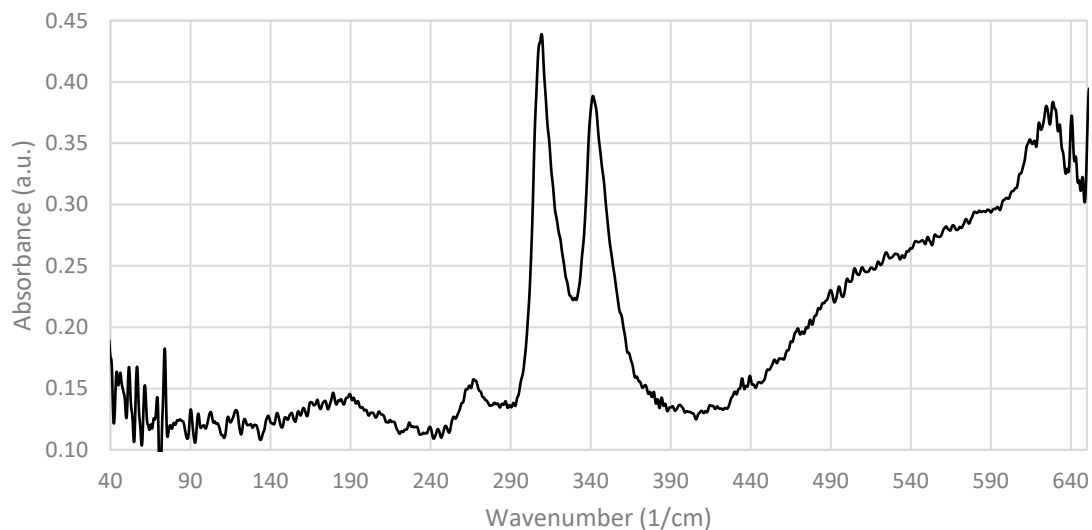


Figure 4-45: FIR spectrum of DMSO-d₆ in DWLC C with a 5 μm spacer, analysed on the THz/FIR beamline at the Australian Synchrotron using a SiBolo detector with amplitude of 7300.

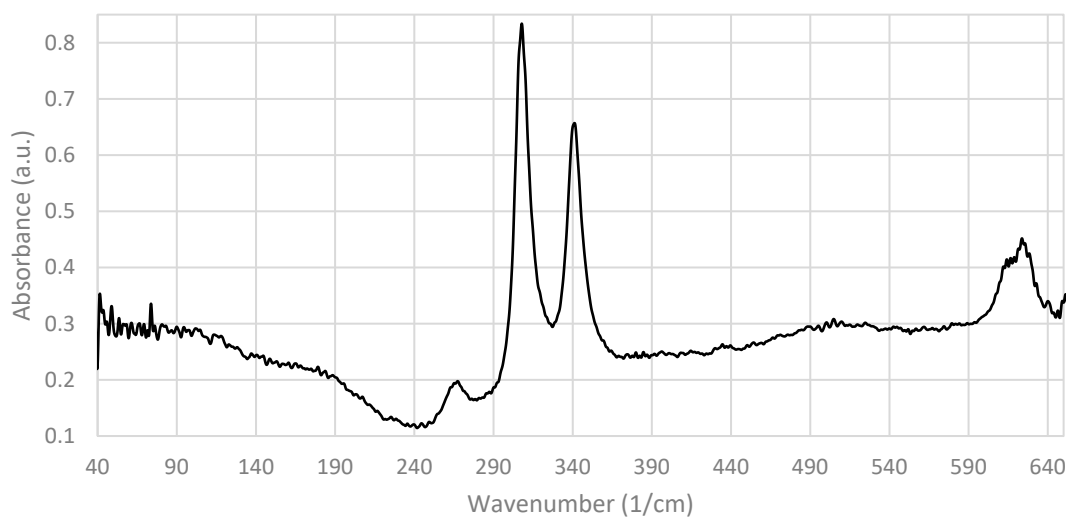


Figure 4-46: FIR spectrum of DMSO-d₆ in DWLC C with a 10 μm spacer, analysed on the THz/FIR beamline at the Australian Synchrotron using a SiBolo detector with amplitude of 6480.

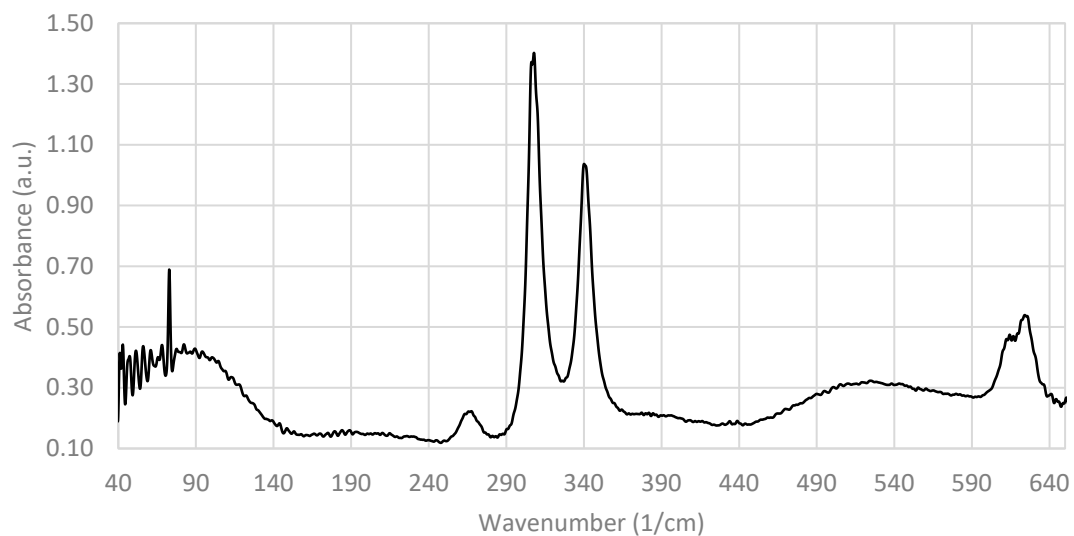


Figure 4-47: FIR spectrum of DMSO-d₆ in DWLC C with a 20 μm spacer, analysed on the THz/FIR beamline at the Australian Synchrotron using a SiBolo detector with amplitude of 5420.

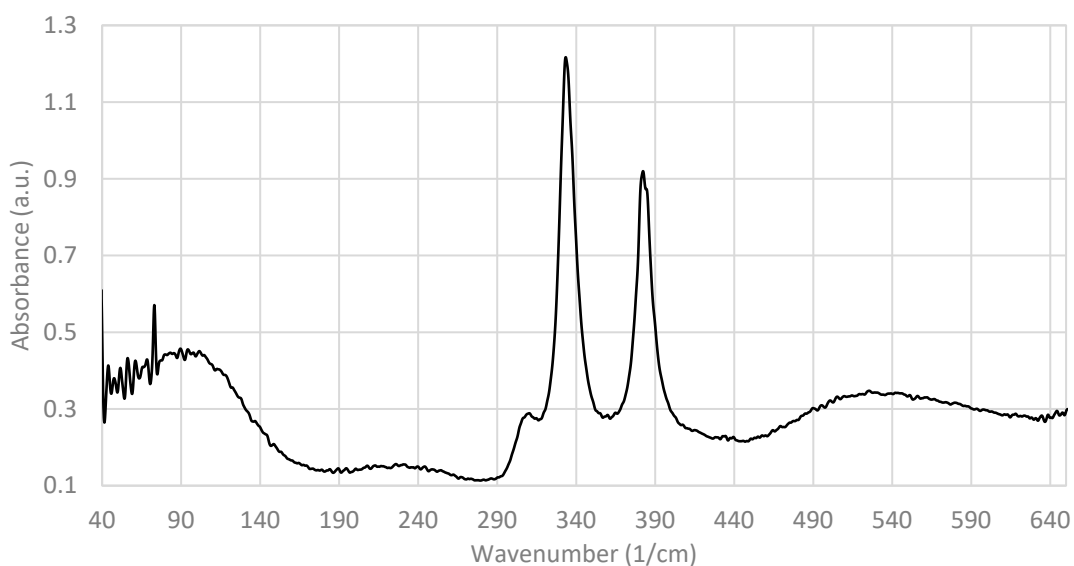


Figure 4-48: FIR spectrum of DMSO-H₆ in DWLC C with a 20 μm spacer, analysed on the THz/FIR beamline at the Australian Synchrotron using a SiBolo detector with amplitude of 5080.

DMSO-d ₆ Peaks (cm ⁻¹)	DMSO-H ₆ Peaks (cm ⁻¹)	Characterisation [118]
90	90	Unidentified
265	-	S-C ₂
305	310	O-S-C in-phase
340	340	O-S-C out-of-phase

-	390	S-C
530	530	S-C

Table 4-3: Characterisation designations to observed peaks for FIR analysis of DMSO analysed on the THz/FIR beamline at the Australian Synchrotron using a SiBolo detector.

DMSO was duplicated multiple times in various cells with various spacers on various days during analysis. Similar characteristic spectra were achieved, hence are not reported here.

Peaks during cryogenic analysis are observed at 89, 151, 190, 247, 278, 301 and 348 wavenumbers. The first peak (89 wavenumbers) appears to be resolved compared to the warm run and the last three appear to be shifted peaks with different ratios.

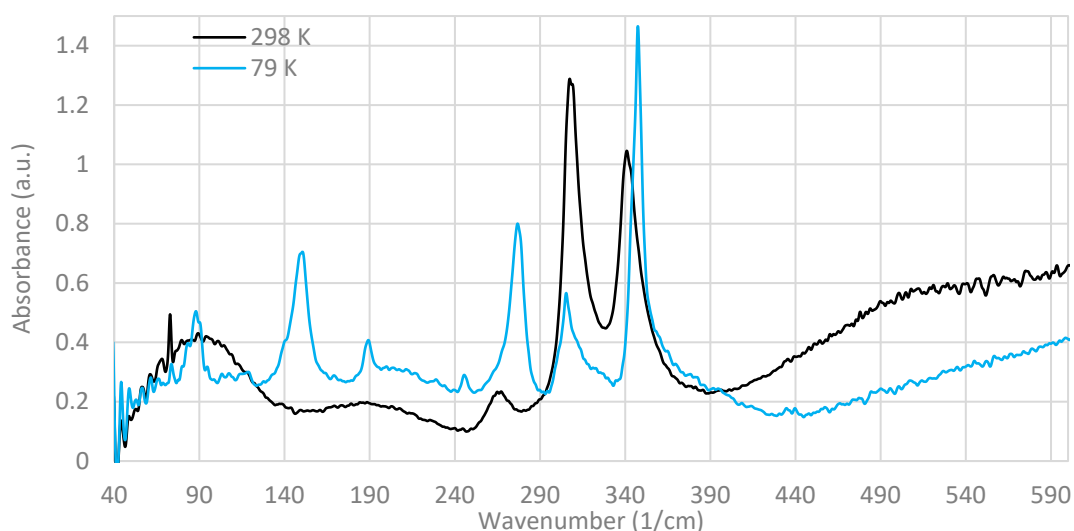


Figure 4-49: FIR overlaid spectra of DMSO-d₆ in DWLC C with a 20 µm spacer when cooled for the first time, analysed at the Australian Synchrotron (THz/FIR Beamline) using a SiBolo detector with starting amplitude 4900.

The peak at 150 wavenumbers arises in run 9, however it took 5 mins into cryogenic analysis (42 secs per spectrum × 7 runs = 294 secs) before it appeared. It disappears between 283 and 297 Kelvin (9.85 and 23.85 degrees Celsius).

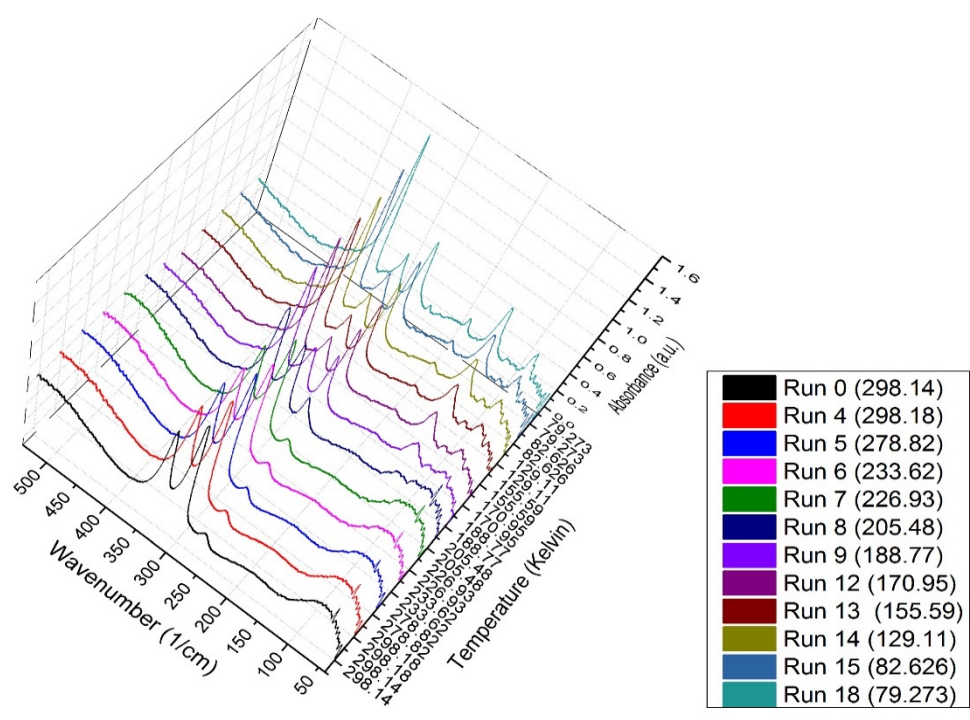


Figure 4-50: 3D Ribbon Plot of FIR absorbance spectra for DMSO-d₆ in DWLC C using 20 μm spacer, when cooled (to 78 K) for the first time, analysed at the Australian Synchrotron (THz/FIR Beamline) with SiBolo detector.

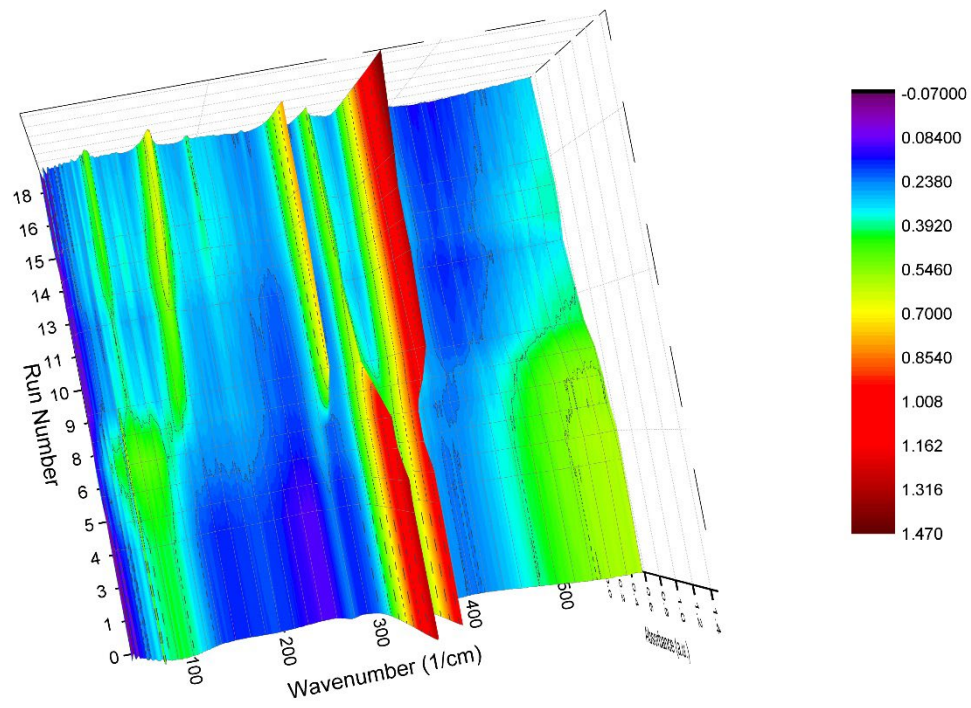


Figure 4-51: 3D Colourmap Surface Contour plot of FIR absorbance spectra for DMSO-d₆ in DWLC C using 20 μm spacer, when cooled (to 78 K) for the first time, analysed at the Australian Synchrotron (THz/FIR Beamline) with SiBolo detector.

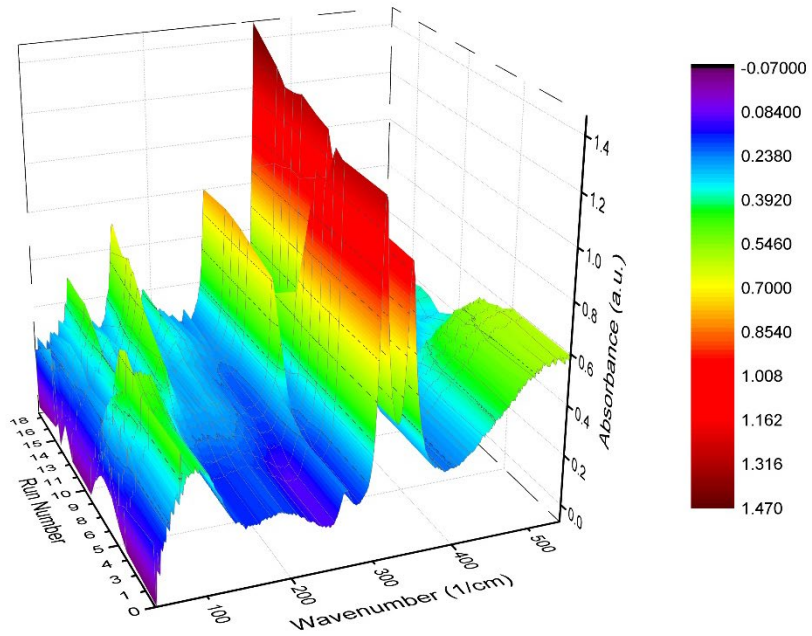


Figure 4-52: 3D Colourmap Surface Contour plot of FIR absorbance spectra for DMSO-d₆ in DWLC C using 20 μm spacer, when cooled (to 78 K) for the first time, analysed at the Australian Synchrotron (THz/FIR Beamline) with SiBolo detector.

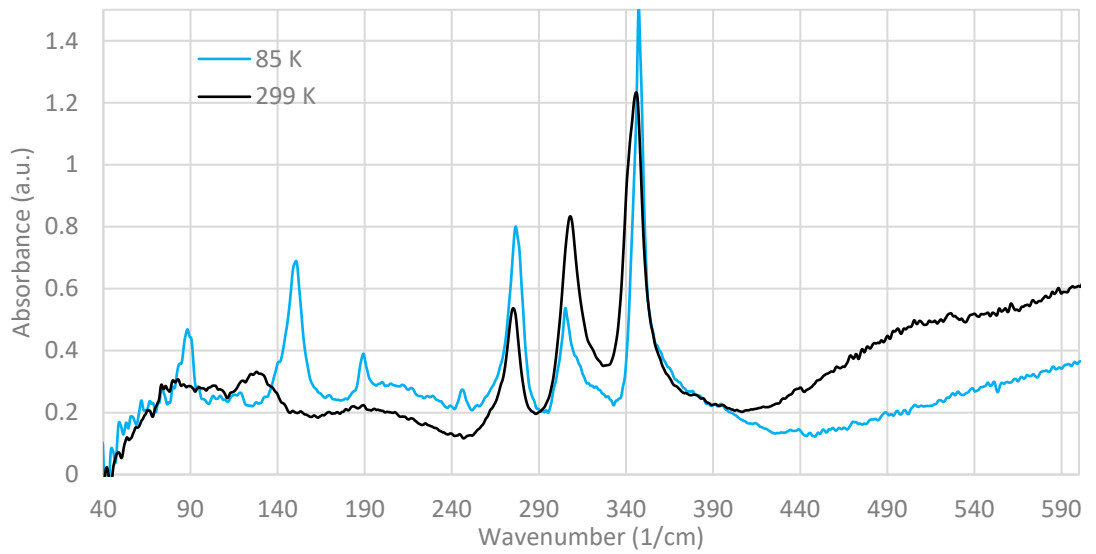


Figure 4-53: FIR overlaid spectra of DMSO-d₆ in DWLC C with a 20 μm spacer when heated (to 298 K) for the first time, analysed at the Australian Synchrotron (THz/FIR Beamline) with SiBolo detector.

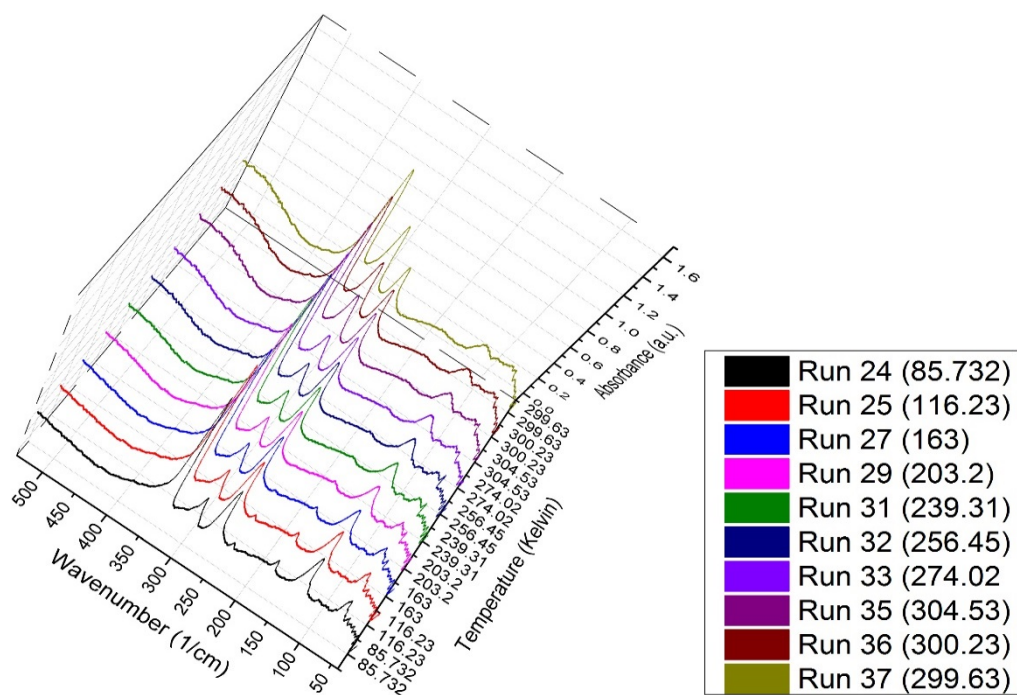


Figure 4-54: 3D Ribbon Plot of FIR absorbance spectra for DMSO-d₆ in DWLC C using 20 μm spacer, when heated (to 298 K) for the first time, analysed at the Australian Synchrotron (THz/FIR Beamline) with SiBolo detector.

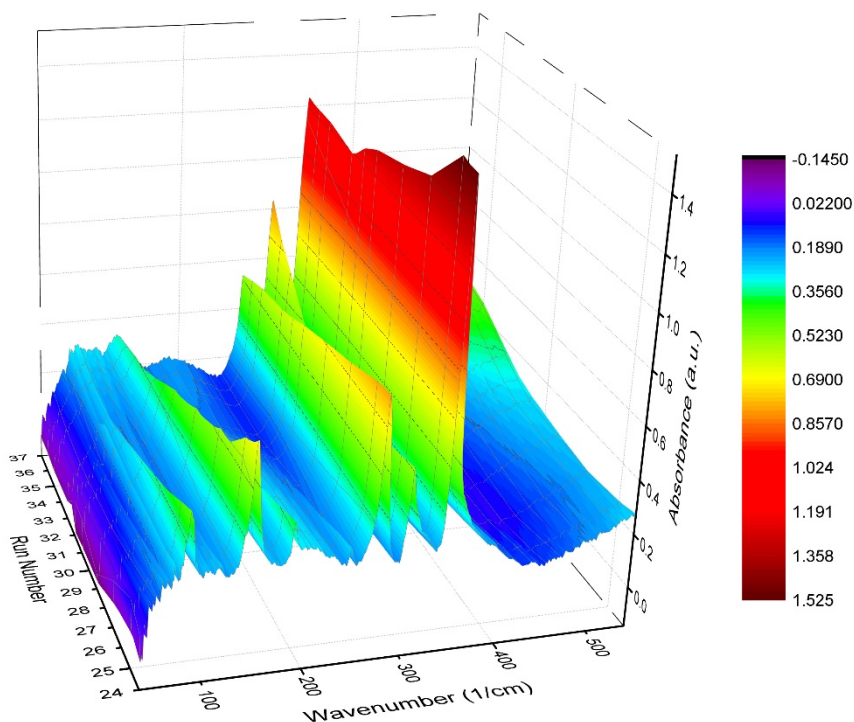


Figure 4-55: 3D Colourmap Surface Contour plot of FIR absorbance spectra for DMSO-d₆ in DWLC C using 20 μm spacer, when heated (to 298 K) for the first time, analysed at the Australian Synchrotron (THz/FIR Beamline) with SiBolo detector.

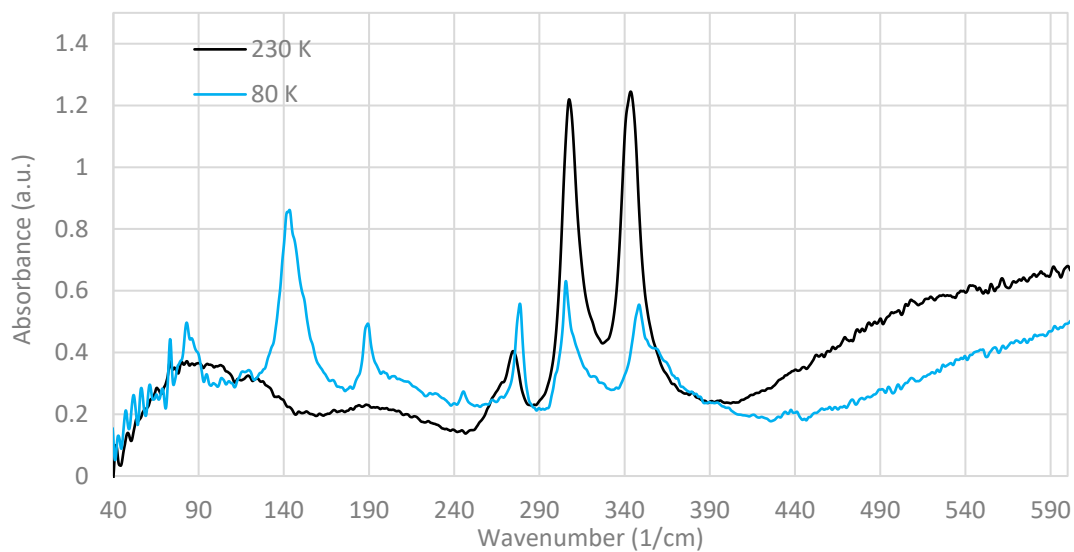


Figure 4-56: Overlaid FIR spectra of DMSO-d6 in DWLC C with a 20 μm spacer when cooled (to 78 K) for the second time, analysed at the Australian Synchrotron (THz/FIR Beamline) with SiBolo detector.

It is noted that when cooled for the second time, peak at 354 wavenumbers decreases in absorbance whereas peak at 144 wavenumbers increases.

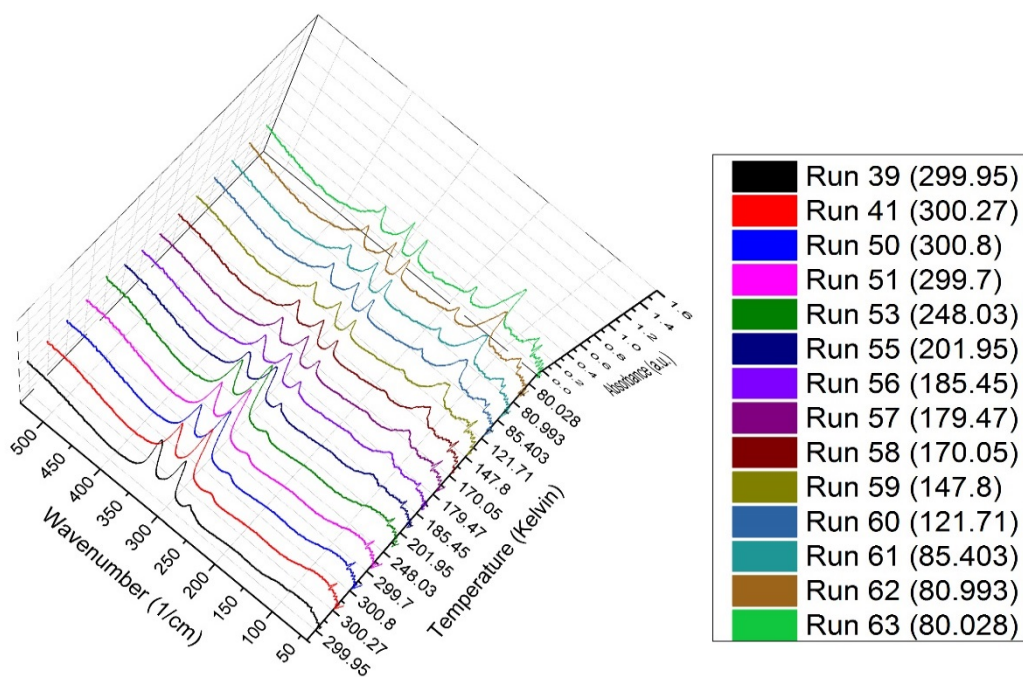


Figure 4-57: 3D Ribbon Plot of FIR absorbance spectra for DMSO-d6 in DWLC C using 20 μm spacer, when cooled (to 78 K) for the second time, analysed at the Australian Synchrotron (THz/FIR Beamline) with SiBolo detector.

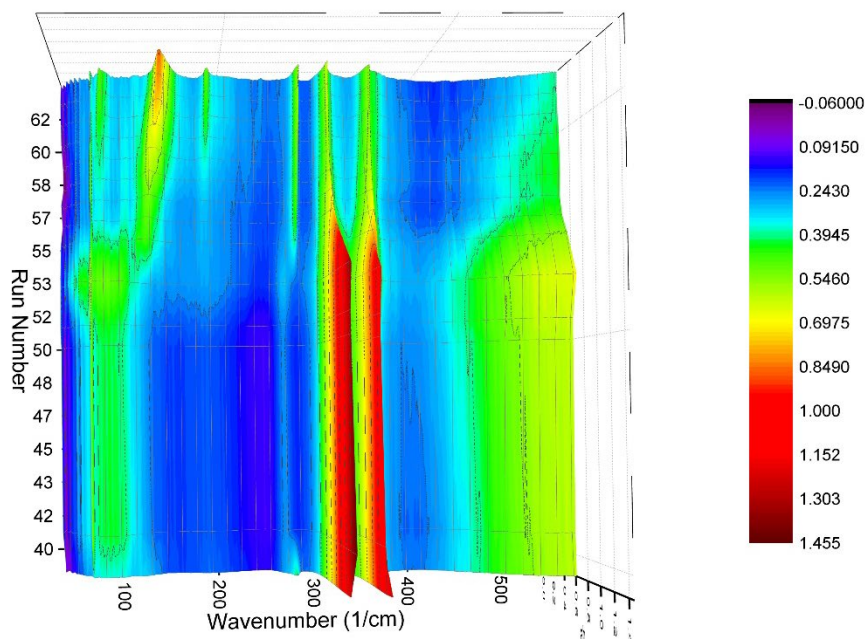


Figure 4-58: 3D Colourmap Surface Contour plot of FIR absorbance spectra for DMSO-d₆ in DWLC C using 20 μm spacer, when cooled (to 78 K) for the second time, analysed at the Australian Synchrotron (THz/FIR Beamline) with SiBolo detector.

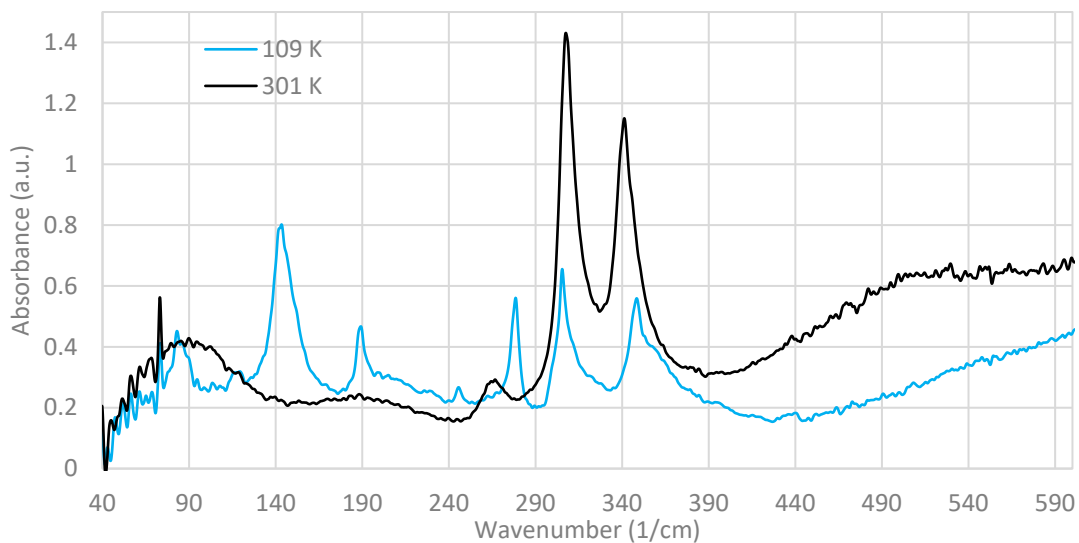


Figure 4-59: FIR overlaid spectra of DMSO-d₆ in DWLC C with a 20 μm spacer when heated (to 298 K) for the second time, analysed at the Australian Synchrotron (THz/FIR Beamline) with SiBolo detector.

It is noted that when cooled for the second time, peak at 354 wavenumbers decreases in absorbance whereas peak at 144 wavenumbers increases.

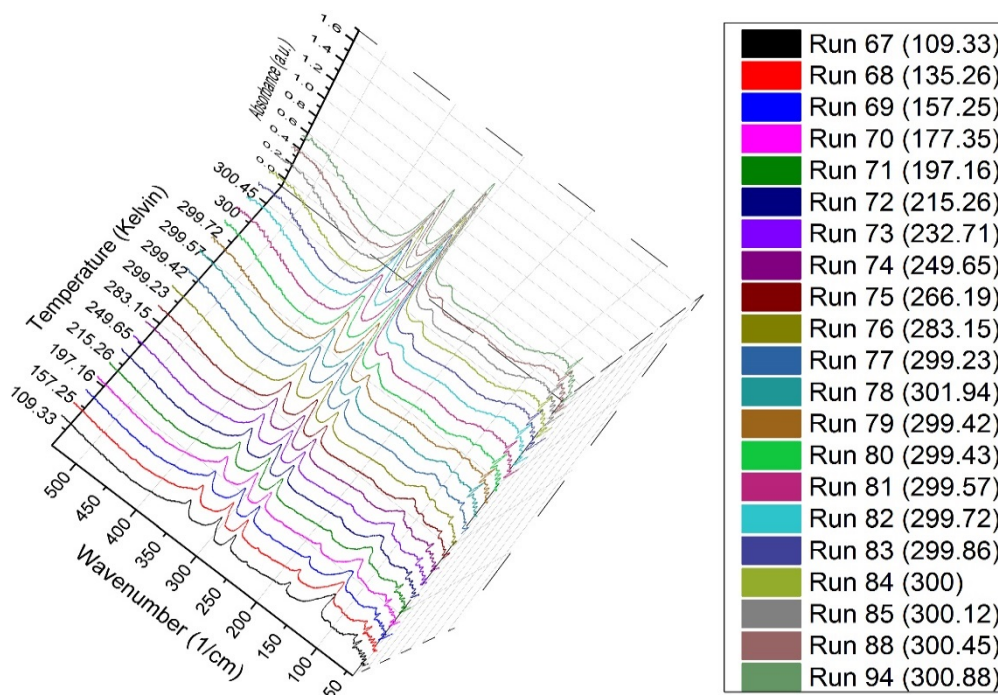


Figure 4-60: 3D Ribbon Plot of FIR absorbance spectra for DMSO-d₆ in DWLC C using 20 μm spacer, when heated (to 298 K) for the second time, analysed at the Australian Synchrotron (Thz/FIR Beamline) with SiBolo detector.

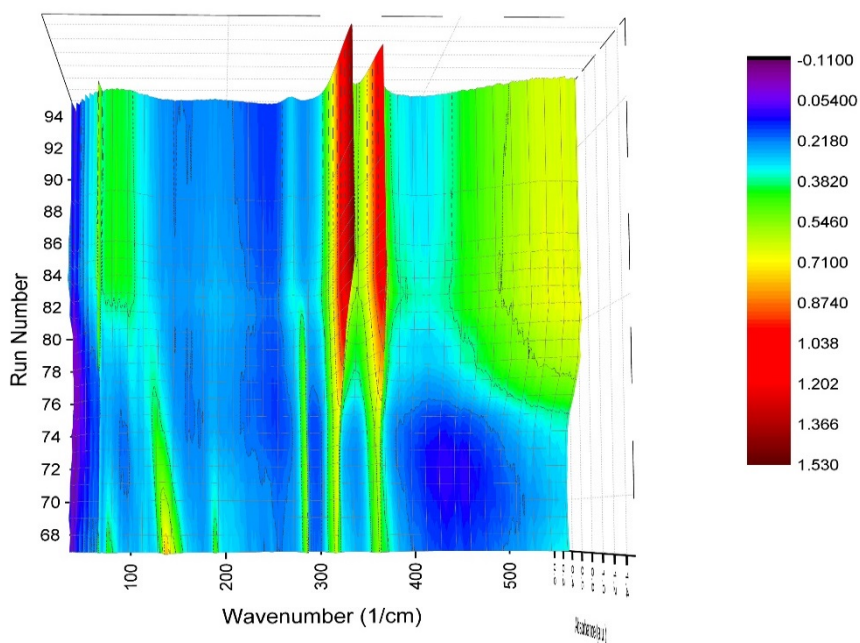


Figure 4-61: 3D Colourmap Surface Contour plot of FIR absorbance spectra for DMSO-d₆ in DWLC C using 20 μm spacer, when heated (to 298 K) for the second time, analysed at the Australian Synchrotron (THz/FIR Beamline) with SiBolo detector.

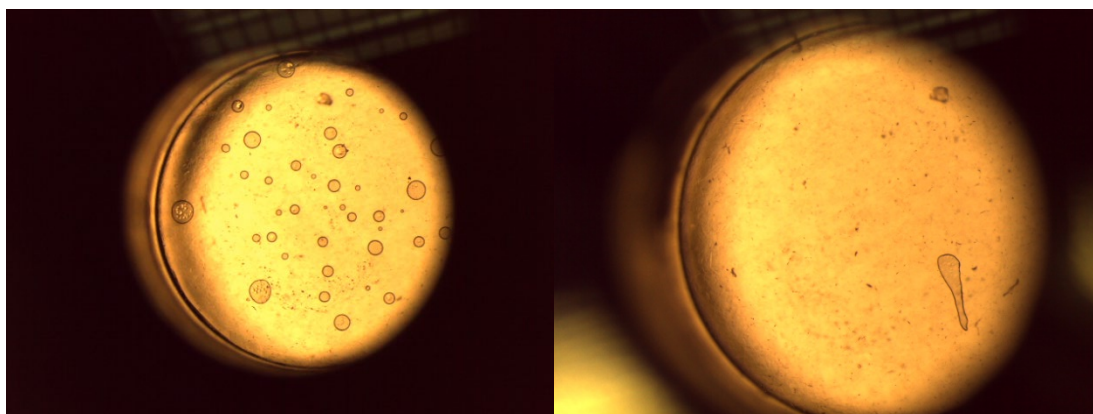


Figure 4-62: Left: Image of assembled DWLC C using 20 μm spacer containing DMSO- d_6 , after cryogenic analysis (two cooling cycles). Right: Image of DWLC C using 20 μm spacer containing DMSO- d_6 , after cryogenic analysis (two cooling cycles), loosened then tightened again.

Microscopic circular shapes observed in DWLC after cryogenic analysis. When the cell is loosened then tightened again, most of the circles disappear and analysing this (at room temperature only) produced the below spectrum.

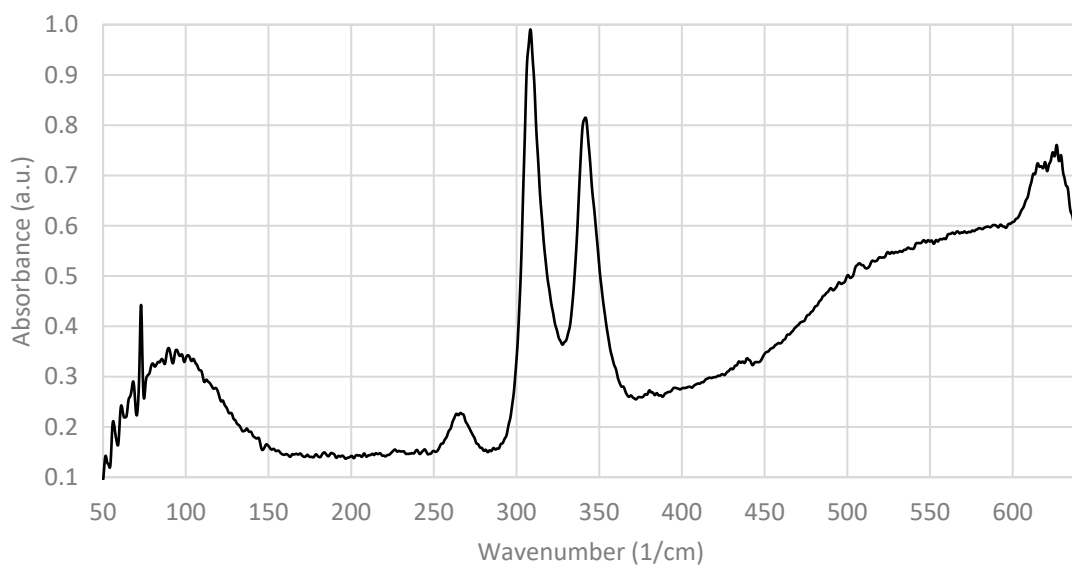


Figure 4-63: FIR spectrum of DMSO- d_6 in DWLC C with a 20 μm spacer after cryogenic analysis at the Australian Synchrotron (THz/FIR Beamline) using a SiBolo detector with amplitude 5400. The cell was loosened and then tightened before this analysis at room temperature.

Cryogenic analysis for DMSO- d_6 was triplicated and presented similar results as the original duplicate except for an additional peak when frozen at approximately 115 wavenumbers as seen below. Detailed results can be found in the Appendix (Additional FIR Results).

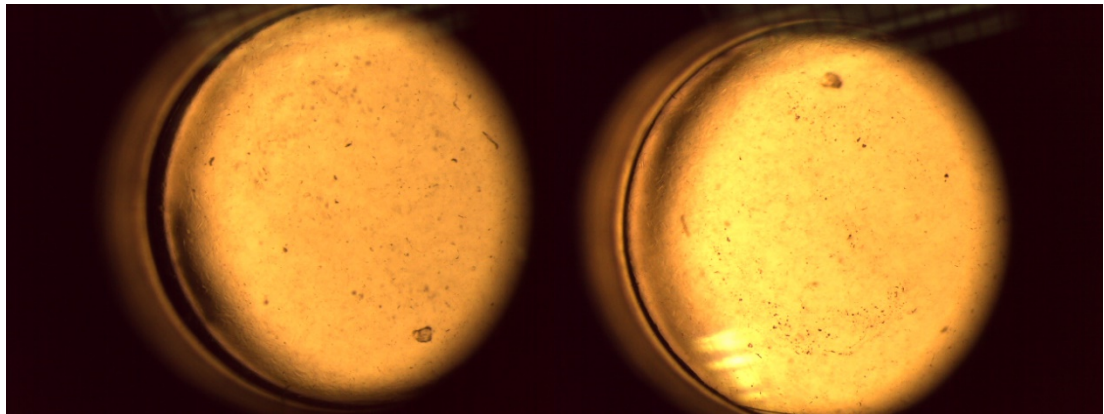


Figure 4-64: Left: Image of DMSO-d₆ in assembled DWLC C with 20 μm spacer before analysis. Right: Image of DMSO-d₆ in DWLC C using 20 μm spacer, after exposure to analysis sample compartment vacuum (9×10^{-5} mBar).

Peaks during cryogenic analysis for non-deuterated DMSO are observed at 98, 123, 148, 164, 258, 307, 329, 389 and 440 wavenumbers. The first peak (89 wavenumbers) appears to be resolved.

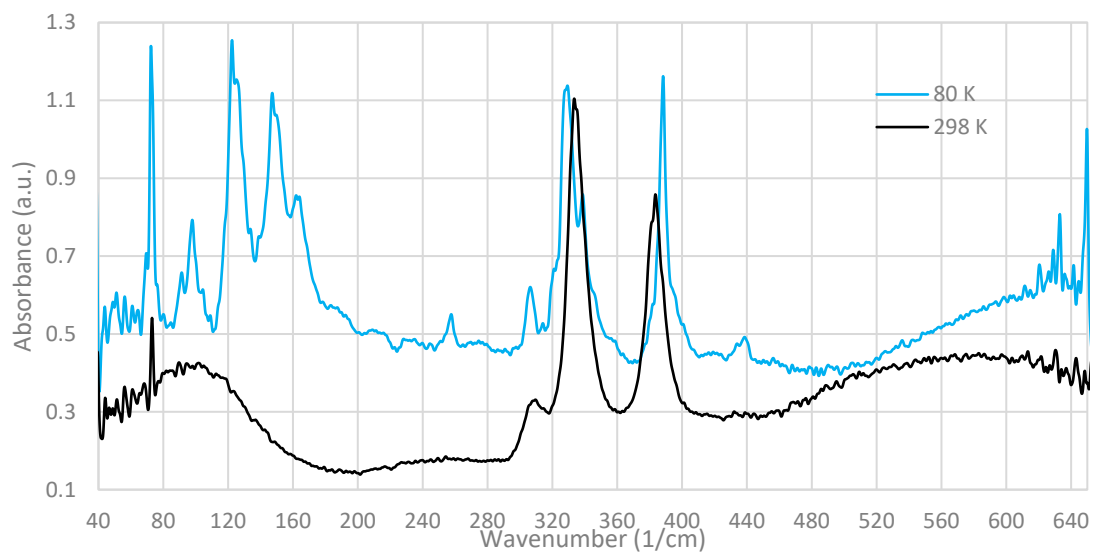


Figure 4-65: FIR overlaid spectra of DMSO-H₆ in DWLC C with a 20 μm spacer when cooled for the first time, analysed at the Australian Synchrotron (THz/FIR Beamline) using a SiBolo detector with starting amplitude of 5660.

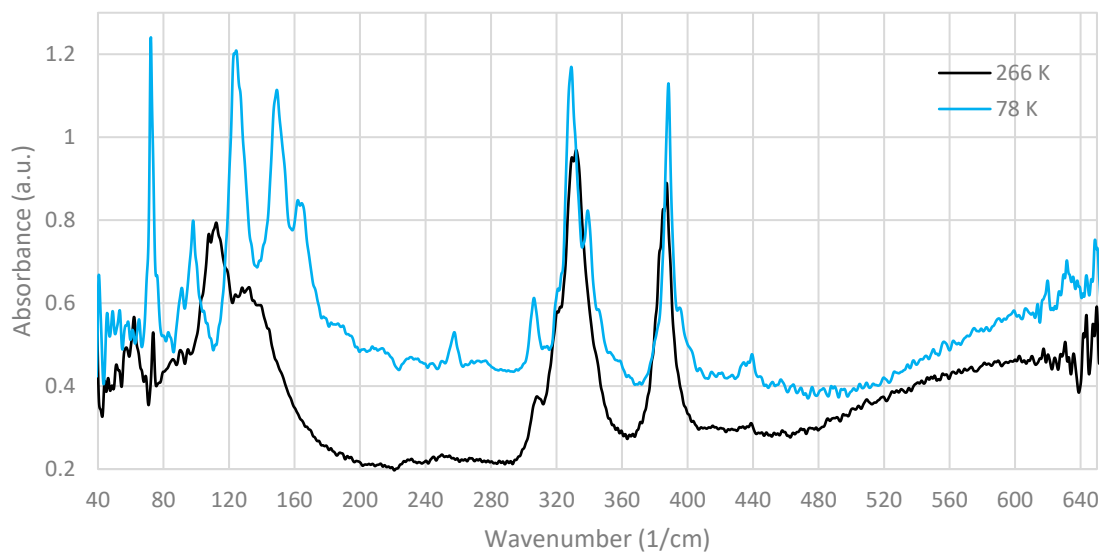


Figure 4-66: FIR overlaid spectra of DMSO-H₆ in DWLC C with a 20 μm spacer when heated for the first time, analysed at the Australian Synchrotron (THz/FIR Beamline) with SiBolo detector.

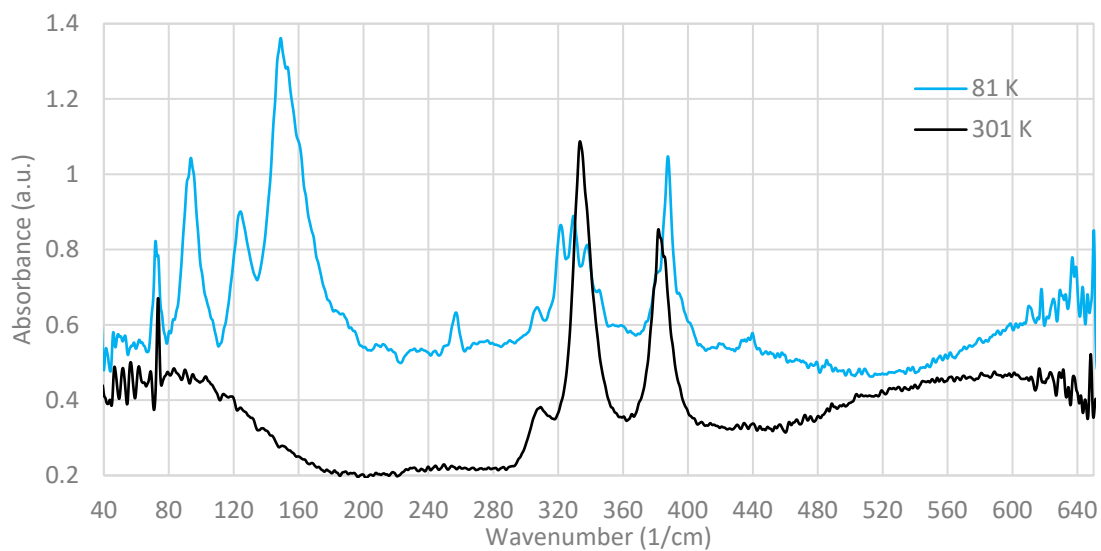


Figure 4-67: FIR overlaid spectra of DMSO-H₆ in DWLC C with a 20 μm spacer when cooled for the second time, analysed at the Australian Synchrotron (THz/FIR Beamline) with SiBolo detector.

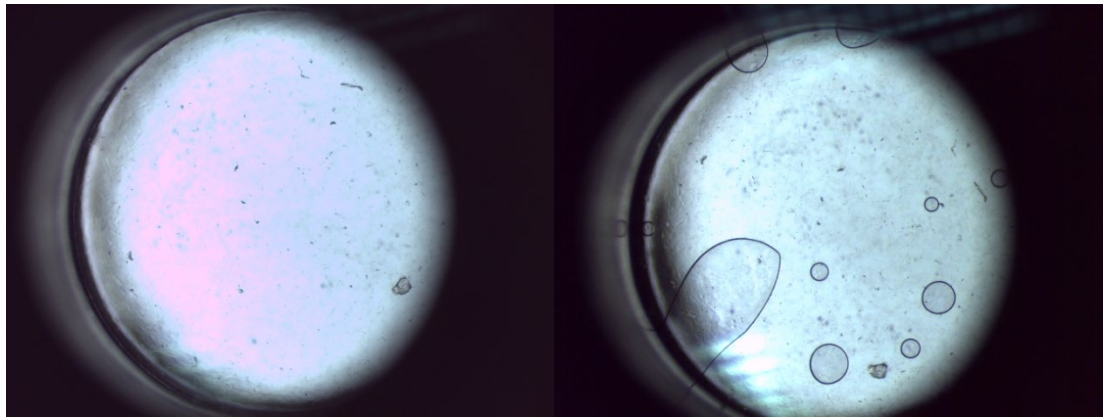


Figure 4-68: Left: Image of assembled DWLC C using 20 μm spacer containing DMSO- H_6 , before cryogenic analysis. Right: Image of DWLC C using 20 μm spacer containing DMSO- H_6 , after cryogenic analysis (two cooling cycles).

4.1.2.2.1.3 CHLOROFORM

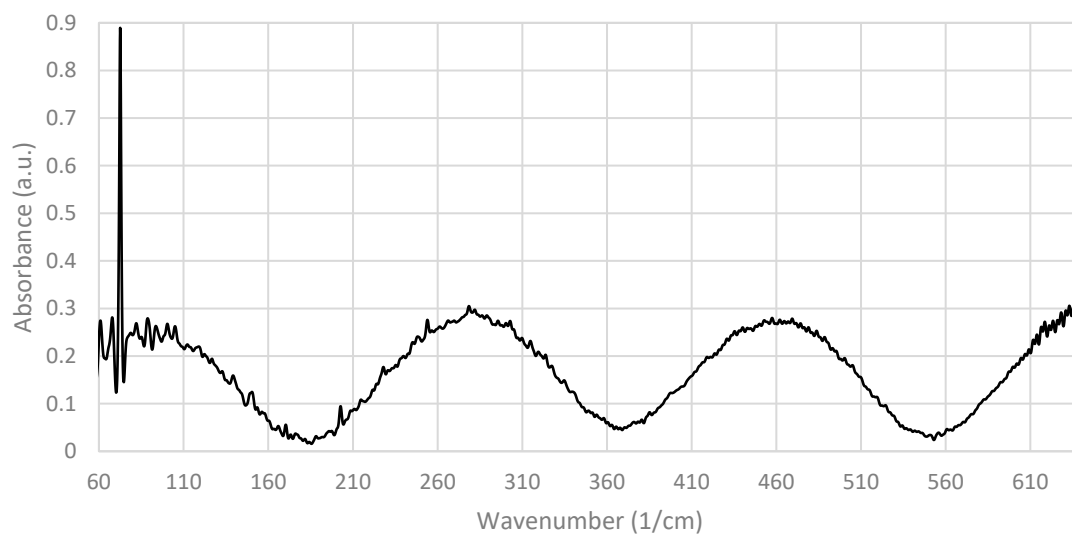


Figure 4-69: FIR spectrum of solvent blank, chloroform in DWLC C with a 20 μm spacer, analysed at the Australian Synchrotron (THz/FIR Beamline) using a SiBolo detector with amplitude of 6690.

Spectrum exhibits undulating waves. Droplets are observed under a microscope on the inside of the DWLC windows.

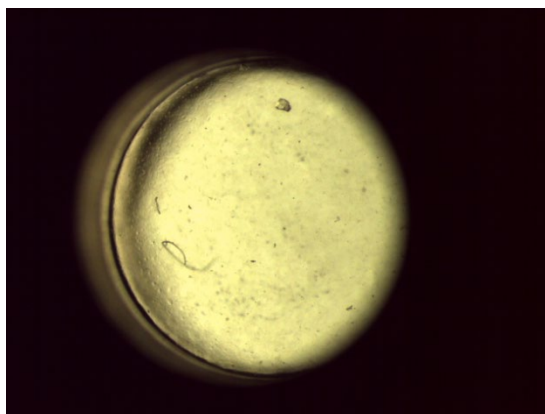


Figure 4-70: Image of assembled DWLC C using 20 μm spacer containing chloroform, after analysis at room temperature.

4.1.2.2.1.4 ETHANOL

A single sharp peak is observed at 435 wavenumbers. Absorbance increases linearly from 510 wavenumbers. Additionally, undulating waves are observed below 310 wavenumbers.

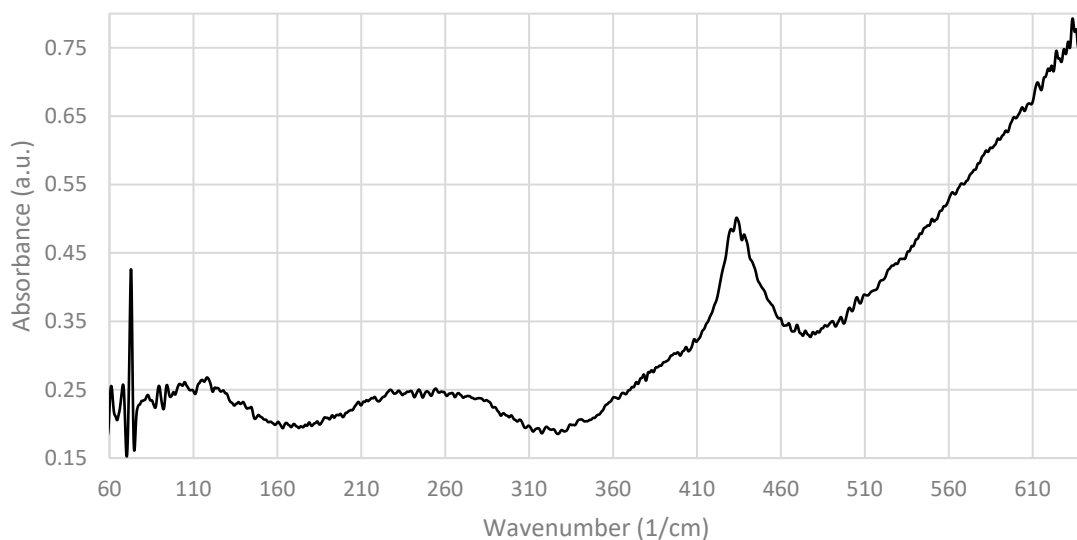


Figure 4-71: FIR spectrum of ethanol in DWLC C with a 20 μm spacer, analysed at the Australian Synchrotron (THz/FIR Beamline) using a SiBolo detector with amplitude of 6300.

4.1.2.2.1.5 METHANOL

Methanol dried quickly when pipetting the small volume (1.2 μL) into the DWLC, forming droplets on the internal windows. Spectra produced from these samples exhibited undulating waves hence are not presented here.

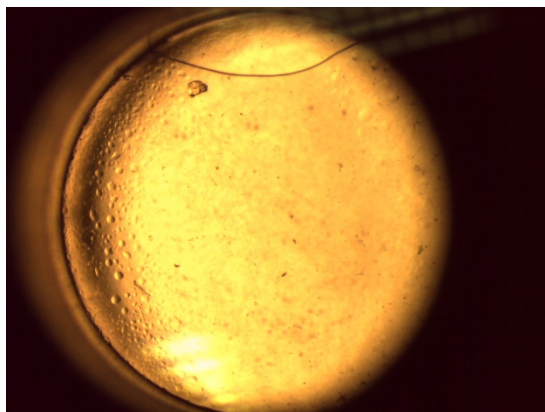


Figure 4-72: Image of assembled DWLC C using 20 μm spacer containing methanol, before analysis at room temperature.

4.1.2.2.2 Human Haemoglobin

For the 10 μm spacer analyses, a large peak is observed at 63 wavenumbers which is replicated. Fringing is also observed throughout spectra. The 10 μm spacer analysis was replicated as signal channel was also observed to increase during analysis, however provided similar results. For the 20 μm spacer analysis, a broad peak is

observed at 150 and 413 wavenumbers.

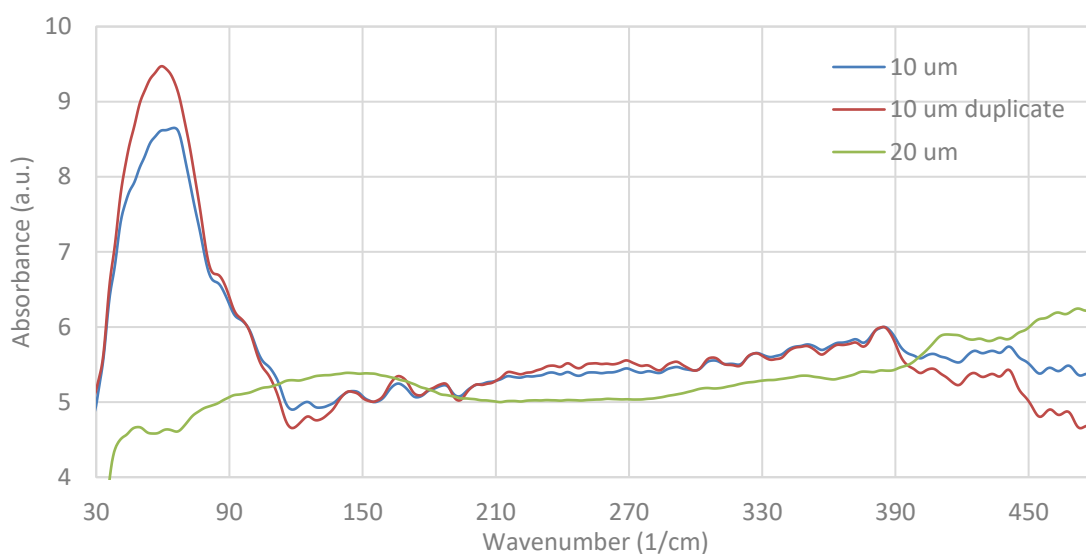


Figure 4-73: Normalised overlaid absorbance spectra of 20 mg/mL Human Haemoglobin in water using DWLC's with 10 and 20 µm spacers, normalised between 150 and 450 wavenumbers, analysed at the Australian Synchrotron (THz/FIR Beamline) using a SiBolo detector with amplitudes of 9900 (10 µm, Cell B), 10200 (duplicate) & 1200 (20 µm, Cell C).

Approximately 3.8 mg was observed not to dissolve in up to 14 µL DMSO-d₆ solvent, even with vortexing. However, the sample dissolved in 20 µL of solvent (concentration of 180 mg/mL).

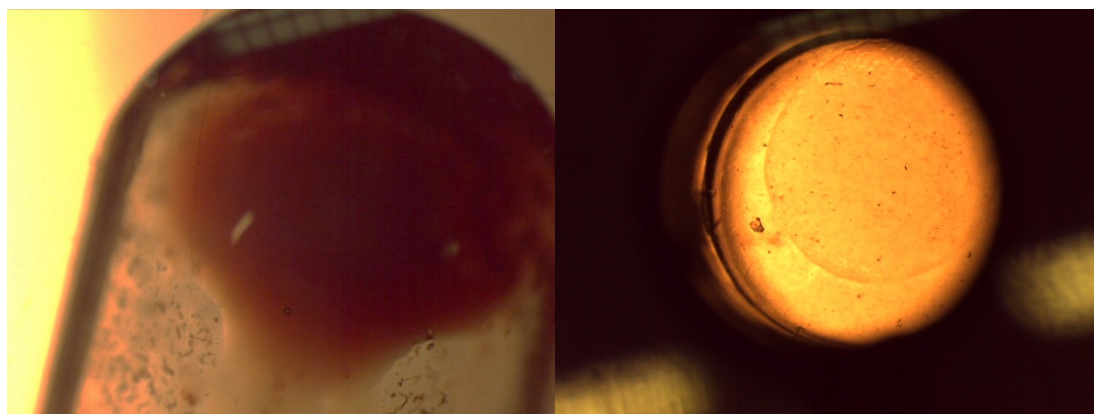


Figure 4-74: Left: Image of human haemoglobin in DMSO-d₆ (180 mg/mL) preparation in a test tube, before analysis. Right: Image of human haemoglobin in DMSO-d₆ (180 mg/mL) in DWLC C using 20 µm spacer, before analysis.

Human haemoglobin in assembled DWLC C appeared to contain a globule, darker in colouration to the remaining area on the window. No significant peaks were observed in the spectrum for this sample, apart from an inverted DMSO-d₆ spectrum. After analysis, there appeared to be many regular globular structures in the DWLC.

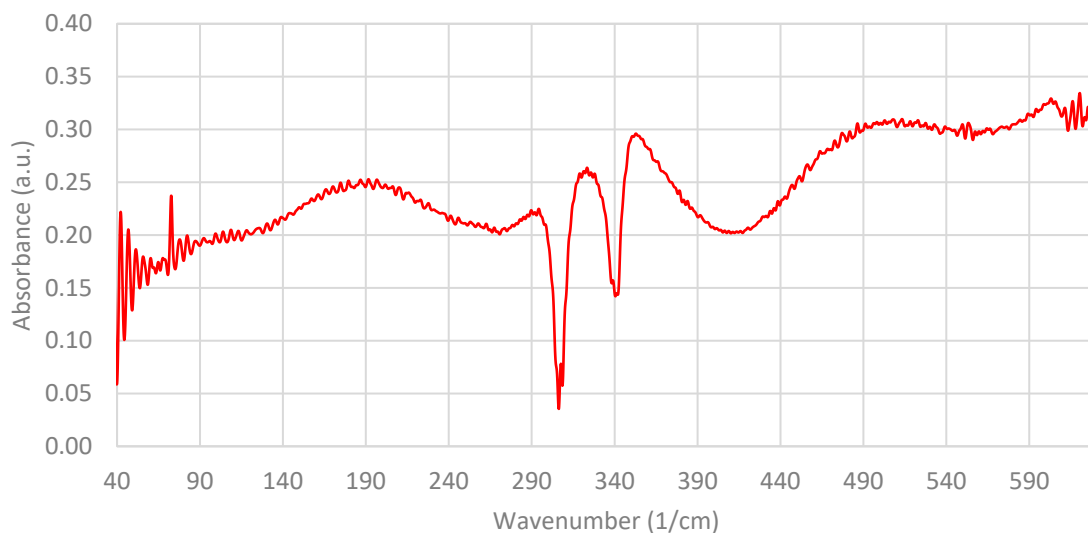


Figure 4-75: FIR spectra of human haemoglobin in DMSO-d₆ (180 mg/mL) in DWLC C using 20 μm spacer, analysed at the Australian Synchrotron (THz/FIR Beamline) using a SiBolo detector with amplitude of 5170.

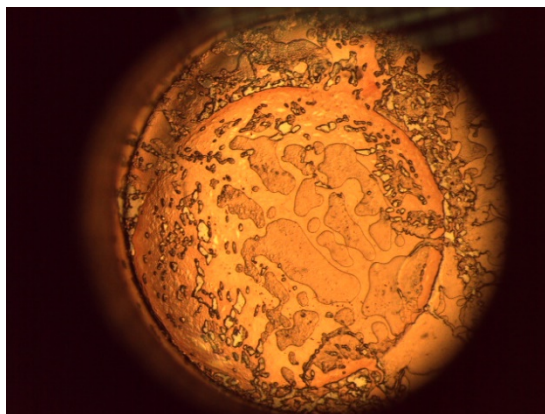


Figure 4-76: Image of human haemoglobin in DMSO-d₆ (180 mg/mL) in DWLC C using 20 μm spacer, after analysis at room temperature.

After cooling and heating the sample twice in the DWLC, absorbance spectra returned to original on the last run.

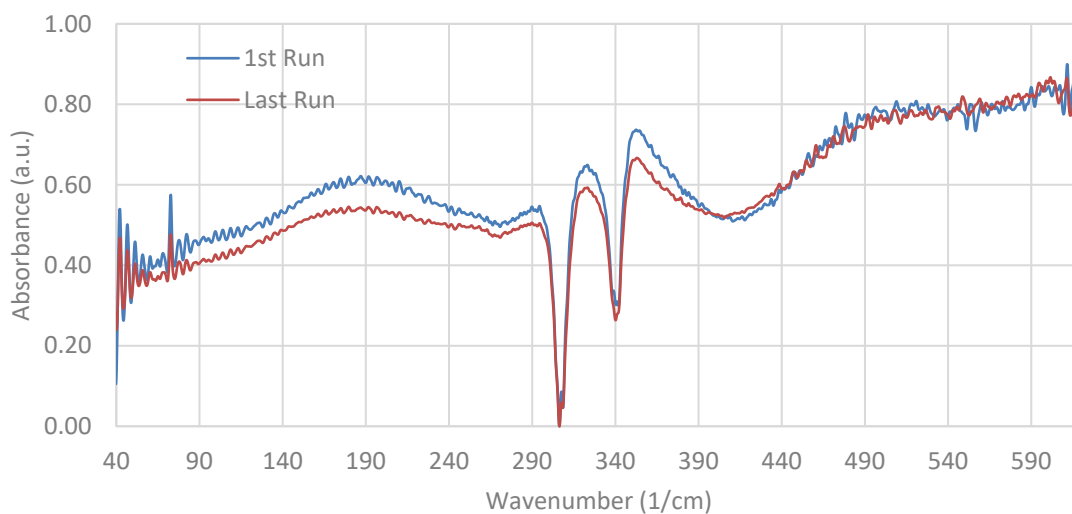


Figure 4-77: Overlaid absorbance spectra of previous human haemoglobin in DMSO-d₆ (180 mg/mL) sample above in DWLC C using 20 μ m spacer, analysed at the Australian Synchrotron (FIR Beamline) with SiBolo detector. Amplitude 7700.

It was noted that once the heating on the Lake Shore program was set to Medium, it took approximately 15 minutes to rise from 78 to 110 degrees Kelvin. Spectra presents inverse solvent peaks with no significant absorbance peaks attributed to human haemoglobin, hence 3D plots were not generated. After cryogenic analysis, the DWLC with sample appeared under microscope to contain bubbles.

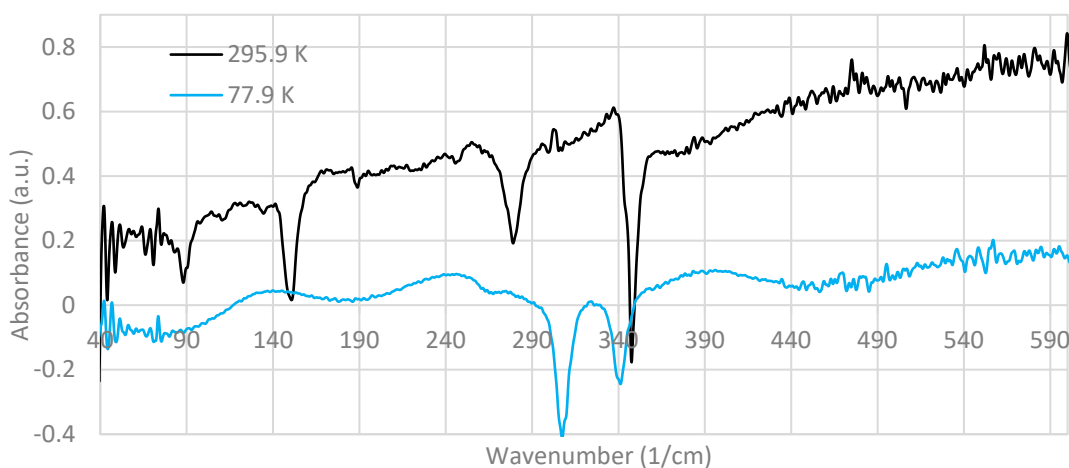


Figure 4-78: FIR overlaid spectra of human haemoglobin in DMSO-d₆ (180 mg/mL) in DWLC C with a 20 μ m spacer when cooled for the first time, analysed at the Australian Synchrotron (THz/FIR Beamline) with SiBolo detector.

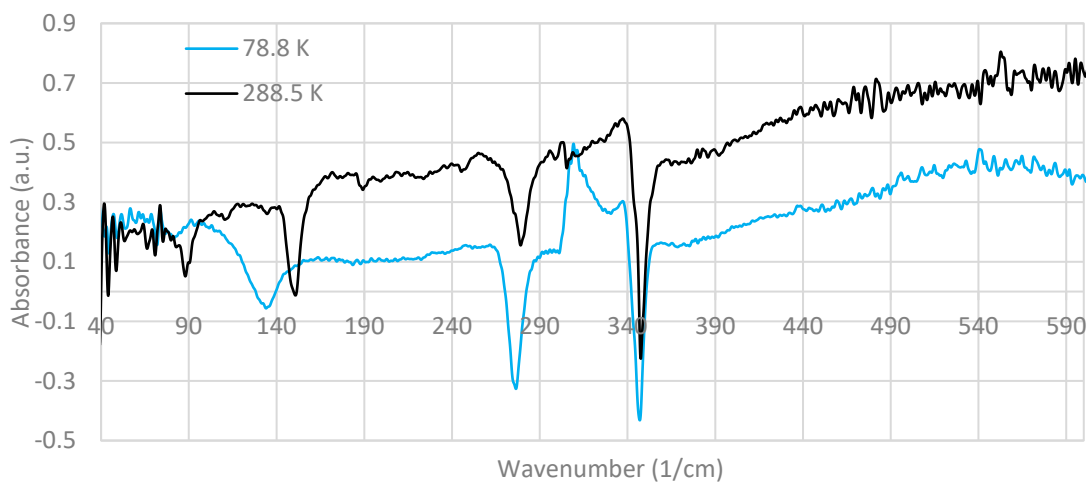


Figure 4-79: FIR overlaid spectra of human haemoglobin in DMSO-d₆ (180 mg/mL) in DWLC C with a 20 μm spacer when heated for the first time, analysed at the Australian Synchrotron (THz/FIR Beamline) with SiBolo detector.

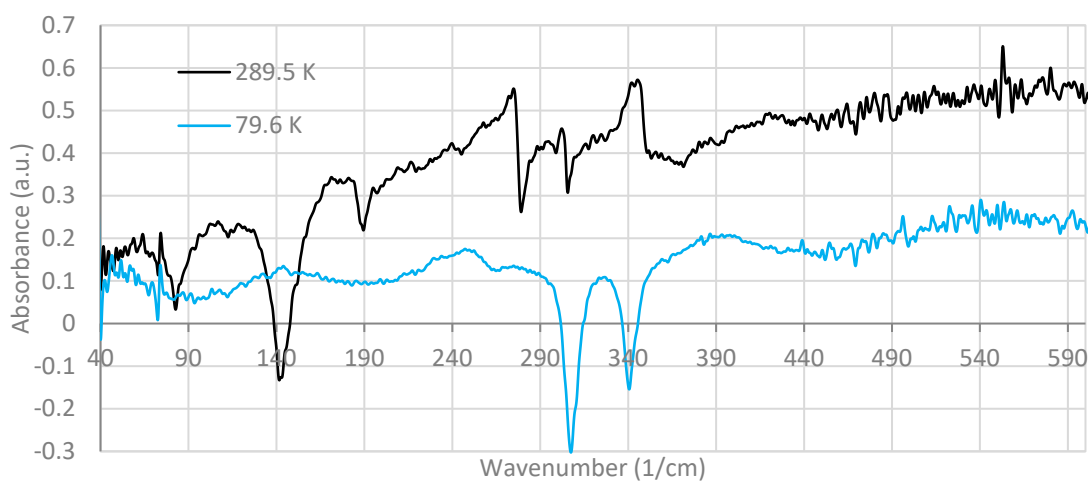


Figure 4-80: FIR overlaid spectra of human haemoglobin in DMSO-d₆ (180 mg/mL) in DWLC C with a 20 μm spacer when cooled for the second time, analysed at the Australian Synchrotron (THz/FIR Beamline) with SiBolo detector.

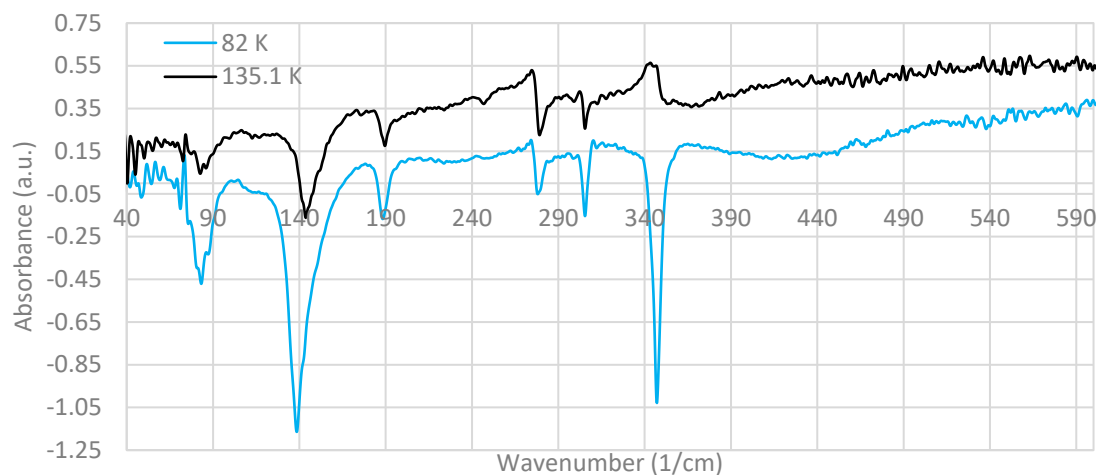


Figure 4-81: FIR overlaid spectra of human haemoglobin in DMSO-d₆ (180 mg/mL) in DWLC C with a 20 μm spacer when heated for the second time, analysed at the Australian Synchrotron (THz/FIR Beamline) with SiBolo detector.

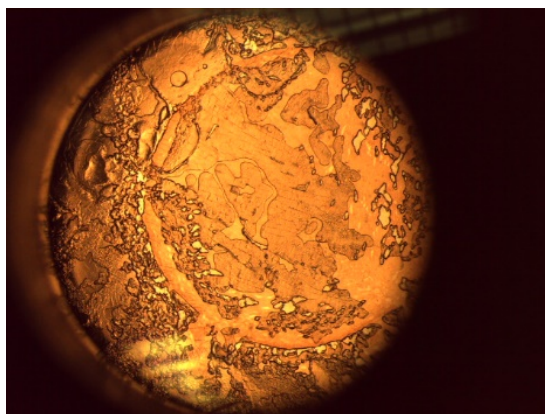


Figure 4-82: Image of human haemoglobin in DMSO-d₆ (180 mg/mL) in DWLC C using 20 μm spacer, after cryogenic analysis.

The solubility of haemoglobin lyophilised powder (human) [119] in water is 20 mg/mL. $20 \text{ mg/mL} = 0.02 \text{ mg}/\mu\text{L} / 0.5 \mu\text{L} = 40 \mu\text{g}$ in DWLC.

4.1.2.2.3 Blood

A broad absorbance is observed at 190 wavenumbers and absorbance increases linearly above 300 wavenumbers. Similar spectral profile to water is observed.

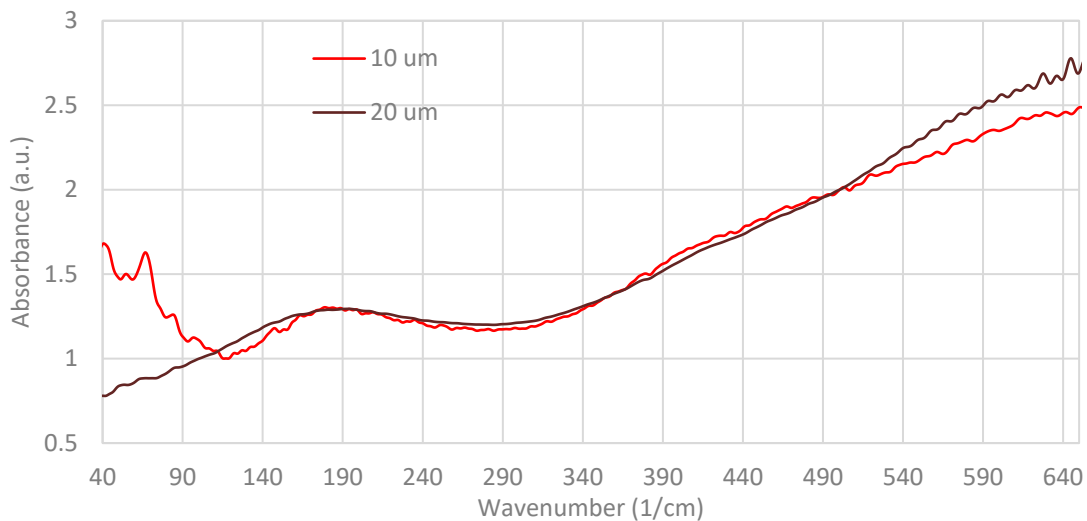


Figure 4-83: Normalised FIR absorbance overlaid spectra of defibrinated sheep's blood in DWLC's using various spacers, normalised between 100 and 500 wavenumbers, analysed at the Australian Synchrotron (THz/FIR Beamline) using a SiBolo detector with amplitudes of 15000 (10 µm, Cell A) & 9000 (20 µm, Cell C).

4.1.2.2.4 Biliverdin

Peaks observed at 60, 100, 307, 388 and 448 wavenumbers, although spectra present oscillations.

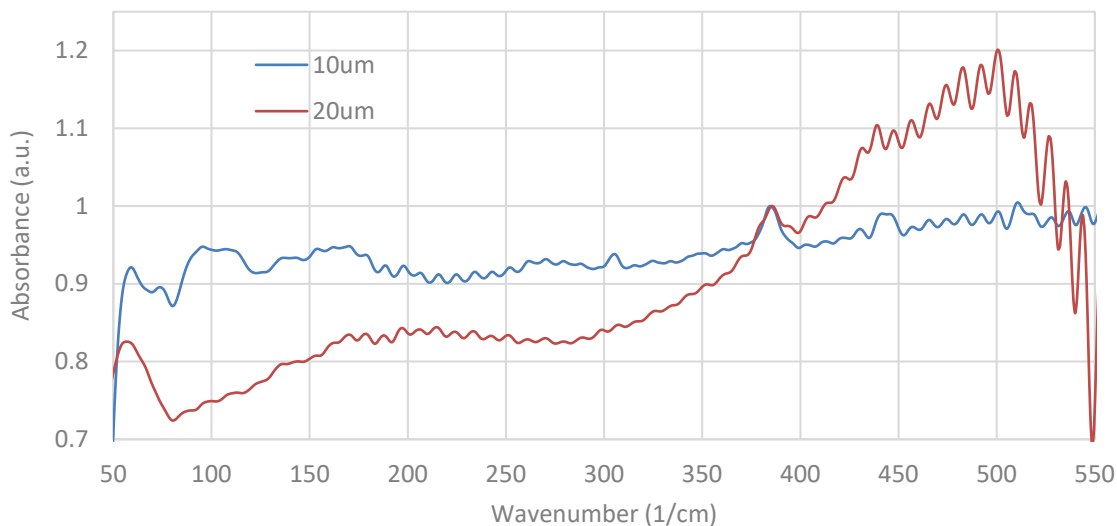


Figure 4-84: Normalised FIR absorbance overlaid spectra of 2.3 mg/mL biliverdin in PBS in DWLC's using various spacers, normalised between 200 and 400 wavenumbers, analysed at the Australian Synchrotron (THz/FIR Beamline) using a SiBolo detector with amplitudes 15300 (10 µm, Cell C) & 5900 (20 µm, Cell C).

Weak and broad peaks are observed for the slurry at 60, 117, 180, 200, 242, 264, 330, 410 and 490 wavenumbers. It is noted that absorbance slopes down from 50 to 490 wavenumbers.

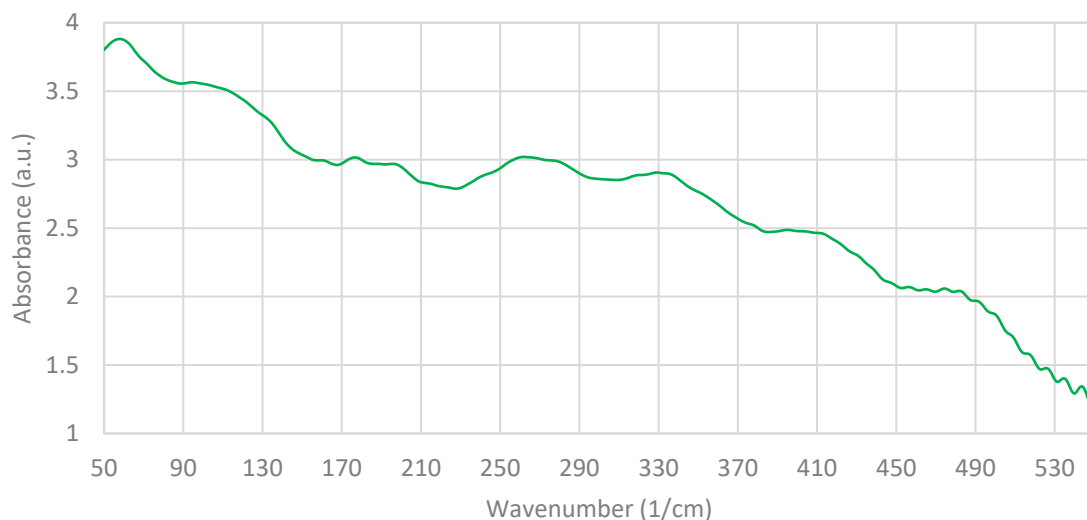


Figure 4-85: FIR spectrum of biliverdin slurry with 0.1 M NaOH (625 mg/mL) in DWLC C using 20 μm spacer, analysed at the Australian Synchrotron (THz/FIR Beamline) using a SiBolo detector with amplitude of 4400.

Diamond liquid cell C was observed to crack when assembling the cell for this analysis. Analysis was carried out with the cracked cell.

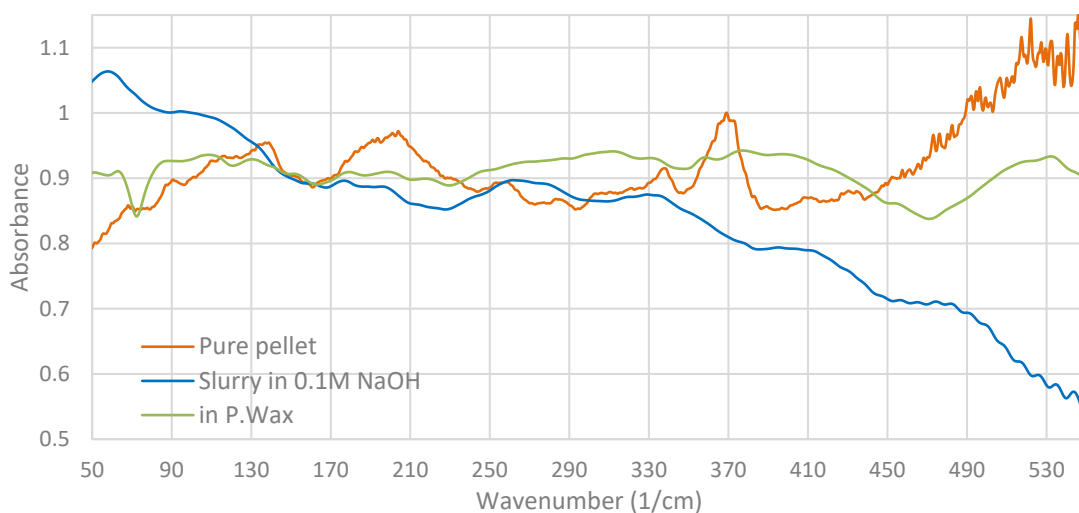


Figure 4-86: Normalised FIR overlaid spectra of biliverdin in various matrices, normalised between 100 and 350 wavenumbers, analysed at the Australian Synchrotron (THz/FIR Beamline) with a SiBolo detector.

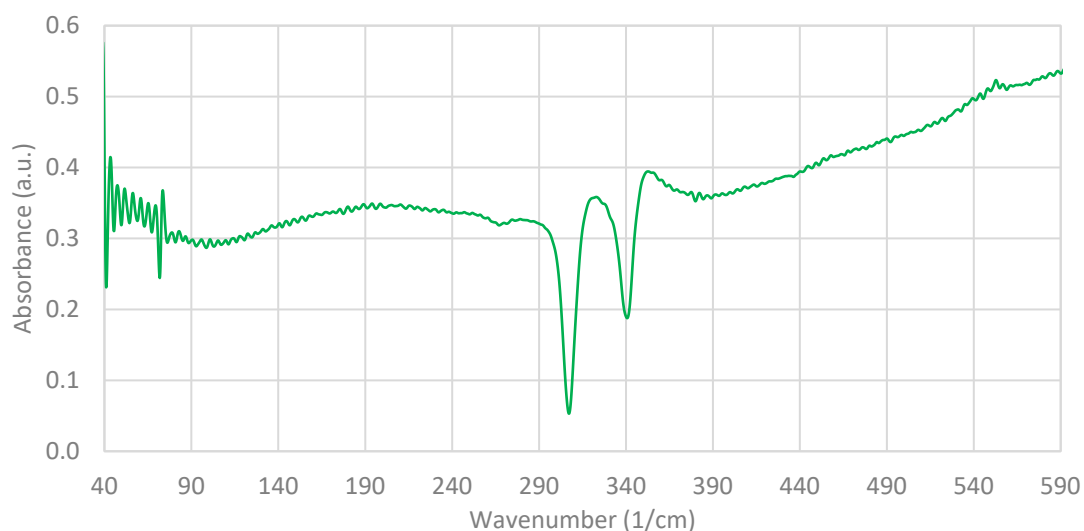


Figure 4-87: FIR absorbance spectrum of biliverdin in DMSO-d₆ (140 mg/mL) in DWLC A using 20 μm spacer, analysed at the Australian Synchrotron (THz/FIR Beamline) with SiBolo detector and amplitude of 4500.

No significant peaks observed, only inverted solvent peaks. Same is expected for non-deuterated DMSO hence biliverdin not analysed in DMSO-H₆.

$$3.5 \text{ mg} / 25 \text{ } \mu\text{L} = 0.14 \text{ mg}/\mu\text{L} \times 1.6 \text{ } \mu\text{L} = 0.22 \text{ mg in DWLC}$$

14% biliverdin sample and 86% solvent, thus $20 \text{ } \mu\text{m} \times (86 \% / 100 \%) = 17.2 \text{ } \mu\text{m}$ spacer (20 μm spacer) for background analysis required to subtract solvent absorbance from spectrum.

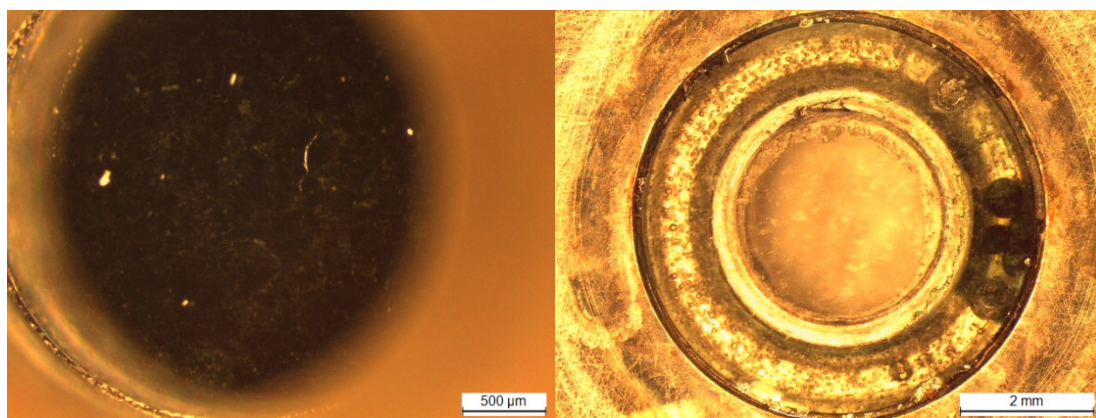


Figure 4-88: Left: Image of biliverdin in DMSO-d₆ (140 mg/mL) in DWLC A using 20 μm spacer, after analysis. Right: Image of biliverdin contamination in glue in dismantled DWLC A.

Some fibres are present on the cell windows post-analysis. Biliverdin contamination was observed in the glue of the cell windows after cleaning the cell. Less was observed on the flange cell window (see Appendix, Additional FIR Results).

Powdered biliverdin in the DWLC presents peaks at 60, 118, 139, 194, 257, 288, 307, 340, 371, 416, 436, 497 wavenumbers. Absorbance saturates above 510 wavenumbers.

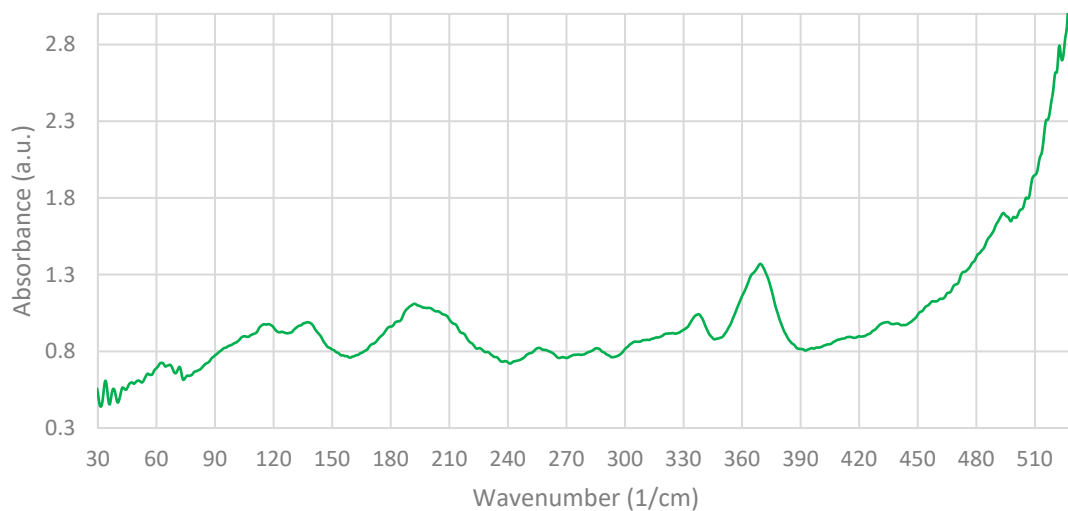


Figure 4-89: Absorbance spectrum of powdered biliverdin (0.5 mg) in DWLC A using 0 μm spacer, analysed at the Australian Synchrotron (THz/FIR Beamline) with SiBolo detector and amplitude of 1300.

When the cell was assembled and tightened, a crack noise was heard. When the cell was observed under microscope, cracks were apparent in one window (non-flange side). Similarly, another crack noise was heard when mounting the cell to the cryostat. After analysis, the cell was observed again under microscope, where cracks were apparent in both windows of the DWLC.

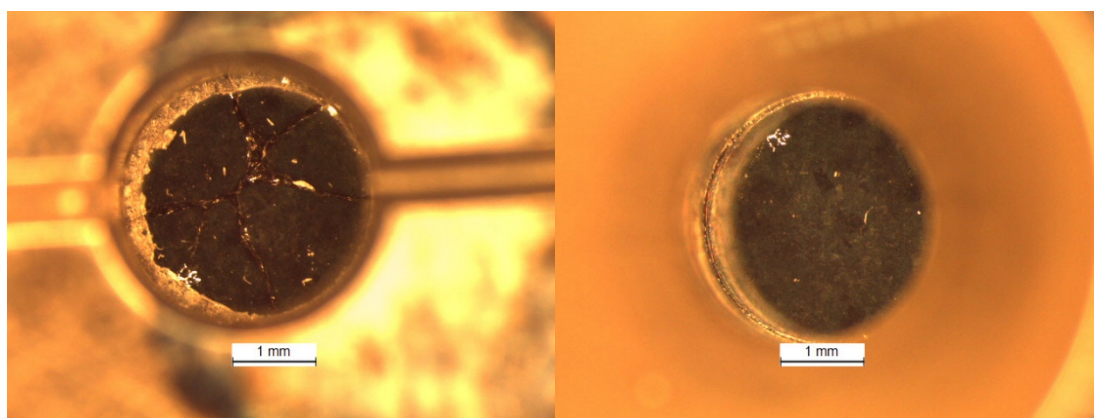


Figure 4-90: Left: non-flange side image of powdered biliverdin in DWLC A using 0 μm spacer, before analysis. Right: Flange side image of powdered biliverdin in DWLC A using 0 μm spacer, before analysis.

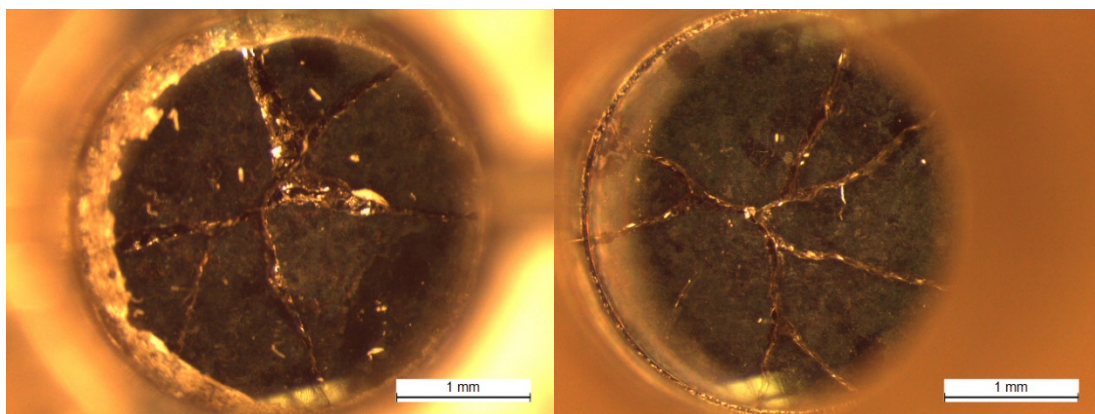


Figure 4-91: Left: non-flange side image of powdered biliverdin in DWLC A using 0 μm spacer, after analysis. Right: Flange side image of powdered biliverdin in DWLC A using 0 μm spacer, after analysis.

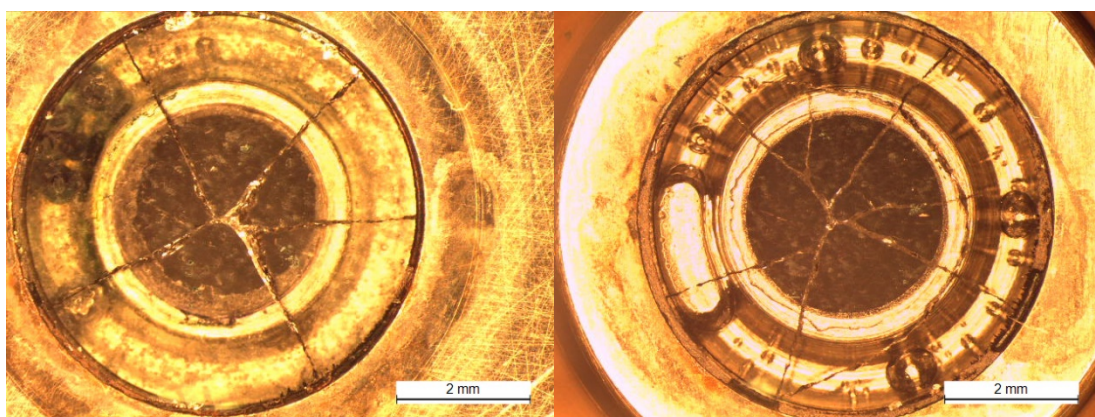


Figure 4-92: Left: non-flange side image of DWLC A after cleaned. Right: Flange side image of DWLC A using 0 μm spacer after cleaned.

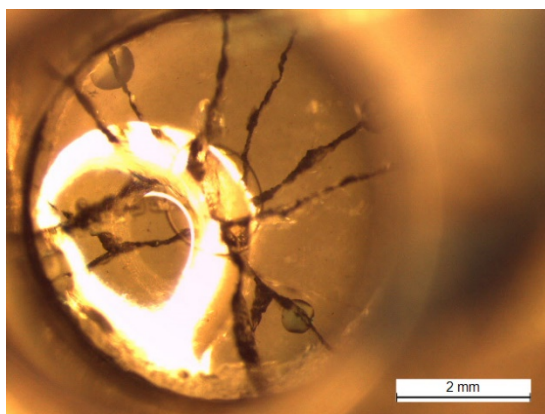


Figure 4-93: Image of assembled cracked DWLC A using 20 μm spacer containing DMSO-d₆.

When solvent was prepared in DWLC A, the assembled cell was observed under the microscope, where liquid appeared to leak from the cracks forming a droplet on the external surface of the window. This left less sample in the assembled cell (shown as

a circle in the centre of the above photograph). There also appears to be green local areas near cracks.

A 3.9 mg biliverdin sample in 5 μL DMSO- d_6 (780 mg/mL) was prepared however was a viscous and lumpy consistency, hence was not used for analysis and further diluted.

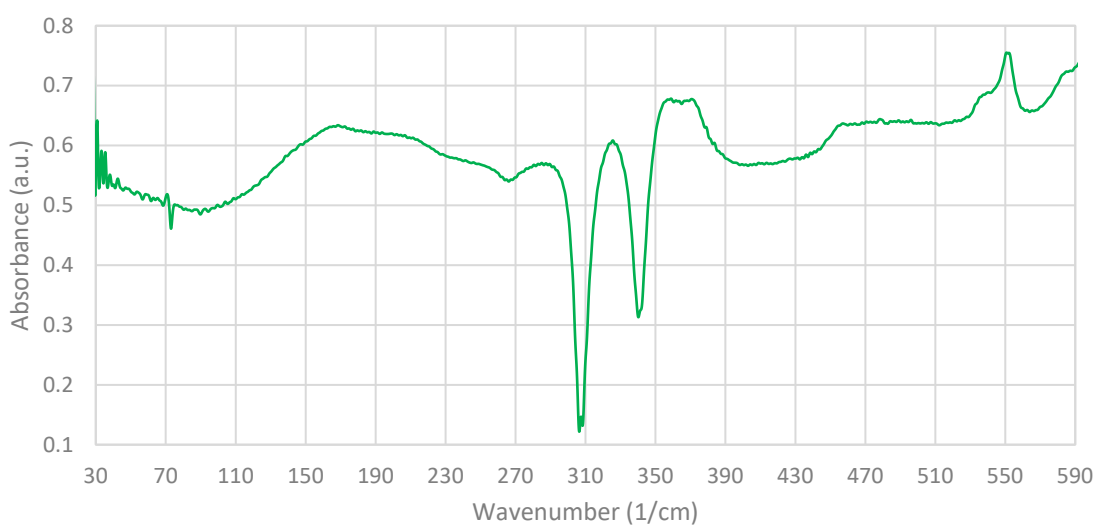


Figure 4-94: FIR absorbance spectrum of biliverdin in DMSO- d_6 (520 mg/mL) in DWLC C using 20 μm spacer, analysed at the Australian Synchrotron (THz/FIR Beamline) with SiBolo detector and amplitude of 5240.

Shoulder peak at 370 wavenumbers is present in dry biliverdin samples. Another peak is also observed at approximately 560 wavenumbers.

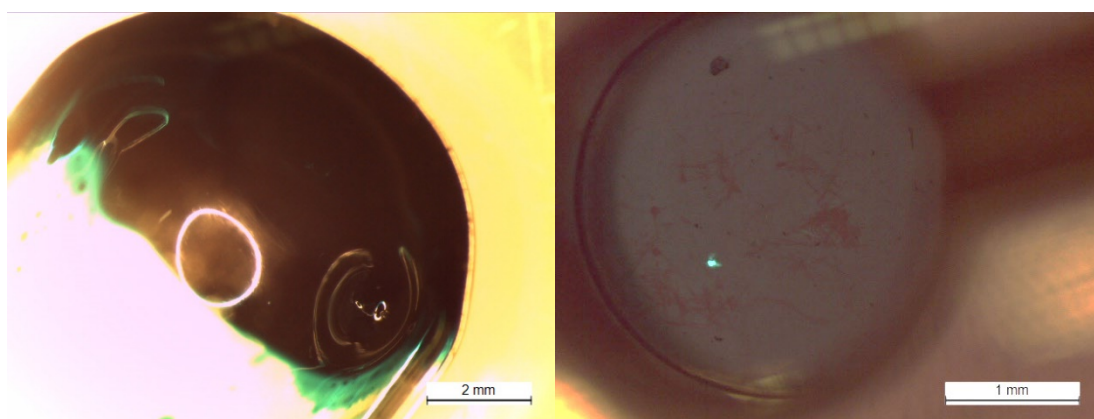


Figure 4-95: Left: Image of biliverdin in DMSO- d_6 (520 mg/mL) preparation in a test tube, before analysis. Right: Image of biliverdin in DMSO- d_6 (520 mg/mL) in DWLC C using 20 μm spacer, before analysis.

Sample was observed to crystallise during analysis in the test tube. Crystallisation was also observed in the DWLC. However, no crystallisation was observed pre- or post-analysis for a duplicate (500 mg/mL).

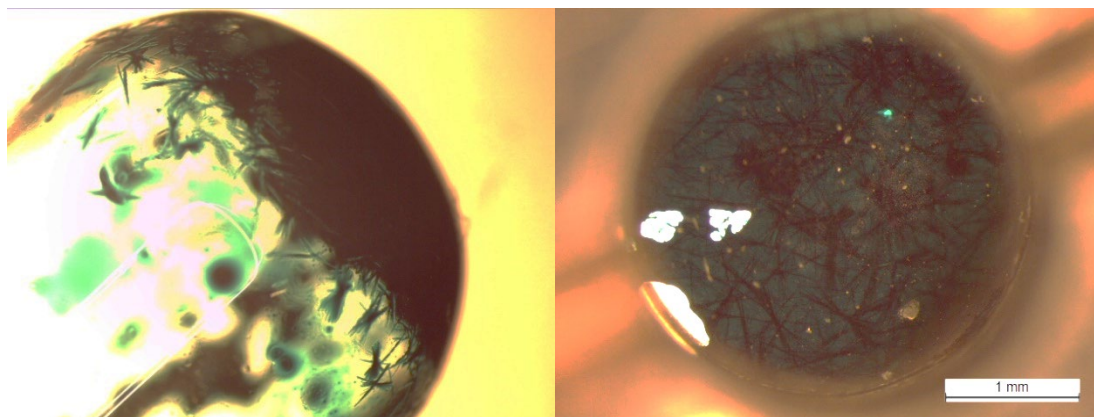


Figure 4-96: Left: Image of biliverdin in DMSO-d₆ (520 mg/mL) preparation in a test tube, after analysis. Right: Image of biliverdin in DMSO-d₆ (520 mg/mL) in DWLC C using 20 µm spacer, after analysis.

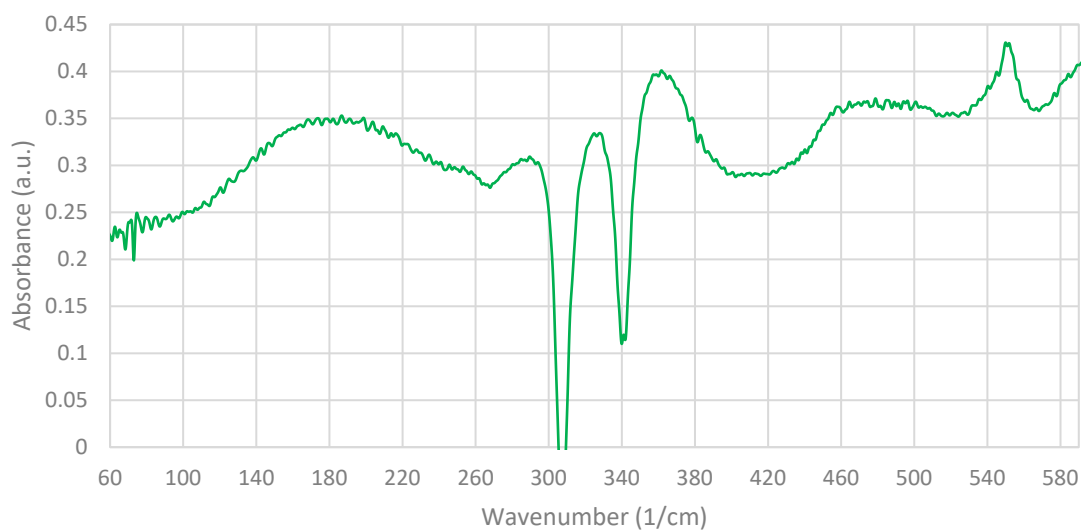


Figure 4-97: FIR absorbance spectrum of duplicate biliverdin in DMSO-d₆ (500 mg/mL) in DWLC C using 20 µm spacer, analysed at the Australian Synchrotron (THz/FIR Beamline) with SiBolo detector and amplitude of 5480.

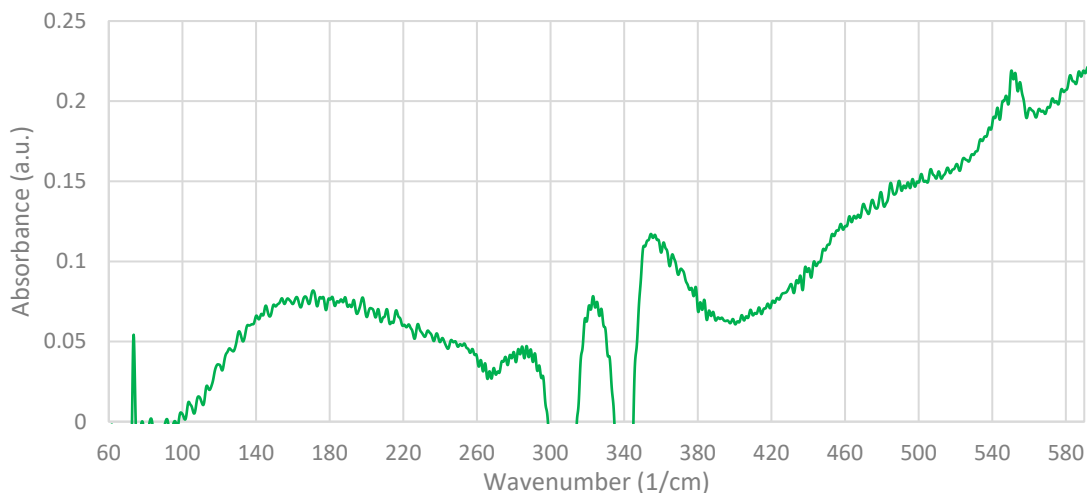


Figure 4-98: FIR absorbance spectrum of biliverdin in DMSO-d₆ (400 mg/mL) in DWLC C using 20 μm spacer, analysed at the Australian Synchrotron (THz/FIR Beamline) with SiBolo detector and an amplitude of 5421.

The 400 mg/mL analysis was duplicated and presented similar results as reported in the Appendix (Additional FIR Results).

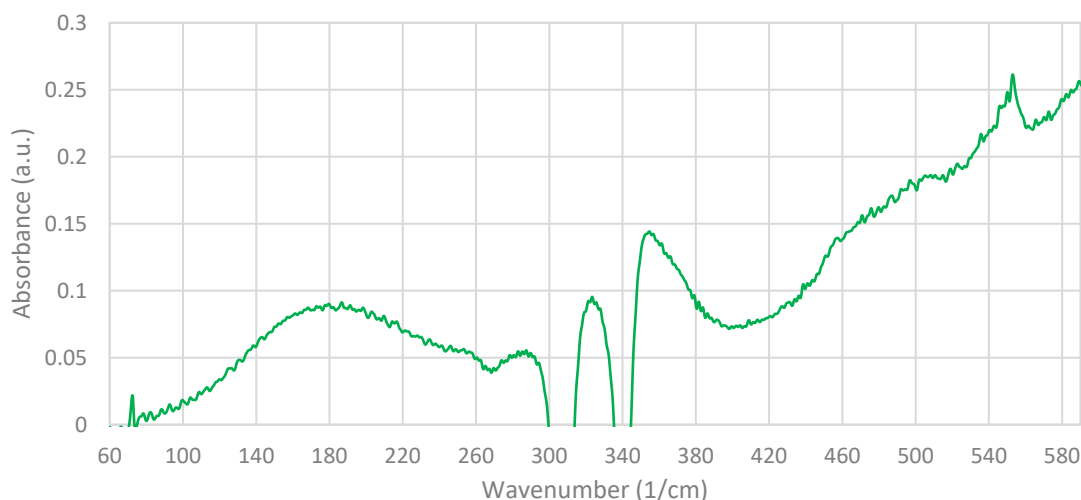


Figure 4-99: FIR absorbance spectrum of biliverdin in DMSO-d₆ (250 mg/mL) in DWLC C using 20 μm spacer, analysed at the Australian Synchrotron (THz/FIR Beamline) with SiBolo detector and amplitude of 5300.

The 250 mg/mL analysis was duplicated as liquid helium was topped up in the SiBolo detector, however presented similar results (see Appendix, Additional FIR Results). Cryogenic analysis of the 200 mg/mL sample provided no additional information. Biliverdin in DMSO-d₆ at a concentration of 400 mg/mL was also cryogenically analysed however provided similar results hence are not reported here.

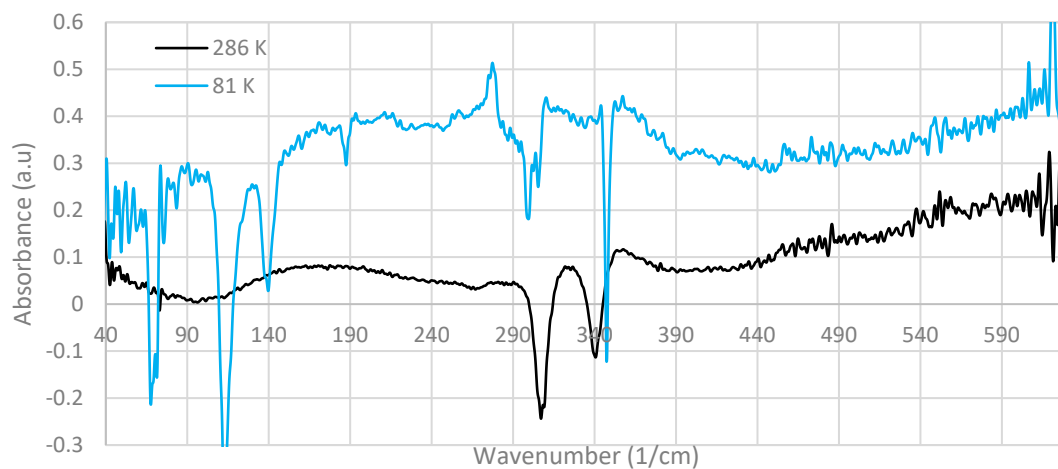


Figure 4-100: FIR overlaid spectra of biliverdin in DMSO-d₆ (250 mg/mL) in DWLC C with a 20 μm spacer when cooled for the first time, analysed at the Australian Synchrotron (THz/FIR Beamline) with SiBolo detector and starting amplitude of 5000.

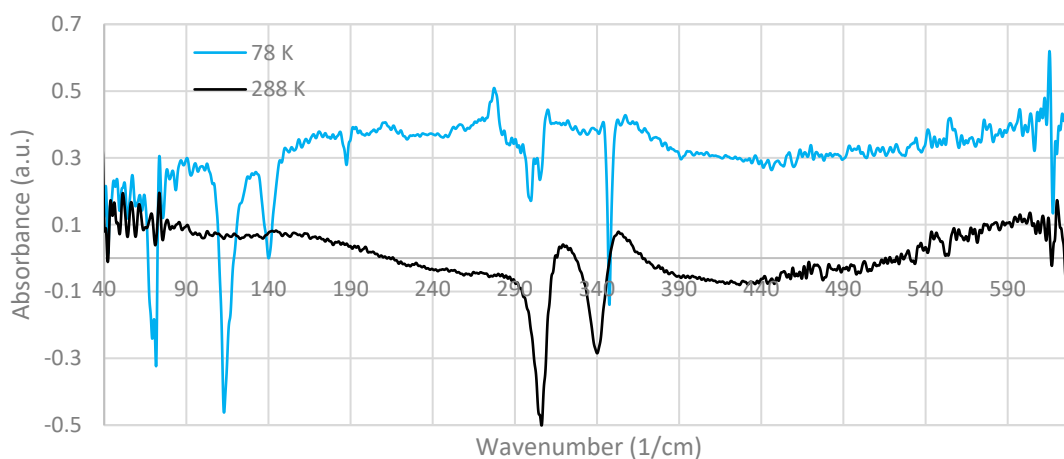


Figure 4-101: FIR overlaid spectra of biliverdin in DMSO-d₆ (250 mg/mL) in DWLC C with a 20 μm spacer when heated for the first time, analysed at the Australian Synchrotron (THz/FIR Beamline) with SiBolo detector.

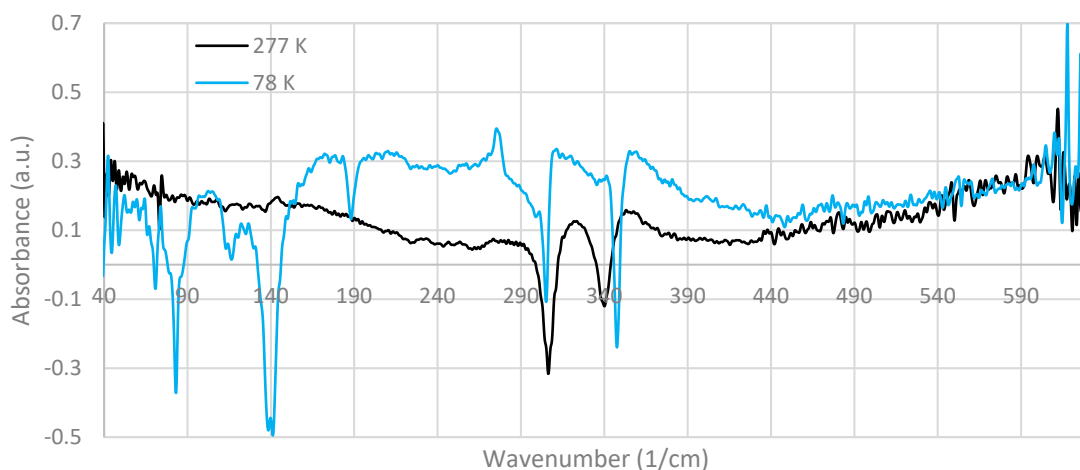


Figure 4-102: FIR overlaid spectra of biliverdin in DMSO-d₆ (250 mg/mL) in DWLC C with a 20 μm spacer when cooled for the second time, analysed at the Australian Synchrotron (THz/FIR Beamline) with SiBolo detector.

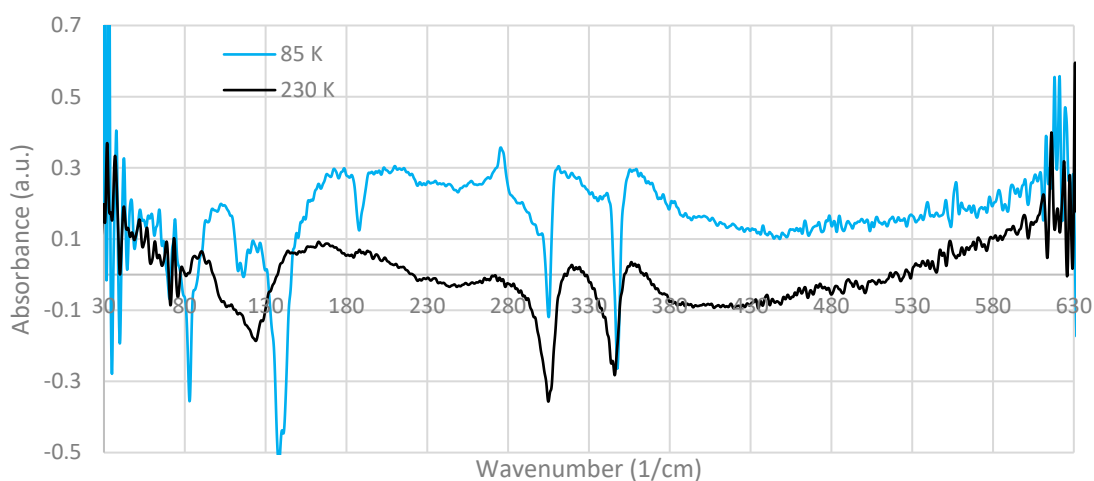


Figure 4-103: FIR overlaid spectra of biliverdin in DMSO-d₆ (250 mg/mL) in DWLC C with a 20 μm spacer when heated for the second time, analysed at the Australian Synchrotron (THz/FIR Beamline) with SiBolo detector.

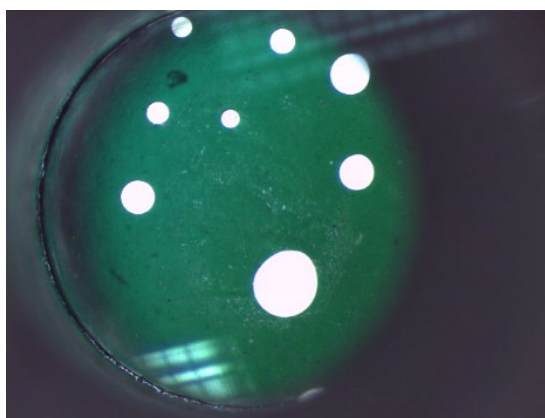


Figure 4-104: Image of assembled DWLC C using 20 μm spacer containing biliverdin in DMSO-d₆ (250 mg/mL), after cryogenic analysis (two cooling cycles).

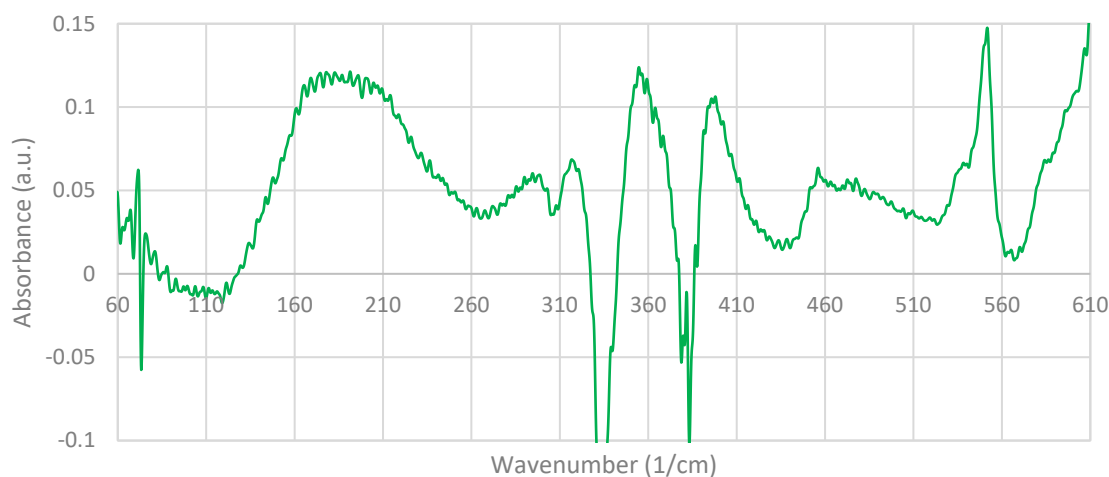


Figure 4-105: FIR absorbance spectrum of biliverdin in DMSO-H₆ (500 mg/mL) in DWLC C using 20 μm spacer, analysed at the Australian Synchrotron (THz/FIR Beamline) with SiBolo detector and amplitude of 5740.

A peak at 458 wavenumbers appears in the 500mg/mL sample. It is noted that the cryostat was colder than previous assemblies when mounting the DWLC containing 500 mg/mL biliverdin that experienced some crystallisation before analysis as local dark green areas were observed. Crystallisation was also observed after cryogenic analysis as thin fibre-like structures. Spectrally, results were like those presented from cryogenic analysis of biliverdin in deuterated DMSO, hence are not presented here.

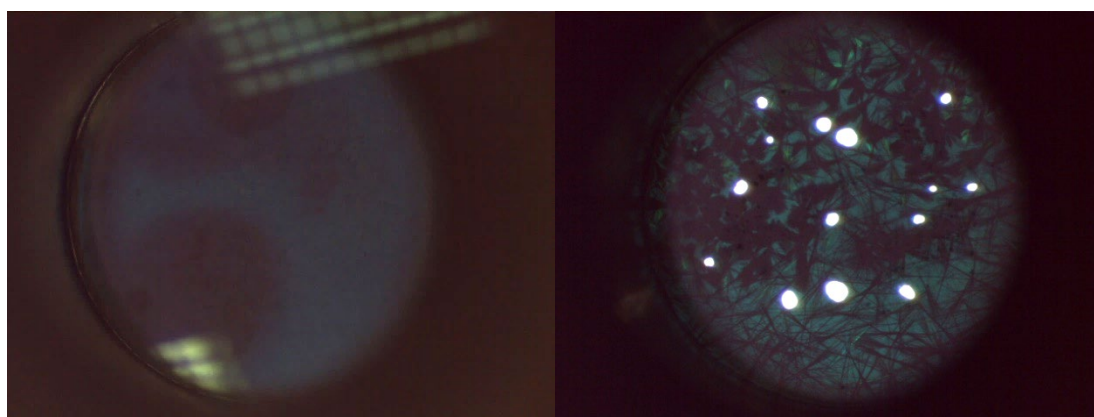


Figure 4-106: Left: Image of biliverdin in DMSO-H₆ (500 mg/mL) in DWLC C using 20 μm spacer, before analysis. Right: Image of biliverdin in DMSO-H₆ (500 mg/mL) in DWLC C using 20 μm spacer, after cryogenic analysis.

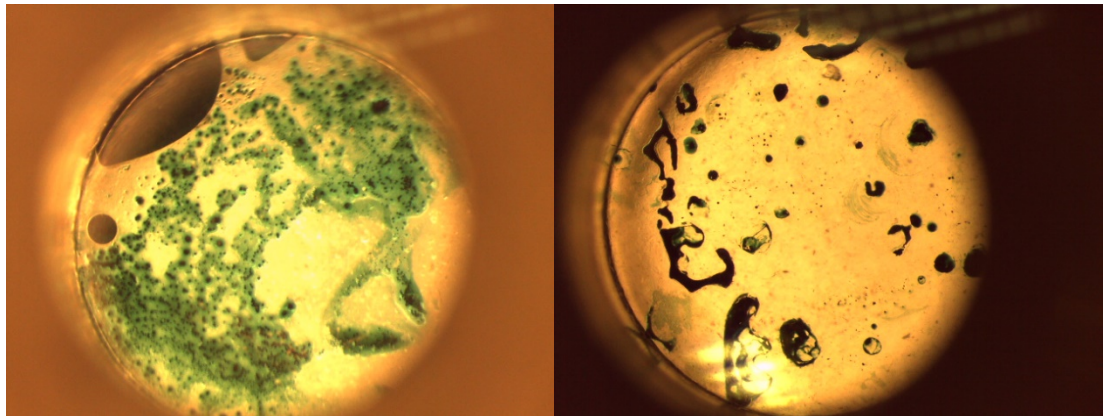


Figure 4-107: Left: Image of assembled DWLC C using 20 μm spacer containing biliverdin in methanol (250 mg/mL), before cryogenic analysis at the Australian Synchrotron using SiBolo detector. Right: Image of assembled DWLC C using 20 μm spacer containing biliverdin in methanol (250 mg/mL), after cryogenic analysis at the Australian Synchrotron using SiBolo detector.

Biliverdin at a concentration of 130 mg/mL in methanol was observed to be inhomogeneous suspensions of sample in solvent alike 250 mg/mL sample.

The biliverdin in paraffin oil was a rough dilution of 10% sample and no discernible peaks were observed spectrally although a large amount of fringing and oscillation was present.

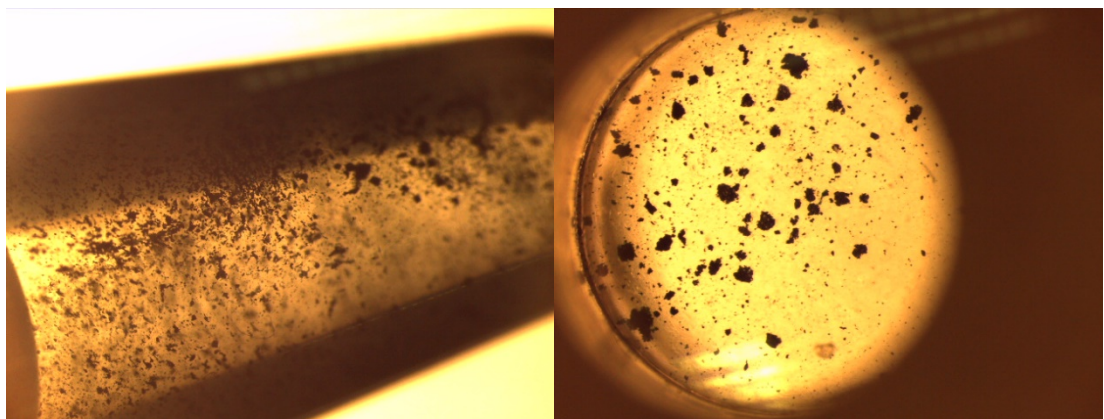


Figure 4-108: Left: Image of biliverdin in paraffin oil preparation in 1.5 mL centrifuge tube. Right: Photograph of assembled DWLC C using 20 μm spacer containing Biliverdin in paraffin oil before analysis at the Australian Synchrotron using SiBolo detector.

4.1.2.2.5 Bilirubin

A broad absorbance is observed at 197 wavenumbers and absorbance increases linearly above 300 wavenumbers in all dilutions with water. Spectra is similar to that of solvent water.

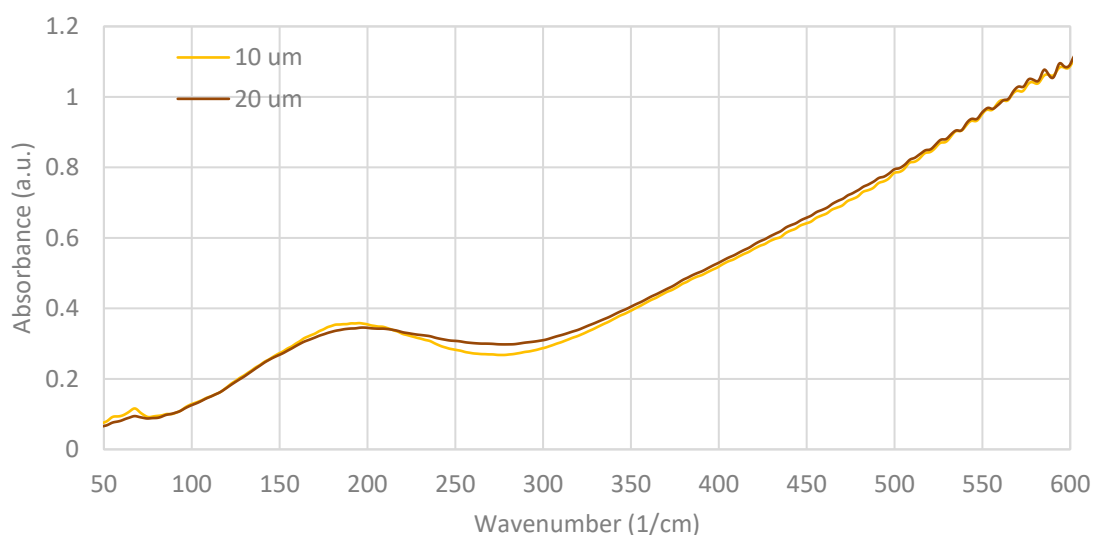


Figure 4-109: FIR overlaid spectra of 0.012 M bilirubin in plasma in DWLC's using various spacers, normalised between 100 and 600 wavenumbers, analysed at the Australian Synchrotron (THz/FIR Beamline) with SiBolo detector and amplitudes of 13500 (10 µm, Cell B) & 6000 (20 µm, Cell B).

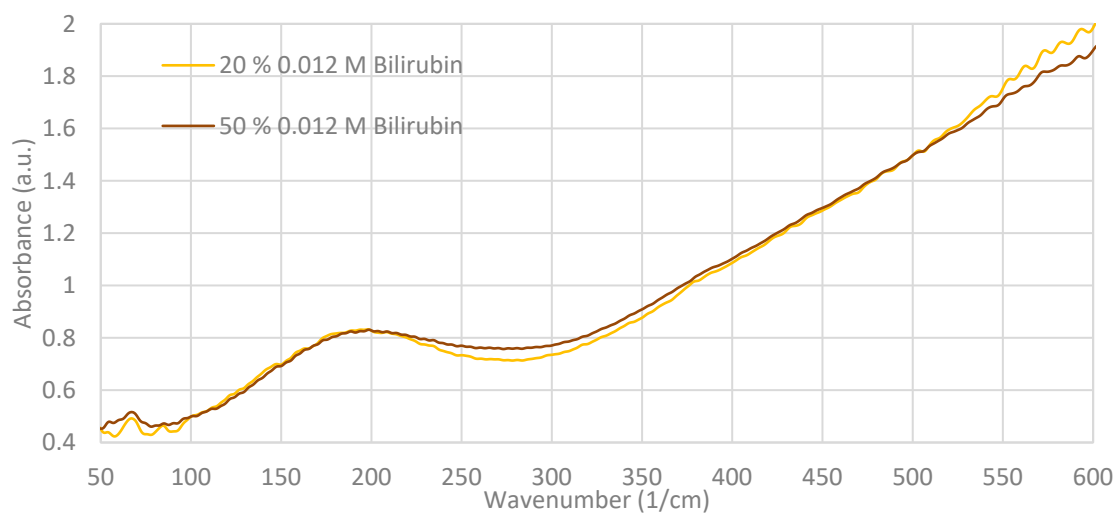


Figure 4-110: FIR overlaid spectra of 0.012 M bilirubin in plasma in DWLC's using 10 µm spacer, normalised between 100 and 500 wavenumbers, analysed at the Australian Synchrotron (THz/FIR Beamline) with a SiBolo detector and amplitudes of 16500 (50%, Cell C) & 12200 (20%, Cell A).

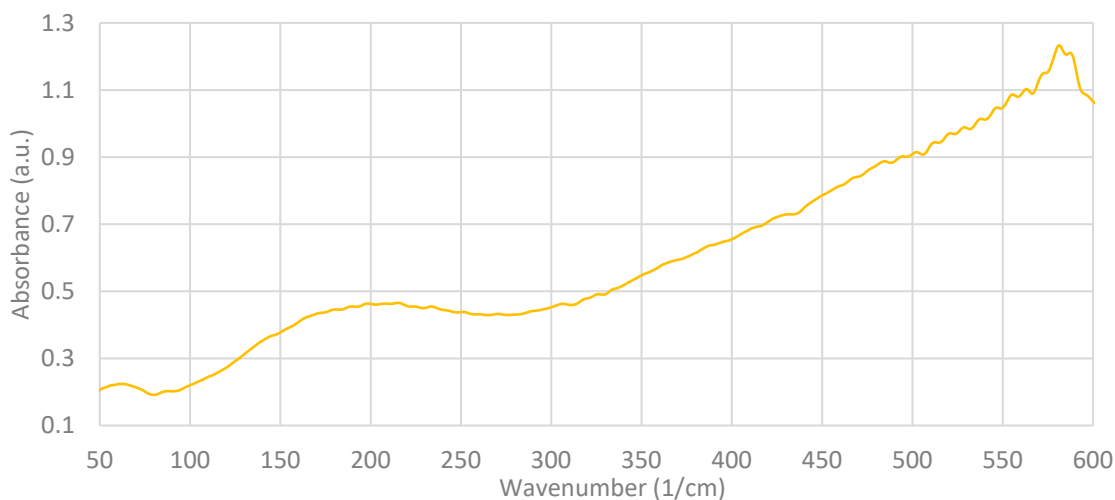


Figure 4-111: FIR spectrum of bilirubin slurry with 0.1 M NaOH (200 mg/mL) in DWLC C using 20 μm spacer, analysed at the Australian Synchrotron (THz/FIR Beamline) with SiBolo detector. Amplitude 6600.

A thicker slurry (higher concentration) of bilirubin in 0.1 M NaOH was prepared to reduce spectral contribution of water and smeared on cracked diamond window liquid cell C (from biliverdin slurry), however spectra exhibited fringing when analysed hence was not processed further.

Particles of bilirubin were observed in the centre of the cell for a 65 mg/mL bilirubin sample preparation. Peaks were observed at 413, 431, 478, 533, 558 and 627 wavenumbers. These were not as distinct when the sample was incubated, although a greater amount of noise is observed.

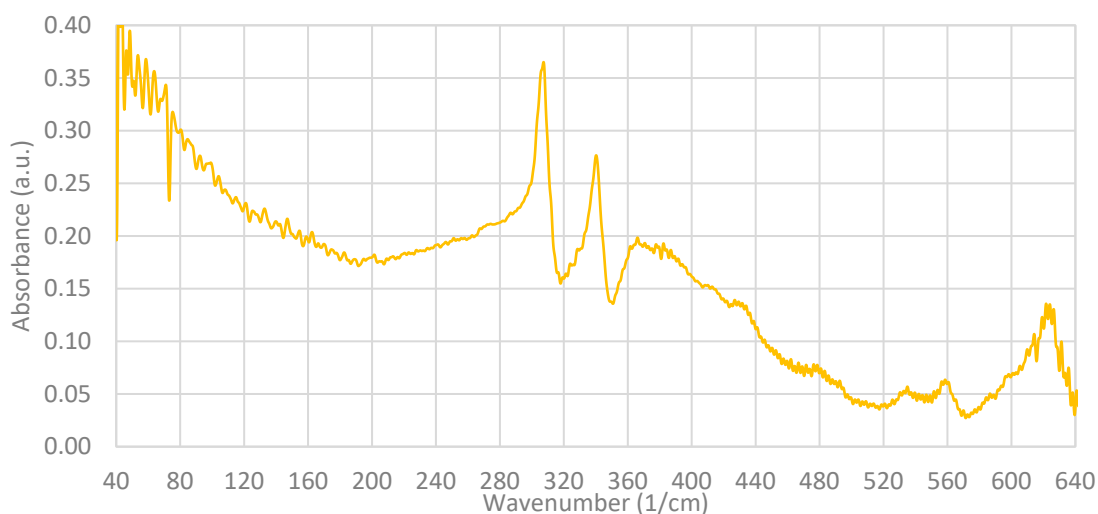


Figure 4-112: FIR spectrum of bilirubin in DMSO- d_6 (65 mg/mL) in DWLC C using 10 μm spacer, analysed at the Australian Synchrotron (THz/FIR Beamline) with SiBolo detector and amplitude of 5500.

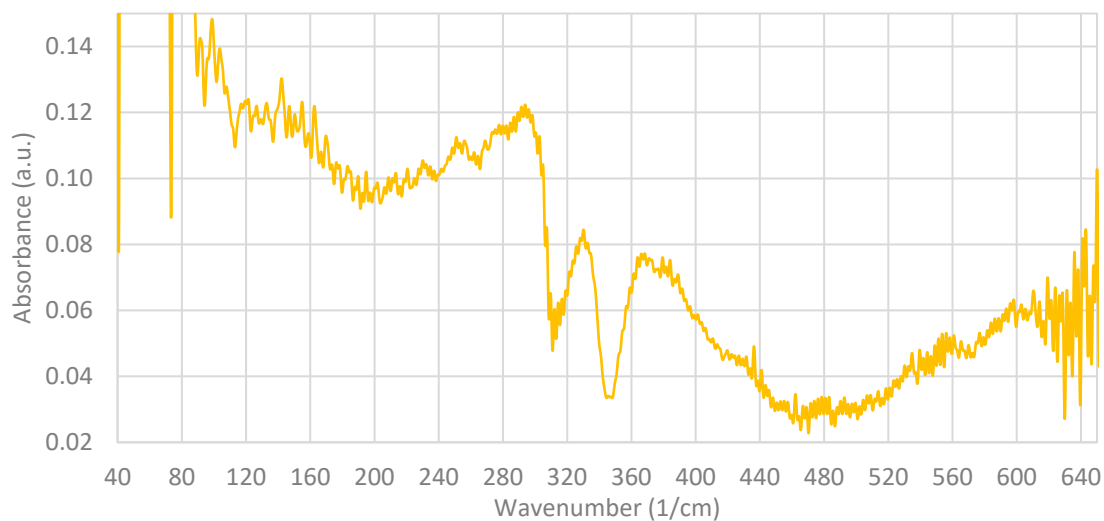


Figure 4-113: FIR spectrum of incubated (40 degrees Celsius water bath) bilirubin in DMSO-d₆ (65 mg/mL) in DWLC C using 10 μm spacer, analysed at the Australian Synchrotron (THz/FIR Beamline) with SiBolo detector and amplitude of 4920.

Double the concentration and pathlength presented distinguishable peaks at 435, 485, 538, 560 and 620 wavenumbers, although some interference is observed. Particles of bilirubin were also observed in the cell. Spectra taken using a 50 μm spacer presented saturated absorbance, hence is not reported here.

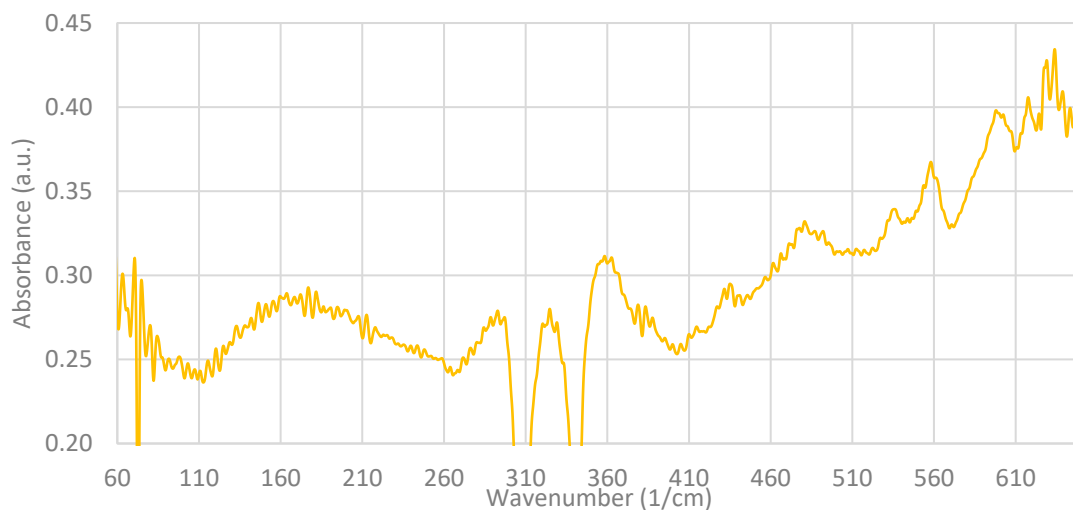


Figure 4-114: FIR spectrum of incubated (40 degrees water bath) bilirubin in DMSO-d₆ (160 mg/mL) in DWLC C using 20 μm spacer, analysed at the Australian Synchrotron (THz/FIR Beamline) with SiBolo detector and amplitude of 5070.

No significant change was observed for the overnight sample, apart from the last run exhibiting noise and fringing. Pressure at beginning of analysis was observed to be higher than pressure before completion of analysis.

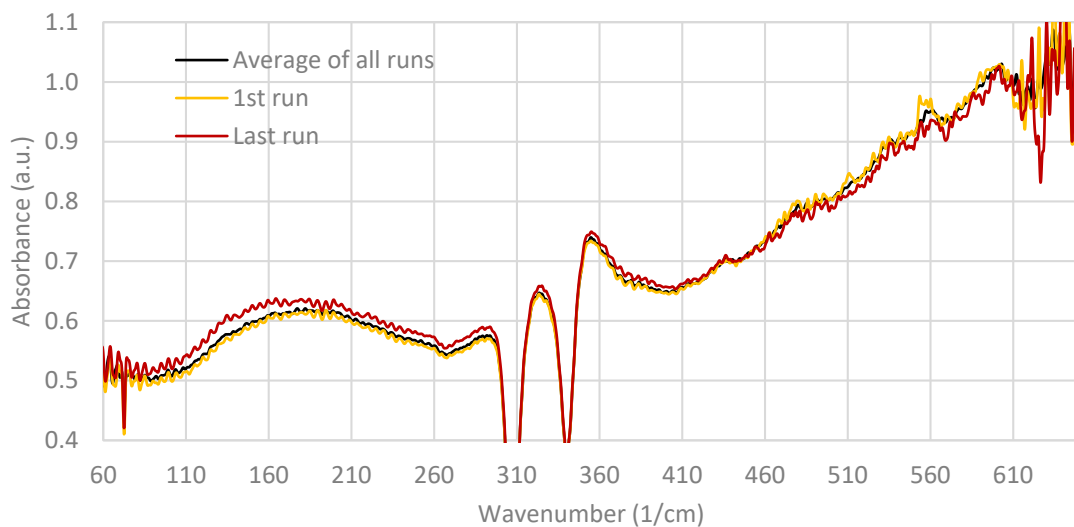


Figure 4-115: FIR overlaid spectra of incubated (40 degrees water bath) bilirubin in DMSO-d₆ (160 mg/mL) in DWLC C using 20 µm spacer, analysed overnight at the Australian Synchrotron (THz/FIR Beamline) with SiBolo detector. Amplitude 4010.

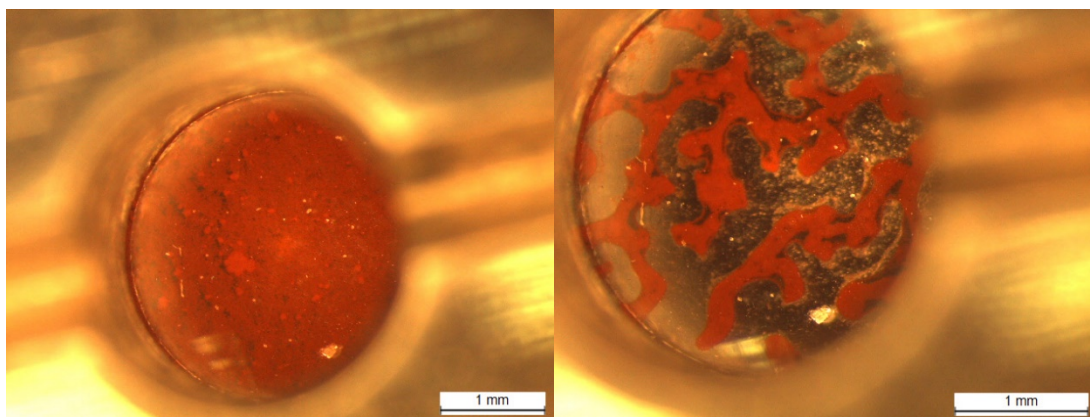


Figure 4-116: Images of incubated (40 degrees water bath) bilirubin sample in DMSO-d₆ (160 mg/mL) in DWLC C using 20 µm spacer, before analysis (left) and after analysis (right) at the Australian Synchrotron (THz/FIR Beamline) with SiBolo detector.

The overnight run was replicated 4 times (the last with adjusted time between measurements of 10 seconds) and showed similar results (see Appendix, Additional FIR Results). Although an isosbestic point was observed at approximately 410 wavenumbers which was reproducible only in the replicates of the same sample over time. This is shown in the below. Spectra in this duplicate changed within the first 14 minutes of analysis.

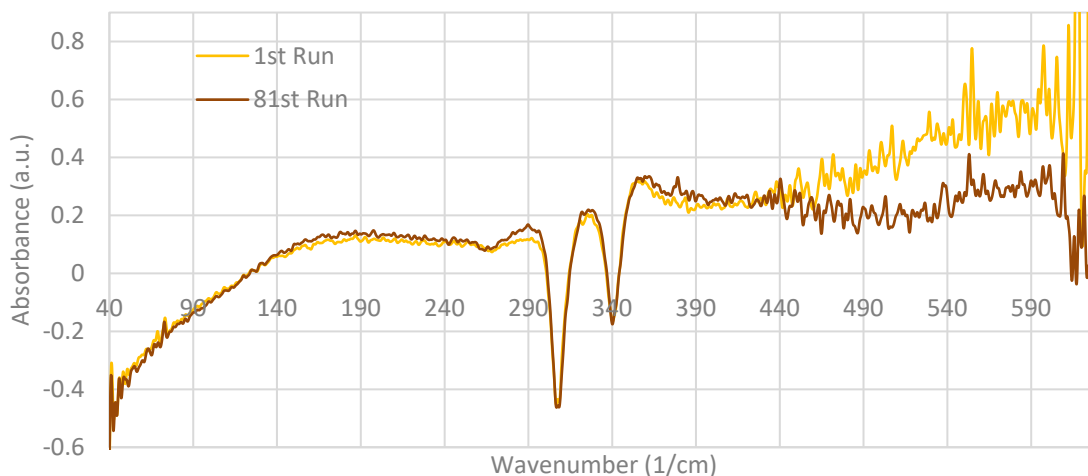


Figure 4-117: FIR overlaid spectra of incubated (40 degrees water bath) bilirubin in DMSO-d₆ (160 mg/mL) in DWLC C using 20 μ m spacer, analysed with 10 sec delay between runs at the Australian Synchrotron (THz/FIR Beamline) with a SiBolo detector.

As chloroform background spectrum was oscillating, beam light alone was used to subtract from bilirubin sample in chloroform spectrum. As a solution, small particles are observed as suspended in solvent. When pipetted onto window of DWLC, chloroform rapidly disappeared, leaving behind these particles.

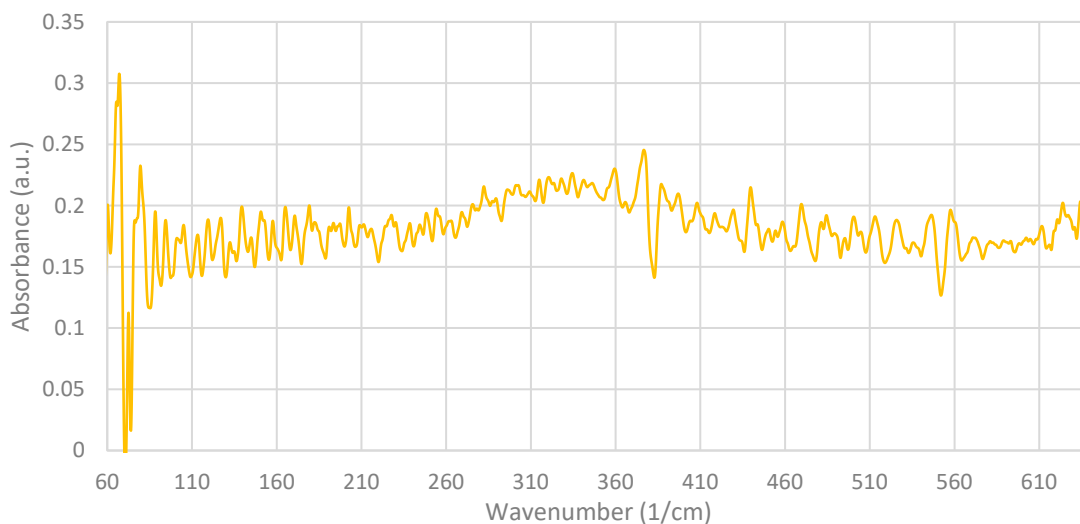


Figure 4-118: FIR spectrum of bilirubin in chloroform (10 mg/mL) in DWLC C with a 20 μ m spacer, analysed at the Australian Synchrotron (THz/FIR Beamline) with SiBolo detector and amplitude of 7030.

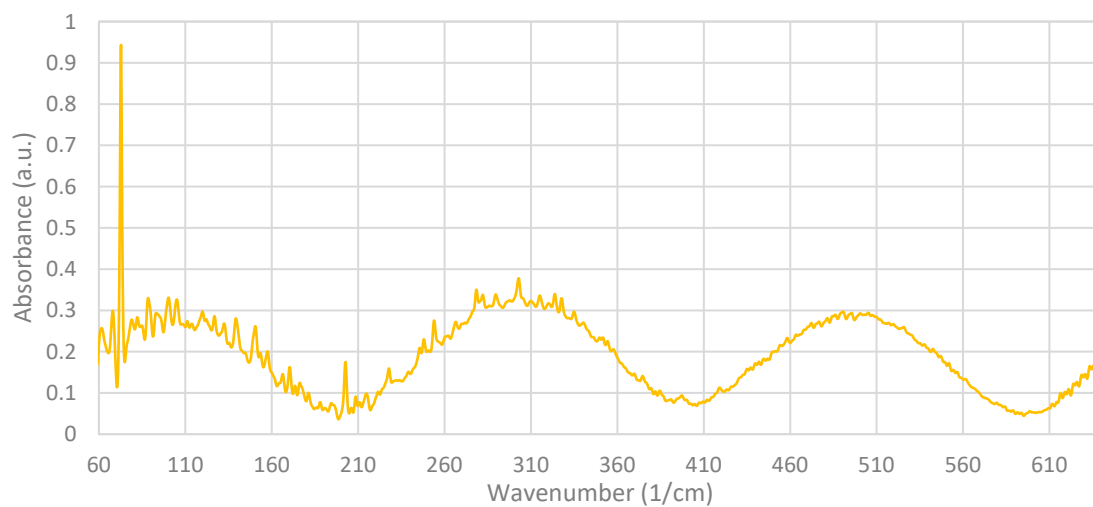


Figure 4-119: FIR spectrum of bilirubin in chloroform (5 mg/mL) in DWLC C with a 20 µm spacer, analysed at the Australian Synchrotron (THz/FIR Beamline) with a SiBolo detector and amplitude of 6690.

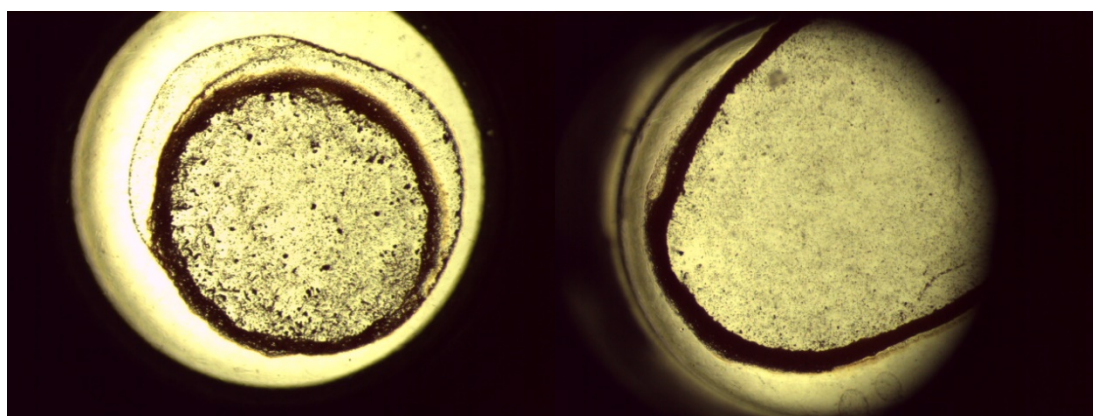


Figure 4-120: Left: Image of assembled DWLC C using 20 µm spacer containing bilirubin in chloroform (10 mg/mL), before analysis at the Australian Synchrotron using SiBolo detector. Right: Image of assembled DWLC C using 20 µm spacer containing bilirubin in chloroform (5 mg/mL), before analysis at the Australian Synchrotron using SiBolo detector.

Bilirubin in ethanol presented similar spectra to samples with chloroform solvent below 400 wavenumbers. Above 400 wavenumbers is non-informative and appears to be the inversion of an ethanol spectrum.

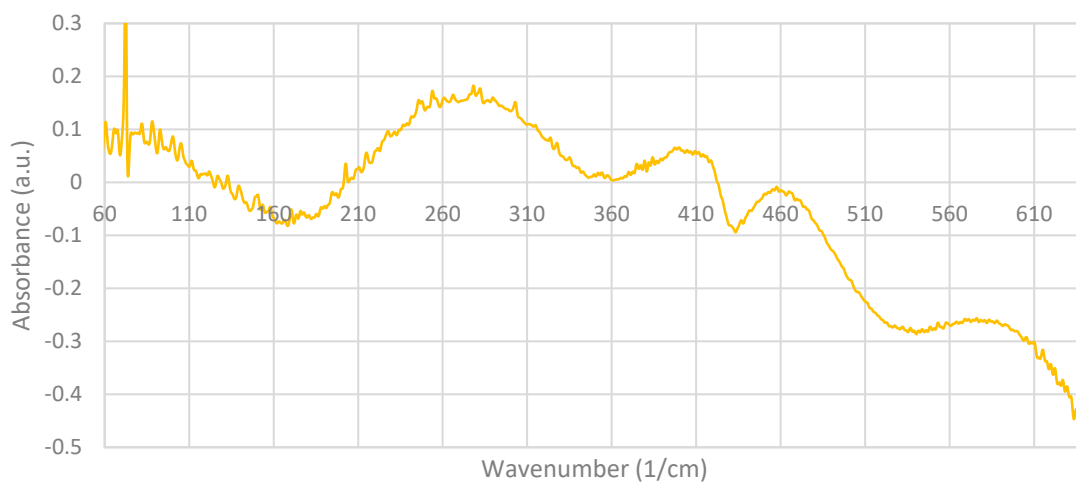


Figure 4-121: FIR spectrum of bilirubin in ethanol (1.45 mg/mL) in DWLC C with a 20 μm spacer, analysed at the Australian Synchrotron (THz/FIR Beamline) with a SiBolo detector and amplitude of 5600.

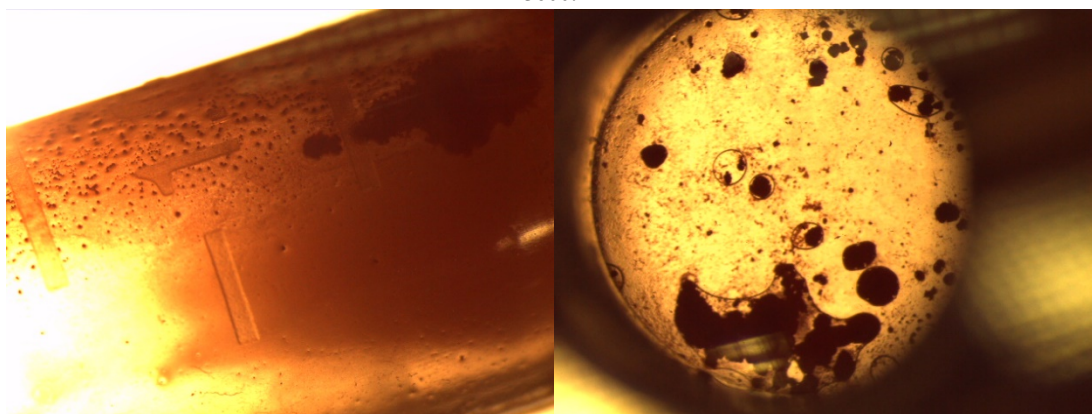


Figure 4-122: Left: Image of bilirubin in ethanol (1.45 mg/mL) preparation in 1.5mL centrifuge tube. Right: Image of assembled DWLC C using 20 μm spacer containing bilirubin in ethanol (1.45 mg/mL), before analysis at the Australian Synchrotron using SiBolo detector.

Observed local areas of suspended sample powder as well as local areas of solvent. This was also observed when methanol and paraffin oil were used as solvents. Bilirubin appeared to have more local particles of powdered sample for methanol samples. After the first cooling cycle of bilirubin in methanol, spectra exhibited large oscillation and did not change, hence the spectra are not presented.

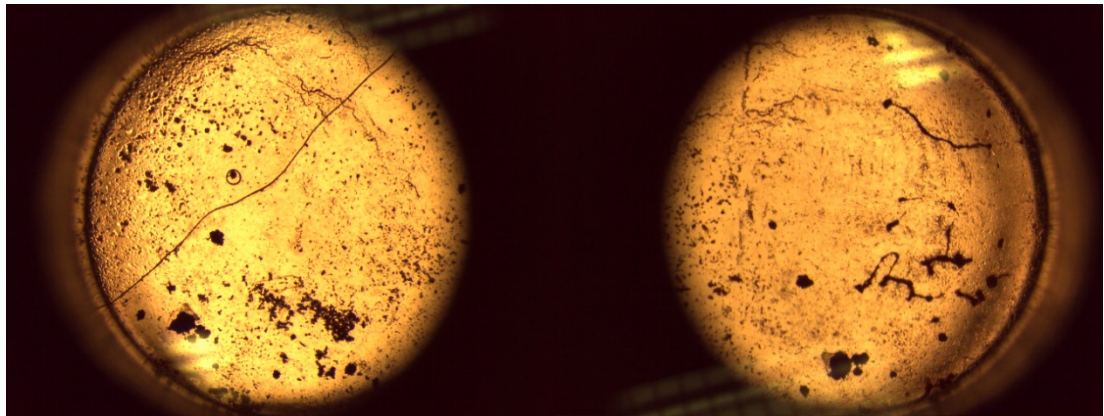


Figure 4-123: Left: Image of assembled DWLC C using 20 μm spacer containing bilirubin in methanol (6.4 mg/mL), before cryogenic analysis at the Australian Synchrotron using SiBolo detector. Right: Image of assembled DWLC C using 20 μm spacer containing bilirubin in methanol (6.4 mg/mL), after cryogenic analysis at the Australian Synchrotron using SiBolo detector.

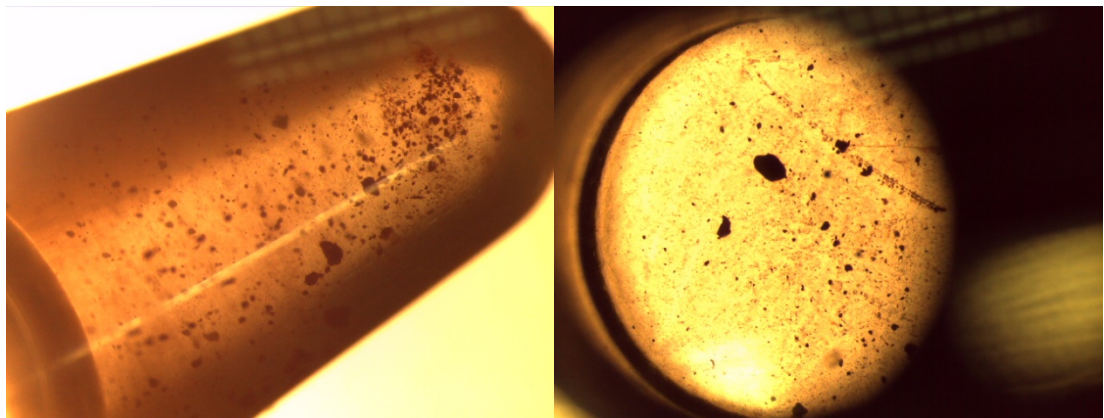


Figure 4-124: Left: Image of bilirubin in paraffin oil preparation in 1.5 mL centrifuge tube. Right: Image of assembled DWLC C using 20 μm spacer containing bilirubin in paraffin oil before analysis at the Australian Synchrotron using SiBolo detector.

Observed some peaks for bilirubin in paraffin oil, hence carried out cryogenic analysis, however large oscillation in spectra was observed hence is not reported here. A large number of bubbles in the DLWC was also observed post-cryogenic analysis.

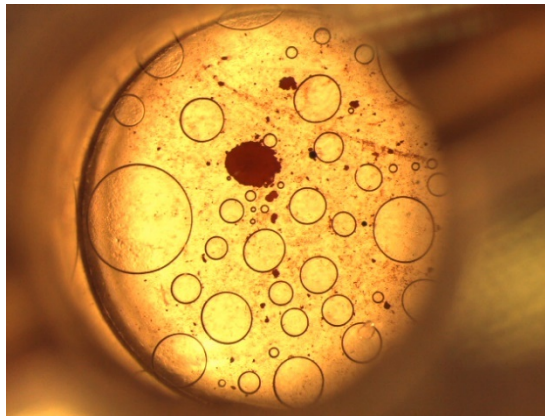


Figure 4-125: Image of assembled DWLC C using 20 μm spacer containing bilirubin in paraffin oil after cryogenic analysis at the Australian Synchrotron using SiBolo detector.

4.1.2.2.6 Bilirubin Conjugate

For a 10 mg/mL dilution, a broad absorbance is observed at 40 and 140 wavenumbers where absorbance decreases steadily after 150 wavenumbers. In a 82.5 mg/mL preparation, spectra is heavily dominated by noise, however a peak at approximately 540 cm^{-1} is noted, although the spectral profile is suspected to be that of water.

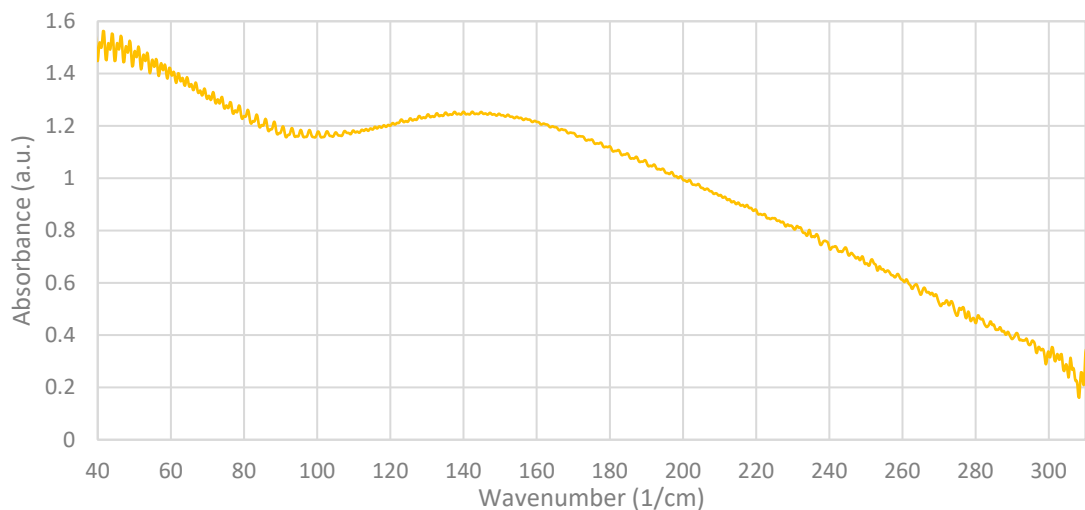


Figure 4-126: FIR spectrum of bilirubin conjugate in water (10 mg/mL) in DWLC C with a 5 μm spacer, analysed at the Australian Synchrotron (THz/FIR Beamline) with SiBolo detector and amplitude of 12100.

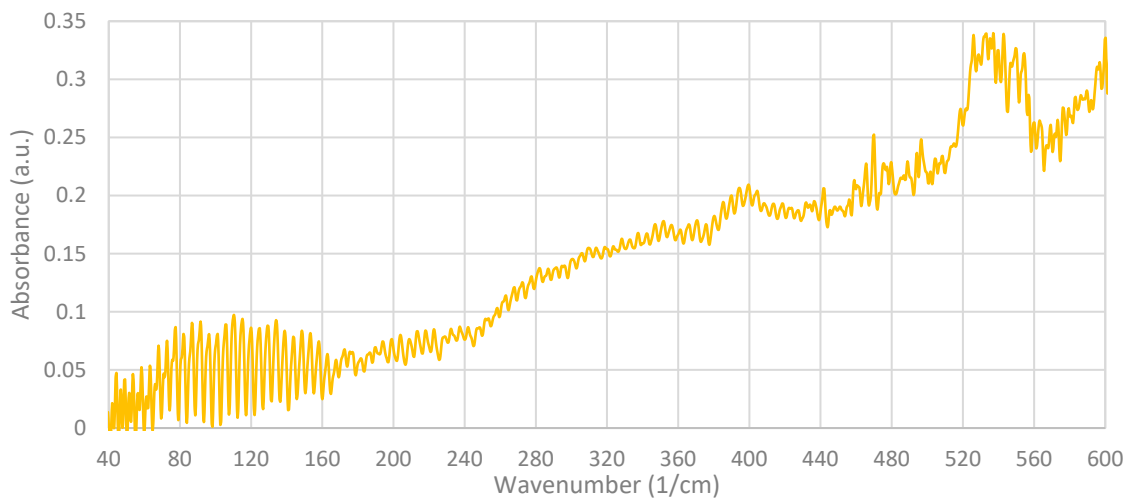


Figure 4-127: FIR spectrum of bilirubin conjugate in blood (82.5 mg/mL) in DWLC C with a 20 µm spacer, analysed at the Australian Synchrotron (THz/FIR Beamline) with SiBolo detector and amplitude of 7000.

For an 800 mg/mL sample, local areas of sample in the DWLC were observed under the microscope prior to analysis. Weak peaks are present at 188, 385, 431, 468 and 530 wavenumbers.

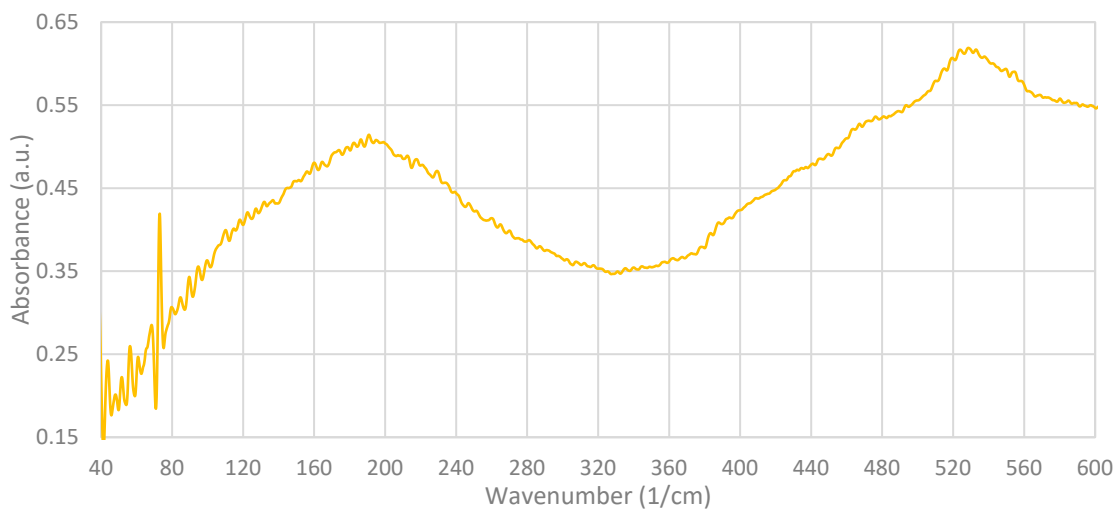


Figure 4-128: FIR spectrum of bilirubin conjugate in blood (800 mg/mL) in DWLC C with a 5 µm spacer, analysed at the Australian Synchrotron (THz/FIR Beamline) with SiBolo detector and amplitude of 9700.

4.2 Reflectance Spectroscopy

4.2.1 Ultraviolet-Visible-Near Infrared (UV-Vis.-NIR)

4.2.1.1 Perkin Elmer UV-Vis.-NIR Spectrophotometer

Samples containing water solvent were damp when placed in the sample compartment for analysis, however when the sample dried (after approximately 1 minute), a slight concavity of the filter paper where the sample was pipetted was observed.

4.2.1.1.1 Solvents

Peaks for water are observed at 1460 and 1951 nm. Notably, there is a slight slope of the baseline. Solvent spectra couldn't be overlaid as PBS solution was analysed with 5 nm intervals whereas water and ethanol were analysed at 1 nm intervals.

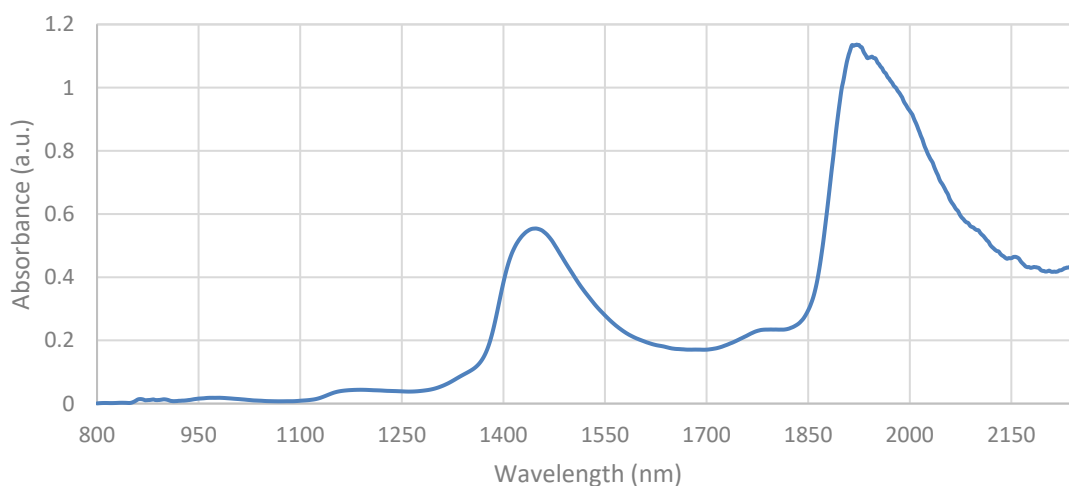


Figure 4-129: Smoothed (width 37) NIR reflectance spectrum of water (reference: filter paper), generated using the UV-Vis.-NIR Lambda 950 Spectrophotometer software at Flinders University. Please refer to the Appendix (Additional FIR Results) for a non-smoothed version.

PBS solution gives a similar spectrum with peaks at approximately 1455 & 1955 nm. Spectral data past 1850 nm exhibits a large amount of noise. Sloping baseline as solvent dries, seeming instrument scans from large to small wavelengths.

4.2.1.1.2 Blood

4.2.1.1.2.1 OXYHAEMOGLOBIN

Spotted blood on filter paper seeps through the first filter paper layer and outwards. Neat blood that was previously refrigerated produces saturation of oxyhaemoglobin Soret peak at approximately 400 nm confirming porphyrin presence. Other oxyhaemoglobin peaks are observed at 545 and 575 nm. The NIR region exhibits regular oscillating noise, however appears similar to that of water observed above.



Figure 4-130: UV-Vis.-NIR reflectance spectrum of previously refrigerated neat sheep's blood (reference: centrifuged serum), analysed using a UV-Vis.-NIR Lambda 950 Spectrophotometer at Flinders University.

Smoothing was applied to the NIR region providing clearer peaks.

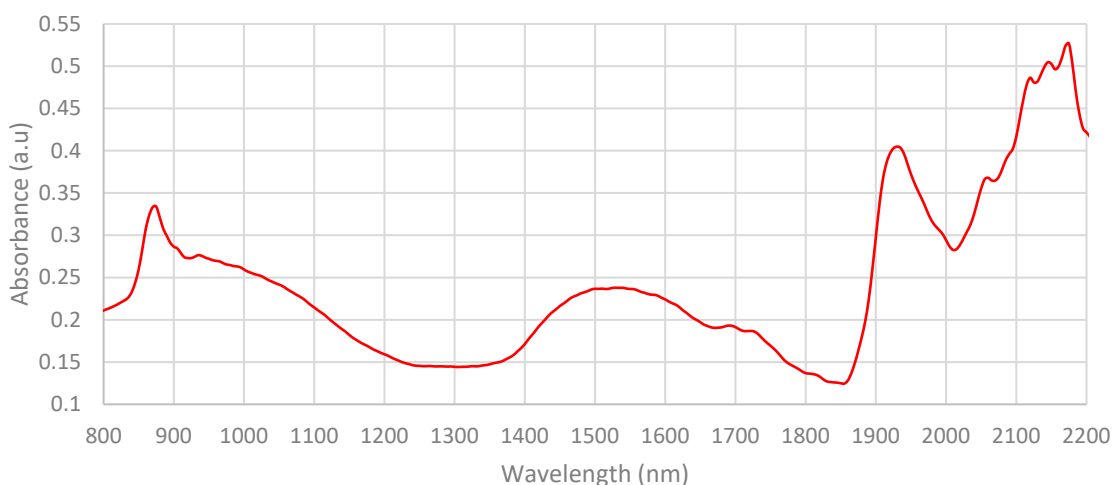


Figure 4-131: Smoothed (width 13) NIR reflectance spectrum of previously refrigerated neat sheep's blood (reference: centrifuged serum), generated using the UV-Vis.-NIR Lambda 950 Spectrophotometer software at Flinders University.

Observed Peaks (nm)	Characterisation
950	Broad, -CH ₂ [117]
1540 (1695 & 1730 shoulder peaks)	Broad, shoulder peaks may be due to contributing CH, -CH ₂ and -CH ₃ functionality [117, 120]
1930	CONH ₂ , R-CO ₂ -R [117]
2065, 2130, 2415, 2170	-CONH ₂ , R-OH, R-NH ₂ , C-C, or saturation of one large absorption peak due to H ₂ O, C-H [117]

Table 4-4: Characterisation designations to observed peaks for NIR analysis of previously refrigerated neat sheep's blood, analysed at Flinders University.

Frozen neat sheep's blood received on 28 November 2013 from the Forensic Science Centre of South Australia (FSSA) produced spectra containing oxyhaemoglobin peaks at 414, 541 and 576 nm, as well as methaemoglobin absorption at 633 nm. This was used for methaemoglobin preparations.

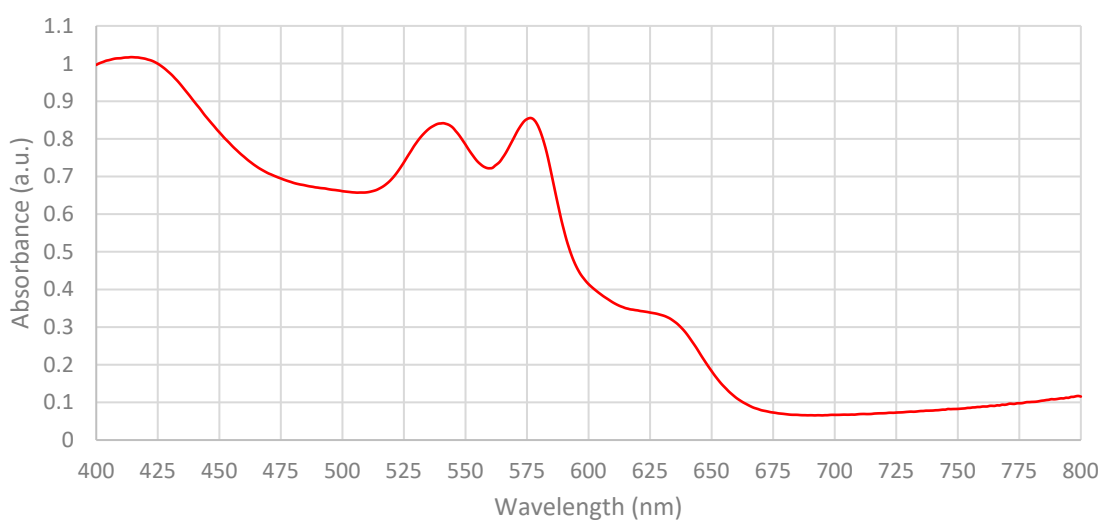


Figure 4-132: UV-Vis. reflectance spectrum of previously frozen neat sheep's blood received on 28 Nov. 2013 from FSSA, analysed on 29/11/2013 using a UV-Vis.-NIR Lambda 950 Spectrophotometer at Flinders University.

Defibrinated sheep's blood is a darker red colouration in comparison to ACD and LiHep blood and defibrinated blood peaks appear to saturate the detector. The solet peak is dissimilar between the three types; 449 nm for defibrinated blood, 441 nm for ACD blood and 431 nm for LiHep blood. Oxyhaemoglobin peaks at 540 and 575 nm are the same between the different blood types. NIR spectra appear to contain the spectral profile of water as observed earlier.

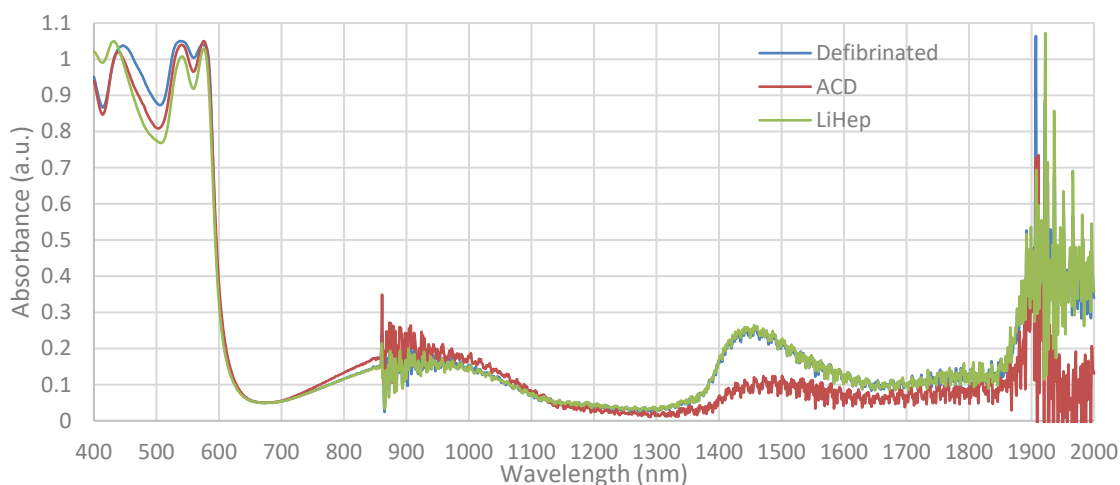


Figure 4-133: UV-Vis.-NIR normalised reflectance spectra of sheep's blood types (defibrinated, contains acid citrate dextrose or contains lithium heparin), analysed using a UV-Vis.-NIR Lambda 950 Spectrophotometer at Flinders University.

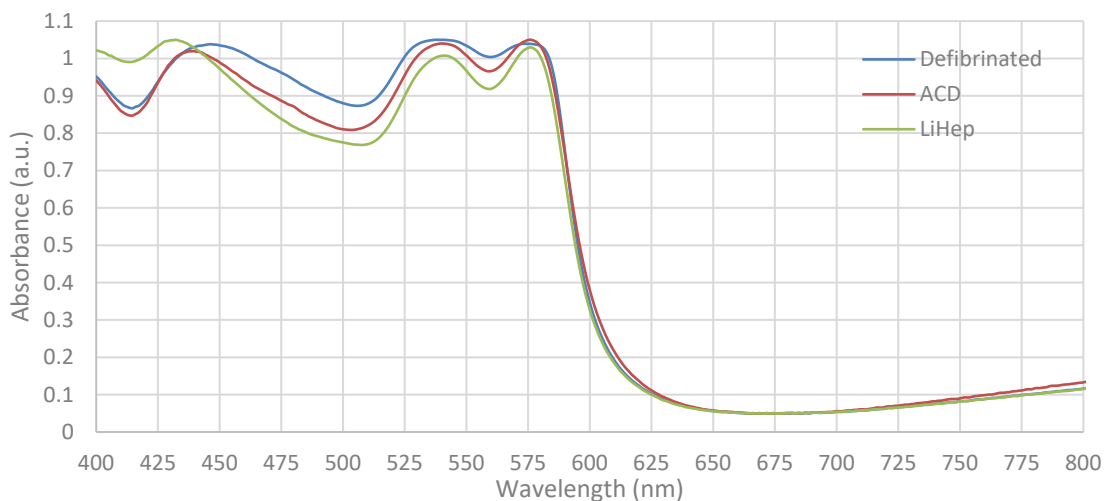


Figure 4-134: UV-Vis. normalised reflectance spectra of sheep's blood types (defibrinated, contains acid citrate dextrose or contains lithium heparin), analysed using a UV-Vis.-NIR Lambda 950 Spectrophotometer at Flinders University.

Analysis of blood drying over time was duplicated and provided in the Appendix (Additional UV-Vis.-NIR Results). It is noted that each acquisition run was approximately 1.5 minutes.

There is an overall decrease in absorbance of the two characteristic oxyhaemoglobin peaks at 540 nm and 577 nm by a factor of at least 1 a.u. There is also an increase in absorbance at approximately 630 nm, which takes definition within 6 hours of analysis. The trough between 540 nm and 577 nm shallows and the solet peak shifts to higher energy wavelengths.

Run	Humidity (%)	Outside Temp. (Degrees Celsius)	Lab Temp. (Degrees Celsius)
1 (0 min)	39	23.4	22
41 (342 mins)	32	25.4	23
42 (4284 mins)	73	19.9	20
43 (7359 mins)	58	21.6	21
44 (40 days)	51	18.6	21

Table 4-5: Humidity and temperature data during analysis of blood as it dries, taken from weatherzone.com with analysis commencing on 14 March 2014.

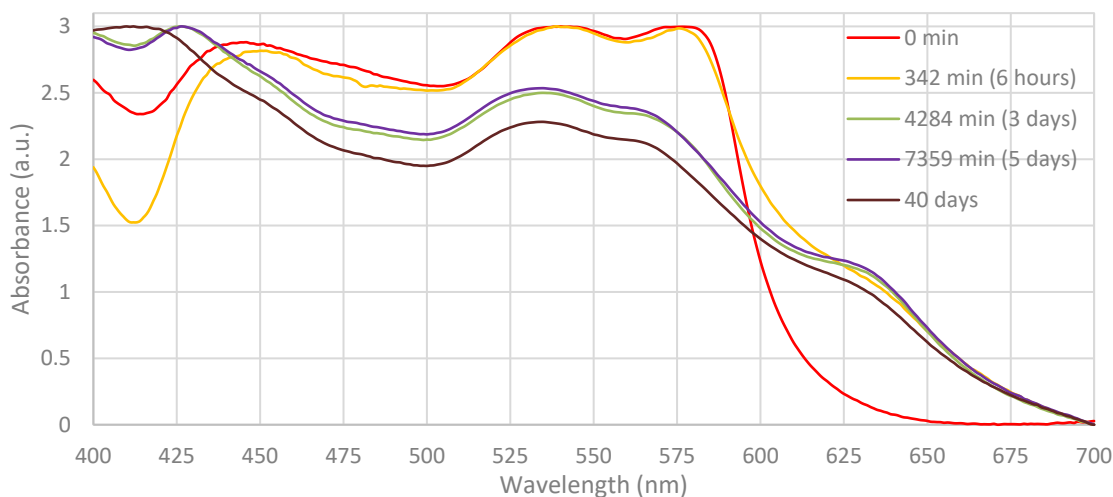


Figure 4-135: UV-Vis. normalised reflectance spectra of defibrinated sheep's blood as it dries, analysed using a UV-Vis.-NIR Lambda 950 Spectrophotometer at Flinders University.

When the 40-day old sample was resuspended in water, the blood mark circumference was observed to travel further outwards into the filter paper than the original spot.

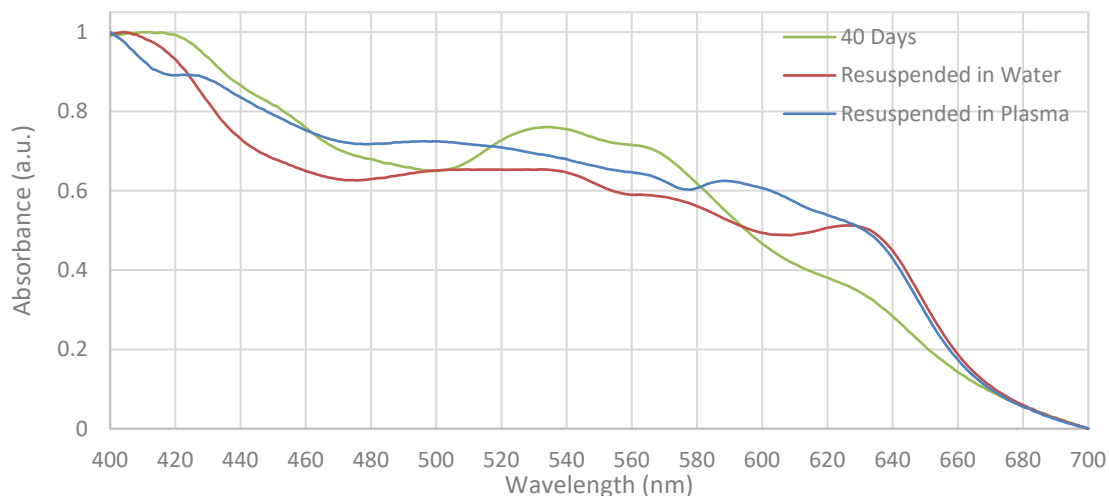


Figure 4-136: UV-Vis. normalised reflectance spectra of dried defibrinated sheep's blood resuspended in water then once dry resuspended in plasma (16 drops), analysed using a UV-Vis.-NIR Lambda 950 Spectrophotometer at Flinders University.

When resuspended in water then plasma, the 630 nm peak intensely re-emerges, and a 500 nm peak becomes more prominent. The 540 and 577 nm peaks decrease in intensity, shifting to 534 and 564 nm with water. The 540 and 577 nm peaks are not distinct with plasma, however a peak at 590 nm develops. Resuspending the dried droplet in water was difficult due to the increased surface tension caused by the dried blood on the filter paper.

The peak at 630 nm was formed at similar time intervals in all types of blood.

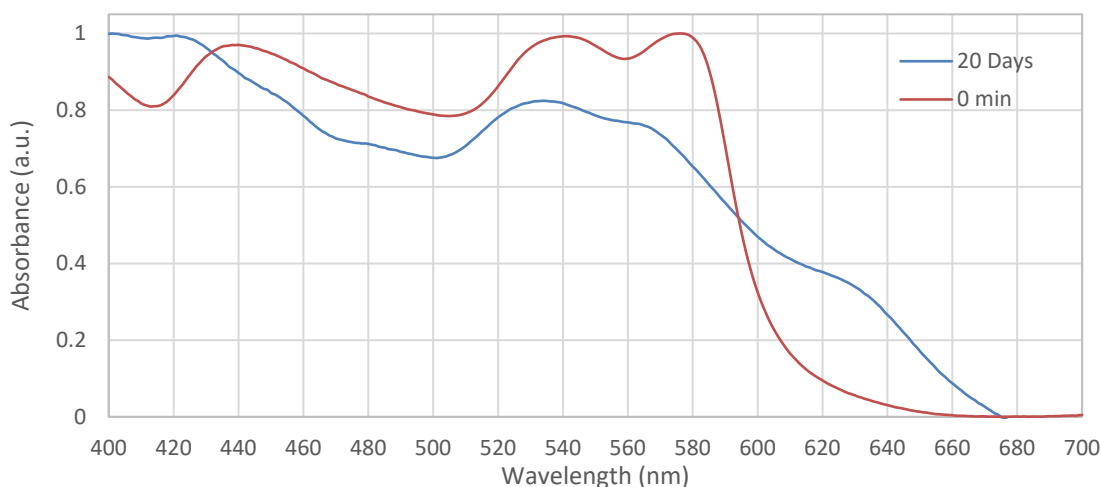


Figure 4-137: UV-Vis. normalised reflectance spectra of sheep's blood containing lithium heparin as it dries, analysed using a UV-Vis.-NIR Lambda 950 Spectrophotometer at Flinders University. At zero minutes, humidity was 38-51% & temperature in the lab was 16 degrees Celsius. After 20 days, humidity was 84% & temperature in the lab was 16 degrees Celsius.

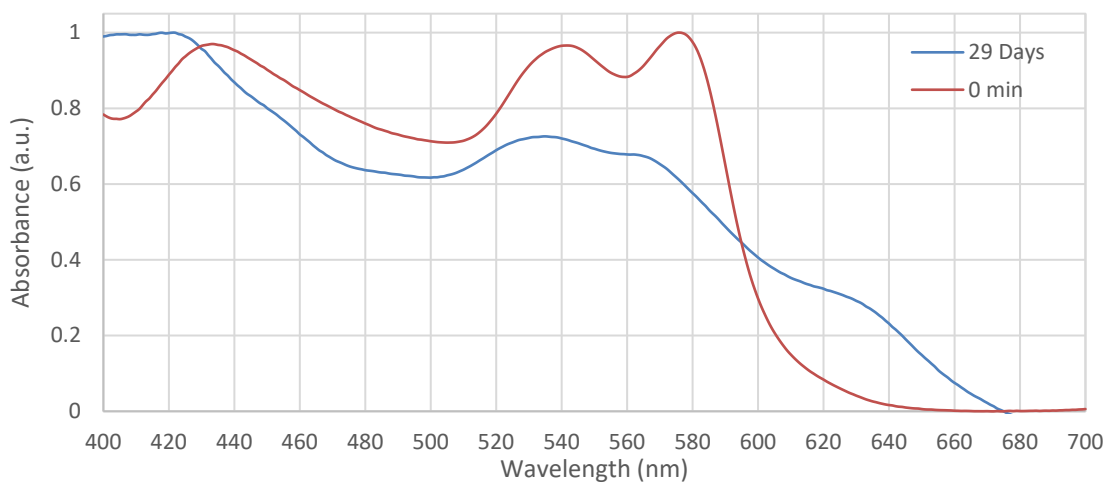


Figure 4-138: UV-Vis. normalised reflectance spectra of sheep's blood containing acid citrate dextrose as it dries, analysed using a UV-Vis.-NIR Lambda 950 Spectrophotometer at Flinders University. At zero minutes, humidity was 30-35% & temperature in the lab was 24 degrees Celsius. After 29 days, humidity was 38% and temperature in the lab was 16 degrees Celsius.

4.2.1.1.2.2 METHAEMOGLOBIN

Solutions required agitation to dissolve sodium nitrite additions. When sodium nitrite was added to the blood samples, the solution exhibited an immediate colour change from red to burgundy-brown.

The 411 nm peak is still intact, however the only other peaks detected are at 535 and 364 nm.

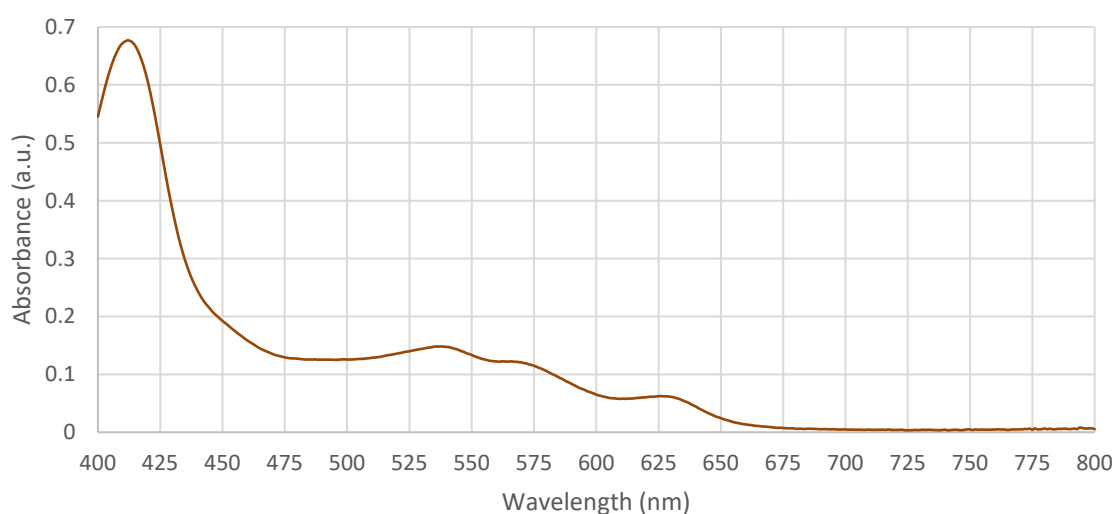


Figure 4-139: UV-Vis. reflectance spectrum of methaemoglobin preparation from defibrinated sheep's blood (100 μ L blood, 1 mL PBS & 294.1 mg sodium nitrite), analysed using a UV-Vis.-NIR Lambda 950 Spectrophotometer at Flinders University.

When attempted in filtered sheep blood plasma, characteristic oxyhaemoglobin peaks shifted slightly to the left.

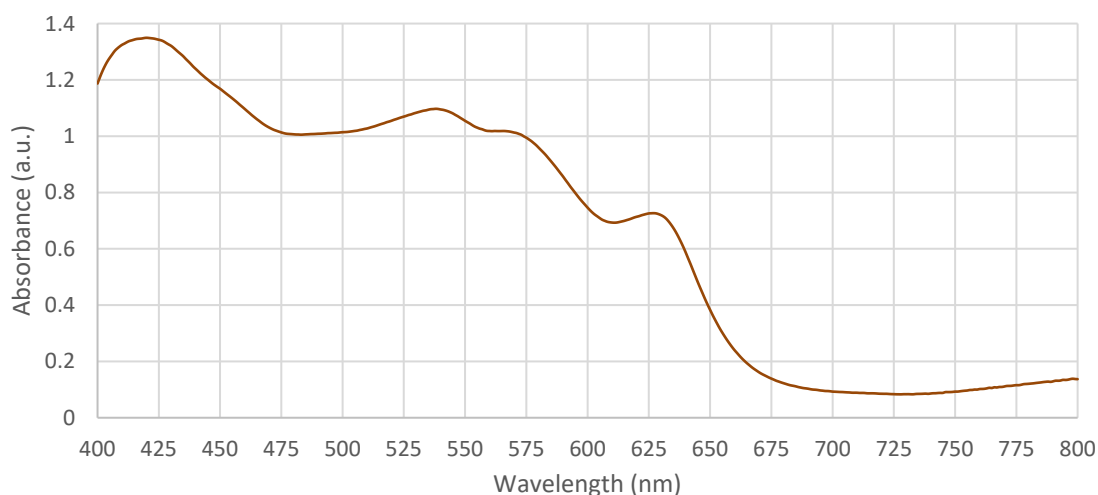


Figure 4-140: UV-Vis. reflectance spectrum of methaemoglobin preparation from defibrinated sheep's blood (300 μ L blood, 1 mL filtered sheep blood plasma & 586.4 mg sodium nitrite), analysed using a UV-Vis.-NIR Lambda 950 Spectrophotometer at Flinders University.

Methaemoglobin was also attempted in blood containing acid citrate dextrose and lithium heparin, however produced similar results and is not reported here (see Appendix, Additional UV-Vis.-NIR Results). It is noted that when sodium nitrite was added to blood containing ACD and LiHep in PBS and swirled, a fine, white precipitate formed in solution (less in LiHep blood sample).

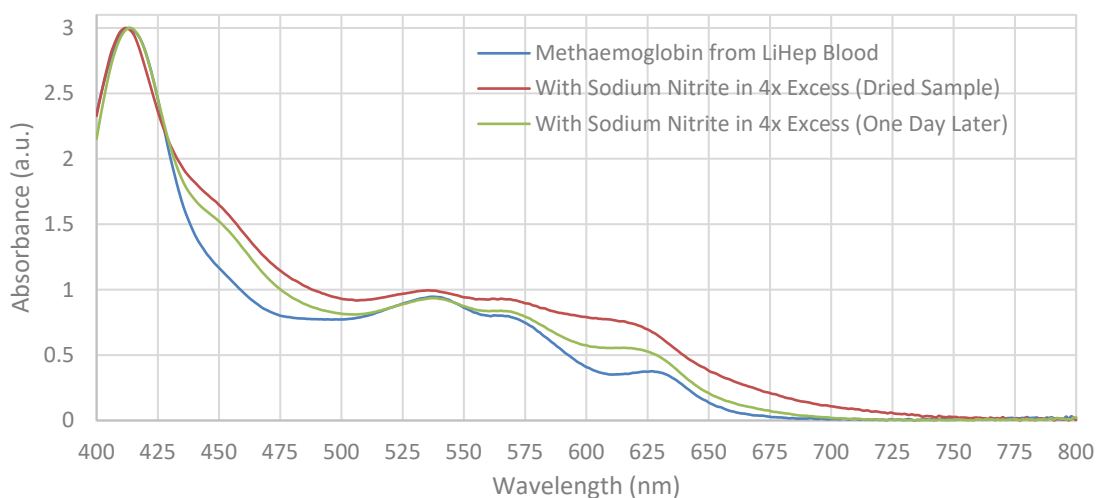


Figure 4-141: UV-Vis. reflectance spectrum of methaemoglobin preparation from sheep's blood containing LiHep (300 μ L blood, 1 mL filtered sheep blood plasma & sodium nitrite addition in a 4:1 with blood ratio by weight), analysed using a UV-Vis.-NIR Lambda 950 Spectrophotometer at Flinders University.

4.2.1.1.3 Biliverdin

Solutions prepared appeared transparent green to dark green in PBS preparations. A broad peak is observed at 665 nm.



Figure 4-142: Biliverdin at 2.28 mg/mL in PBS (volumetric flask), diluted in PBS (beaker) and a reflectance sample of the 2.28 mg/mL biliverdin in PBS solution (circular filter paper).

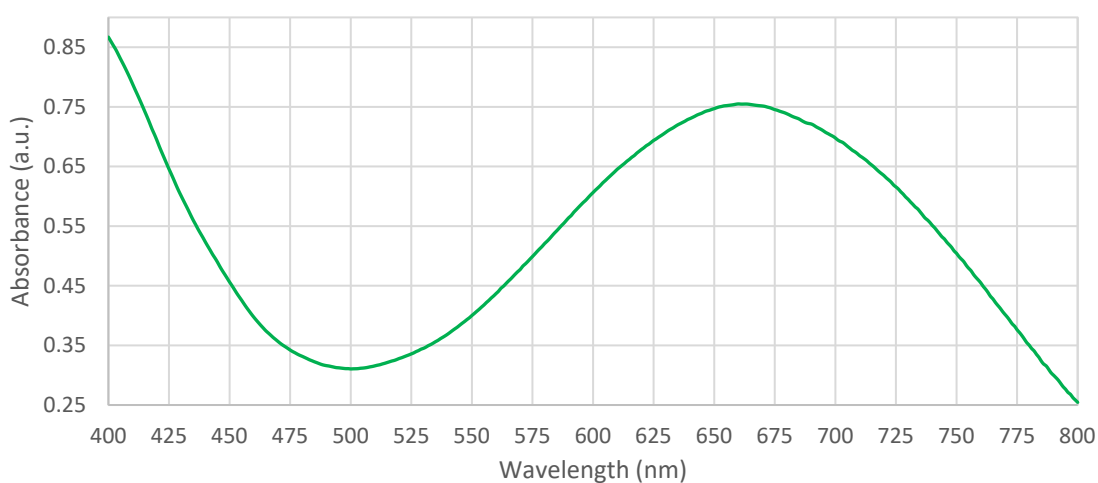


Figure 4-143: UV-Vis. reflectance spectrum of biliverdin in PBS preparation (2.28 mg/mL), analysed using a UV-Vis.-NIR Lambda 950 Spectrophotometer at Flinders University.

Diluted biliverdin exhibits a shifted peak at approximately 650 nm, with greater noise. The NIR spectral profile is similar to that of water observed earlier.

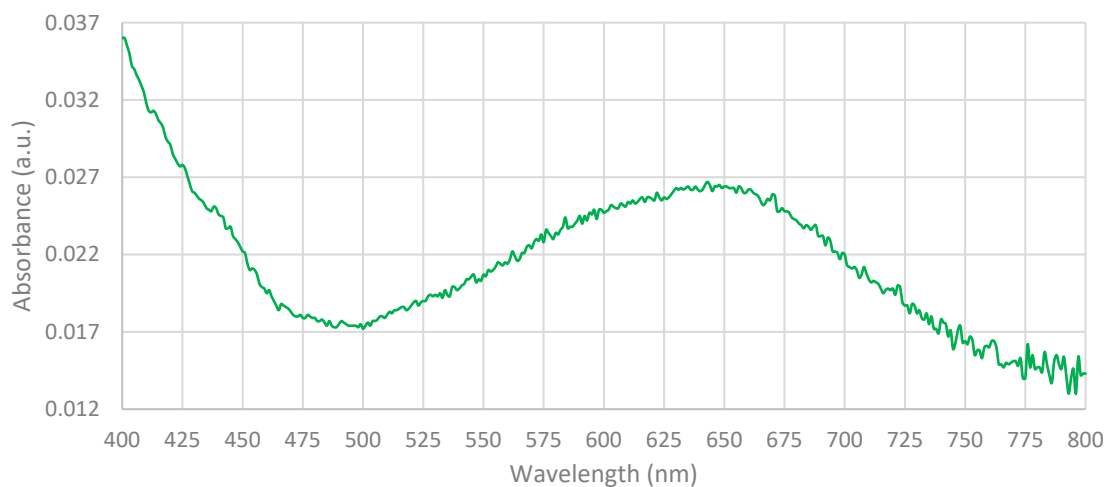


Figure 4-144: UV-Vis. reflectance spectrum of dilute biliverdin in PBS preparation (1.14 mg/mL), analysed using a UV-Vis.-NIR Lambda 950 Spectrophotometer at Flinders University.

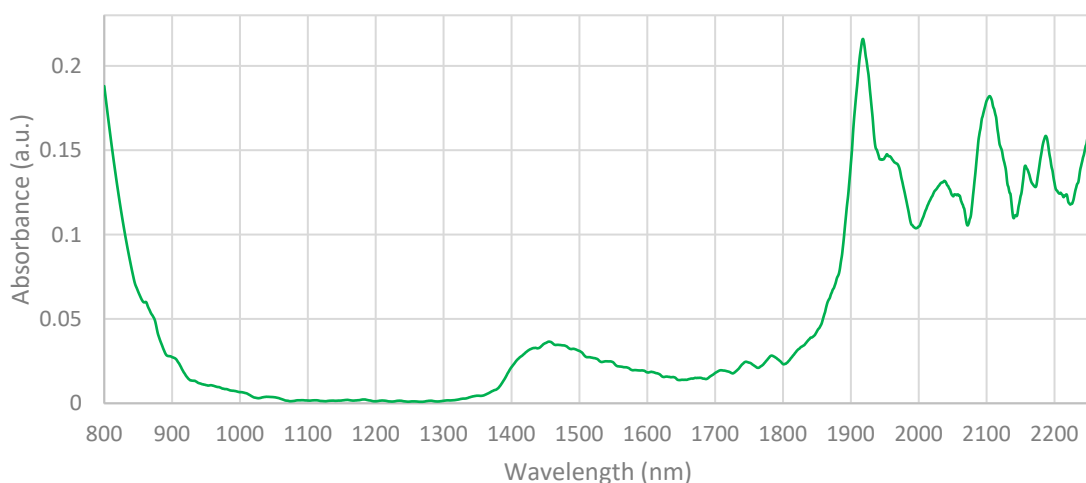


Figure 4-145: Smoothed (width 49) NIR reflectance spectrum of biliverdin in PBS preparation (2.28 mg/mL), generated using a UV-Vis.-NIR Lambda 950 Spectrophotometer software at Flinders University.

4.2.1.1.4 Bilirubin

Bilirubin pH shifted solution preparation is a deep red colour and opaque. When the last few drops of acid were added, bilirubin fell out of solution before slowly re-dissolving with agitation. Resulting solution is red-brown and opaque, containing a small amount of particulate bilirubin that has fallen out of solution at the bottom of the flask. Spectrum exhibits a sloping baseline between 400 and 575 nm with a peak observed at approximately 434 nm.

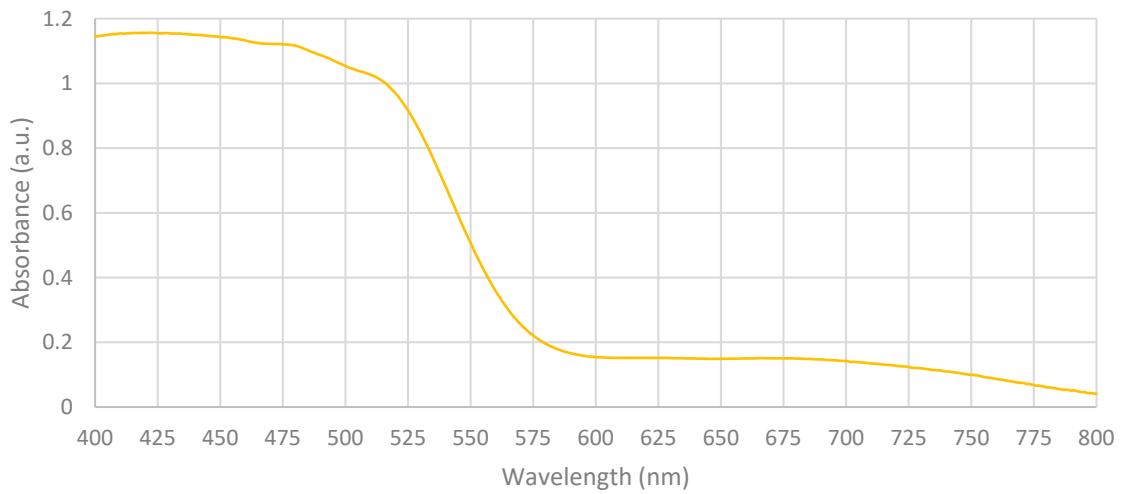


Figure 4-146: UV-Vis. reflectance spectrum of bilirubin in pH shifted preparation in PBS (1.2×10^{-2} M, expected concentration in blood), analysed using a UV-Vis.-NIR Lambda 950 Spectrophotometer at Flinders University.

Bilirubin in sheep blood solution is particulate and over time (1-2 days) bilirubin precipitated. Analysis of the prepared solution gave a peak at 470 nm. The NIR spectral profile is similar to that of water observed earlier.

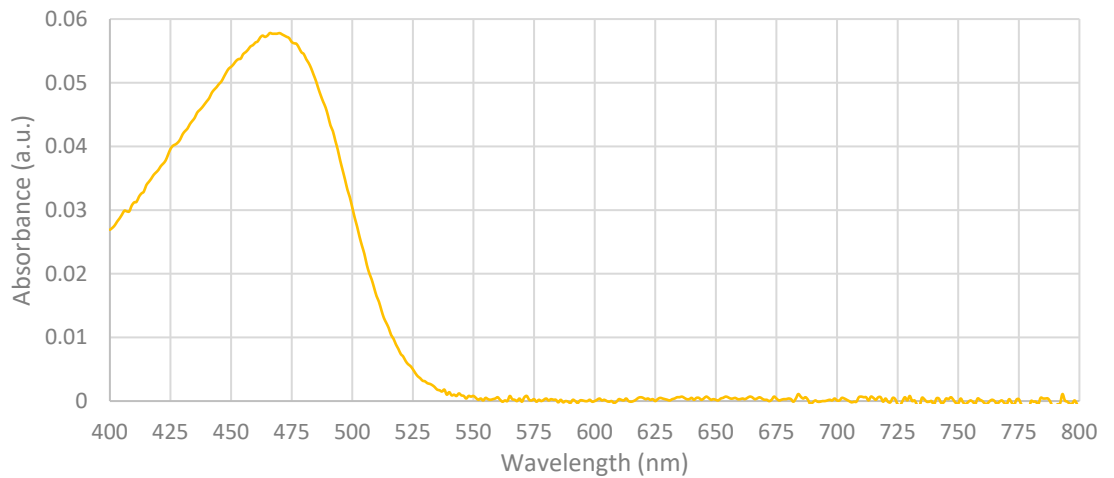


Figure 4-147: UV-Vis.-NIR reflectance spectrum of bilirubin in pH shifted preparation in sheep's blood (1.9×10^{-2} M), analysed using a UV-Vis.-NIR Lambda 950 Spectrophotometer at Flinders University.

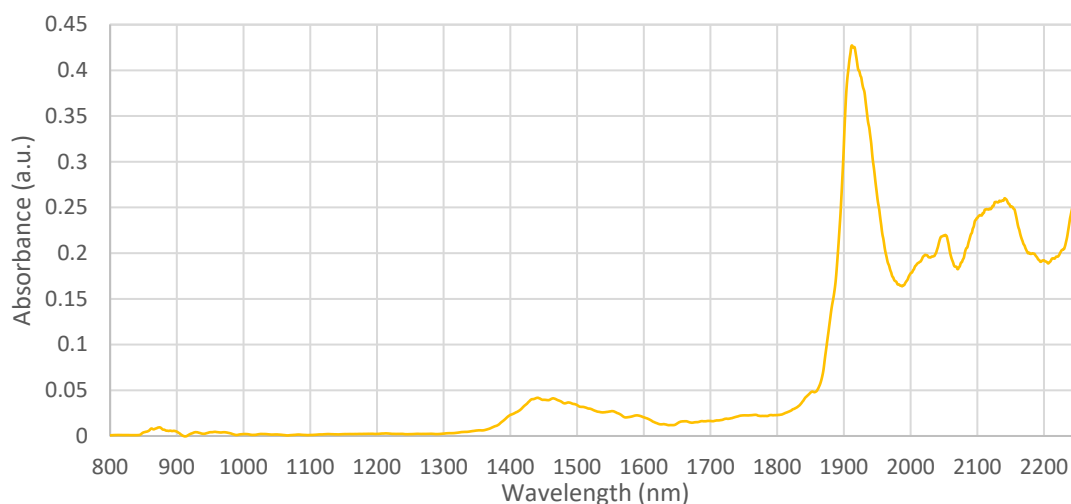


Figure 4-148: Smoothed (width 49) NIR reflectance spectrum of bilirubin in pH shifted preparation in sheep's blood (1.9×10^{-2} M), analysed using a UV-Vis.-NIR Lambda 950 Spectrophotometer at Flinders University.

Observed Peaks (nm)	Characterisation
1470	H ₂ O, -OH, -CONH-, -CONH ₂ [120, 121]
1930	H ₂ O, -OH, -COO-, -CONH ₂ [120, 121]

Table 4-6: Characterisation designations to observed peaks for NIR analysis of bilirubin in blood, analysed at Flinders University.

4.2.1.1.5 Ferritin

Ferritin solutions at the concentration 1.0×10^{-4} mg/mL were colourless and transparent, although increasing concentrations of ferritins (0.88 and 1.76 mg/mL) demonstrate an increase in apparent yellow-brown colour.

The reflectance spectrum in the UV-Vis. region shows a broad sloping absorbance from 400 to 650 nm, after which absorbance plateaus. Two small absorbance signals are detectable at 481 and 515 nm. Ferritin at concentration 0.88 mg/mL produces concave spectra and at concentration 1.0×10^{-4} mg/mL, exhibits a large amount of noise.

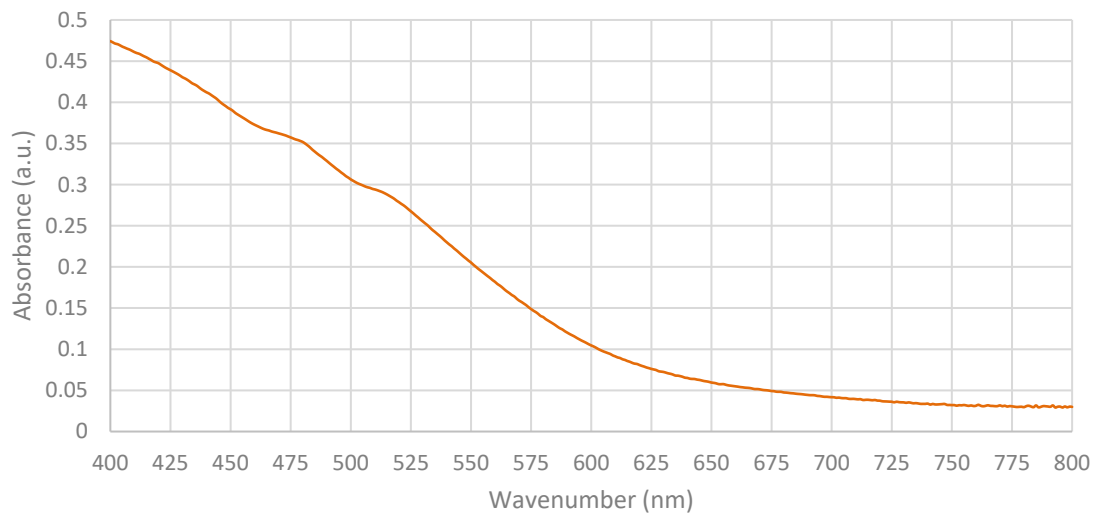


Figure 4-149: UV-Vis. reflectance spectrum of ferritins in 0.15 M NaCl (44 mg/mL), analysed using a UV-Vis.-NIR Lambda 950 Spectrophotometer at Flinders University.

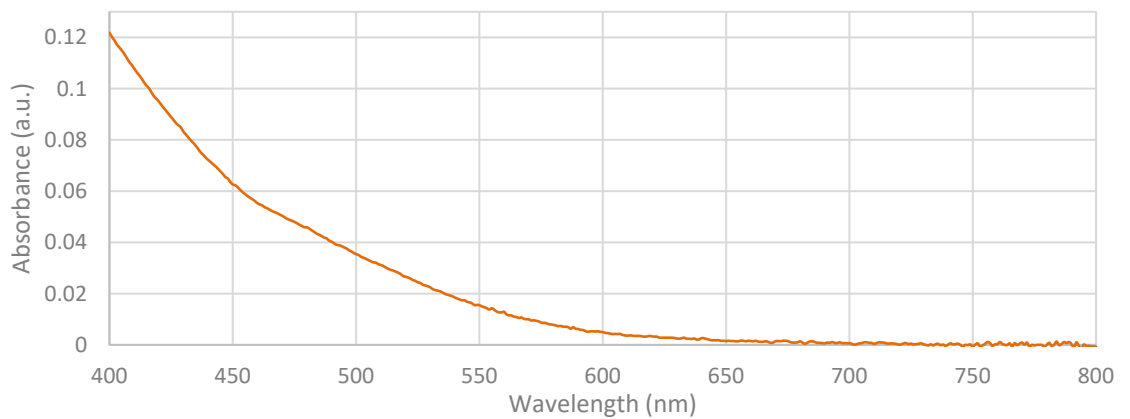


Figure 4-150: UV-Vis. reflectance spectrum of ferritins in 0.15 M NaCl (0.88 mg/mL), analysed using a UV-Vis.-NIR Lambda 950 Spectrophotometer at Flinders University.

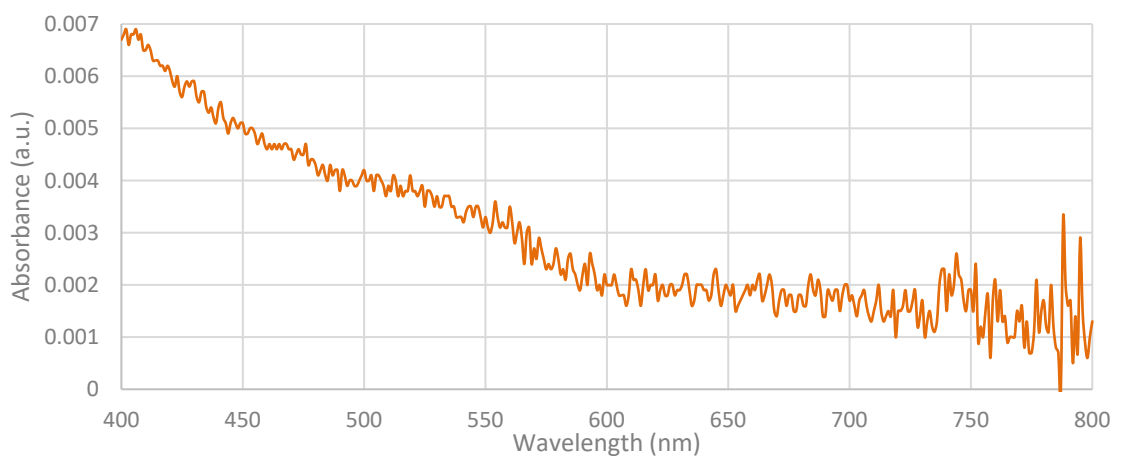


Figure 4-151: UV-Vis. reflectance spectrum of ferritins in 0.15 M NaCl (1.0×10^{-4} mg/mL, concentration in blood), analysed using a UV-Vis.-NIR Lambda 950 Spectrophotometer at Flinders University.

4.2.1.2 ASD FieldSpec.[®] 4 Hi-Res Spectroradiometer with ISP-REF Integrating Sphere

The fibre optic cable is sensitive to movement, where spectral noise is produced if the cable is moved. Every 100% scan was completed in 4 seconds.

4.2.1.2.1 Blood

Dried spot of defibrinated blood appears brown after last run. The starting NIR spectral profile is similar to that of water observed earlier. This is in line with the loss of these peaks as the reflectance sample dries over time.

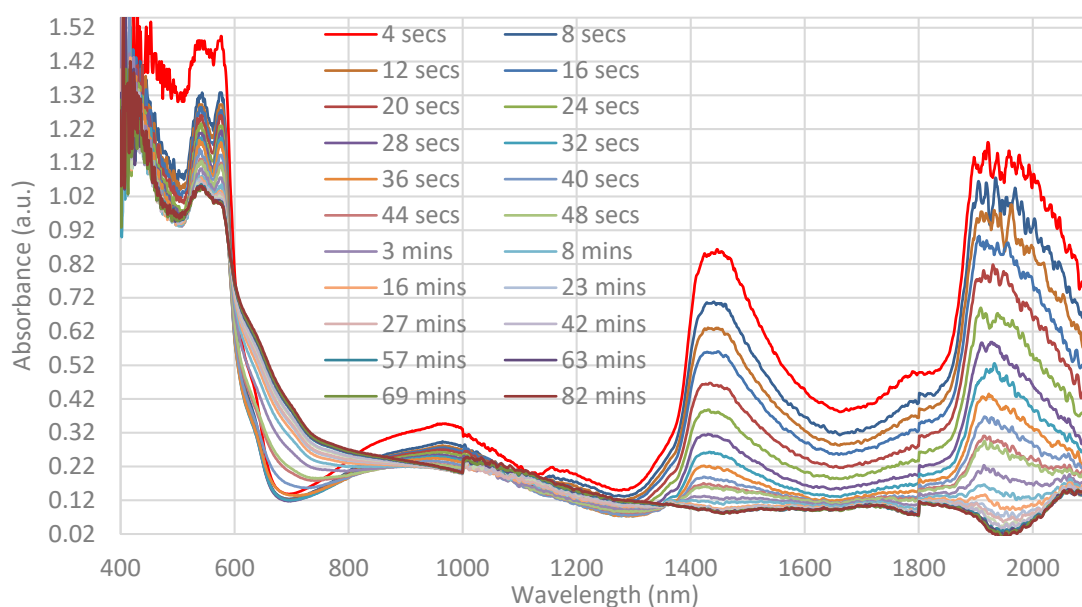


Figure 4-152: UV-Vis.-NIR spectra of defibrinated blood droplet on filter paper as it dries (white reference: filtered plasma), analysed using an ASD FieldSpec. 4 coupled to an ISP-REF integrating sphere at Flinders University.

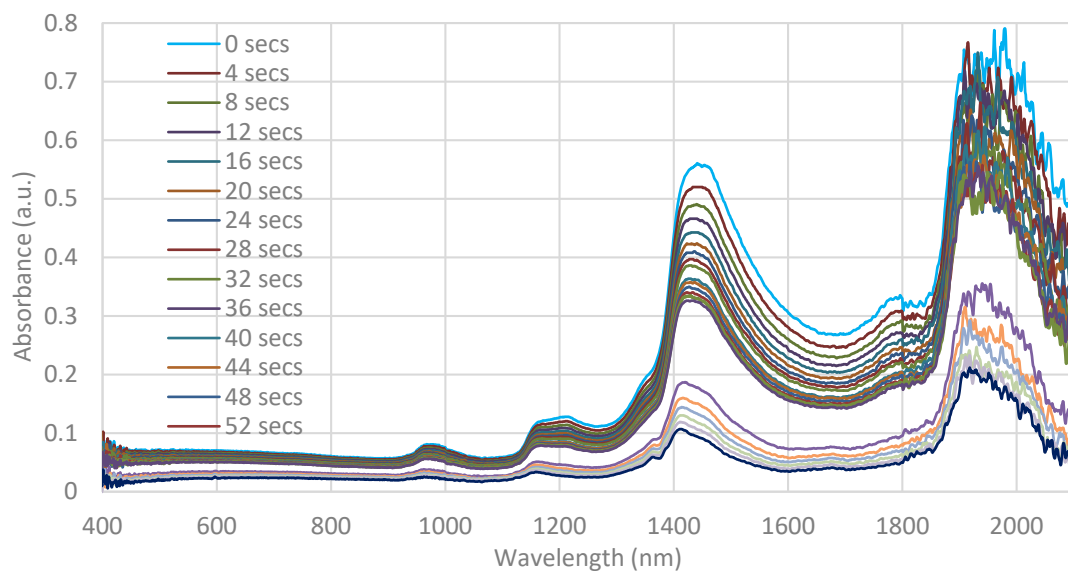


Figure 4-153: UV-Vis.-NIR spectra of water droplet on filter paper (white reference: filter paper), analysed using an ASD FieldSpec. 4 coupled to an ISP-REF integrating sphere at Flinders University.

4.2.1.2.2 Biliverdin

UV-Vis spectral profile is similar to that observed in transmission and reflectance spectroscopy results previously. Interestingly, there is no peaks observed in the NIR region. Hence ASD appears to be better at subtracting a liquid-based background.

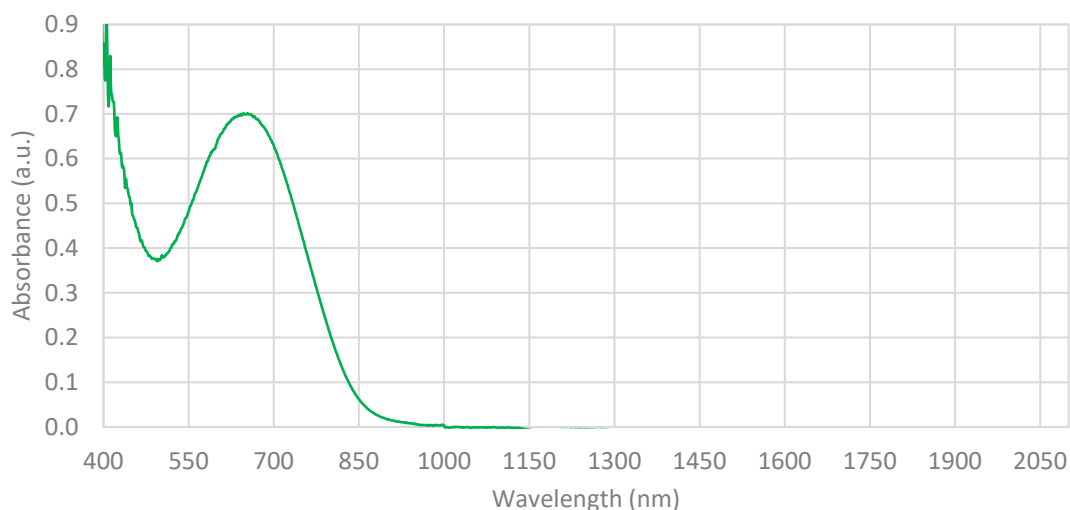


Figure 4-154: UV-Vis.-NIR spectrum of dry biliverdin in PBS (2.28 mg/mL) stored in fridge (white reference: PBS and NaOH), analysed using an ASD FieldSpec. 4 coupled to an ISP-REF integrating sphere at Flinders University.

4.2.1.2.3 Ferritin

A steady increase in absorbance is observed to 558 nm, then saturates for the entire region of interest. Interestingly, there is no peaks observed in the NIR region. Hence ASD appears to be better at subtracting a liquid-based background in this instance as well.

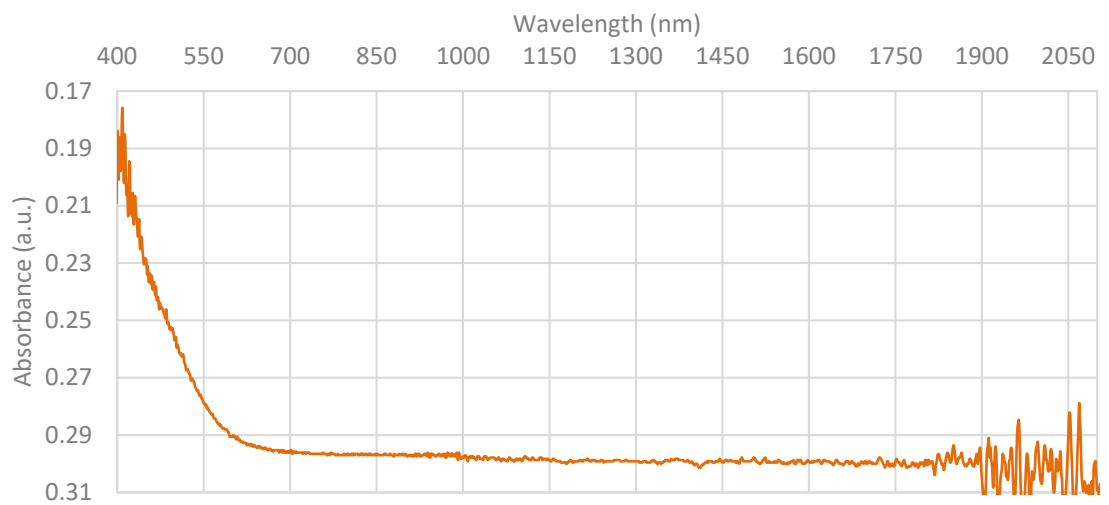


Figure 4-155: UV-Vis.-NIR spectrum of ferritin in 0.15 M sodium chloride (0.88 mg/mL, white reference: 0.15 M NaCl), analysed using an ASD FieldSpec. 4 coupled to an ISP-REF integrating sphere at Flinders University.

4.2.1.3 Ocean Optics CHEMUSB4-Vis.-NIR Spectrophotometer with ISP-REF Integrating Sphere

4.2.1.3.1 Blood

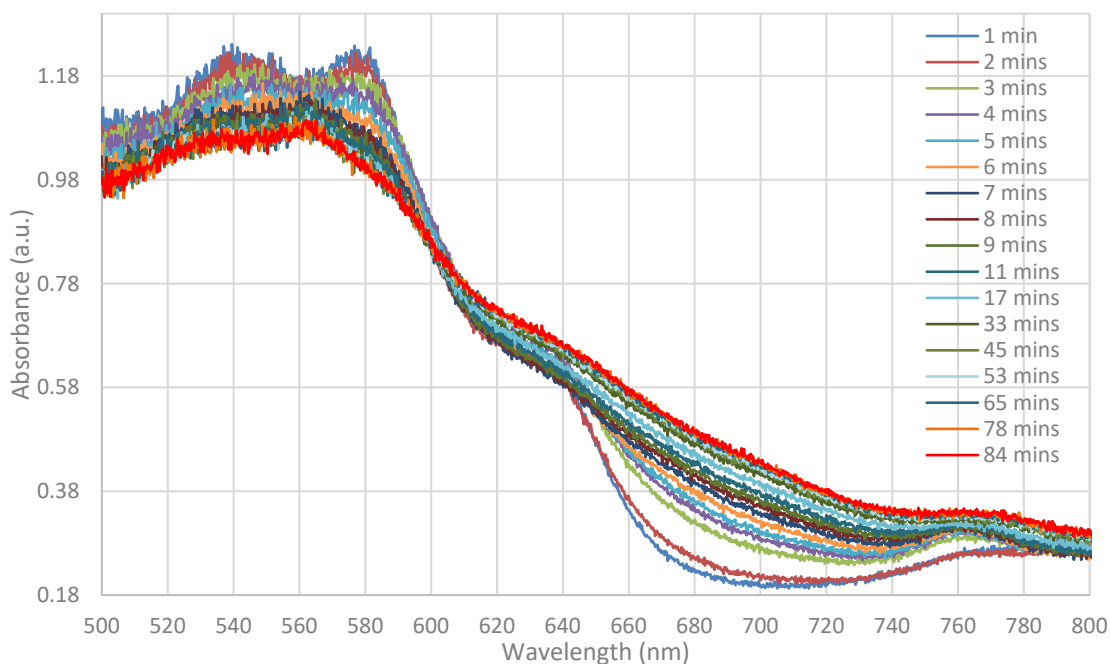


Figure 4-156: UV-Vis. overlaid spectra of defibrinated sheep's blood (methaemoglobin) as it dries (light & dark reference: filter paper) in nitrogen atmosphere, analysed using a CHEMUSB4-Vis.-NIR Spectrophotometer coupled to an ISP-REF Integrating Sphere at Flinders University.

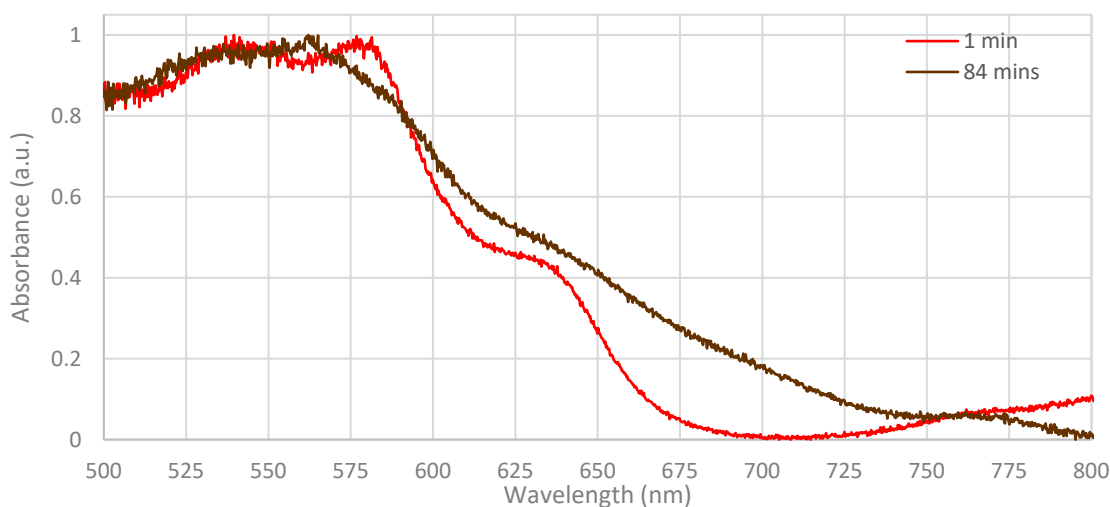


Figure 4-157: UV-Vis. overlaid normalised spectra of defibrinated sheep's blood (methaemoglobin) as it dries (light & dark reference: filter paper) in nitrogen atmosphere, analysed using a CHEMUSB4-Vis.-NIR Spectrophotometer coupled to an ISP-REF Integrating Sphere at Flinders University.

Oxyhaemoglobin deoxygenation attempted in low volume solutions prior to analysis presented darker blood with greater viscosity. It is noted that bubbling nitrogen in less than 5 mL of blood produces over aeration, where sample escapes the reaction vessel. Analysis using this instrument produced noisy spectra regardless of integration optimisation – technique is best suited for real time, fast-throughput analysis.

4.2.2 Mid Infrared (MIR)

4.2.2.1 Thermo Fisher Nicolet™ Continuum™ FTIR Microscope with ATR Accessory

Workable range for the ATR microscope was approximately 650-4000 wavenumbers.

4.2.2.1.1 Blood

Raw spectra are reported in the Appendix (Additional MIR Results). Additional fine peaks that were designated wavenumbers by software approaching the 500 cm⁻¹ regions are not presented here. When cleaning sample from the ATR contact surface, brown colouration was observed.

Observed Peaks (cm ⁻¹)	Characterisation
3273	Amine or amide N-H stretch, -CONH- or -CONH ₂ - in solid state, carboxylic acid -O-H, H-bonded -O-H [89, 117]
2957	Carboxylic acid -O-H, alkane C-H stretch [89, 117]
1642	C=N, amine or amide N-H bend, amide C=O, amides in solid state, alkene C=C, aromatic C=C, aldehydes or ketones with intramolecular H-bonds [89, 117]
1530	N=O (R-NO ₂), N-H bend, conjugated cyclic -C=N-, amides in solid state or solution [89, 117]
1451	Aromatic C=C, alkane C-H in -CH ₃ bend, -N-N=O [89, 117]
1386	N=O (R-NO ₂), alkane C-H in -CH ₃ bend, -C(CH ₃) ₃ , -O-H [117]
1301	S=O (sulfates), -O-H [89, 117]
1165	S=O (sulfates), amine C-N, carboxylic acid C-O, -C=S, -SO [89, 117]
1104	Amine C-N, carboxylic acid C-O, -C=S [89, 117]

Table 4-7: Characterisation designations to observed peaks for ATR analysis of vacuum dried defibrinated sheep's blood, analysed using an ATR-FTIR Microscope at Flinders University.

4.2.2.1.2 Biliverdin

The full FTIR spectrum is reported in the Appendix (Additional MIR Results); here it is split into two regions before and after detector change. The 4000-2000 region exhibits a strong, broad absorption between 3583-2299 cm^{-1} .

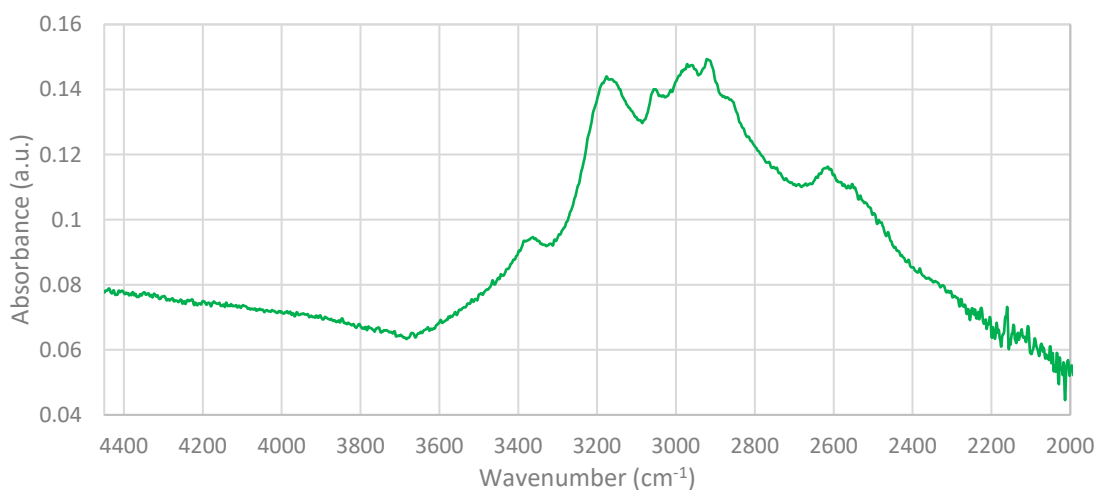


Figure 4-158: ATR-FTIR spectrum of biliverdin hydrochloride powder, analysed using an FT-IR Microscope with ATR accessory at Flinders University.

Observed Peaks (cm^{-1})	Characterisation
3371	Amine or amide N-H stretch, =NH, carboxylic acid -O-H, H-Bonded -O-H [89, 117]
3176	Amine or amide N-H stretch, carboxylic acid -O-H, aromatic C-H stretch, -CONH ₂ - or -CONH- in solid state [89, 117]
3045	Carboxylic acid -O-H, aromatic C-H stretch, alkene C-H stretch, -CONH ₂ - or -CONH- in solid state [89, 117]
2605	Carboxylic acid -O-H, -NH ₂ ⁺ [89, 117]
2921, 2950	Carboxylic acid -O-H, C-H alkane stretch [89, 117]

Table 4-8: Characterisation designations to observed peaks for ATR analysis of biliverdin hydrochloride, analysed using an ATR-FTIR Microscope at Flinders University.

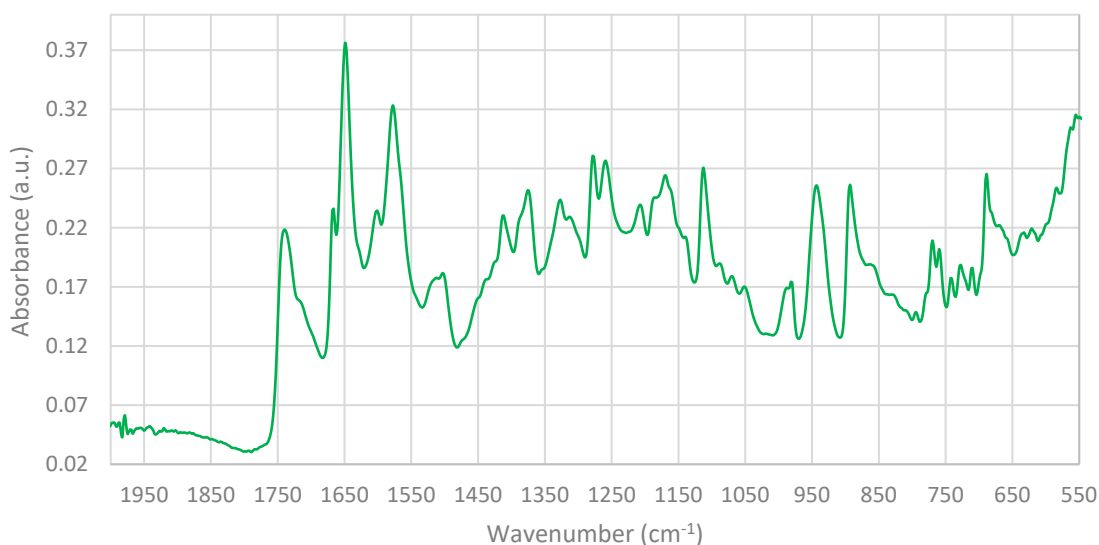


Figure 4-159: ATR-FTIR spectrum of biliverdin hydrochloride powder, analysed using an FT-IR Microscope with ATR accessory at Flinders University.

Observed Peaks (cm⁻¹)	Characterisation
1740	C=O, ester, acid chlorides [89, 117]
1667, 1649	Imine and oxime C=N, alkene or aromatic C=C, amide C=O, C=C-C=N-, -C=C-O-, ketones with intramolecular H-bonds, unsaturated ketones, amides in solid state [89, 117]
1577, 1503	Amine or amide N-H bend, conjugated cyclic -C=N- [89, 117]
1412	Aromatic C=C, alkane C-H bend in -CH ₃ [89, 117]
1375	Amine C-N, alkane C-H bend in -CH ₃ , -O-H [89, 117]
1327	Amine C-N, -O-H [89, 117]
1278, 1259, 1207, 1170, 1113, 1051	Alcohol or carboxylic acid C-O, amine C-N [89, 117]
981, 943, 710	Aromatic or alkene C-H out-of-plane bend [89, 117]
893	Aromatic or alkene C-H out-of-plane bend, 1 isolated aromatic C-H [89, 117]
770	Aromatic or alkene C-H out-of-plane bend, 3 neighbouring aromatic C-H [89, 117]
759	Aromatic or alkene C-H out-of-plane bend, 3 or 4 neighbouring aromatic C-H [89, 117]

728	Aromatic or alkene C-H out-of-plane bend, 4 or 5 neighbouring aromatic C-H [89, 117]
689, 531	Chloride C-X [89]

Table 4-9: Characterisation designations to observed peaks for ATR analysis of biliverdin hydrochloride, analysed using an ATR-FTIR Microscope at Flinders University.

4.2.2.1.3 Bilirubin

The two jumps in absorbance at 3452-3324 cm⁻¹ and 1745-1471 cm⁻¹ present changes in refractive indices.

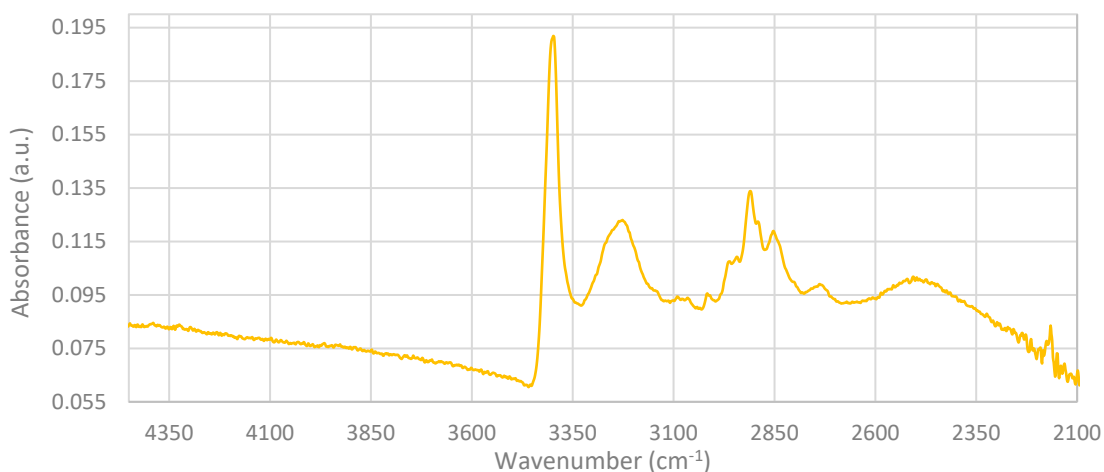


Figure 4-160: ATR-FTIR spectrum of bilirubin powder, analysed using an FT-IR Microscope with ATR accessory at Flinders University.

Observed Peaks (cm ⁻¹)	Characterisation
3398	H-bonded or carboxylic acid O-H, amine or amide N-H stretch, =NH, -CONH ₂ - in solution [89, 117]
3227	H-bonded O-H, amine or amide N-H stretch, -CONH ₂ - or -CONH- in solid state [89, 117]
2910, 2480	Carboxylic acid -O-H, alkane C-H stretch [89, 117]

Table 4-10: Characterisation designations to observed peaks for ATR analysis of bilirubin, analysed using an ATR-FTIR Microscope at Flinders University.

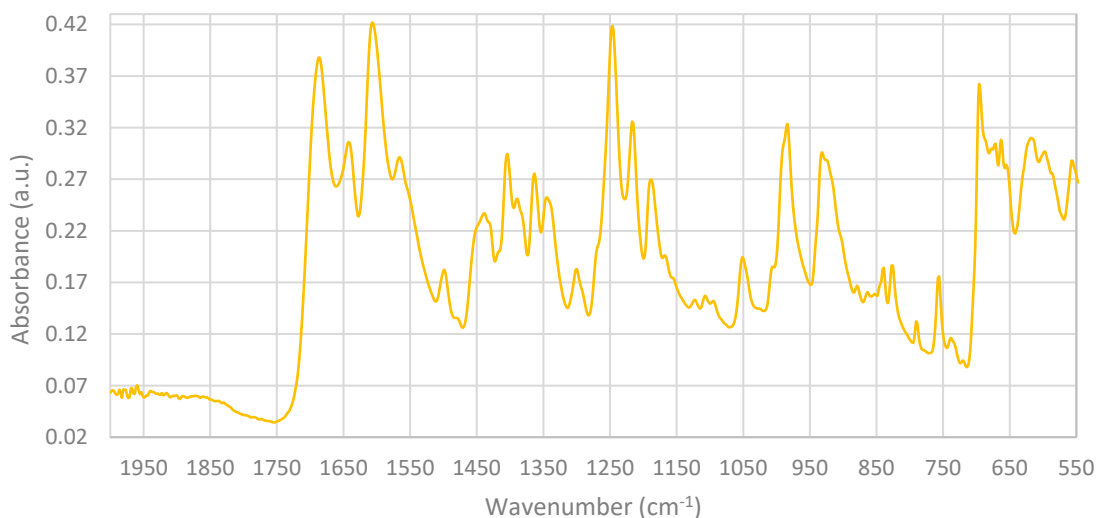


Figure 4-161: ATR-FTIR spectrum of bilirubin powder, analysed using an FT-IR Microscope with ATR accessory at Flinders University.

Observed Peaks (cm⁻¹)	Characterisation
1687	Imines and oximes C=N, amide C=O, -C=C-O-, alkene C=C, unsaturated ketones or carboxylic acids, amides in solid state [89, 117]
1642	Imines and oximes C=N, amide C=O, alkene C=C, conjugated cyclic -C=N-, amine or amide N-H bend, ketones with intramolecular bonds, amides in solid state [89, 117]
1606	Amine or amide N-H bend, alkene C=C, aromatic C=C, conjugated cyclic -C=N-, -C=C-CO-, carboxylate ions [89, 117]
1566	Amine or amide N-H bend, -C=N-, carboxylate ions [89, 117]
1499	Aromatic C=C, -C=N- [89, 117]
1439, 1404	Aromatic C=C, alkane C-H bend in -CH ₂ - or -CH ₃ [89, 117]
1364	Amine C-N, alkane C-H bend in -CH ₃ , -O-H [89, 117]
1345	Amine C-N, -O-H [89, 117]
1300, 1246, 1216, 1188	Alcohol or carboxylic acid C-O, amine C-N, -O-H [89, 117]
984, 932, 663, 618, 556	Alkene C-H out-of-plane bend, -CH=CH- trans [89, 117]
840, 826, 695	Alkene or aromatic C-H out-of-plane bend, 2 neighbouring aromatic C-H, 1 isolated aromatic C-H [89, 117]

790	Alkene or aromatic C-H out-of-plane bend, 3 neighbouring aromatic C-H [89, 117]
757	Alkene or aromatic C-H out-of-plane bend, 3 or 4 neighbouring aromatic C-H [89, 117]
742	Alkene or aromatic C-H out-of-plane bend, 4 or 5 neighbouring aromatic C-H [89, 117]

Table 4-11: Characterisation designations to observed peaks for ATR analysis of bilirubin, analysed using an ATR-FTIR Microscope at Flinders University.

4.2.2.1.4 Biliverdin & Bilirubin Mixtures

There were many observable differences in characteristic biliverdin and bilirubin MIR spectra above, hence mixtures of the two related compounds in various ratios were analysed. Samples appeared green as it was cleaned from the contact surfaces. Peaks where there are distinct differences between biliverdin and bilirubin: 3398, 3227, 3176, 1740, 1667, 1649, 1577, 1566, 1412, 1404, 1375, 1363, 1345, 1327, 1300, 1278, 1259, 1246, 1216, 1207, 943, 932, 893, 840, 826, 770, 728 & 710 cm^{-1} .

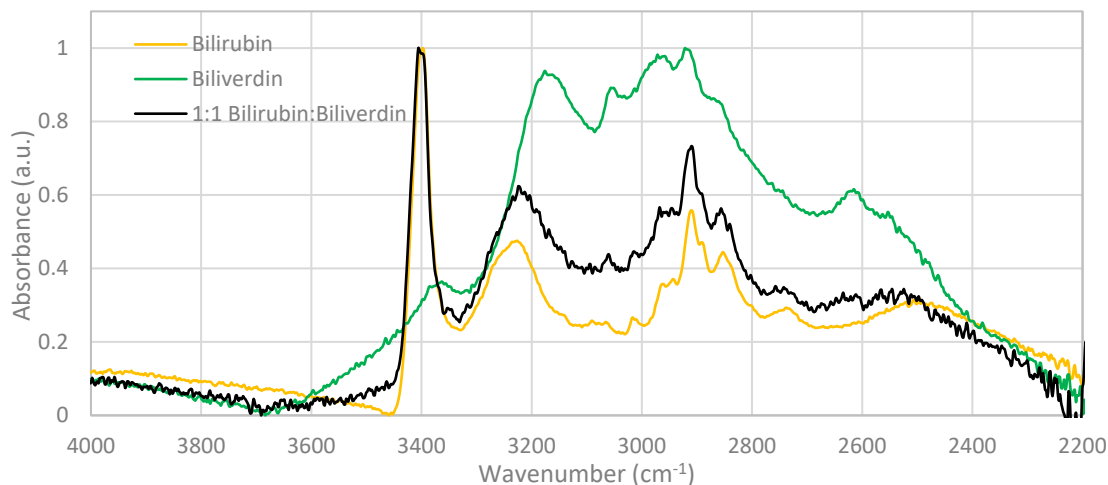


Figure 4-162: ATR-FTIR spectrum of biliverdin & bilirubin (1:1 mixture), normalised between 2350-4400 cm^{-1} , analysed using an FT-IR Microscope with ATR accessory at Flinders University.

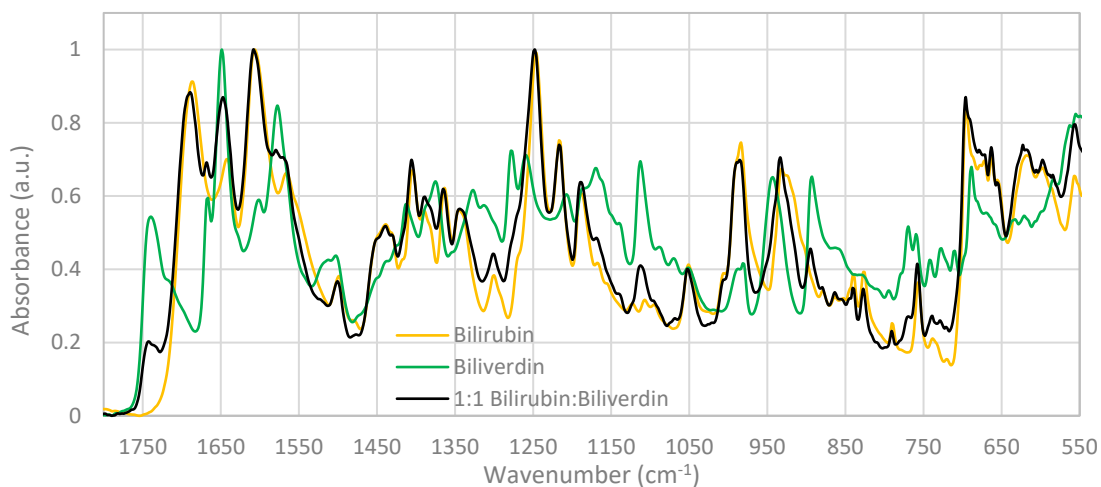


Figure 4-163: ATR-FTIR spectrum of biliverdin & bilirubin (1:1 mixture), normalised between 1750-550 cm⁻¹, analysed using an FT-IR Microscope with ATR accessory at Flinders University.

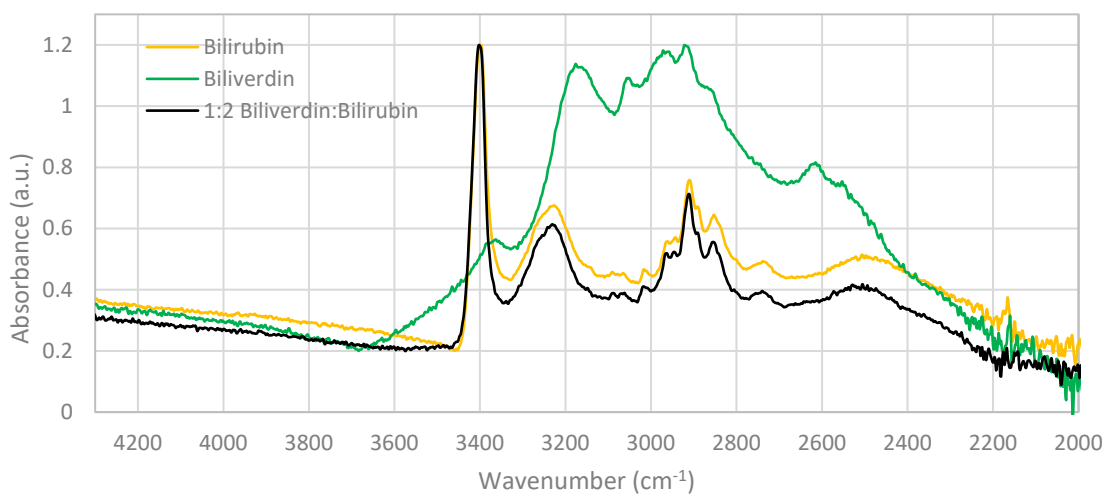


Figure 4-164: ATR-FTIR spectrum of bilirubin & biliverdin (1:2 mixture; 1.5 mg bilirubin & 0.6 mg biliverdin), normalised between 2350-4400 cm⁻¹, analysed using an FT-IR Microscope with ATR accessory at Flinders University.

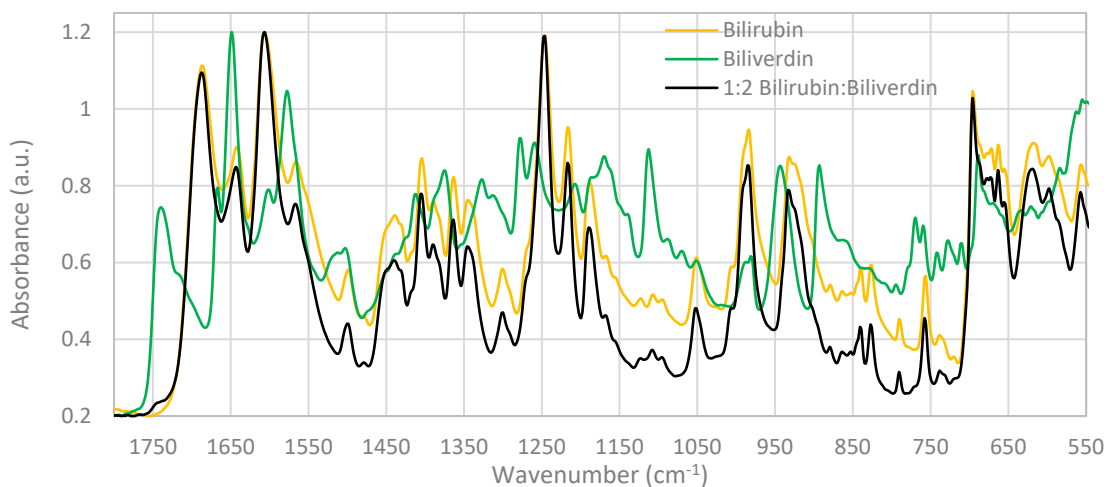


Figure 4-165: ATR-FTIR spectrum of bilirubin & biliverdin (1:2 mixture; 1.5 mg bilirubin & 0.6 mg biliverdin), normalised between 1750-550 cm^{-1} , analysed using an FT-IR Microscope with ATR accessory at Flinders University.

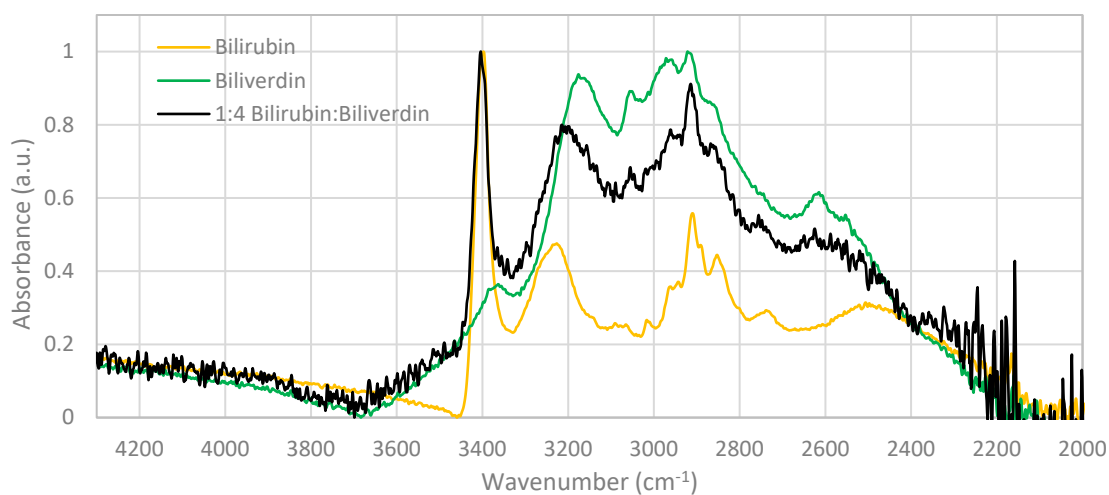


Figure 4-166: ATR-FTIR spectrum of bilirubin & biliverdin (1:4 mixture; 0.6 mg bilirubin & 2.6 mg biliverdin), normalised between 2350-4400 cm^{-1} , analysed using an FT-IR Microscope with ATR accessory at Flinders University.

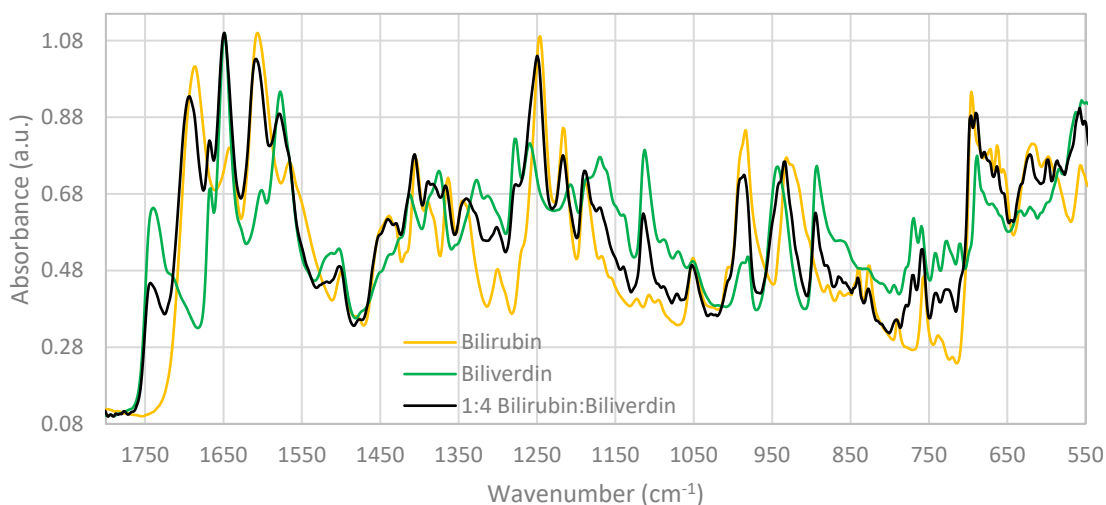


Figure 4-167: ATR-FTIR spectrum of bilirubin & biliverdin (1:4 mixture; 0.6 mg bilirubin & 2.6 mg biliverdin), normalised between 1750-550 cm^{-1} , analysed using an FT-IR Microscope with ATR accessory at Flinders University.

4.2.2.1.5 Ferritin

Raw spectra are reported in the Appendix (Additional MIR Results).

Observed Peaks (cm^{-1})	Characterisation
3277	Amine or amide N-H stretch, carboxylic acid -OH, H-bonded -OH, -CONH ₂ - or -CONH- in solid state [89, 117]
2955	Carboxylic acid -OH, aldehyde C-H, Alkane C-H stretch [89, 117]
1637	Amine or amide N-H bend, -NH ₂ , Amide C=O, Alkene C=C, conjugated cyclic -C=N-, -C=C-CO-, aldehydes or ketones with intramolecular H-bonds, amides in solid state [89, 117]
1537	N=O (R-NO ₂), -N=N ⁺ -O ⁻ , C-N=O amine or amide N-H, conjugated cyclic -C=N-, amides in solid state [89, 117]
1403	N=O (R-NO ₂), alkane C-H in -CH ₂ - or -CH ₃ bend, -O-H [89, 117]
1078	Amine C-N, alcohol or carboxylic acid C-O [89, 117]

Table 4-12: Characterisation designations to observed peaks for ATR analysis of vacuum dried ferritins, analysed using an ATR-FTIR Microscope at Flinders University.

4.2.3 Far Infrared (FIR)

4.2.3.1 ATR

4.2.3.1.1 Blood

Previously, blood has been analysed in pellet form, however the spectra varied with different drying methods. Hence in these analyses, wet and dry blood was analysed. Peaks are observed at 325, 351, 374, 411, 441, 456, 520 and 618 wavenumbers. The peaks at 325, 351 and 441 wavenumbers are not discernible in the wet samples.

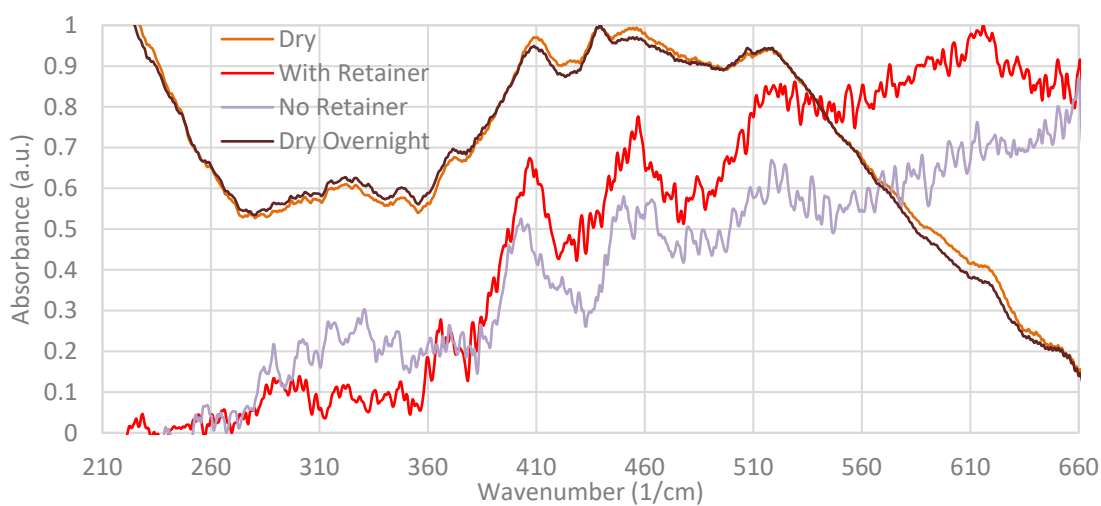


Figure 4-168: FIR-ATR overlaid spectra of defibrinated sheep's blood in liquid and solid states, analysed at the Australian Synchrotron (THz/FIR beamline) with SiBolo detector and amplitudes of 5200 (no retainer), 5400 (with retainer), 12500 (dried) & 13500 (overnight).

There appears to be no significant differences in the characteristic spectra of defibrinated, ACD and Lithium Heparin blood types as shown below.

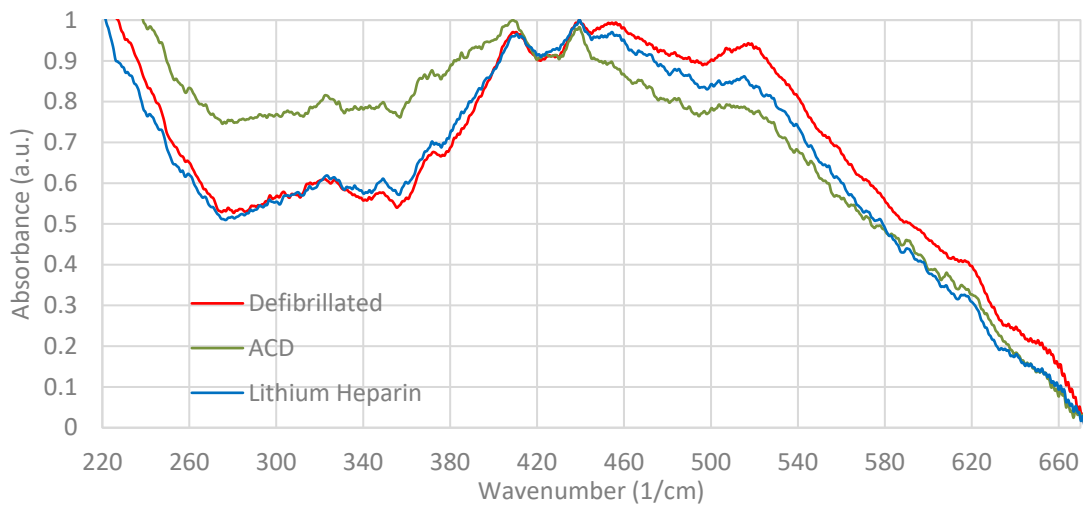


Figure 4-169: FIR-ATR overlaid spectra of defibrinated, ACD and lithium heparin sheep's blood in solid state (dried), analysed at the Australian Synchrotron (THz/FIR beamline) with SiBolo detector and amplitudes of 5200 (Def), 13300 (LiHep) & 14000 (ACD).

4.2.3.1.2 Methaemoglobin

Presents similar peaks to blood spectra – no discernible difference between haemoglobin and methaemoglobin using this analytical method.

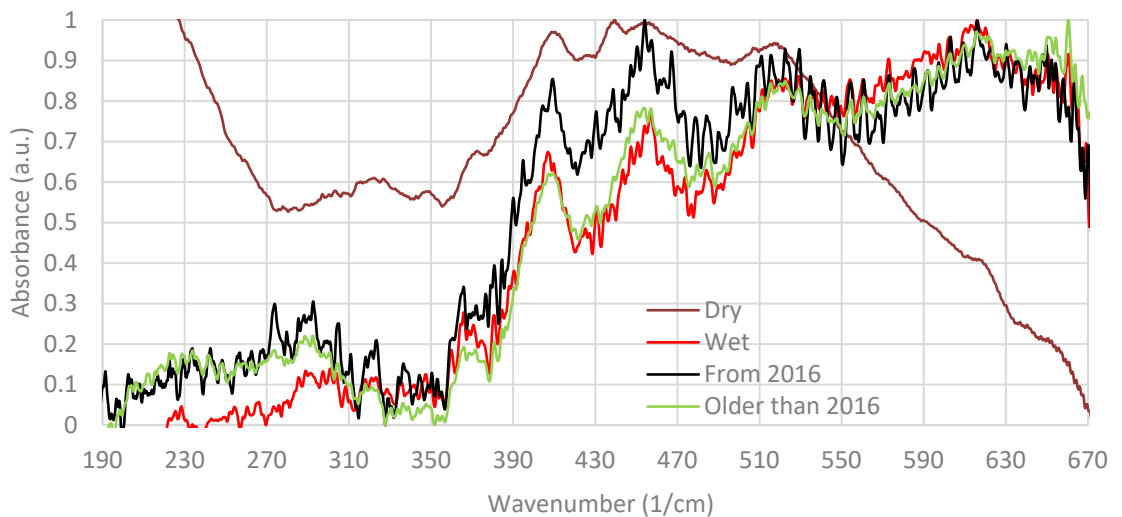


Figure 4-170: FIR-ATR overlaid spectra of fresh (Wet – liquid state & Vacuum Dry – solid state) and old (From 2016 & Older than 2016 – liquid states) defibrinated sheep's blood, analysed at the Australian Synchrotron (THz/FIR beamline) with SiBolo detector and amplitudes of 5400 (Fresh) & 5200 (from & older than 2016).

4.2.3.1.3 Human Haemoglobin

Peaks are observed at 294, 400, 450, 516, 618 and 655 wavenumbers for both samples.

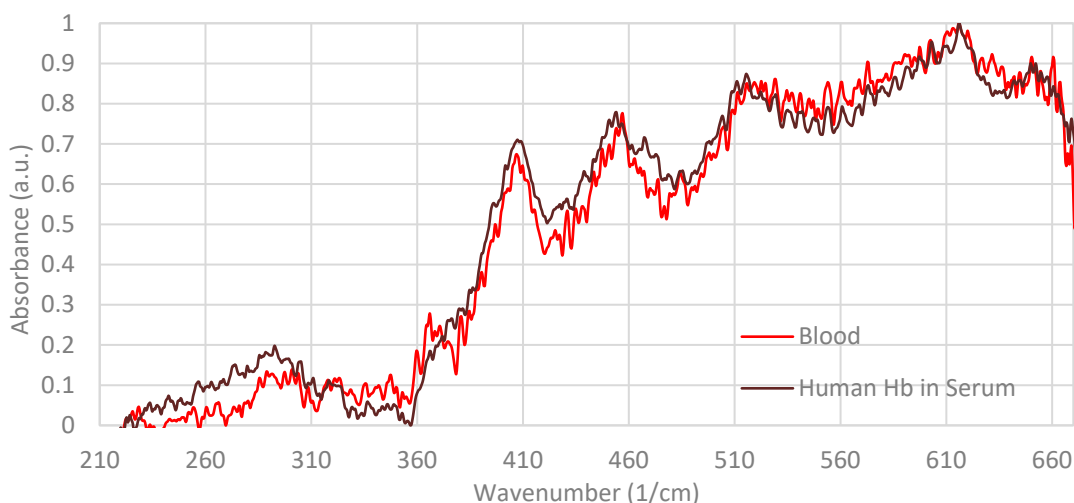


Figure 4-171: FIR-ATR overlaid spectra of defibrinated sheep's blood (aqueous) and human haemoglobin in plasma (1:2 ratio by weight) analysed at the Australian Synchrotron (THz/FIR beamline) with SiBolo detector and amplitudes of 5400 (blood) & 5180 (human Hb in serum).

Peaks for ground human haemoglobin are observed at 324, 415, 440, 463, 522, 622 and 658 wavenumbers (duplicated as reported in the Appendix, Additional FIR Results), which are not discernible in the sample when in flake form. Additional peaks at 355 and 374 were observed in dry sheep blood.

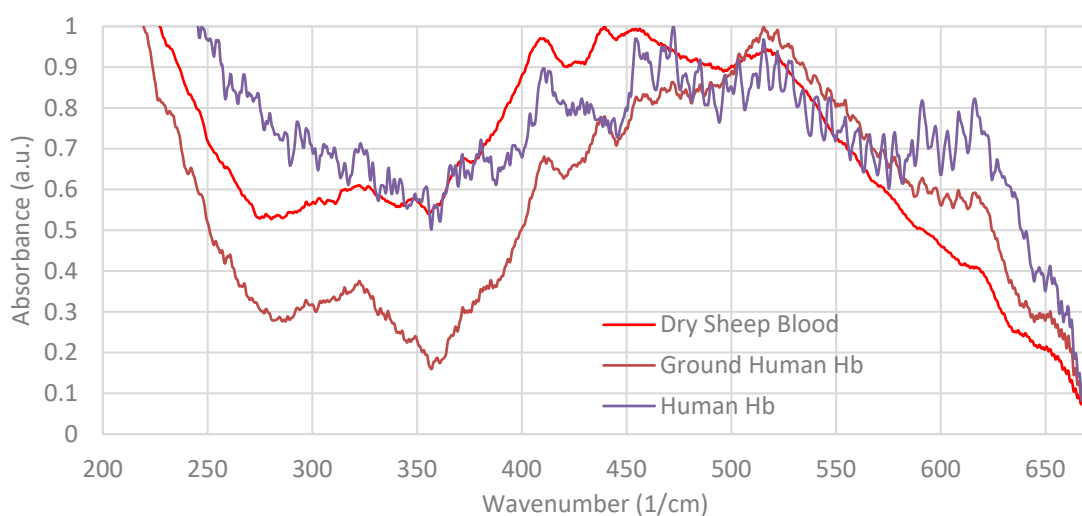


Figure 4-172: FIR-ATR overlaid spectra of dried defibrinated sheep's blood, human haemoglobin (flakes) and human haemoglobin (ground) analysed at the Australian Synchrotron (THz/FIR beamline) with SiBolo detector and amplitudes of 16600 (human Hb ground), 21300 (human Hb flakes) & 12500 (sheep blood).

4.2.3.1.4 Biliverdin

Peaks are observed at 63, 100, 135, 179, 191, 266, 294, 298, 340, 371, 440, 494, 535, 558, 586 and 640 wavenumbers. These are in line with those found when biliverdin is analysed in PE, KBr and in DWLC's.

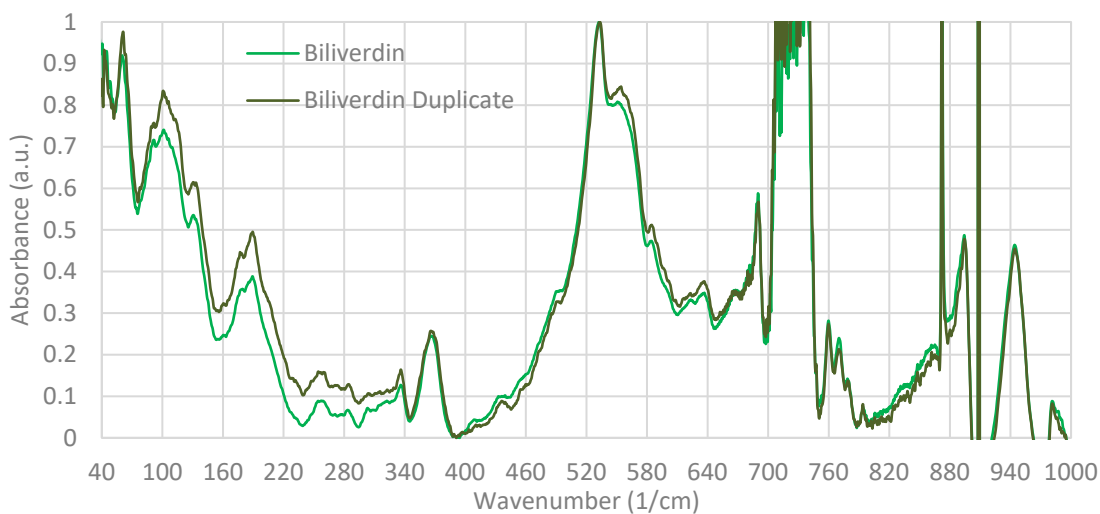


Figure 4-173: FIR-ATR overlaid spectra of biliverdin (powdered) samples, analysed at the Australian Synchrotron (THz/FIR beamline) with a SiBolo detector and amplitudes of 18000 & 19800 (duplicate).

It is noted that the biliverdin in blood sample was not completely dissolved even after vortex mixing. Peaks are observed from this sample at approximately 161, 290 and 434 wavenumbers.

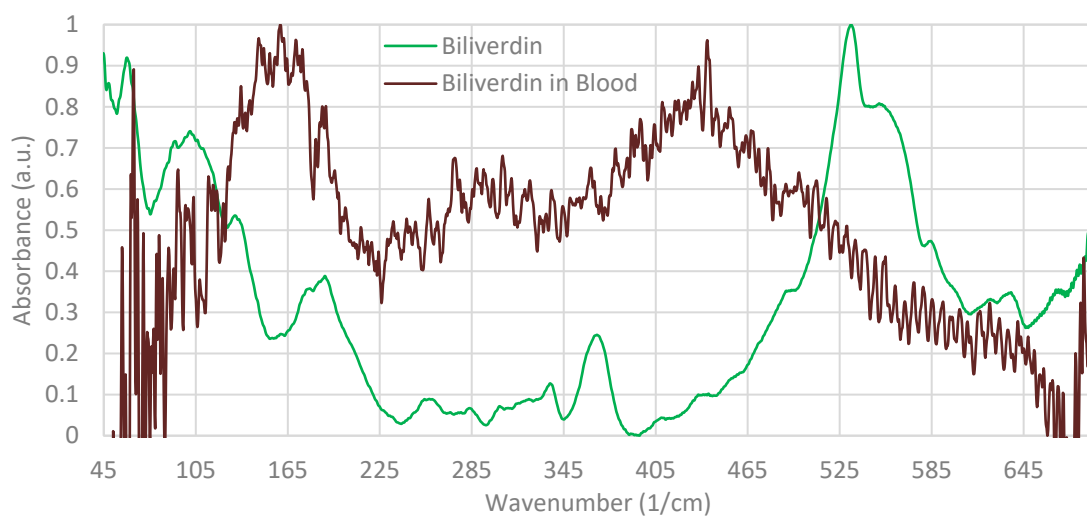


Figure 4-174: FIR-ATR overlaid spectra of biliverdin and biliverdin in defibrinated sheep's blood (aqueous) at a 1:1 ratio (0.8 mg of each), analysed at the Australian Synchrotron (THz/FIR beamline) with a SiBolo detector and amplitudes of 18000 & 5200 (biliverdin in blood).

The spectral profile of dried blood with biliverdin appears like that of dried blood.

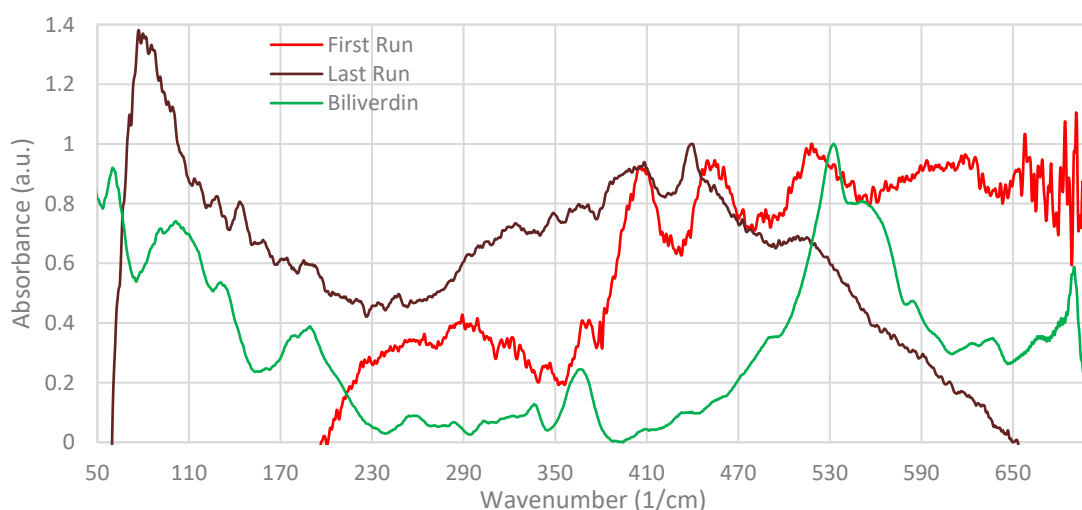


Figure 4-175: FIR-ATR overlaid spectra of biliverdin in defibrinated sheep's blood (17 mg/mL) as it dries, analysed at the Australian Synchrotron (THz/FIR beamline) with SiBolo detector and amplitudes of 5200 (first run) & 18000 (biliverdin powder).

4.2.3.1.5 Bilirubin

Main peaks for bilirubin are present at 93, 102, 131, 146, 162, 230, 298, 330, 364, 387, 418, 435, 479, 493, 545, 558, 598, 624, 660 and 663 wavenumbers. A minimum amount of 0.8 mg bilirubin powder is detectable exhibiting the same spectrum as bilirubin sample with unknown amount on the ATR crystal. Bilirubin peaks are detected in blood at 161, 290, 322, 360, 386, 406, 430, 475, 534, 556, 588, 615 and 654 wavenumbers, although the spectrum exhibits noise. The strong peak at 131

appears to have shifted to 117 wavenumbers. At a greater concentration in blood and when dry, the spectrum appears to be a summation of dried blood and bilirubin.

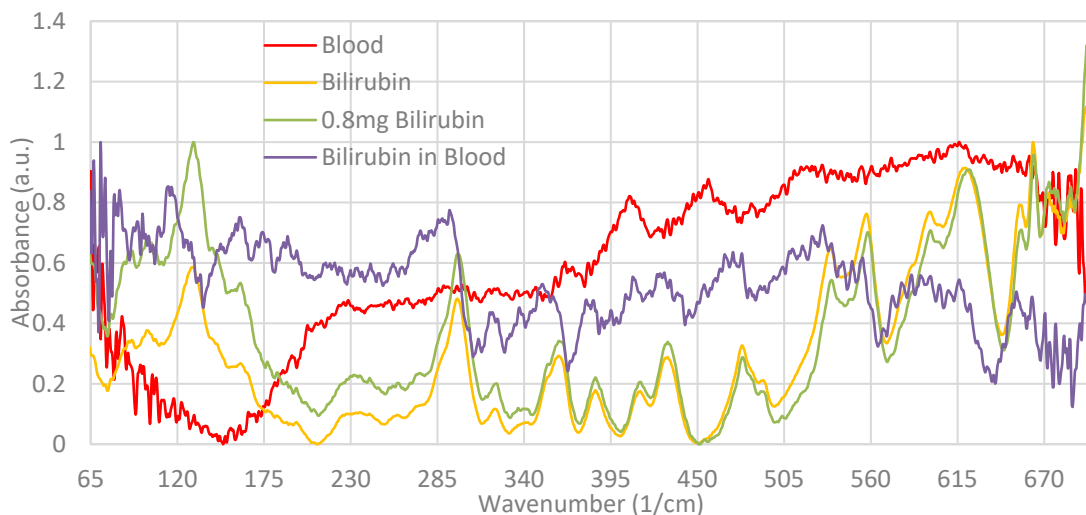


Figure 4-176: FIR-ATR overlaid spectra of defibrinated sheep's blood (liquid), bilirubin and bilirubin in defibrinated sheep's blood (1.33 mg/mL), analysed at the Australian Synchrotron (THz/FIR beamline) with SiBolo detector and amplitudes of 5400 (blood), 5070 (bilirubin in blood), 21000 (0.8 mg bilirubin) & 18100 (bilirubin).

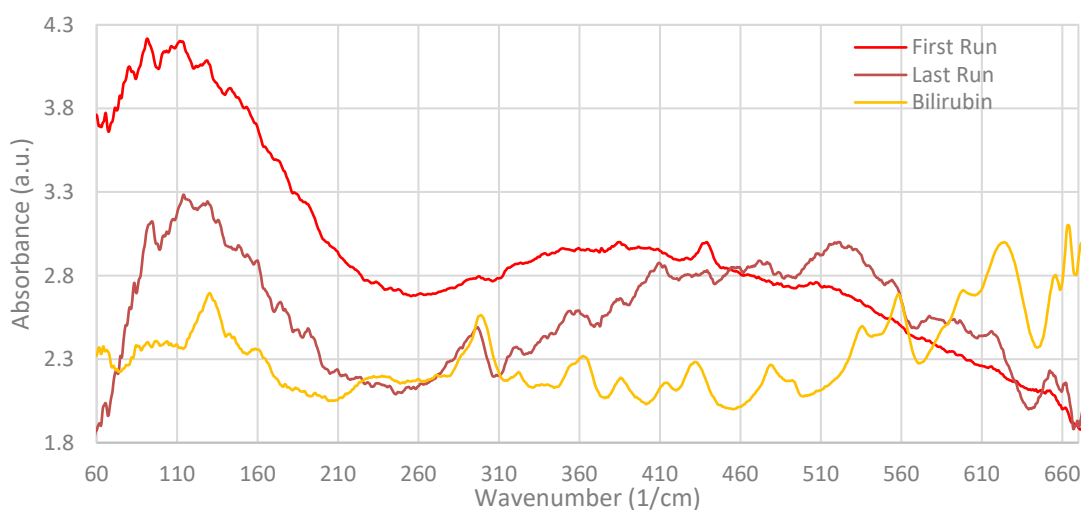


Figure 4-177: FIR-ATR overlaid spectra of bilirubin in defibrinated sheep's blood (71 mg/mL) as it dries, analysed at the Australian Synchrotron (THz/FIR beamline) with SiBolo detector and amplitudes 18100 (bilirubin) & 5000 (first run).

The above analysis was conducted such that drying occurred overnight (without a fan) and presented similar results, which are reported in the Appendix, Additional FIR Results.

Bilirubin in solvent spectrum appears to be a summation of the individual spectra.

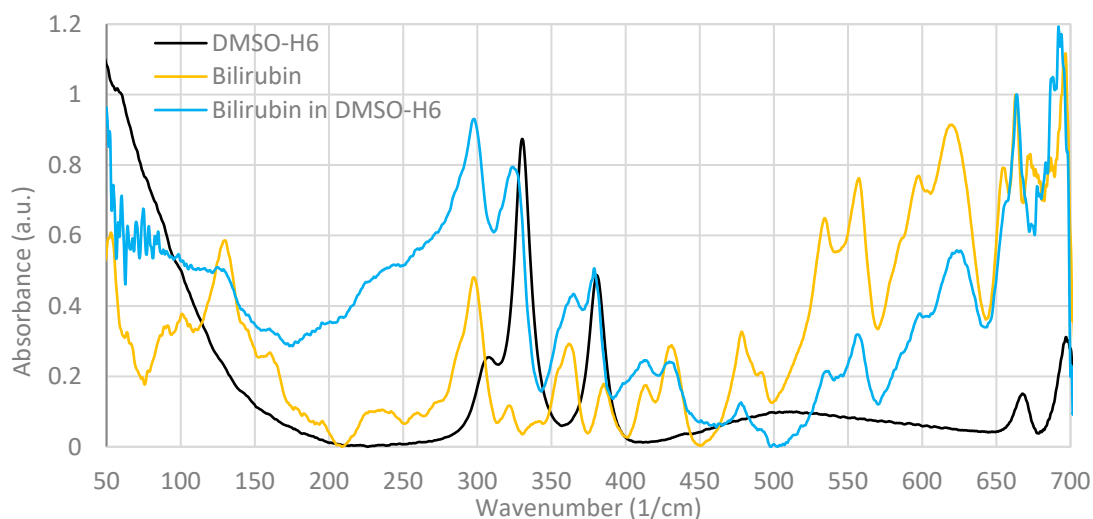


Figure 4-178: FIR-ATR overlaid spectra of bilirubin (powdered), DMSO-H₆ (liquid) and bilirubin in DMSO-H₆ (45 mg/mL), analysed at the Australian Synchrotron (THz/FIR beamline) with SiBolo detector and amplitudes of 17700 (DMSO-H₆), 17800 (bilirubin in DMSO-H₆) & 18100 (bilirubin).

4.2.3.1.6 Bilirubin Conjugate

There is strong absorption at approximately 725 wavenumbers and below 210 wavenumbers. Peaks are observed at 298, 348, 397, 420, 435, 468, 525, 617, 691, 797, 856, 964 and 989 wavenumbers.

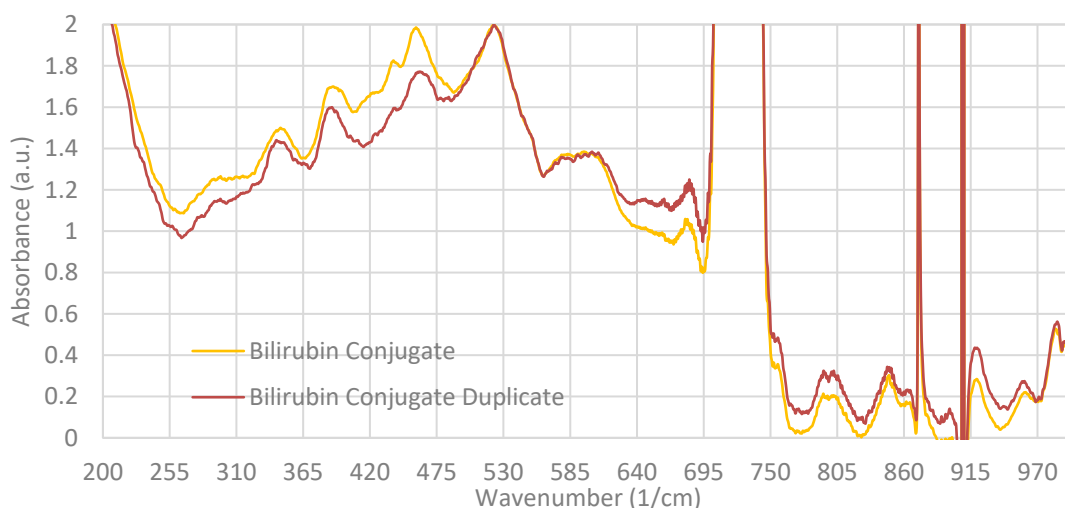


Figure 4-179: FIR-ATR overlaid spectra of bilirubin conjugate (powdered), analysed at the Australian Synchrotron (THz/FIR beamline) with SiBolo detector and amplitudes of 13900 & 14200 (duplicate).

Compared to bilirubin, the conjugate compound peaks that don't match are at 444, 461, 520 and 570 wavenumbers.

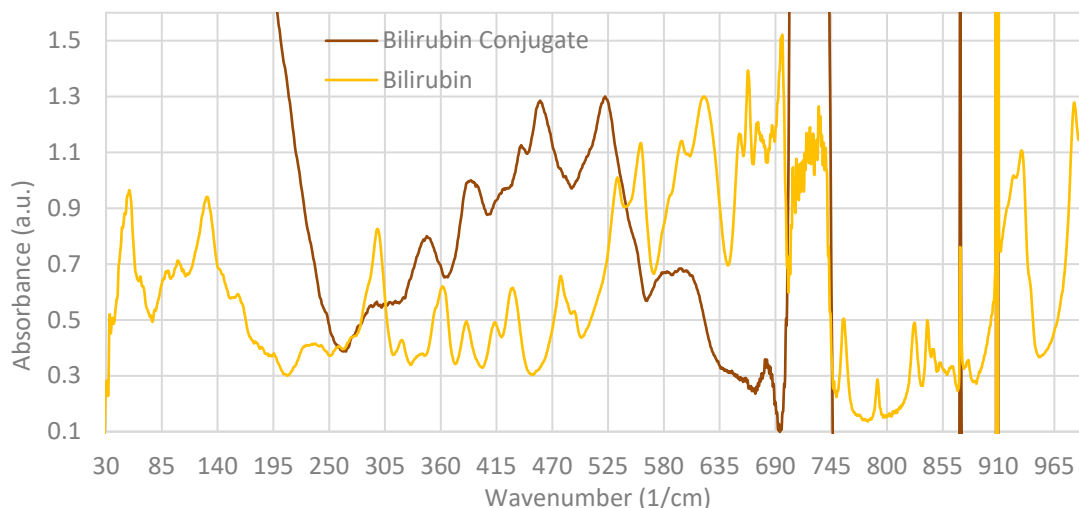


Figure 4-180: FIR-ATR overlaid spectra of bilirubin conjugate and bilirubin, analysed at the Australian Synchrotron (THz/FIR beamline) with SiBolo detector and amplitudes of 18100 & 13900 (conjugated bilirubin).

Bilirubin conjugate in blood gives peaks at approximately 164, 291, 392, 439 and 505 wavenumbers. These appear to be bilirubin conjugate peaks that have shifted to the lower wavenumbers.

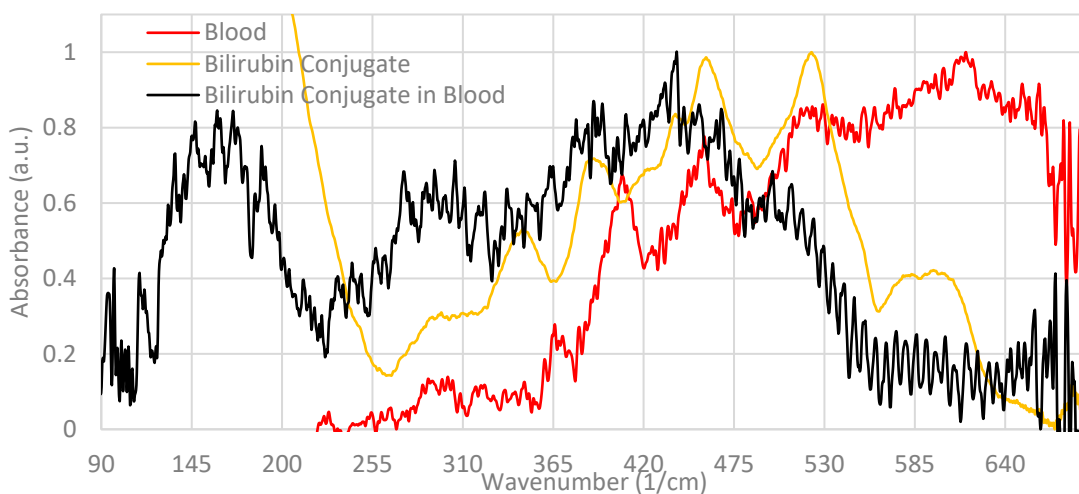


Figure 4-181: FIR-ATR overlaid spectra of bilirubin conjugate, defibrinated sheep's blood (aqueous) and bilirubin conjugate in dried sheep's blood at a 1:1 ratio (0.8 mg of each), analysed at the Australian Synchrotron (THz/FIR beamline) with SiBolo detector and amplitudes of 13900 (bilirubin conjugate), 5400 (blood) & 14800 (bilirubin conjugate in blood).

Bilirubin conjugate peaks reduce in intensity when the compound is exposed to a nitrogen atmosphere, particularly the one at 380 wavenumbers.

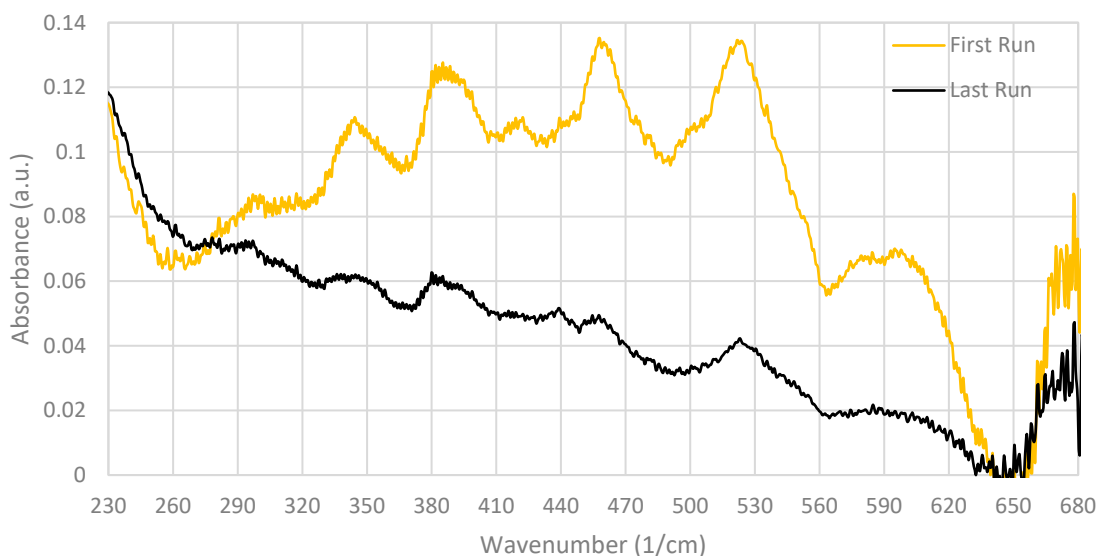


Figure 4-182: FIR-ATR overlaid spectra of bilirubin conjugate in a nitrogen atmosphere, normalised between 40 & 60 wavenumbers, analysed at the Australian Synchrotron (THz/FIR beamline) with SiBolo detector.

4.2.3.1.7 Biliverdin & Bilirubin Mixtures

The spectrum for mixtures of biliverdin and bilirubin appears to be a summation of individual spectra. For some peaks, intensity is reduced as compared to the individual spectra due to the halved concentration of the individual compound when in a mixture, for example the bilirubin peak at 300 cm^{-1} and the biliverdin peak at 530 cm^{-1} .

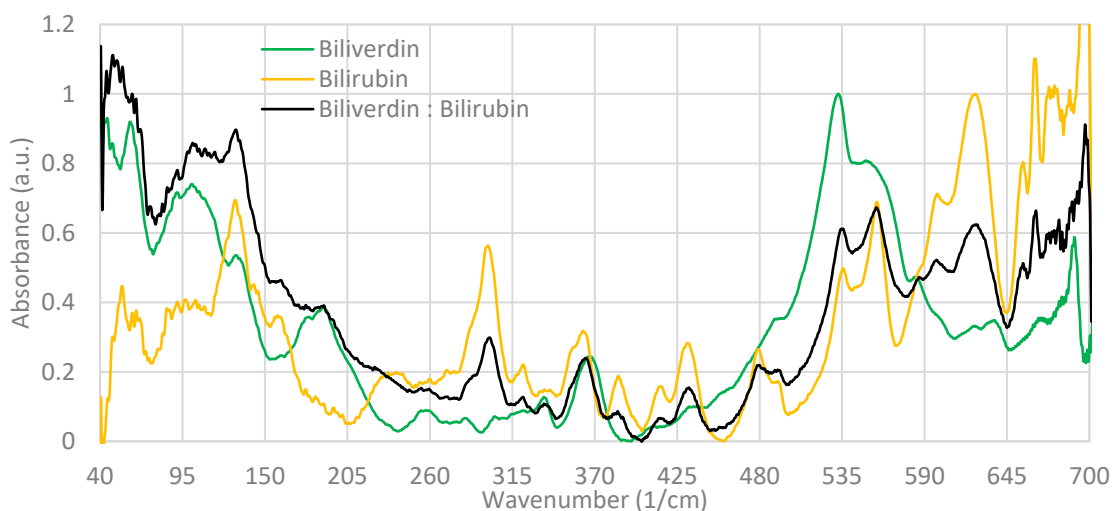


Figure 4-183: FIR-ATR overlaid spectra of biliverdin, bilirubin and the two combined in an approximate 1:1 ratio (0.5 mg biliverdin and 0.9 mg bilirubin), analysed at the Australian Synchrotron (THz/FIR beamline) with a SiBolo detector and amplitudes of 18000 (biliverdin), 18100 (bilirubin) & 22500 (mixture).

Biliverdin and bilirubin in blood was analysed however the first run as been excluded from the overlay spectra due to large noise observed, although this is presented in the Appendix, Additional FIR Results. Peaks observed in the individual spectrum of bilirubin are detectable in the blood, however biliverdin peaks appear weakly and are difficult to distinguish.

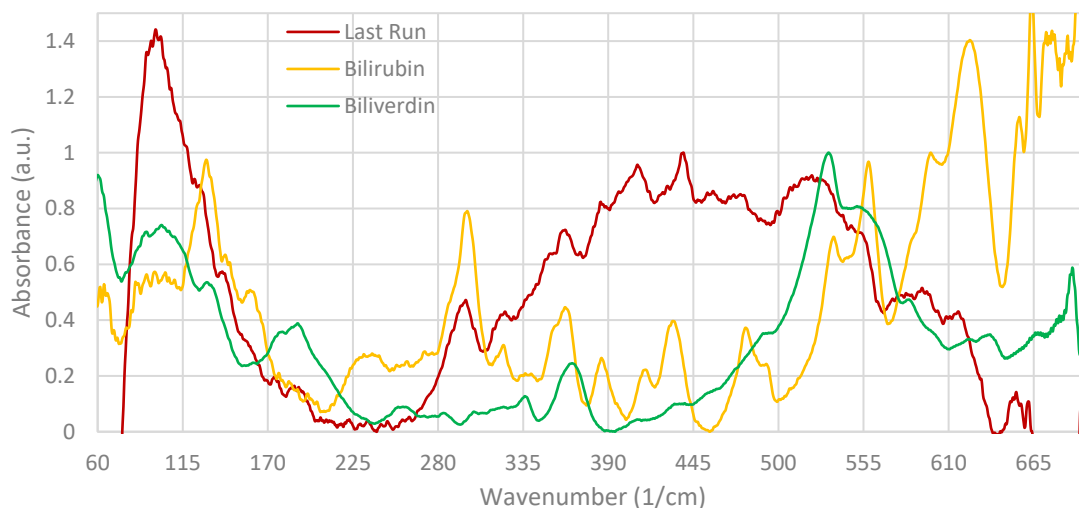


Figure 4-184: FIR-ATR overlaid spectra of biliverdin and bilirubin (1:1 ratio) in defibrinated sheep's blood (33 mg/mL) as it dries, analysed at the Australian Synchrotron (THz/FIR beamline) with a SiBolo detector and amplitudes of 18000 (biliverdin), 18100 (bilirubin) & 5100 (mixture in blood).

4.2.3.1.8 Ferritins

Weak and broad peaks are observed when ferritin is dried at approximately 180, 330, 405, 460 and 580 wavenumbers. These are less apparent when the protein is in aqueous form. There is a strong absorbance at approximately 80 wavenumbers in the aqueous sample as well as greater overall absorbance intensity, however the spectral profile appears to exhibit similarity to that of water solvent.

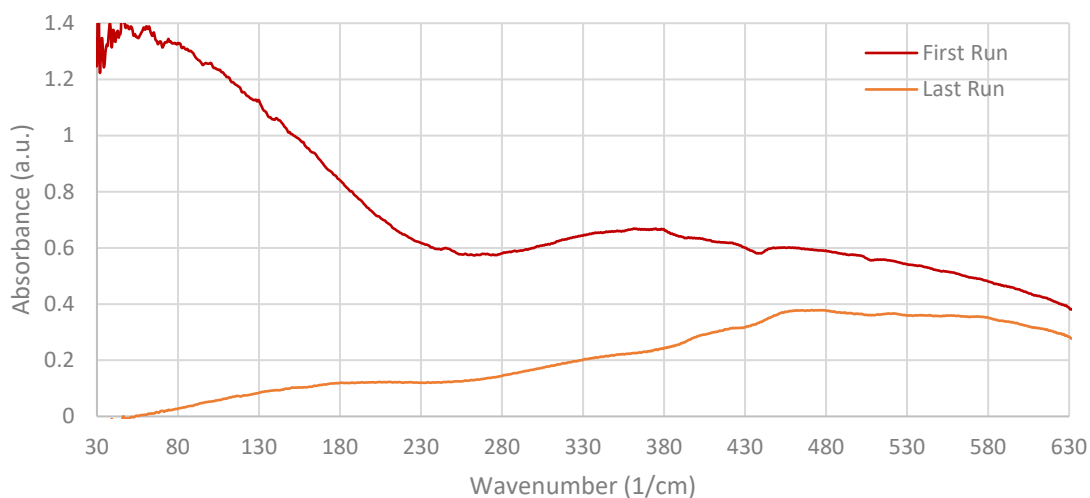


Figure 4-185: FIR-ATR overlaid spectra of ferritin (from stock solution of 44 mg/mL in NaCl) as it dries, analysed at the Australian Synchrotron with SiBolo detector.

5 Discussion and Conclusions

The age of a bruise is based on the breakdown process of haemoglobin and is currently established using UV-Vis. transmission and reflectance measurements as well as expert observation. However, information from the breakdown process may be misleading as spectral characteristics of individual components in bruises overlap. Other methods of establishing the age of a bruise age include: Raman spectroscopy [59], hyperspectral imaging [11], dual-photon imaging of skin [109], histology, math models, and HO-1 gene expression (immunohistochemistry) [6, 21, 81, 110, 111]. These methods are less common and have not been explored in this project due to impracticality and unavailability at the time the project was initiated. Accurate bruise age is crucial in forensic investigations into suspicious deaths and assaults of silent victims including the young, elderly or deceased. Thus, optimisation of UV-Vis-NIR and THz/FIR analytical methodology and techniques for identification of haemoglobin and its various breakdown derivatives will improve understanding of the process, development and aging of bruise marks.

5.1 UV-Vis. Spectroscopy

This project successfully produced individual reflectance spectra for haemoglobin (sheep and human), methaemoglobin, biliverdin, bilirubin, bilirubin conjugate and ferritin. Previously this was achieved for sheep blood, biliverdin, bilirubin and ferritin using a Varian Cary 5G UV-Vis.-NIR spectrometer with DRA-CA-50M diffuse reflectance accessory at Flinders University [63], for example Figures 4-13 and 4-14 in the Appendix (Additional UV-Vis.-NIR Results). In comparison, the Perkin Elmer UV-Vis.-NIR Lambda 950 spectrophotometer with 150 mm integrating sphere produces spectra with higher resolution (less noise) and greater signal intensity by at least 0.6 units for same solutions of same concentration (Figures 4-152 & 4-155). This gain of spectral signal detection is due to most reflections from incident light being captured internally by the integrating sphere, rather than lost to the environment. The sloping baseline for these spectra may be due to the drying of solvent on filter paper, considering the spectrophotometer took over 1 minute to scan from the longest to shortest wavelength analysed in this project.

In these spectra, biliverdin in buffer solution is characterised by a broad peak at 650 nm [11, 53, 55, 56, 64], which is detected at a concentration as low as 1.14 mg/mL in Figure 4-153, less than 16% of the concentration expected of bilirubin in adult human blood (0.012 M) [122] as shown visually in Figure 4-151. This is a significant finding as biliverdin rapidly converts to bilirubin affording difficulty in identification of small amounts of the pigment in a bruise. Bilirubin in blood (Figure 4-156) is characterised by a peak at 470 nm [7, 56] and oxyhaemoglobin's characteristic peaks are confirmed at approximately 539 and 576 nm [7, 11, 21, 22, 55] as shown in Figures 4-1 and 4-141, regardless of whether anticoagulants such as acid citrate dextrose (ACD) or lithium heparin (LiHep) have been added as seen in Figure 4-143.

In contrast, deoxyhaemoglobin [7, 21, 22] presents a peak at 564 nm in Figure 4-166 when utilising an Ocean Optics CHEMUSB4-Vis.-NIR spectrophotometer with ISP-REF integrating sphere in the presence of nitrogen. This is observed in real time over 84 minutes (Figure 1-165) by the shallowing of the trough between characteristic oxyhaemoglobin peaks, indicative of oxygen loss and hence the formation of

deoxyhaemoglobin. There is also a reduction in signal intensity due to the evaporation of water. These conclusions are supported by the partial deoxygenation of oxyhaemoglobin in defibrinated blood (Figure 4-144), ACD blood (Figure 4-147) and LiHep blood (Figure 4-146) using the Perkin Elmer UV-Vis.-NIR Lambda 950 spectrophotometer with integrating sphere when dried over a period of at least 20 days. Notably, these samples did not completely deoxygenate, even after 40 days in the case of defibrinated blood as the samples were not kept in a nitrogen atmosphere.

Oxidised haemoglobin (methaemoglobin) presents characteristic peaks [7, 21] at 500 and 635 wavenumbers (Figure 4-2). Although this is a transmission spectrum of dilute methaemoglobin produced in vitro. The addition of sodium nitrite to a solution of sheep's blood in PBS or plasma produced partially oxidised forms of oxyhaemoglobin as observed in Figures 4-148 and 4-149, respectively. The addition of sodium nitrite in excess or when left for a day for oxidation reaction to complete as shown in Figure 4-150 also only partially oxidised blood. This may be due to excessive blood concentration or that haem is inaccessible for oxidation by sodium nitrite. It is considered that some red blood cells may still be intact after refrigeration and freeze-storage, which may affect the oxidation reaction of ferrous iron with sodium nitrite in comparison to exposed haemoglobin. Resuspending dried partially oxidised blood in water and then plasma (Figure 4-145) intensifies methaemoglobin peaks detected by spectroscopy and produces an unidentifiable peak at 590 nm. Due to the difficulty in methaemoglobin formation, it was not investigated any further.

For haemoglobin-related samples in reflectance analysis, a sloping baseline between 400 nm and 600 nm is commonly witnessed and is postulated to be on account of the presence of ferritin as this protein produces an exponentially increasing absorbance in this region of the electromagnetic spectrum towards 400 nm (Figure 4-158). Increasing the ferritin protein concentration gives a more apparent yellow-brown colouration, where absorbance of incident light is proportional to ferritin concentration. Such is observed from Figures 4-158 to 4-160, where signal intensity increases with increasing ferritin protein concentration. A normal ferritin concentration in the blood that falls into the range of both male and female sex is 100 ng/mL or 1.0×10^{-4} mg/mL, which is colourless and hence may yield no visible

colouration to contribute to a bruise. Although it is feasible that ferritin molecules may congregate to the area of a bruise when it occurs, to bind and store released iron atoms as oxyhaemoglobin breaks down in the skin tissue [11]. With the local increase in ferritin concentration, the proteins may polymerise to hemosiderin, which may further add to a bruise mark's apparent colour. This notion challenges the conception of bilirubin presence in the later stages of bruising [11].

Considering the collection of individual spectra from oxyhaemoglobin, deoxyhaemoglobin, methaemoglobin, biliverdin, bilirubin and possibly ferritin components in the bruise environment, it can be appreciated that amalgamated spectra overlays and creates a large, broad absorbance across the UV-Vis. wavenumber region. For this reason, longer wavelengths of the electromagnetic spectrum nearby UV-Vis. (near infrared) were employed in the investigation.

5.2 NIR Spectroscopy

Near infrared (NIR) transmission spectra of stored sheep's blood (Figure 4-1) and biliverdin (Figure 4-4) produced a strong absorbance at approximately 980 nm, however analysis was restricted to below 1150 nm as signal became saturated. Using reflectance spectroscopy, this was extended to 2200 nm and provided additional absorption at 1450 and 1950 nm using the Perkin Elmer UV-Vis.-NIR Spectrophotometer for the stored blood (Figure 4-140) as listed in Table 6 and characterised as water, which is confirmed in Figure 4-136. These peaks are analogous to that in Defibrinated, LiHep and ACD blood (Figure 4-142) as well as biliverdin (Figure 4-154) and bilirubin (Figure 4-157) when analysed on the same instrument. Above 1950 nm will not be considered due to excessive spectral noise (observed in Figures 4-137 & 4-139), which may invalidate smoothed peaks.

The noise may be attributed to the detector for the NIR region reaching its limitation. Such is also seen for the UV-Vis. region detector in the form of the peak at 880 nm. This was able to be overcome by increasing integration time to 4 times the amount, at the expense of run time (approximately 2 minutes), which is a concern for analyses involving drying of blood (time-sensitive analyses).

Blood (defibrinated) as it dries (Figure 4-161) was analysed in the NIR region using an ASD FieldSpec. 4 Hi-Res Spectroradiometer with ISP-REF integrating sphere and presented water in the NIR region which decreased in absorbance over time, indicative of water evaporation from the sample (Figure 4-162). Water was used as the background, but still contributed to absorbance at half the maximum units, which may be due to either additional water in red blood cells in the sample or that the reference was drier than the sample.

Interestingly, biliverdin (Figure 4-163) and ferritin (Figure 4-164) analysed using the ASD FieldSpec. produced spectra with no peaks in the NIR region, demonstrating the instrument's lower sensitivity or improved ability to subtract a liquid-based background. However, analysis time per run was 4 seconds compared to previous results using the Perkin Elmer spectrophotometer. Hence the ASD FieldSpec instrument demonstrated potential for a rapid preliminary scanning method for any size sample.

5.3 MIR Spectroscopy

Ultimately only water was detected in the NIR region of the electromagnetic spectrum, which consequently leads to spectral exploration utilising mid infrared radiation. This was carried out using ATR and presented significant differences in spectra between dried defibrinated blood, biliverdin, bilirubin and dried ferritins, particularly between 550-1800 cm^{-1} .

Vacuum dried defibrinated blood and vacuum dried ferritin both contain proteins, thus ATR spectra offered similar signals representative of their complex structure characterised in Tables 4-9 & 4-14 with amine or amide in solid state, carboxylic acid, alkene and carbon to nitrogen functionalities, as well as intramolecular hydrogen bonding. Ferritin is observed to contain dissimilar alkane, amine, alcohol or carboxylic acid functionality as peaks 1403 and 1078 cm^{-1} which may indicate diverse molecular bonding in its structure compared to haemoglobin [117, 123]. Although, haemoglobin possesses peaks at 1451, 1386, 1301, 1165 & 1104 cm^{-1} , which are representative of a variety of aromatic alkene, alkane methyl bending,

amine and carboxylic acid vibrations unlike in ferritin [117, 123]. Such reflects the protein's distinct three-dimensional structure suiting a specific function. It should be noted that ATR of dried blood samples may contain methaemoglobin as when cleaned from the ATR crystal, brown colouration was observed; oxidation may have occurred during analysis, where results are representative of both haemoglobin and methaemoglobin.

ATR of biliverdin (Figures 4-167 & 4-168) exhibits broad salt absorption behaviour between 2400-3400 cm^{-1} as it is in salt form (biliverdin hydrochloride) [56]. This is not observed for bilirubin (Figure 4-169) which is in its isomeric carboxylic acid form. Regardless, biliverdin and bilirubin essentially differ by the lack or presence of a double bond about the central carbon atom in the compound structure (Figure 1-14). Therefore, it is a significant finding that the MIR spectra of the individual pigments are unique. Particularly as biliverdin is reduced to bilirubin, hence detection of the green pigment could indicate early stages of a bruise.

For example, biliverdin contains peaks at 3176, 3045 and 2605 cm^{-1} that are not present in bilirubin. Conversely bilirubin contains peaks at 3227 and 2480 cm^{-1} that are not evident in biliverdin. Such indicates that not only are there a greater amount of amine or amide vibrational signals in biliverdin compared to bilirubin, but also that these groups are protonated, having the implication that bilirubin is unconjugated; it contains intramolecular hydrogen bonds due to allowable rotation about the single-bonded carbon where in biliverdin possessed a double bond [117, 123]. As such, possible bilirubin vibrational modes are restricted, and it is reasonable that less signals are observed for this pigment.

Additionally, peaks in biliverdin observed at 728 & 1577 cm^{-1} represent an amine or amide bend [70] that doesn't appear in bilirubin as the nitrogen groups in bilirubin are involved in intramolecular hydrogen bonding as discussed. Emphasising this are the peaks in bilirubin spectra at 1566 & 1606 cm^{-1} indicative of an amine/amide bend, alkene, $-\text{C}=\text{N}-$ or carboxylate ion vibration not present in biliverdin [117, 123]. The 618 cm^{-1} peak in bilirubin may be on account of the additional C-H functionality about the central single-bonded carbon in between 4 pyrrole rings (in biliverdin this

carbon possesses a double bond) as a result of reduction by biliverdin reductase [117, 123]. Biliverdin also contains peaks at 531, 689 & 1740 cm^{-1} implying carbonyl or chloride presence [64], although this is expected considering biliverdin is in salt form [117, 123]. These results provide a variety of options, from which single peaks can be a focus when identifying a pigment.

There are instances in Figures 4-168 & 4-170 where peaks denote similar functionality, but the signals are observed at dissimilar wavenumber. This suggests different vibrations occur in each molecule due to diverse bonding or different symmetry in molecular structure. For example, the vibrations attributed to imine/oxime, amide carbonyl in solid state, alkene or unsaturated ketones/carboxylic acid functionality by peaks in biliverdin at 1649 cm^{-1} and 1687 cm^{-1} in bilirubin where there is a 20 cm^{-1} difference [117, 123]. Likewise, alkene/aromatic out-of-plane bending C-H vibrations with 1 or 2 neighbouring aromatic C-H functional groups is observed at 893 cm^{-1} in biliverdin and 840 as well as 826 cm^{-1} in bilirubin [117, 123]. Similarly, 4 or 5 neighbouring aromatic C-H vibration signals are observed at 728 cm^{-1} in biliverdin and 742 cm^{-1} in bilirubin [117, 123].

An added significant finding for ATR measurements in MIR is biliverdin and biliverdin mixtures in various ratios (Figures 4-171 to 4-176), revealing summation spectra of the individual compounds, with absorbance intensity dependent on the concentration of the individual component. Although it is noted that the pigments may not possess the same signal intensity characteristic, in fact bilirubin was observed to provide stronger absorbance bands in comparison to biliverdin; for example, in Figure 4-176 bilirubin is at the lowest concentration but does not appear a quarter of the pure compound's signal intensity.

5.4 FIR Spectroscopy

The large amount of spectral difference in bruise components in the mid infrared region of the electromagnetic spectrum, particularly between biliverdin and bilirubin whose purity is confirmed in NMR analysis (see Appendix) [53, 56, 69, 124, 125], justifies further examination of the compounds by means of far infrared (FIR)

radiation. Such instrumentation for this was unavailable at the home institution, hence six successful applications (4 days beamtime each) to use the Australian Synchrotron FIR/THz beamline provided an avenue for this study.

5.4.1 Pellets

Initially, transmission analysis was available and utilised to analyse 3-7 mm in diameter pellets, pressed by a hand pellet press. Pellets from pure materials provided spectra for biliverdin (Figure 4-5) and bilirubin conjugate (Figure 4-6) between specific wavenumber ranges as above and below these regions was either saturated or exhibited substantial noise. Strong signals observed between 0-50 cm^{-1} are not valid as they may be due to beamline mechanical, pump and electrical noise which is expected to occur below 50 Hz [126]. Nonetheless, spectral information that is available from Figure 4-5 displays crystal lattice or amide VII vibrations (peaks between 10-200 cm^{-1}) [127, 128], aliphatic chain C-C vibrations (peaks between 250-400 cm^{-1}) [129] and amide C-C=N or C=O vibrations (peaks above 400 cm^{-1}) [130, 131]. These vibrations are in line with that expected of the pigment's open porphyrin structure.

Similar vibrations are also observed in bilirubin conjugate, save crystal lattice signals, although absorbance occurs at unique wavenumbers. Bilirubin conjugate is not a compound likely to be present in a bruise as conjugation is performed by the liver, though is utilised in this FIR study to investigate and overcome solubility difficulties experienced with bilirubin, which will be discussed later. Pellets for pure bilirubin and dried ferritin materials proved unsuccessful due to physical issues creating the pellet (staticity) and saturated absorbance signal, respectively.

Polyethylene (PE), polytetrafluoroethylene (PTFE) and potassium bromide (KBr) are diluting materials that can be used for pelletising compounds of interest [117] in cases where pure pellets of the analyte could not be formed. Each diluting compound used in this project was chosen due to it being common, readily available and having a workable wavelength and wavenumber range suited to the variety of analyte the project presented, i.e. PE is recommended in the lower wavenumbers [117]. PTFE has an interference peak at approximately 200 cm^{-1} where in instances such as in

analysis of bilirubin, spectra was split into two separate figures (Figures 4-22 & 4-23). Nonetheless, crystal lattice or N-H amide (VII) vibrations (peaks from 68-162 cm^{-1}) [127], aliphatic chain C-C vibrations (peaks from 300-387 cm^{-1}) [129] and an amide C-C=N vibrations (peak at 432 cm^{-1}) [130] were observed. The peaks at 415 & 476 cm^{-1} are unidentified.

These results for bilirubin are similar when it is in PE at various concentrations (Figure 4-12), however less peaks are observed, peaks that are observed are less resolved and there is no interference at 200 cm^{-1} on account of the diluting matrix. Instead there is a strong and saturated absorbance at approximately 540 cm^{-1} that can be attributed to PE [117] which is carried through all spectra containing this matrix. Biliverdin in PE at various concentrations (Figure 4-10) presents similar spectra to bilirubin in that its only resolved spectral peaks at 210 and 370 (from aliphatic chain C-C vibrations) overlay (see Figure 4-41 and Tables 4-1 & 4-2 for comparisons). This implies that the concentration of biliverdin may be too low for comparison against bilirubin at the same concentration. Such is substantiated by Figure 4-42, where the two pigments can be easily differentiated by several characteristic peaks possibly originating from different N-H amide VII (peaks at 165, 205, 229, 241 & 201 cm^{-1}) [127, 128] and aliphatic chain C-C (peak at 337 cm^{-1}) vibrations [129]. These results are significant as the concentration of biliverdin in early to late stages of bruise breakdown may provide fundamental information regarding age determination.

It is noted that as low as 12.5% biliverdin and bilirubin can be detected in PE, although peaks become less distinguishable with lower concentration as expected, which is particularly reflected in the concentration mixtures created to generate Figure 4-16. Such is also the case for bilirubin conjugate (Figures 4-13, 4-14 & 4-15) and ferritin at various concentrations in PE (Figures 4-20 & 4-21), where any distinguishable features attributed to analyte may be lost to oscillation or diluting matrix contributions to the spectra. These results imply that mixtures of the analytes as they would be found in a bruise would be indiscernible at very low concentration i.e. when they begin to form at the site of a bruise, using these methods of analysis.

Bilirubin conjugate in PE presented similar spectra to that of its pure pellet with an additional strong peak observed at 461 cm^{-1} , which was saturated in the pure pellet spectrum. This may be indicative of a unique C=O vibration attributed to the glucuronide component of the molecule [131]. Interestingly, bilirubin conjugate may be differentiated from bilirubin/biliverdin when in PE as shown in Figures 4-17, 4-18 & 4-19, where mixtures in various ratios represent proportional summation spectra to concentration of each analyte. In this case, the peak at 300 cm^{-1} (aliphatic chain C-C vibrations) is the only common point.

Ferritin in PE (Figures 4-20 & 4-21) exhibited a broad absorbance at approximately 175 cm^{-1} , and a steady absorbance across wavenumbers between $300\text{-}600\text{ cm}^{-1}$. This is consistent with free iron(III) [74] or may imply crystal lattice, aliphatic chain C-C [129], metal-oxygen, N-H amide (VI, VII) [127, 132] or amide C-C-N [130], carbonyl or C-N-N [131] vibrations. Although legitimacy of peaks at lower concentrations of ferritin is questionable considering they may be exhibiting oscillation. In addition, the absorbance peak at approximately 175 cm^{-1} appears to shift to lower wavenumbers, which is contrary to results of pigments at lower concentrations, though this pattern may be exclusive to the different types of bonding in the protein. Complicating ferritin analysis is the possibility that salt absorbance contributes to spectra as salt was not added to PE to subtract as a background. However, the results presented in this thesis appear to emphasise the protein's numerous interactions involved in its complex three-dimensional structure which may be dependent on the proteins state of matter, symmetry and degrees of freedom suiting it to a specific function [85], also explaining why detector amplitude is low and absorbance becomes saturated with higher concentrations of the protein.

This inference is comparable to various types of dried sheep blood in PE (Figure 4-7) in the sense that due to the complexity of the structure of haemoglobin, not only is a large steady absorbance observed, but also many vibrational modes (indicative of crystal lattice, N-H amide VII, metal-oxygen and aliphatic chain C-C vibrations) [117, 123, 128]. Other fine vibration signals are unidentified; however, it is reported in literature that acoustic phonons, torsion of the peptide backbone and skeletal deformation may be responsible for low frequency vibrations (below 300 cm^{-1}) [85].

Absorbance appears to be influenced by the method of drying the protein as seen in Figures 4-8 & 4-9, although it should be considered that the protein structure may vary with the mechanics of dehydration and that the protein may interact with PE when wet and during the drying process [85].

It is considered that biliverdin and bilirubin in PE present similar signals in analysis at low concentration for this region of the electromagnetic spectrum. For this reason, Si:B and MCT_N detectors may be utilised to explore wavenumbers just above 400 cm⁻¹, such that biliverdin and bilirubin may be differentiated. Potassium bromide (KBr) is used as the diluting compound and supporting matrix in these analyses as it is IR inactive in this region [117].

Bilirubin in KBr is shown in Figure 4-30 to produce spectra with resolved peaks at a concentration of 5% analyte (also in Figure 4-31) and when diluted 100-fold. Biliverdin in KBr also revealed resolved peaks at a 5% concentration (Figures 4-28 & 4-29) albeit with a large amount of fringing. Hence low concentrations of the pigments are detectable using the Si:B and MCT_N detectors. When compared as overlaid spectra taken using the Si:B detector (Figure 4-43), biliverdin's peak at 585 cm⁻¹ (an N-H amide VI vibration not present in bilirubin [116, 127, 128]) is notable and accentuates previous findings regarding intramolecular hydrogen bonding in bilirubin.

On this note, when compared using the MCT_N detector in Figure 4-44, biliverdin and bilirubin both present O-O (peaks at 897, 842 & 883 cm⁻¹) and aliphatic chain C-C (peaks at 946-953, 936, 1072, 1009, 1099, 1127, 1158, 1212, 1219, 1251, 1263 & 1281 cm⁻¹) vibrational modes responsible for a variety of characteristic peaks (897, 946-953, 1072, 1212, 1263 and 1281 cm⁻¹ in biliverdin) [116, 129]. Although bilirubin exhibits a greater number of these modes; carbonyl electrons may be shared in intramolecular hydrogen bonding and bilirubin contains less double bonded carbons. Importantly, differences also exist in the form of peaks 730 & 770-773 cm⁻¹ in biliverdin and 792 cm⁻¹ in bilirubin. It is possible that the vibrations responsible for the 770-773 & 792 cm⁻¹ signals are N-H amide (IV/V/VI) functionality [127, 131, 132], however of key interest is the 730 & 792 cm⁻¹ peaks as these may be

vibrations from amide O=C-N and R-CO-NH-R functionality, respectively [128, 131, 132]. This further strengthens the postulation that the carbonyl groups in bilirubin are involved in intramolecular hydrogen bonding, however it is also considered that the PE windows in the sample compartment may contribute between 700-750 cm^{-1} [126].

Biliverdin and bilirubin mixtures in KBr analysed with Si:B (Figure 4-32) and MCT_N (Figure 4-33) detectors appear to be a summation of combined individual spectra, confirming previous mixture analyses by ATR in MIR and PE pellets in FIR. Greater sensitivity compared to the SiBolo detector is noted, however extensive oscillation is experienced for these samples when using the Si:B detector. Unfortunately, this was a direct result from beamline issues unable to be troubleshooted by the Beamline Scientist during that beamtime.

Analysis of dried defibrinated blood in KBr using the MCT_N detector (Figure 4-25) exhibited change in spectra over time (4.8 hours), where a peak at 1214 cm^{-1} develops, indicative of protein nature [116]. This spectral behaviour may be an indication of deoxygenation or structural decay under the beamline's vacuum. As such, the pellet sample preparation method may not be appropriate for haemoglobin FIR analysis. Additionally, spectra exhibit fringing which may be from a resonance effect due to the protein structure, particularly when dried. This may also explain the greater absorbance and less distinct peaks for proteins containing iron. Otherwise, the spectra could reflect a large amount of vibrational possibilities as discussed previously.

5.4.2 Paraffin Wax Pellets

Compounds mixed in paraffin wax (transparent in FIR as discussed with the beamline Scientist) flakes then pressed into a pellet are thought to reduce interaction with water, however preparations presented physical problems; the wax is malleable and escapes the steel sleeve when compressed by the pushing rod. This creates inhomogeneous pellets as samples 'stick' to the wax rather than become incorporated. Analyses presented questionable spectra (Figures 4-36 to 4-40) as oscillations and inconsistencies were observed; when samples were reheated to 298

K after freezing, they did not return their original spectral profile. It is deduced that this is due to either alteration to the pellet's orientation in the sample compartment under vacuum during analysis, or an effect of cryogenic analysis where the wax may cool, become brittle and contract. Both are confirmed as pellets were concave and popped, forming a crack, when surveyed after analysis. In this condition, synchrotron light interacts with the interfaces of the pellet and is reflected internally, which may have contributed to the spectra results. It should also be considered that the duplicate may represent the sample when still chilled due to the programmed temperature control delay, which will be discussed later. Comparing to pure pellet results, no characteristic peaks were observed for biliverdin when using paraffin wax, however some expected peaks for bilirubin and bilirubin conjugate are exhibited. Notably, bilirubin conjugate needs to be at a concentration of 2:1 (sample:wax) or greater to observe the characteristic 300 cm^{-1} peak also seen in its pure pellet form.

5.4.3 Diamond Window Liquid Cells

The concentrations of samples analysed in pellets provided an indication of the amount required for a diamond window liquid cell (DWLC). DWLC's were employed as an alternative method for analysing samples in liquid phase as this may be more appropriate for a biological setting, such as a bruise. The engineering of the cells is such that varying the spacer, varies the pathlength and hence amount of liquid can be encompassed. As the spacer volume is increased from $5\text{ }\mu\text{m}$ to $50\text{ }\mu\text{m}$, the absorbance of solvent also increases (Figure 4-45), hence volume and absorbance are proportional [104]. Technically a sample concentration at 50:50 ratio analysed in a $10\text{ }\mu\text{m}$ spacer should require a background subtraction from the appropriate solvent analysed with a $5\text{ }\mu\text{m}$ spacer. A random user error that needs to be considered in this is pipetting volume variation. Supplementary information gathered from these spectra is that each spacer has a workable wavenumber range, for example if using the $50\text{ }\mu\text{m}$ spacer, the wavenumber range for usable analysis is approximately $60\text{-}360\text{ cm}^{-1}$ as absorbance of water saturates the detector above 360 cm^{-1} .

The spacers that show suitability over the largest range of wavenumbers is the $20\text{ }\mu\text{m}$ spacer ($60\text{-}480\text{ cm}^{-1}$) and the $5\text{ }\mu\text{m}$ spacer ($60\text{-}1000\text{ cm}^{-1}$). Analysis of DWLC's A, B

and C with their respective 5, 10 and 20 μm spacers (Figures 4-46 to 4-48) shows that the greatest variation is present when using the 10 μm spacer and the least variation is observed when using the 5 μm spacer. However, the 5 μm spacer volume is very small (0.5 μL from Table 3-1) and hence volatility and characteristics of solvent and sample needs to be considered. Also, variation in absorbance, hence volume between cells was observed when swapping their respective 5 μm spacers (Figure 4-51), whereas this isn't seen for the 20 μm spacers (Figure 4-50), rather spectra is consistent given the cell's windows are the same. This may be due to difficulty in pipetting into a 5 μm spacer as compared to one with larger volume.

Samples in water produced water absorbance, where any contribution to the spectra from the sample was quenched [133]. To remedy this, dimethyl sulfoxide (DMSO) is an organic solvent that was utilised in DWLC analyses, also for cases where non-polar samples have difficulty dissolving in water-based solvents [66]. The 20 μm spacer was also shown to be the most suitable for this organic solvent (Figures 4-52 to 4-54). DMSO- H_6 (non-deuterated) peaks that are confirmed by literature are at 390, 340 and 310 wavenumbers [118]. Two of these are shifted in DMSO- d_6 (deuterated DMSO) indicating deuterated bonding instead of to hydrogens, where peaks exist at 265, 305 & 340 cm^{-1} (see Table 4-3 for comparisons) [134].

Cryogenic analysis of DMSO- d_6 presents additional peaks at 151, 190 & 247 cm^{-1} (Figures 4-56 to 4-59). DMSO- d_6 has a melting point of 20.2 degrees Celsius, boiling point of 190 degrees Celsius and its triple point (the point at which it is in solid, liquid and gas phase) is 18.4 degrees Celsius [135, 136]. As DMSO- d_6 would be deduced in a phase diagram to be denser as a solid compared to as a liquid [1], the extra peaks when cooled in vacuum may be attributed to additional interactions between molecules when in proximity during liquid to solid phase change. For example, as a peak at approximately 150 wavenumbers arises in Figure 4-56, we could be seeing instant liquid to solid transformation.

This concept is strengthened by the peak disappearing when it reaches melting point (liquid state) of approximately 24 degrees Celsius when warmed, returning to original spectral characteristics (Figures 4-60 to 4-62), corroborating the concept of

molecular interaction when cold. Another cycle of cooling and heating generally produced similar results (Figures 4-63 to 4-68). Similar results are gathered from cryogenic analysis of DMSO-H₆ (Figures 4-72 to 4-74), however additional peaks are observed at 98, 123, 148, 164, 258, 307, 329, 389 & 440 cm⁻¹. Thus, spectra generated during the cryogenic process is highly dependent on temperature. This offers the ability to investigate characteristic differences between analyte molecular interactions, however as discussed later these were not found in haemoglobin and its derivatives.

Bubbles were observed in the cell post-cryogenic analysis (Figure 4-49) which didn't affect spectra if the cell was loosened to release the gas, then tightened and re-analysed (Figures 4-69 & 4-70). Sample compartment vacuum is not a cause as investigated and shown in Figure 4-71. Bubbles were present for all DLWC samples analysed cryogenically (eg. Figure 4-75). It is considered that the bubbles could be dissolved gases in liquid and their appearance is susceptible to vacuum and changing temperatures, where they do not redissolve in solution.

Relating to cryogenic analysis, a temperature control reading delay of several minutes is observed, where the sample takes time to equilibrate to the temperature reading output by the thermocouple. There is also an interruption in temperature profile data when ice becomes stuck in the funnel feeding liquid nitrogen into the cryostat during cooling. Hence it is appreciated that cryogenic cycles require regular attention during analysis, contributing to the tribulations of analysis using DWLC's.

Other solvents explored considering variable sample solubility in DWLC analysis were chloroform, ethanol and methanol. The spectrum of chloroform (Figure 4-76) presents large oscillations likely due to a sample change during analysis that is solvent evaporation. This is confirmed by the droplets observed on the inside of the DWLC in Figure 4-77. It is noted that assembly of the cell takes time which allows for evaporation of solvent. Methanol and ethanol presented similar results to chloroform (Figures 4-78 & 4-79), although methanol evaporated faster than ethanol.

Human haemoglobin in water analysed in a DWLC exhibited inconsistent spectra with change in spacer (Figure 4-80). This may be due to undissolved haemoglobin or

relaxing of the protein in solution within the DWLC during analysis as the signal channel was observed to increase. Such may also be the case for human haemoglobin in DMSO-d₆. Interestingly, a globule was observed in the DWLC for human haemoglobin in DMSO-d₆ (Figure 4-81). A spectrum of this sample (Figure 4-82) produced the inverse of solvent absorption as the background subtracted may contain more vibrations causing these peaks in the background compared to the sample. That is there is larger solvent volume in the cell hence more solvent absorbance from the blank than from the sample. Regular globules observed after analysis (Figure 4-83) may be from interactions with solvent, however these were not reflected in spectra during cooling and heating cycles (Figure 4-84). In fact, cryogenic analysis did not present any significant peaks when excluding inverted solvent (Figures 4-85 to 4-89).

DWLC analysis of defibrinated sheep's blood (Figure 4-90) exhibited water absorbance even though this background was processed to be removed from the spectra. Such is also the case for biliverdin in PBS when analysed in a DWLC using a 20 µm spacer (Figure 4-91). However, some peaks were observed when using the 10 µm spacer, such as the 380 cm⁻¹ peak of which may be a shifted peak observed in the pure pellet (370 cm⁻¹ in Figure 4-5), possibly representing a sample-solvent interaction.

No significant peaks were observed from the spectrum of biliverdin in DMSO-d₆ (Figure 4-94), perhaps due to biliverdin being completely solvated or biliverdin signals are masked by the solvent, as the concentration analysed (140 mg/mL) should yield results (see Figure 4-95 for visual spread and colour of sample in DWLC). The peak at 560 cm⁻¹ may be present on account of sample compartment windows or synchrotron light [126] and was later observed in other biliverdin spectra. However, the peak could also be from a vibration attributed to pyrrole groups [137], although shifted possibly due to a combination of this functional group in one molecule and electronegativity of additional C=O functionality in biliverdin, or because it is in liquid phase.

Biliverdin slurry with sodium hydroxide (Figure 4-92) produced a spectrum with weak and broad biliverdin signals observed in the pure pellet (see Figure 4-93 for

comparisons), which may be due to interaction of biliverdin with solvent. Although it is considered that the spectrum may possess an undertone of large oscillation masking possible peaks.

Powdered biliverdin in a DWLC cracks the windows as shown in Figure 4-97. Further cracking is probable when mounting the cell to the cryostat for analysis as illustrated in Figures 4-98 to 4-99. A biliverdin spectrum was produced from this nonetheless (Figure 4-96) matching all peaks visualised from the pure pellet analysed (Figure 4-5). Although this analysis is successful in producing biliverdin spectra, it may represent biliverdin when in solid state, hence is not reflective of biliverdin in solution.

Solution analysis cannot be carried out in cracked DWLC's as previous sample residue in cracks may cause contamination. Also, the cell may leak solution through the cracks, particularly under vacuum conditions such as that in the sample compartment. See Figure 4-100 for an example of both circumstances. A cell with a crack in the window may also create internal reflection and/or diffraction from the cracked edges of diamond, which may shift beam reflection upon exit from the cell in a different direction to that of incident radiation and not be detected by the detector. Ultimately, this could increase the effects of any fringing that may occur due to differences in refractive indices between the material and diamond windows. With relation to fringing, some spectra were corrected by applied computational algorithms, although it is noted that there is loss of information with smoothing functions.

Another cell was employed to continue investigation of biliverdin solvation and the amount required to produce characteristic peaks. Biliverdin at concentration of 520 mg/mL in DMSO-d₆ was examined (Figure 4-101) providing a peak at 370 cm⁻¹, which is also present in the pure pellet. Examination of the DWLC containing sample after analysis revealed crystallisation (Figures 4-103) that was not present prior to analysis (Figure 4-102). Hence the 370 cm⁻¹ peak may represent a vibration due to solid state only, an attribute from excessively high concentration, and the spectrum may represent a combination of solvated as well as crystallised sample. It

should be considered that a cause of crystallisation is solvent evaporation over time in the sample test tube, cooling the sample which lowers energy required for interactions hence vibrations, or that recrystallisation occurred in vitro.

Crystallisation in biliverdin solutions of concentrations below 500 mg/mL (Figures 4-105 & 4-106) is not observed, even with or during cryogenic analysis (Figures 4-107 to 4-111) possibly due to the lower concentration, hence reduced chance of molecular interaction to cause crystallisation. Crystallisation also did not occur in duplicate analysis (Figure 4-104) but is observed in a triplicate analysis (Figure 4-113), although no significant peaks were detected (Figure 4-112). It is possible that a crystal growth phenomenon may have ensued in the original and triplicate sample where a single crystal was present to initiate a recrystallisation process, transpiring at different times during analysis. This rationalises the lack of the 370 cm^{-1} peak in the triplicate, although the peak was also not observed during cryogenic analysis.

Preparations of biliverdin in methanol (Figure 4-114) and paraffin oil (Figure 4-115) provided inhomogeneous suspensions of sample in solvent and presented no significant spectral peaks on account of this sample inhomogeneity. This was also experienced by the bilirubin in methanol (Figure 4-130) and paraffin oil (Figure 4-131) preparations. Cryogenic analysis also appeared to dry the DWLC's of methanol and create a large amount of bubbles with paraffin oil (Figure 4-132) which translated to large spectral oscillation. It is noted that sample compartment pressure didn't appear to fluctuate, only decreased over time as expected, hence change to sample composition or behaviour such as evaporation and escape of solvent from the cell is not reflected. However, it is possible that solvent inside the cell congregates to the rubber O-ring seal, away from the central windows to escape the cell under vacuum. The loss of solvent from the beam path may also justify inverted solvent peaks observed in analyses during this thesis.

Due to the volatility of chloroform and ethanol, spectra of bilirubin preparations in these solvents produced noise or undulating oscillations (Figures 4-125, 4-126 & 4-128). A remedy attempted was an increase in solvent concentration and lower sample concentration, however the preparations present inhomogeneity, where in

chloroform, a circle of particles is observed (Figure 4-127) and in ethanol bilirubin is a suspension in solvent (Figure 4-129).

Bilirubin in plasma at various concentrations including that expected in the blood and a slurry, presents spectra of water (Figures 4-116 to 4-118), which masked any peaks associated with this molecule. Bilirubin is also shown not to be transparent when in liquid phase when analysed in DMSO-d₆ (Figure 4-119) which presented characteristic bilirubin peaks between 400-640 cm⁻¹ when the pigment is analysed in solid state, inferring bilirubin is in solid state; it may not be fully solvated. Incubation (40 degree Celsius) of bilirubin in DMSO-d₆ to relax the compound into solvent presented a spectrum with a large amount of noise (Figure 4-120), where peaks are difficult to distinguish. This was overcome by doubling the spacer size and sample concentration (Figure 4-121) where characteristic bilirubin peaks between 400-640 cm⁻¹ were detected again. Leaving the solution overnight presented no spectral change (Figure 4-122).

Cryogenic analysis of bilirubin in deuterated DMSO-d₆ shows an isosbestic point (Figure 4-124) indicating sample change within the first 14 minutes of analysis time, which may be assigned to either the sample relaxing in or precipitating from solution. This is supported by the branched structures observed in the cell post-analysis (Figure 4-123), where it appears bilirubin in solvent has formed rivers between vacuum gaps. As postulated earlier, solvent may escape the cell or congregate to the O-ring in the cell, which may also be the case here hence the unique sample change behaviour.

In many instances where bilirubin was analysed in a DWLC, the solutions appeared to be suspended particles of pigment in solvent rather than dissolved. This leads to the investigation of bilirubin conjugate in similar solvents, based on the understanding that in a bruise, bilirubin will be in a soluble form. Bilirubin conjugate in water presented water absorbance (Figure 4-133). Significantly, characteristic bilirubin conjugate peaks observed in pellets were detected as very weak and broad vibrations (Figure 4-135) and this needs to be achieved with high concentrations (compared to Figure 4-134), although it is noted that Figure 4-134 may contain the

similar 540 cm^{-1} peak as observed at higher concentration (Figure 4-135). These results may validate the notion that solvated or dissolved compound may not be identified due to interactions with solvent, the vibrations for which are unclear in the FIR region of the electromagnetic spectrum.

5.4.4 ATR-FIR Spectroscopy

ATR at the Australian Synchrotron could be carried out on the FIR/THz beamline external to the instrument's vacuum, which proves suitable for samples in solid and liquid phase. Some considerations for this novel technique in analysis of bruise components is that the angle of incidence is set with one reflection, and the depth of penetration at 100 cm^{-1} is approximately $200\text{ }\mu\text{m}$, as compared to $20\text{-}30\text{ }\mu\text{m}$ at 500 cm^{-1} where wavelength is proportional to depth of penetration; wavenumber and depth of penetration are inversely proportional. These analyses are qualitative hence refractive index corrections (to reduce divergence of synchrotron beam focus thus apparent saturation and fringing) are not applied and standards to measure against are reliable. Additionally, strong absorption at 725 wavenumbers due to the PE window in the beamline [117].

ATR-FIR haemoglobin-based samples exhibit saturation or noise at lower wavenumbers although these are explored when blood is in PE pellet form. In Figure 4-177 liquid blood provides similar spectra with or without the use of a retainer. Although it is evident that greater resolution is acquired with dried blood samples. Whether blood is dried overnight or with fan assistance spectra is alike (Figure 4-177) and there is also little variance between various blood types (Figure 4-178). Additionally, human haemoglobin in plasma produces analogous spectra to that of sheep blood (Figure 4-181). Notably, human haemoglobin flakes (as supplied in purchased materials) require grinding to fine powder to achieve spectral resolution (Figure 4-182) as this increases surface contact with the ATR crystal (flake surfaces may create diffraction).

As mentioned earlier in this discussion, methaemoglobin formation in vitro produced partially oxidised samples, hence stored blood samples from 2016 that exhibited oxidation breakdown were analysed giving Figure 4-180. Alike human haemoglobin,

methaemoglobin samples also present comparable spectra to that of sheep's blood (oxyhaemoglobin). Such is indicative of the oxidative state of iron in haemoglobin possibly being spectrally transparent or masked by a variety of other protein vibrations attributed to components in blood in this analysis [138].

Haemoglobin displays aliphatic chain C-C (peaks at 325, 351, 374 & 618 cm^{-1}), metal-oxygen (peaks at 325, 351, 374, 411, 441 & 456 cm^{-1}), S-S (peaks at 441, 456 & 520 cm^{-1}), amide α -helix (520 cm^{-1} peak), amide IV/V/VI (peaks at 520 & 618 cm^{-1}) and $-\text{CH}_2\text{CONH}-$ (618 cm^{-1} peak) vibrations [127-132]. The broad character in spectra of blood and human haemoglobin is prominently reflected in ferritin spectra (Figure 4-195). This spectral signature is consistent with that reported in literature for globular proteins, which states amino acids may be responsible for many distinct vibrations (such as the torsion of the peptide backbone and skeletal deformation) that all contribute to the broad absorptions observed [128, 138]. This is also in line with the very low amplitude readings, hence high absorbance of synchrotron radiation when analysing haemoglobin and ferritin.

ATR-FIR of biliverdin (Figure 4-183) presented crystal lattice/amide VII (peaks at 63, 100, 135, 179 & 191 cm^{-1}), aliphatic chain C-C (Peaks at 266, 294, 298, 340, 371 & 640 cm^{-1}), amide C=O or C-N-N (440 cm^{-1} peak), amide IV/V/VI (peaks at 535, 558, 586 & 640 cm^{-1}) and in-plane amide I-IV (640 cm^{-1} peak) vibrations [127-132]. Bilirubin (Figure 4-186) gave crystal lattice/amide VII (peaks at 93, 102, 131, 146, 162 & 230 cm^{-1}), aliphatic chain C-C (Peaks at 230, 298, 330, 364, 387, 624, 660 & 663 cm^{-1}), amide C-N-N (435 cm^{-1} peak), amide IV/V/VI (peaks at 545, 598, 624, 660 & 663 cm^{-1}), in-plane amide I-IV (peaks at 624, 660 & 663 cm^{-1}) and $-\text{CH}_2\text{CONH}-$ (624 cm^{-1} peak) vibrations [127-132]. From this, the main difference between the two pigments observed is the 440 cm^{-1} peak in biliverdin indicating that it contains carbonyl functionality bilirubin lacks, suggesting hydrogen bond presence in bilirubin. Other functionality is shown to be similar although the vibrations occurring at discrete wavenumbers can be attributed to variation in intra- or intermolecular bonding.

Bilirubin conjugate analysed using ATR in the FIR region (Figure 4-189) presents

saturation below 210 cm^{-1} which can be attributed to a refractive index correction not being applied. This compound exhibited aliphatic chain C-C (peaks at 298, 348, 397, & 617 cm^{-1}), amide C-C-N (435 cm^{-1} peak), S-S ($435, 468$ & 525 cm^{-1} peaks) and amide IV/V/VI (ν) vibrations [127, 130]. These were reduced in intensity when bilirubin conjugate is exposed to a nitrogen atmosphere (Figure 4-192), which may be due to the hygroscopic nature of the compound [139].

ATR-FIR spectral profiles of biliverdin, bilirubin and bilirubin conjugate (Figure 4-189) confirm those created from pure (biliverdin) and PE (bilirubin & bilirubin conjugate) pellets (Figures 4-13 & 4-42), however extend the range of analysis, resolve peaks (in the case of bilirubin conjugate) and do not require dilution. Biliverdin and bilirubin (Figure 4-193) as well as bilirubin and bilirubin conjugate (Figure 4-190) mixtures were hence undiluted and analysed to provide equivalent, if not enhanced results as seen previously with pellets.

Peaks for biliverdin in blood (Figure 4-184) appear to have shifted to lower wavenumbers as compared to the dry sample of biliverdin. This may be due to hydrogen bonding stabilisation of secondary nitrogen functionality by plasma from blood, hence interaction with plasma [131]. This is also observed for bilirubin conjugate in blood (Figure 4-191). In contrast, when biliverdin is in blood at a lower concentration and left to dry, only peaks attributed to dried blood are identified (Figure 4-185). Hence the peak shift may only be observed with larger pigment quantities, possibly because larger amounts of material in a set volume promotes interaction.

ATR-FIR of bilirubin (Figure 4-186) shows that 0.8 mg bilirubin is detectable should it be fully in contact with the ATR diamond window. This is the minimum amount that could be weighed and transferred to the window. The bilirubin in blood sample presented characteristic bilirubin peaks, meaning that at least 0.8 mg was detected by the instrument when bilirubin is in blood, although this is dependent on the contact the pigment has with the crystal surface. It needs to be considered here that the spectrum of bilirubin in blood may be a summation of bilirubin and blood rather than that of solvated bilirubin in blood. Such is also the case for when bilirubin in blood is

dried (Figure 4-187).

Spectra of dried biliverdin and bilirubin in a 1:1 ratio in blood (Figure 4-194) appears to be a summation of characteristic biliverdin and bilirubin peaks previously identified, but also contains a broad absorbance from 300-600 cm^{-1} which may be attributed to blood protein contribution to the spectrum. This indicates that at the concentrations of pigments tested in this scenario, solvation was not reflected. Bilirubin in DMSO- H_6 (Figure 4-188) also presents this behaviour, although it is noted that this is the first spectrum of bilirubin at a low concentration to be detected in DMSO. Such tests the idea of unobservable peaks when compounds are in solvent, however it may be that bilirubin peaks are detected in DMSO in this instance due to solution saturation.

5.5 Concluding Remarks

Overall, the project has provided a greater depth in chemical understanding, through spectroscopic investigations at Flinders University and the Australian Synchrotron (THz/FIR beamline) utilising pure materials, PE, PTFE and paraffin wax pellets, DWLC's and out-of-vacuum ATR of blood and its breakdown products likely to be present in a bruise. MIR and THz/FIR spectroscopy can differentiate the key components responsible for bruise colouration, biliverdin and bilirubin. However, the intermolecular interactions between these compounds with ions and organic material also likely to be present in a bruise environment offer an intermixing physiological process. Alas, there is much concerning the complexities of the molecular environment in a bruise that remains unknown.

6 Future Studies

Issues were experienced when attempting to oxidise fresh blood. Thus, it is suggested that the blood be deoxygenised prior to the addition of sodium nitrite to investigate methaemoglobin formation from undiluted blood samples. In conjunction to this is further investigation of interconversion cycles between oxyhaemoglobin to deoxyhaemoglobin utilising the ISP-REF integrating sphere coupled to the CHEMUSB4-Vis.-NIR spectrophotometer. This set up could also be used to qualitatively and if possible, quantitatively examine the biliverdin to bilirubin conversion with biliverdin reductase in a controlled environment.

The ISP-REF integrating sphere could be coupled to a spectrophotometer of greater resolution to detect minor peaks in the NIR region otherwise saturated by water absorbance and has the potential to be utilised as a portable setup. Scanning time for one spectrum using the sphere setup is also considerably fast, hence the novel apparatus combination may be used as an initial screening technique for mixtures of the variety of compounds analysed in this project, for example a combination of blood, ferritin in solution and bilirubin, to investigate spectral deconvolution. In this sense, there is potential for optimisation for and analysis of real case bruises.

Future analysis at the Australian Synchrotron could be undertaken with beam current higher than 200 mA as to increase spectral quality, and further research and development of the diamond window liquid cells (DWLC's), including solvent suitability (FIR transparent) for biological analyses and reproducibility with spacers and assembly method (sometimes cells needed to be assembled 3 times before analysis as bubbles from uneven clamping are observed), is required for liquid phase analysis progression. Deconvolution of pigments in blood matrices using ATR-FIR is another potential suggestion, where the pigment-solvent interaction is investigated. Modelling and DFT calculations could also be carried out for the pigments to confirm understanding surrounding intramolecular bonding.

Optimisation of cryogenic analyses at the Australian Synchrotron is recommended to improve the delay between thermocouple temperature measurements and true sample

temperature (physically further from the thermocouple) as this may be significant regarding identification of molecular interactions of compounds in frozen forensic samples otherwise not observed. Moreover, crystallisation of compounds in saturated solvent with freezing could be further studied as to investigate liquid to solid state molecular mechanisms.

The analysis of smaller molecules, possibly protein subunits, polypeptide chains, amino acids (eg. Melanin) or iron-containing porphyrins could be attempted to focus on functionality groups and molecular interactions, then compare these results to more complex or convoluted spectra of mixtures of blood with biliverdin and bilirubin, or even other larger proteins such as ferritin. A quantitative approach for this future suggestion is commended. Also, it needs to be considered that vibrational interactions may vary with solvation.

To confirm validation of MIR analyses, it is suggested that ATR analyses be carried out on biliverdin and bilirubin in the same form; either salt or unconjugated. This may involve stability testing of bilirubin as a salt where bilirubin is solvated in an alkali solution, then acid is added to balance out the counterion on bilirubin and precipitate a salt for comparison against biliverdin hydrochloride. Refractive index corrections applied in these analyses would also reduce time processing spectra, however this insinuates a study regarding refractive indices of the breakdown components in a bruise.

Additionally, the study of biliverdin destruction when exposed to UV light over time and if this influences visualisation of haemoglobin breakdown is proposed.

It was anticipated that the novel spectroscopic techniques and resultant spectral information acquired in this thesis be applied to bruised human tissue. Unfortunately, this thesis did not reach this goal, however this work has the potential to contribute to the greater understanding of the behaviour of chemical components that may be found in and contribute to the apparent colour of a bruise, ultimately assisting in determination of the process of compound breakdown and hence bruise age.

7 References

1. Campbell, N.A., Reece, J.B. & Meyers, N., *Biology*. 7th edn. ed. 2006, Frenchs Forest NSW: Pearson Education Australia.
2. Sherwood, L., *Human Physiology: From Cells to Systems*. Sixth ed. 2007, USA: Thomson Brooks/Cole.
3. Mann, E.B., Motterlini, R., *CO and NO in medicine*. Chemical Communications, 2007: p. 4197-4208.
4. Shuster, S., Black, M. M. & McVitie, E., *The influence of age and sex on skin thickness, skin collagen and density*. British Journal of Dermatology, 1975. **93**(6): p. 639-643.
5. ForensicMed. *bruises*. 2012 [28 August, 2013]; Available from: <http://www.forensicmed.co.uk/wounds/blunt-force-trauma/bruises/>.
6. Langlois, N.E.I., *The science behind the quest to determine the age of bruises-a review of the English language literature*. Forensic Science Medicine and Pathology, 2007. **3**: p. 241-251.
7. Randeberg, L.L., Winnem, A., Blindheim, S. Haugen, O.A. & Svaasand, L.O., *Optical Classification of Bruises*. Proceedings of SPIE, 2004. **5312**: p. 54-64.
8. Page, M., Taylor, J. & Blenkin, M., *Expert Interpretation of Bite-mark Injuries - A Contemporary Qualitative Study*. Journal of Forensic Sciences, 2013. **58**(3): p. 664-672.
9. Kim, O., McMurdy, J., Lines, C., Duffy, S., Crawford, G., Alber, M., *Reflectance spectrometry of normal and bruised human skins: experiments and modeling*. Physiological measurement, 2012. **33**(2): p. 159.
10. Wankhede, A., *The bruise which depicted the pattern of subjacent bone*. Forensic Science International, 2009. **186**: p. 5-7.
11. Langlois, N.E.I., Gresham, G., *The Ageing of Bruises: A Review and Study of the Colour Changes with Time*. Forensic Science International, 1991. **50**: p. 227-238.
12. Koehler, S.A., Wecht, C.H. , *Postmortem, Establishing the cause of death*. 2006, Smithfield NSW: Gary Allen Pty Ltd.
13. Vanezis, P., *Interpreting bruises at necropsy*. Journal of Clinical Pathology, 2001. **54**: p. 348-355.
14. Kienle, A., Lilge, L., Vitkin, I., Patterson, M., Wilson, B., Hibst, R. & Steiner, R., *Why do veins appear blue? A new look at an old question*. Applied Optics, 1996. **35**(7): p. 1151-1160.
15. Edwards, E.A., Duntley, S.Q., *The Pigments and Color of Living Human Skin*. The American Journal of Anatomy, 1939. **65**(1): p. 1-33.
16. Lines, C., Kim, O., Duffy, S., Alber, M. & Crawford, G.P. *Modelling and Measuring Extravascular Hemoglobin: Aging Contusions*. Proceedings of SPIE, 2011. **8087**, DOI: 10.1117/12.896610.
17. Yajima, Y., Funayama, M., *Spectroscopic and tristimulus analysis of the colors of subcutaneous bleeding in living persons*. Forensic Science International, 2006. **156**: p. 131-137.
18. Pilling, M.L., Vanezis, P., Perrett, D. & Johnston, A., *Visual assessment of the timing of bruising by forensic experts*. Journal of Forensic and Legal Medicine, 2010. **17**: p. 143-149.

19. Watchman, H.M., Walker, G.S., Randeberg, L.L., & Langlois, N.E., *Re-oxygenation of post-mortem lividity by passive diffusion through the skin at low temperature*. Forensic Science, Medicine, and Pathology, 2011. **7**(4): p. 333-335.
20. Randeberg, L.L., Winnem, A.M., Langlois, N.E., Larsen, E.L.P., Haaverstad, R., Skallerud, B., Haugen, O.A. & Svaasand, L.O., *Skin Changes Following Minor Trauma*. Lasers in Surgery and Medicine, 2007. **39**: p. 403-413.
21. Randeberg, L.L., Haugen, O.A., Haaverstad, R. & Svaasand, L.O., *A Novel Approach to Age Determination of Traumatic Injuries by Reflectance Spectroscopy*. Lasers in Surgery and Medicine, 2006. **38**: p. 277-289.
22. Randeberg, L.L., Hernandez-Palacios *Hyperspectral Imaging of Bruises in the SWIR Spectral Region*. Proceedings of SPIE, 2012. **8207**, DOI: 10.1117/12.909137.
23. Academy, K. *Components of blood*. 2018 [24 June 2018]; Available from: <https://www.khanacademy.org/science/biology/human-biology/circulatory-pulmonary/a/components-of-the-blood>.
24. Kulkarni, R., Basu, D., *Overview of blood components and their preparation*. Indian Journal of Anaesthesia, 2014. **58**(5): p. 529-537.
25. Nelson, D.L., Cox, M.M., *Lehninger Principles of Biochemistry*. Fifth ed. 2008, New York, U.S.A.: W. H. Freeman and Company.
26. Mandal, A. *Macrophage Function*. 2018 [24 June 2018]; Available from: <https://www.news-medical.net/life-sciences/Macrophage-Function.aspx>.
27. Tao, X., Xu, A., *Amphioxus Immunity: Tracing the Origins of Human Immunity*. Chapter 2 - Basic Knowledge of Immunology. 2016, London Wall, UK: Elsevier Inc.
28. McDonagh, A.F., Lightner, D.A., *'Like a Shrivelled Blood Orange'- Bilirubin, Jaundice, and Phototherapy*. Pediatrics, 1985. **75**(3): p. 443-457.
29. Cotton, F.A., Wilkinson, G. & Gaus, P.L. , *Basic Inorganic Chemistry*. 7th edn ed. 1995, Canada US: John Wiley & Sons, Inc.
30. Perutz, M., Rossmann, M., Cullis, A., Muirhead, H., Will, G. & North, A., *Structure of Haemoglobin: A Three-Dimensional Fourier Synthesis at 5.5-Å Resolution, Obtained by X-Ray Analysis*. Nature, 1960. **185**: p. 416-422.
31. Bian, K., Gao, Z., Weisbrodt, N. & Murad, F., *The nature of heme/iron-induced protein tyrosine nitration*. Proceedings of the National Academy of Sciences of the United States of America, 2003. **100**(10): p. 5712-5717.
32. Constantopoulos, K., *CPES3162 Metal Ions in Biology Lectrue: Dioxigen Carriers, Flinders University*. 2010.
33. Constantopoulos, K., *CPES3162 Metal Ions in Biology Lecture: Introduction to metalloproteins, Flinders University*. 2010.
34. Soares, M., Hamza, I., *Macrophages and iron metabolism*. Immunity, 2016. **44**(3): p. 492-504.
35. Maines, M.D., Cohn, J. , *Bile Pigment Formation by Skin Heme Oxygenase: Studies on the Response of the Enzyme to Heme Compounds and Tissue Injury*. The Journal of Experimental Medicine, 1977. **145**.
36. Moretta, A., Langlois, NEI & Walker, S *CHEM3702 Research Project Report*. 2001, Flinders University.
37. Otterbein, L.E., Choi, A.M.K., *Heme oxygenase: colors of defense against cellular stress*. American Journal of Physiology - Lung Cellular and

- Molecular Physiology, 2000. **279**: p. L1029-L1037.
38. Sully, C., Walker, G. & Langlois N.E.I., *Investigation into the potential for post-mortem formation of carboxyhemoglobin in bodies retrieved from fires*. Forensic Science, Medicine, and Pathology, 2018. **Jul 4**.
 39. Carrico, R.J., Peisach, J. & Alben, J.O. , *The Preparation and Some Physical Properties of Sulfhemoglobin*. The Journal of Biological Chemistry, 1977. **253**(7, Issue of April 10): p. 2386-2391.
 40. Dijkhuizen, P., Buursma, A., Gerding, A.M. & Zijlstra, W.G. , *Sulphaemoglobin. Absorption spectrum, millimolar extinction coefficient at $\lambda=620\text{nm}$, and the intergerence with the determination of haemoglobin and haemiglobincyanide*. Clinica Chimica Acta, 1977. **79 (1977)**: p. 479-487.
 41. Ferguson, J., Langlois, N.E.I. & Walker, S *CHEM3702 Research Project Report*. 2009, Flinders University.
 42. Berzofsky, J.A., Peisach, J. & Blumberg, W.E., *Sulfheme Proteins I. Optical and Magnetic Properties of Sulfhemoglobin and Its Derivatives*. The Journal of Biological Chemistry, 1971. **246**(10): p. 3367-3377.
 43. Hauowitz, H., *The Prosthetic Group of Sulphaemoglobin*. 1940, Institute of Med/Vet Science: Turkey. p. 771-781.
 44. Park, C.M., Nagel, R.L., Blumberg, W.E., Peisach, J. & Magliozzo, R.S., *Sulfhemoglobin: properties of partially sulfurated tetramers*. The Journal of Biological Chemistry, 1986. **261**(July 5): p. 8905-8911.
 45. Siggaard-Andersen, O., Norgaard-Pedersen, B. & Rem, J., *Hemoglobin Pigments. Spectrophotometric Determination of Oxy-, Carboxy-, Met-, and Sulfhemoglobin in Capillary Blood*. Clinica Chimica Acta, 1972. **42**: p. 85-100.
 46. Pimstone, N.R., Tenhunen, R., Seitz, P.T., Marver, H.S. & Schmid, R. , *The Enzymatic Degradation of Hemoglobin to Bile Pigments by Macrophages*. Department of Medicine, University of California, San Francisco, 1971: p. 1264-1281.
 47. Umbreit, J., *Methemoglobin - It's Not Just Blue: A Concise Review*. American Journal of Hematology, 2007. **82**: p. 134-144.
 48. Bradberry, S.M., Aw, T-C., Williams, N.R. & Vale, J.V., *Occupational Methaemoglobinaemia*. 2001, Occupational Toxicology Section, National Poisons Information Service, City Hospital, Birmingham: UK. p. 611-616.
 49. Weiss, S., *Neutrophil-mediated Methemoglobin Formation in the Erythrocyte*. The Journal of Biological Chemistry, 1982. **257**(6): p. 2947-2953.
 50. Dixon, S. *Neutrophils*. Colon Cancer 2009 21 July, 2009 23 August, 2013]; Available from: <http://coloncancer.about.com/od/glossary/g/neutrophils.htm>.
 51. Hughes, V., Ellis, P. & Langlois, N.E.I., *The perception of yellow in bruises*. Journal of Clinical Forensic Medicine, 2004. **11**: p. 257-259.
 52. Zahedi, M., Bahrami, H., Shahbazian, S. Safari, N. & Ng, S., *An ab initio/hybrid (ONIOM) investigation of biliverdin isomers and metal-biliverdin analogue complexes*. Journal of Molecular Structure (Theochem), 2003. **633**: p. 21-33.
 53. Chen, D., Brown, J., Kawasaki, Y., Bommer, J. & Takemoto, J., *Scalable production of biliverdin IX α by Escherichia coli*. BMC Biotechnology, 2012. **12**(89).
 54. Tenhunen, R., Marver, H., Pinstone, N.R., Trager, W.F., Cooper, D.Y., Schmid, R., *Enzymic degradation of heme. Oxygenative cleavage requiring*

- cytochrome P-450*. *Biochemistry*, 1972. **11**(9): p. 1716-1720.
55. Hughes, V.K., Ellis, P.S., Burt, T. & Langlois, N.E.I., *The practical application of reflectance spectrophotometry for the demonstration of haemoglobin and its degradation in bruises*. *Journal of Clinical Pathology*, 2004. **57**: p. 335-343.
 56. McDonagh, A., Palma, L., *Preparation and Properties of Crystalline Biliverdin IX α* . *Biochem Journal*, 1980. **189**: p. 193-208.
 57. Mann, F., Sheard, C. & Bollman, J., *The formation of bile pigment from hemoglobin*. *American Journal of Physiology*, 1926. **76**: p. 306-315.
 58. Motterlini, R., Clark, J.E., Foresti, R., Sarathchandra, P., Mann, B.E. & Green, C.J., *Carbon Monoxide-Releasing Molecules : Characterization of Biochemical and Vascular Activities*. *Journal of the American Heart Association*, 2002. **90**(17-24).
 59. Lay, P. *Multi-modal imaging/Mapping: Understanding Disease Processes and Their Treatments*. in *Australasian Conference on Vibrational Spectroscopy*. 2015. Australian Synchrotron, Melbourne, Australia.
 60. Fedorko, M., Cross, N. & Hirsch, J., *Appearance and Distribution of Ferritin in Mouse Peritoneal Macrophages in Vitro After Uptake of Hereologous Erythrocytes*. *The Journal of Cell Biology*, 1973. **57**: p. 289-305.
 61. Whitby, F.G., Phillips, J.D., Hill, C.P., McCoubrey, W. & Maines, M.D., *Crystal Structure of a Biliverdin IX α Reductase Enzyme–Cofactor Complex*. *Journal of Molecular Biology*, 2002. **319**: p. 1199-1210.
 62. Scientific, T., *Total Bilirubin Reagent: Acid Diazo Method*. 2008: Sussex UK.
 63. Nunn, J., *Spectroscopic Identification and Analysis of Haemoglobin Derivative Coloured Components to Determine Aging of Bruises*, in *Chemical and Physical Sciences*. 2012, Flinders University: Australia. p. 36.
 64. Juttner, F., Stiesch, M. & Ternes, W., *Biliverdin: the blue-green pigment in the bones of the garfish (Belone belone) and eelpout (Zoarces viviparus)*. *European Food Research and Technology*, 2013. **236**: p. 943-953.
 65. McDonagh, A., Assisi, F., *Commercial Bilirubin: A Trinity of Isomers*. *FEBS Letters*, 1971. **18**(2): p. 315-317.
 66. Ostrow, J.D., Celic L., *Bilirubin Chemistry, Ionisation and Solubilization by Bile Salts*. *Hepatology*, 1984. **4**(5): p. 38S-45S.
 67. WebMD. *Bilirubin Blood Test, Prep, Results*. 2012 [21 June 2012]; Available from: <http://www.webmd.com/digestive-disorders/bilirubin-15434?page=3>.
 68. Denney, J.W., *Assay for total and direct bilirubin*, in *US 6326208 B1*. 2001, Synermed International Inc: US.
 69. Puranam, K., Raghothama, S. & Balaram, P., *A 1H-NMR study of bilirubin IX- α solubilization by cholate micelles: application of nuclear Overhauser effects*. *Biochimica et Biophysica Acta*, 1987. **922**: p. 67-77.
 70. Kleiner, O., Ramesh, J., Huleihel, M., Cohen, B., Kantarovich, K., Levi, C., Polyak, B., Marks, R., Mordehai, J., Cohen, Z. & Mordechai, S., *A comparative study of gallstones from children and adults using FTIR spectroscopy and fluorescence microscopy*. *BMC Gastroenterology*, 2002. **2**(3).
 71. Bunn, H.F., Goldman L, & Schafer AI, *Approach to the anemias*, in *Cecil Medicine*. 2011, Saunders Elsevier: Philadelphia, Pa.
 72. Hoffman, R., Benz, E.J., Shattil, S.J., *Hematology: Basic Principles and*

- Practice*. 4th edn ed. 2005, Philadelphia, Pa: Churchill Livingstone.
73. Marchetti, A., Parker, M.S., Moccia, L.P., Lin, E.O., Arrieta, A.L., Ribalet, F., Murphy, M.E.P., Maldonado, M.T. & Armbrust, E.V., *Ferritin is used for iron storage in bloom-forming marine pennate diatoms*. *Nature*, 2009. **457**: p. 467-470.
 74. Sipos, P., Berkesi, O., Tombacz, E., Pierre, T. & Webb, J., *Formation of spherical iron(III) oxyhydroxide nanoparticles sterically stabilized by chitosan in aqueous solutions*. *Journal of Inorganic Biochemistry*, 2003. **95**: p. 55-63.
 75. Fischbach, F., Gregory, D., Harrison, P., Hoy, T. & Williams, J., *On the Structure of Hemosiderin and its Relationship to Ferritin*. *Journal of Ultrastructure REsearch*, 1971. **37**: p. 495-503.
 76. McAuley, G., Schrag, M., Sipos, P., Sun, W., Obenaus, A., Neelavilli, J., Haacke, E., Holshouser, B., Madacsi, R. & Kirsch, W., *Quantification of Punctate Iron Sources Using Magnetic Resonance Phase*. *Magnetic Resonance in Medicine*, 2010. **63**: p. 106-115.
 77. Webb, J., St.Pierre, T.G., Tran, K.C., Chua-anusorn, W., Macey, D.J. & Pootrakul, P., *Biologically significant iron(III) oxyhydroxy polymers: Mössbauer spectroscopic study of ferritin and hemosiderin in pancreas tissue of β -thalassemia/hemoglobin E disease*. *Inorganica Chimica Acta*, 1996. **243**: p. 121-125.
 78. Nuzzolese, E., Di Vella, G., *The Development of a Colorimetric Scale as a Visual Aid for the Bruise Age Determination of Bite Marks and Blunt Trauma*. *Journal of Forensic Odontostomatology*, 2012. **30**(2): p. 1-6.
 79. West, M., Hayne, S. & Barsley, R., *Wound patterns: detection, documentation and analysis*. *Journal of Clinical Forensic Medicine*, 1996. **3**: p. 21-27.
 80. Lecomte, M., Holmes, T, Kay, DP, Simons, JL & Vintiner SK., *The use of photographs to record variation in bruising response in humans*. *Forensic Science International*, 2013. **231**: p. 213-218.
 81. Kostadino-Petrova, I., Mitevska, E., Janeska, B., *Histological Characteristics of Bruises with Different Age*. *Open Access Macedonian Journal of Medical Sciences*, 2017. **5**(7): p. 813-817.
 82. Beschoner, R., Adjodah, D, Schwab, J, Mittelbronn, M, Pedal, I, Mattern, R, Schluesener, H & Meyermann, R., *Long-term expression of heme oxygenase-1 (HO-1, HSP-32) following focal cerebral infarctions and traumatic brain injury in humans*. *Acta Neuropathology*, 2000. **100**: p. 377-384.
 83. Langlois, N., Olds, K, Ross, C & Byard, R, *Heme oxygenase-1 and heme oxygenase-2 expression in bruises*. *Forensic Science, Medicine and Pathology*, 2015: p. 482-487.
 84. Dictionary, F.P.M., *Invasive definition*. 2012.
 85. Shan, P., Peng, S., Zhao, Y. & Tang, L., *Application of the Polynomial-Based Least Squares and Total Least Squares Models for the Attenuated Total Reflection Fourier Transform Infrared Spectra of Binary Mixtures of Hydroxyl Compounds*. *Applied Spectroscopy*, 2016. **70**(3).
 86. Britannica, E.o.E., *Electromagnetic spectrum*, in *Encyclopaedia Britannica, Inc.* 2018, Encyclopaedia Britannica, inc.
 87. Chu, S., Graybeal, J., Stoner, J., Hurst, G., Chauhan, Y., Chopra, S., Gregersen, E., Lewis, R., Pallardy, R., Promeet, D., Sampaolo, M. & Sinha, S.,

- Spectroscopy*, in *Encyclopaedia Britannica, inc.* 2018.
88. Scafide, K., Sheridan, D., Campbell, J., Deleon, V. & Hayat, M., *Evaluating change in bruise colorimetry and the effect of subject characteristics over time*. *Forensic Science, Medicine and Pathology*, 2013. **9**(3): p. 367-376.
 89. Pavia, D.L., Lampman, G.M., Kriz, G.S. & Vyvyan, J.R. , *Introduction to Spectroscopy*. 4th edn ed. 2009, Belmont USA: Brooks/Cole, Cengage Learning.
 90. Merrill, R., Bartick, E., *Analysis of Ballpoint Pen Inks by Diffuse Reflectance Infrared Spectrometry*. *Journal of Forensic Sciences*, 1992. **37**(2): p. 528-541.
 91. Somma, F., Aloe, P. & Schirripa Spanolo, G., *Defects in UV-vis-NIR reflectance spectra as method for forgery detections in writing documents*. *Journal of Physics: Conference Series*, 2010. **249**(1).
 92. Silva, C., Borba, F., Pimentel, M., Pontes, M., Honorato, R. & Pasquini, C., *Classification of blue pen ink using infrared spectroscopy and linear discriminant analysis*. *Microchemical Journal*, 2013. **109**: p. 122-127.
 93. da Silva, V., Talhavinii, M., Zacca, J., Trindade, B. & Braga, J., *Discrimination of black pen inks on writing documents using visible reflectance spectroscopy and PLS-DA*. *Journal of the Brazilian Chemical Society*, 2014. **25**(9).
 94. Bartick, E., Tungol, M. & Reffner, J., *A new approach to forensic analysis with infrared microscopy: Internal reflection spectroscopy*. *Analytica Chimica Acta*, 1994. **288**(1-2): p. 35-42.
 95. Hoffman, E.B., D., *Paint Analysis Using Visible Reflectance Spectroscopy: An Undergraduate Forensic Lab*. *Journal of Chemical Education*, 2007. **84**(11): p. 1806-1808.
 96. Sauzier, G., Maric, M., Bronswijk, W. & Lewis, S., *Preliminary studies into the effect of environmental degradation on the characterisation of automotive clear coats by attenuated total reflectance infrared spectroscopy*. *Analytical Methods*, 2013. **5**(19): p. 4984-4990.
 97. Robertson, I. *Analysis of Automobile Paint Chips Using an Automated IR Microscope*. *Infrared (IR) Microscopy 2015 August 20, 2018*]; Available from: https://www.perkinelmer.com/lab-solutions/resources/docs/APP_Analysis-Automobile-Paint-Chips-012077_01.pdf.
 98. Jacques, S. *SpectRx develops portable optical spectrometer for monitoring hyperbilirubineamia in newborn infants*. *Oregon Medical Laser Center Newsletter 1997 October 29, 2016*]; Available from: <https://omlc.org/news/nov97/bilirubin11-97.html>.
 99. PerkinElmer, I., *Sphere Accessories User's Guide*, in *UV-Vis Spectroscopy*. 2010, PerkinElmer Ltd: UK. p. 56.
 100. RSC. *Attenuated total reflectance Fourier transform infrared spectroscopy*. 2018 August 27, 2018]; Available from: <http://www.rsc.org/publishing/journals/prospect/ontology.asp?id=CMO:0000763&MSID=C2JM31941A>.
 101. Sciences, P.L.a.A., *FT-IR Spectroscopy Attenuated Total Reflectance (ATR)*. 2005, PerkinElmer, Inc: USA.
 102. ANSTO. *Nuclear Facts, What is synchrotron light?* 2018 August 27, 2018]; Available from: <https://www.synchrotron.org.au/education/nuclear-facts/what-is-synchrotron-light>.

103. ANSTO. *Beamlines FTIR Introduction*. 2018 August 27, 2018]; Available from: <http://archive.synchrotron.org.au/aussyncbeamlines/ftir/introduction>.
104. Falconer, R. *THz spectroscopy of proteins*. in *Australasian Conference on Vibrational Spectroscopy*. 2015. Australian Synchrotron, Melbourne, Australia.
105. ANSTO. *Beamlines FTIR Technical Information*. 2018 August 27, 2018]; Available from: <http://archive.synchrotron.org.au/aussyncbeamlines/ftir/technical-information>.
106. Zhukas, L., Veber, S., Mikenas, T., Yurkin, M., Karpova, E., Maltsev, V., Mamatyuk, V., Echevskaya, L., Bagryanskaya, E. & Zakharov, V., *Size-dependent optical properties of polyethylene powders in far-IR region: On the way to universal matrix*. *Journal of Quantitative Spectroscopy & Radiative Transfer* 2014. **147**: p. 1-7.
107. Appadoo, D. *New & Future Techniques at the THz/Far-IR Beamline*. in *Australasian Conference on Vibrational Spectroscopy*. 2015. Australian Synchrotron, Melbourne, Australia.
108. *Diamond Liquid Cells*. *Optical Components* September 1, 2018]; Diamond Materials:[Available from: http://www.diamond-materials.com/EN/products/optical_components/liquid_cells.htm.
109. Obeidy, P., Tong, P. & Weninger, W., *Research Techniques Made Simple: Two-Photon Intravital Imaging of the Skin*. *Journal of Investigative Dermatology*, 2018. **138**: p. 720-725.
110. Lines, C., Kim, O., Duffy, S., Alber, M. & Crawford, G., *Modelling and Measuring Extravascular Hemoglobin: Aging Contusions*. *Proceedings of SPIE-OSA Biomedical Optics*, 2011. **8087**.
111. Thornton, R., Jolly, R., *The Objective Interpretation of Histopathological Data: An Application to the Ageing of Ovine Bruises*. *Forensic Science International*, 1986. **31**: p. 225-239.
112. Online, P. *Phosphate Buffered Saline | Protocols Online*. 2012 28 July 2012]; Available from: <http://protocolsonline.com/recipes/phosphate-buffered-saline-pbs/>.
113. Hoxter, G., *Suggested Isosbestic Wavelength Calibration in Clinical Analyses*. *Clinical Chemistry*, 1979. **25**(1): p. 143-146.
114. PerkinElmer, I., *UV WinLab Software Guide*, in *UV-Vis Spectroscopy*. 2011: UK. p. 1018.
115. May, J., Hickey, M, Triantis, I, Palazidou, E & Kyriacou, P, *Spectrophotometric analysis of lithium carbonate used for bipolar disorder*. *Biomedical Optics Express*, 2015. **6**(3): p. 1067-1073.
116. Zohdi, V., Wood, B., Pearson, J., Bambury, K. & Black, J., *Evidence of altered biochemical composition in the hearts of adult intrauterine growth-restricted rats*. *European Journal of Nutrition*, 2012. **52**: p. 749-758.
117. Inc., B.O., *Guide for Infrared Spectroscopy*. 2018, Bruker Optics Inc.: USA.
118. Skripkin, M., Lindqvist-Reis, P., Abbasi, A., Mink, J., Perssone, I. & Sandstrom, M., *Vibrational spectroscopic force field studies of dimethylsulfoxide and hexakis(dimethyl sulfoxide)scandium(III) iodide, and crystal and solution structure of the hexakis(dimethyl sulfoxide)scandium(III) ion*. *The Royal*

- Society of Chemistry, 2004: p. 4038-4049.
119. Sigma-Aldrich, *Hemoglobin human*, in *Products*. 2018, Merck KGaA: Germany.
 120. *Near-IR Absorption Bands*. 2013, NDC Infrared Engineering.
 121. *NIR Spectroscopy*, in *A guide to near-infrared spectroscopic analysis of industrial manufacturing processes*. 2013, Metrohm AG: Switzerland.
 122. Munoz, M.E., Gonzalez, J. & Esteller, A. , *Bile pigment formation and excretion in the rabbit*. *Comparative Biochemistry and Physiology. A Comparative Physiology*, 1986. **85**(1): p. 67-71.
 123. Pavia, D., Lampman, G., Kriz, G. & Vyvyan, J., *Introduction to Spectroscopy*. 5th ed, ed. M. Limited. 2015, USA: Sengage Learning.
 124. Feliz, M., Ribo, J., Salgado, A., Trull, F. & Valles, M., *On the ¹H NMR Spectra of Biliverdins with Free Propionic Acid Substituents*. *Monatshefte fur Chemie*, 1989. **120**: p. 445-451.
 125. *Bilirubin*. 2015, Spectral Database for Organic Compounds.
 126. Appaddoo, D., *Beamline Information*. 2018, Beamline Scientist: ANSTO, Australian Synchrotron.
 127. Khoury, Y.E., Hielscher, R., Voicescu, M., Gross, J. & Hellwig, P., *On the specificity of the amide VI band for the secondary structure proteins*. *Vibrational Spectroscopy*, 2011. **55**: p. 258-266.
 128. Fontaine-Vive, F., Merzel, F. Johnson, M.R. & Kearley, G.J., *Gollagen and component polypeptides: Low frequency and amide vibrations*. *Chemical Physics*, 2009. **355**: p. 141-148.
 129. Yvon, H.J., *Raman Data and Analysis - Raman Bands*. 2018, Horiba Jobin Yvon.
 130. Cheam, T., Krimm, S, *Infrared intensities of amide modes in N-methylacetamide and poly(glycine I) from ab initio calculations of dipole moment derivatives of N-methylacetamide*. *Journal of Chemical Physics*, 1984. **82**(4): p. 1631-1641.
 131. Miyazawa, T., Shimanouchi, T. & Mizushima, S., *Characteristic Infrared Bands of Monosubstituted Amides*. *The Journal of Chemical Physics*, 1956. **24**(2): p. 408-418.
 132. Miyazawa, T., Shimanouchi, T. & Mizushima, S., *Normal Vibrations of N-Methylacetamide*. *The Journal of Chemical Physics*, 1958. **29**(3): p. 611-616.
 133. Bambury, K. *Data analysis methods for synchrotron IR microspectroscopy*. in *Australasian Conference on Vibrational Spectroscopy*. 2015. Australian Synchrotron, Melbourne, Australia.
 134. Skripkin, M., Lindqvist-Reis, P., Abbasi, A., Mink, J., Persson, I. & Sandstrom, M., *Vibrational spectroscopic force field studies of dimethylsulfoxide and hexakis(dimethyl sulfoxide)scandium(III) iodide, and crystal and solution structure of the hexakis(dimethyl sulfoxide)scandium(III) ion*. *The Royal Society of Chemistry*, 2004. **2004**: p. 4038-4049.
 135. CEMRI. *Pure Component Properties*. 2018 October 2016]; Available from: <https://www.chemic.org/research/kdb/hcprop/showprop.php?cmpid=1859>.
 136. Sigma-Aldrich, *Dimethyl sulfoxide*. 2018, Merck KGaA: Germany.
 137. Mellouki, A., Leivin, J. & Herman, M., *The vibrational spectrum of pyrrole and furan in the gas phase*. *Chemical Physics*, 2001. **271**: p. 239-266.
 138. Han, Y., Ling, S., Qi, Z., Shao, Z. & Chen, X., *Application of far-infrared*

- spectroscopy to the structural identification of protein materials*. Chemical Physics, 2018. **20**: p. 11643-11648.
139. Sigma-Aldrich, *Bilirubin Conjugate, Ditaurate, Disodium Salt - Calbiochem*, in *Products*. 2018, Merck KGaA: Germany.